Technische Universität München

Ingenieurfakultät Bau Geo Umwelt

Lehrstuhl für Statik

ISOGEOMETRIC ANALYSIS OF THIN-WALLED STRUCTURES ON MULTIPATCH SURFACES IN FLUID-STRUCTURE INTERACTION

Andreas Apostolatos

Vollständiger Abdruck der von der Ingenieurfakultät Bau Geo Umwelt der Technischen Universität München zur Erlangung des akademischen Grades eines

Doktor-Ingenieurs

genehmigten Dissertation.

Vorsitzender:

Prof. Dr.-Ing. habil. Fabian Duddeck

Prüfer der Dissertation:

1. Prof. Dr.-Ing. Kai-Uwe Bletzinger
2. Prof. Dr. rer. nat. Bernd Simeon
3. Prof. Manolis Papadrakakis, Ph.D.

Die Dissertation wurde am 12.09.2018 bei der Technischen Universität München eingereicht und durch die Ingenieurfakultät Bau Geo Umwelt am 08.01.2019 angenommen.

Schriftenreihe des Lehrstuhls für Statik TU München

Band 38

Andreas Apostolatos

ISOGEOMETRIC ANALYSIS OF THIN-WALLED STRUCTURES ON MULTIPATCH SURFACES IN FLUID-STRUCTURE INTERACTION

München 2018

Veröffentlicht durch

Kai-Uwe Bletzinger
Lehrstuhl für Statik
Technische Universität München
Arcisstr. 21
80333 München

Telefon: +49(0)89 289 22422
Telefax: +49(0)89 289 22421
E-Mail: kub@tum.de
Internet: `www.st.bgu.tum.de`

ISBN: 978-3-943683-51-6

Abstract

In this thesis, the *Isogeometric Analysis* (IGA) of thin-walled structures modelled by trimmed *Non-Uniform Rational B-Spline* (NURBS) multipatches and its application to partitioned *Fluid-Structure Interaction* (FSI) is detailed. The structural analysis spans from linear two-dimensional elasticity up to three-dimensional geometrically non-linear membrane and Kirchhoff-Love shell analysis. IGA is a modern numerical method for solving *Boundary Value Problems* (BVPs) which in contrast to the standard *Finite Element Method* (FEM) uses the exact geometric description of the problem. In the present work, special emphasis is put on the continuity of the solution between trimmed NURBS multipatch surfaces which are standard in *Computer-Aided Design* (CAD). In this way, no effort is spent in preparing the analysis model as opposed to meshing in standard FEM and smoother approximations of the unknown fields are enabled. The latter is critical for the approximation of problems with high variational index such as the Kirchhoff-Love shell problem. Additionally, surface coupled multiphysics problems such as FSI especially benefit from the smoothness of the solution provided by isogeometric structural analysis. Accordingly, Penalty, Lagrange Multipliers and Nitsche-type methods are detailed and elaborated for the multipatch coupling and the application of weak Dirichlet boundary conditions on such structural models. FSI simulation is of high importance for the prediction of the mutual interaction between a fluid flow and a flexible structure. Typically, the fluid and the structural problems are solved separately while the coupling conditions are satisfied in an iterative manner along their common interface. In this way, the independent use of suitable methods for the discretization of each physical field is enabled. To exploit the benefits of isogeometric structural analysis on multipatches in FSI, a novel isogeometric mortar-based mapping method for real world CAD geometries is elaborated and detailed. Accordingly, field transformations between low order discretized fluid surfaces and trimmed multipatch NURBS representations of the structural surfaces are enabled in order to satisfy the interface constraints. The thesis is complemented with numerical examples in a sequence of increasing complexity, thus extending isogeometric analysis of thin-walled structures on multipatch surfaces to multiphysics problems of the fluid-structure interaction type.

Zusammenfassung

In dieser Arbeit wird die Simulation der Fluid-Struktur-Interaktion (FSI) bei Leichtbaustrukturen unter Verwendung der *Isogeometrischen Analyse* (IGA) basierend auf getrimmten Multi-Patch *Non-Uniform Rational B-Spline* (NURBS) Geometrien behandelt. Die Strukturanalyse reicht von Ebenen in linear elastischen Modellen und bis zu räumlichen Problemen, die mittels geometrisch nichtlinearen Membran- und Kirchhoff-Love-Schalen Formulierungen beschrieben werden. IGA ist eine moderne numerische Methode, die in dieser Arbeit auf der exakten Geometriebeschreibung mittels getrimmten Multi-Patch NURBS basiert, was ein quasi-Standard in *Computer-Aided Design* (CAD) ist. Durch die direkte Verwendung dieser Modelle wird die Aufbereitung der Rechenmodelle stark erleichtert. Die Hauptvorteile dieser Vorgehensweise bestehen darin, dass das Analysemodell nicht modifiziert wird und dass durch die Verwendung von Ansatzfunktionen mit höherer Ordnung die volle Genauigkeit bestehen bleibt. Dadurch bleibt die hohe Kontinuität erhalten, was eine wichtige Eigenschaft für Randwertprobleme mit hohem Variationsindex ist. Des Weiteren ist die höhere Glattheit der Lösung und der Geometrie bei IGA besonders vorteilhaft bei Oberflächengekoppelten Problemen, wie z. B. Fluid-Struktur Interaktion. Generell sind CAD Modelle durch mehrere NURBS Patches beschrieben, die zudem getrimmt sein können. Deshalb werden in dieser Arbeit Verfahren auf der Basis von Penalty, Lagrange-Multiplikator und Nitsche-Methode für IGA entwickelt, um die Aufbringung von inter-Patch Kontinuitäten und von schwachen Dirichlet Randbedingungen zu ermöglichen. FSI Simulationen dienen der Vorhersage der Wechselwirkung von Strömungen mit flexiblen Strukturen. Dabei werden typischerweise Strömungs- und Strukturmodell getrennt mit den jeweils am besten geeigneten Methoden und Diskretisierungen gelöst und die entsprechenden Kopplungsbedingungen an der gemeinsamen Oberfläche iterativ erfüllt. Um die Vorteile der CAD-basierten IGA in der FSI-Simulation nutzbar zu machen, wird eine neuartige Mortar-basierte Formulierung zur Kopplung von Fluid-Diskretisierungen niedriger Ordnung mit getrimmten Multi-Patch NURBS Oberflächen entwickelt und umgesetzt. In der vorliegenden Arbeit werden Benchmarks und Beispiele mit steigender Komplexität gezeigt, um die entwickelten Methoden zu erläutern und systematisch zu evaluieren.

Acknowledgments

As I see my work of the past six years materializing in this dissertation, I can only feel grateful for the amazing opportunities I was given, for having the chance to work with inspiring colleagues and have the brightest minds in the field as my mentors. Issuing a publication that I feel proud of, was my only goal. Today I feel that I have finally reached that goal and so it gives me immense pleasure to thank all the people without whom this would not have been possible. First and foremost, Prof. Kai-Uwe Bletzinger, thank you for giving me the opportunity to work on the research topic of my top interest by providing me with all the necessary means. Prof. Fabian Duddeck, Prof. Bernd Simeon and Prof. Manoli Papadrakaki thank you for being part of my examination board and for your interest in my work. Dr. Roland Wüchner your help has been invaluable, thank you for the assistance and endless discussions leading to a plethora of results and conclusions. Dr. Robert Schmidt, thank you for introducing me to the challenging world of isogeometric analysis on multipatches. Prof. Michael Breuer and Dr. Guillaume De Nayer from the Department of Fluid Mechanics at the Helmut Schmidt University in Hamburg, I am deeply grateful for having the opportunity to work with you, thank you for the outstanding collaboration. I would also like to express my gratitude to all of my colleagues and in particular: Altug Emiroglu, thanks for the joint development of the isogeometric mortar-based mapping method which is central part of this work. Shahrokh Shayegan, thanks for your endless help in setting up the fluid-structure interaction cases and for reading and helping me improve the corresponding parts of this thesis. Hosam AlSofi, many thanks for providing me with the computational fluid model of the hangar simulation and for your help on setting up the case. Anna Bauer, Tobias Teschemacher and Iñigo López, I would like to sincerely thank you for reading and helping me improve parts of this work. Michael Andre and Aditya Ghantasala, thank you for your support in using and troubleshooting within the cluster environment. Special thanks to my family and all dear friends from both cities of my heart, Piraeus♡ foremost and Munich, I am deeply grateful for having you. Irina, thank you for your support and patience throughout the last and hardest years of this work.

Andreas Apostolatos
Technical University of Munich
September 9, 2018

Contents

List of Symbols and Abbreviations

Units

m, cm, mm	Meter, centimeter [m^{-2}], millimeter [m^{-3}]
s	Second
Hz	Hertz [s^{-1}]
rad	Radian
Kg	Kilogram
N	Newton [$\mathrm{Kg} \times \mathrm{m/s}^2$]
Pa, KPa	Pascal [$\mathrm{N/m}^2$], kilopascal [$\mathrm{Pa} \times 10^3$]

Sets

$\mathbb{N}$	Set of natural numbers
$\mathbb{R}$, $\mathbb{R}_+^\star$	Set of real and strictly positive real numbers
$\mathbb{T}$	Time interval
$\mathcal{I}$	Set of all pairs of domain interfaces in a non-overlapping partition of $\mathit{\Omega}$

Indices

$\alpha, \beta, \gamma, \ldots$	Greek indices spanning from 1 to 2 if not otherwise defined
$i, j, k, \ldots$	Latin indices spanning from 1 to 3 if not otherwise defined
$\hat{\imath}$, i_r, $\hat{n}$, $\hat{k}$	Nonlinear iteration, refinement, time step and coupling iteration indices

Constants

π	3.14159265359...
e	2.71828182845...
g	Gravitational acceleration 9.81 m/s^2

Geometric constants

$\bar{R}$, $\bar{R}_{\mathrm{i}}$, $\bar{R}_{\mathrm{o}}$	Radii
$\bar{h}$, $\bar{h}_{\mathrm{plexiglas}}$	Structural thickness
$\hat{D}$, $\hat{D}_{\mathrm{inner}}$, $\hat{D}_{\mathrm{outer}}$	Cross sectional diameter of cables
$\hat{A}$, $\hat{A}_{\mathrm{inner}}$	Cross sectional area of cables
$\bar{L}$, $\bar{L}_1$, $\bar{L}_2$, $\bar{l}$	Characteristic lengths
I_{i}	Moment of inertia
$\bar{\phi}$	Angle
$h_{\mathrm{i}}^{(i,j)}$	Minimum element edge size on an interface trimming curve
$h_{\mathrm{d}}^{(i)}$	Minimum element edge size on a Dirichlet trimming curve

Material constants

E, E_{steel}, $\hat{E}$	Young's modulus of structure, steel material and cables
ν	Poisson ratio
μ, $\tilde{\nu}$	Dynamic and kinematic viscosity of the fluid
ρ, $\hat{\rho}$	Structural and cables' density
ρ_{steel}, $\rho_{\mathrm{plexiglas}}$	Steel and plexiglas density
$\tilde{\rho}$	Fluid density
c, $\hat{c}$	Structural and cables' damping coefficient
ζ_i	Damping ratio corresponding to natural frequency $\hat{f}_i$
β_{n}, γ_{n}	Newmark parameters
α_{r}, β_{r}	Rayleigh damping parameters

Curves

$\tilde{\gamma}$, $\hat{\gamma}$, γ	Parametric, physical and geometric images of curve
$\tilde{\gamma}_i$, $\hat{\gamma}_i$, γ_i	Parametric, physical and geometric images of trimming curve
$\tilde{\gamma}_j^{(i)}$, $\hat{\gamma}_j^{(i)}$, $\gamma_j^{(i)}$	Parametric, physical and geometric images of trimming curve in $\Omega^{(i)}$

$\gamma_{\mathrm{i}}^{(i,j)}$	Interface curve between two patches
γ_{i}	Union of all patch interfaces
$\hat{\gamma}_{\mathrm{d}}^{(i)}$	Trimming curve associated with Dirichlet boundary
$\varGamma_{\mathrm{d}}, \varGamma_{\mathrm{d}}^{(i)}$	Dirichlet boundary of a surface and its restriction along a patch boundary
$\varGamma_{\mathrm{n}}$	Neumann boundary of a surface
$\hat{\varGamma}_{\mathrm{c}}, \varGamma_{\mathrm{c}}$	Parametric and geometric image of cables
$\varGamma_{\mathrm{c}}^{(i)}$	Restriction of the cables' geometric image along $\partial\varOmega^{(i)}$
$\partial\varOmega, \partial\varOmega^{(i)}$	Boundary of surface $\varOmega$ and patch $\varOmega^{(i)}$

Surfaces

$\hat{\varOmega}, \varOmega$	Parametric and geometric space of a surface
$\overline{\varOmega}$	Closure of a surface in the Euclidean norm
$\hat{\varOmega}^{(i)}, \varOmega^{(i)}$	Parametric and geometric image of surface patch
$\varOmega_t$	Current configuration of a surface at time t
$\varOmega_{\mathrm{d}}$	Union of non-overlapping surfaces excluding the interfaces
$\tilde{\varOmega}_{\mathrm{d}}$	Inlet boundary of the fluid iBVP
$\tilde{\varOmega}_{\mathrm{n}}$	Outlet boundary of the fluid iBVP
$\varOmega_{\mathrm{h}}$	Discrete representation of a surface
$\varOmega_{\mathrm{h}}^{(i)}$	Part of $\varOmega_{\mathrm{h}}$ which has projection on $\varOmega^{(i)}$
$\mathcal{T}_{\mathrm{h}}$	Partition of a surface into finite elements
$\mathcal{T}_i, \mathcal{T}_k^{(i)}$	A finite element in partition $\mathcal{T}_{\mathrm{h}}$ and an isogeometric element in patch $\varOmega^{(i)}$
$\mathscr{S}, \mathscr{S}^{(i)}$	FSI interface and its restriction on $\varOmega^{(i)}$
$\mathscr{S}_{\mathrm{h}}$	Discrete representation of the FSI interface

Volumes

$\hat{V}, V$	Parametric and geometric images of a volume
V_t	Current volume configuration at time t
$\tilde{V}$	Domain of the fluid iBVP

Parametric coordinates

θ	Parametric coordinate of a curve
θ_α, θ_3	Parametric coordinates tangent and normal to a surface

θ_i	Parametric coordinates of a volume
$\boldsymbol{\Theta}, \boldsymbol{\Theta}_\alpha$	Knot vectors of a curve and a surface
$\hat{\theta}_i$	Knot in a knot vector
$\theta_\alpha^{(i)}$	Parametric coordinates of $\Omega^{(i)}$
$\boldsymbol{\theta}_{i,r}^{(j)}$	Intersection of all knot lines in $\hat{\Omega}^{(j)}$ with trimming curve $\hat{\gamma}_i^{(j)}$
$\mathrm{proj}_{\hat{\gamma}_j^{(i)}} \boldsymbol{\theta}_{i,r}^{(j)}$	Projection of $\boldsymbol{\theta}_{i,r}^{(j)}$ on trimming curve $\hat{\gamma}_j^{(i)}$ in $\Omega^{(i)}$
$\bar{\boldsymbol{\theta}}_{j,q}^{(i)}$	Sorted intersections of trimming curves with knot lines along $\hat{\gamma}_j^{(i)}$
$\tilde{\theta}_{j,q}^{(i)}$	Image of $\bar{\boldsymbol{\theta}}_{j,q}^{(i)} \in \hat{\gamma}_j^{(i)}$ in $\tilde{\gamma}_j^{(i)}$
$\boldsymbol{\theta}_{\mathrm{d},s}^{(i)}$	Intersections of $\hat{\gamma}_\mathrm{d}^{(i)}$ with knot lines in $\hat{\Omega}^{(i)}$
$\tilde{\theta}_{\mathrm{d},s}^{(i)}$	Parametric images of $\boldsymbol{\theta}_{\mathrm{d},s}^{(i)} \in \hat{\gamma}_\mathrm{d}^{(i)}$ in $\tilde{\gamma}_\mathrm{d}^{(i)}$
$\boldsymbol{\theta}_j^{(i)}$	Parametric coordinates of projected node $\mathbf{X}_j$ in $\hat{\Omega}^{(i)}$
$\tilde{\boldsymbol{\theta}}_j^{(i)}$	Fictitious parametric coordinates of node $\mathbf{X}_j$ in $\hat{\Omega}^{(i)}$

Parametrizations

$\mathbf{C}, \hat{\mathbf{C}}$	Parametrizations of a curve
$\hat{\mathbf{C}}_i, \mathbf{C}_i$	Parametrizations of a trimming curve in $\hat{\Omega}$ and Ω
$\hat{\mathbf{C}}_j^{(i)}$	Parametrization of a trimming curve in $\hat{\Omega}^{(i)}$
$\mathbf{S}, \mathbf{S}_t$	Parametrization of a surface in the reference and current configuration
$\mathbf{S}^{(i)}$	Parametrization of a surface patch
$\mathbf{V}$	Parametrization of a volume

Scalars

$\tilde{\epsilon}$	Small number in the neighbourhood of zero
n, n_α	Number of basis functions of a curve and a surface in θ_α-direction
$n_\alpha^{(i)}$	Number of basis functions in $\Omega^{(i)}$ along θ_α-direction
$n_\mathrm{t}, n_\mathrm{t}^{(i)}$	Number of trimming curves in Ω and in $\Omega^{(i)}$
n_s	Number of patches in a multipatch geometry
n_d	Number of non-empty Dirichlet boundaries in a multipatch geometry
n_i	Number of non-empty interfaces in a multipatch geometry
$\hat{n}_\mathrm{d}^{(i)}$	Number of intersections of trimming curve $\hat{\gamma}_\mathrm{d}^{(i)}$ with the knot lines in $\hat{\Omega}^{(i)}$

$\hat{n}_i^{(j)}$	Number of intersections of trimming curve $\hat{\gamma}_i^{(j)}$ with the knot lines in $\hat{\mathit{\Omega}}^{(j)}$
$\bar{n}_j^{(i)}$	Total number of sorted points $\boldsymbol{\theta}_{j,r}^{(i)}$ and $\mathrm{proj}_{\hat{\gamma}_j^{(i)}} \boldsymbol{\theta}_{i,r}^{(j)}$ along $\hat{\gamma}_j^{(i)}$
$\hat{n}^{(i,j)}$, $\tilde{n}^{(i,j)}$	Number of elements for the Lagrange Multipliers discretizations
n_n	Number of nodes in a finite element mesh
n_e	Number of elements in a finite element mesh
n_p	Number of programs participating in a co-simulation
$n_\mathrm{f}^{[i]}$	Number of fields of the i-th program in a co-simulation
$\bar{n}_\mathrm{f}$	Number of filters in a co-simulation
$\lvert\gamma\rvert$	Length of curve γ
$\dim \boldsymbol{\mathcal{V}}_\mathrm{h}$	Dimension of space $\boldsymbol{\mathcal{V}}_\mathrm{h}$
m, m_α	Number of knots in $\boldsymbol{\Theta}$ and in $\boldsymbol{\Theta}_\alpha$
$\bar{m}$	Variational index of a weak form
T_0, T_∞	Start and end time of a time-dependent process
t, $t_{\hat{n}}$	Time instance and time step
Δt	Time step size
$\hat{\omega}$, $\hat{\omega}_i$	Circular frequencies in modal analysis
ω	Angular velocity of the flexible NREL phase VI wind turbine blades
$\hat{p}$, $\hat{p}_\alpha$	Polynomial order of the basis for a curve and a surface along θ_α-direction
$\hat{p}_\mathrm{max}^{(i)}$, $\hat{p}_\mathrm{max}^{(i,j)}$	Maximum polynomial order of patch $\mathit{\Omega}^{(i)}$ and between patches $\mathit{\Omega}^{(i)}$, $\mathit{\Omega}^{(j)}$
$\hat{p}_k^{(i)}$	Polynomial order of trimming curve $\hat{\gamma}_k^{(i)}$ in $\mathit{\Omega}^{(i)}$
$\hat{q}$	Integer ranging from 0 to $\hat{p}$
$\hat{k}_i$	Multiplicity of knot $\hat{\theta}_i$ in $\boldsymbol{\Theta}$
$\hat{w}_i$, $\hat{w}_{i,j}$	Weight of an 1D and a 2D NURBS basis function
λ_i, λ_o	Line parameters between zero and one
f_i, f_i^h	Natural frequencies for the reference and the numerical solution
C, $\bar{C}$, $\hat{C}$	Coercivity, continuity and LBB constant
$\hat{C}^{(i,j)}$	Coercivity constant for the interface Nitsche method
$\bar{C}^{(i)}$	Coercivity constant for the boundary Nitsche method
$\hat{C}_r^{(i,j)}$, $\bar{C}_r^{(i)}$	Eigenvalues for the estimation of the Nitsche stabilization parameters

h	Discretization density
Re	Reynolds number

Scalar fields

$\varGamma^{\lambda}_{\alpha\beta}$	Christoffel symbols $\mathbf{A}^{\lambda}\cdot\partial\mathbf{A}_{\alpha}/\partial\theta_{\beta}$
$\bar{k}$	Curvature along a surface
$\bar{k}_{\alpha}$	Principal curvatures of a surface
$\bar{K}$	Gaussian curvature
q^{α}	Contravariant components of the shear force
$\hat{\alpha}$, $\hat{\alpha}^{(i,j)}$	Penalty parameters for the displacement continuity
$\tilde{\alpha}$, $\tilde{\alpha}^{(i,j)}$	Penalty parameters for the rotation continuity
$\bar{\alpha}$, $\bar{\alpha}^{(i)}$	Penalty parameters along the Dirichlet boundaries
$\hat{\beta}$, $\hat{\beta}^{(i,j)}$	Stabilization parameters for the displacement continuity
$\bar{\beta}$, $\bar{\beta}^{(i)}$	Stabilization parameters along the Dirichlet boundaries
n^{p}_{α}	Principal stress-resultant force fields
p	Fluid pressure

Unit vectors

$\mathbf{e}_i$	Cartesian base vectors in geometric space
$\hat{\mathbf{e}}$, $\hat{e}_{\alpha}$	Unit normal to Neumann boundary vector and its covariant components
$\tilde{\mathbf{e}}_{\mathrm{n}}$	Outward normal to the boundary of the fluid domain
$\hat{\mathbf{e}}_{\mathrm{t}}$, $\hat{\mathbf{e}}_{\mathrm{n}}$, $\hat{\mathbf{e}}_{\mathrm{b}}$	Tangent, normal and binormal unit vectors of a curve (Frenet basis)
$\hat{e}^{\alpha}_{\mathrm{t}}$, $\hat{e}^{\alpha}_{\mathrm{n}}$	Contravariant components of the tangent and normal vectors
$\hat{\mathbf{e}}^{(i)}_{\mathrm{t}}$, $\hat{\mathbf{e}}^{(i)}_{\mathrm{n}}$	Tangent and normal vectors of a curve in $\varOmega^{(i)}$

Position vectors

$\mathbf{X}$, X_i	Material point in the reference configuration and its Cartesian components
$\mathbf{x}$	Material point in the current configuration
$\mathbf{x}_{\mathrm{a}}$, $\mathbf{x}_{\mathrm{b}}$	Tip coordinates at the current configuration of the slit annular plate
$\mathbf{X}_{\mathrm{m}}$, $\mathbf{X}_{\mathrm{a}}$	Mid-point and inspection point in the reference configuration of a structure
$\mathbf{X}_j$, $\mathbf{X}^{(i)}_j$	Node in a mesh and its projection on $\varOmega^{(i)}$
$\mathbf{X}_{\mathrm{i}}$, $\mathbf{X}_{\mathrm{o}}$	Vertices of a finite element edge with and without projection on $\varOmega^{(i)}$
$\mathbf{X}_{\mathrm{t}}$, $\mathbf{X}_{\mathrm{u}}$, $\mathbf{X}_{\mathrm{d}}$	Tip, upstream and downstream points of the right NREL wind turbine blade

$\hat{\mathbf{X}}_i$, $\hat{\mathbf{X}}_{i,j}$	Control point of a curve and a surface

Base vectors

$\hat{\mathbf{A}}$, $\mathbf{A}$	Base vector in the parametric and the geometric space of a curve
$\tilde{\mathbf{A}}$	Contravariant base vector of a curve
$\mathbf{a}$	Base vector in the current configuration of the cables
$\mathbf{A}_\alpha$, $\mathbf{A}_3$	Tangent and normal base vectors of a surface in the reference configuration
$\mathbf{a}_\alpha$, $\mathbf{a}_3$	Tangent and normal base vectors of a surface in the current configuration
$\tilde{\mathbf{a}}_3$, $\bar{a}_3$	Not normalized surface normal vector $\mathbf{a}_1 \times \mathbf{a}_2$ and its length
$\mathbf{A}^\alpha$	Contravariant base vectors of a surface in the reference configuration
$\hat{\mathbf{A}}_i$, $\mathbf{A}_i$	Base vectors in the parametric and the geometric space of a volume
$\mathbf{A}^i$	Contravariant base vectors of a volume in the reference configuration
$\mathbf{a}_i$	Covariant base vectors of a volume in the current configuration

Vector fields

$\mathbf{F}$	Vector-valued function field
$\mathbf{c}$	Vector constraint
$\mathbf{v}$, v^β	Curvature direction vector and its contravariant components
$\mathbf{v}_\alpha$	Principal curvature direction vectors on a surface
$\mathbf{h}$	Vector-valued function in $\boldsymbol{\mathcal{V}}$
$\boldsymbol{\omega}$, ω^ζ	Rotation vector and its contravariant components on a surface
ω_t, ω_n	Rotation around the tangent and the normal vector
$\boldsymbol{\omega}^{(i)}$	Rotation vector in $\Omega^{(i)}$
$\mathbf{d}$, $\dot{\mathbf{d}}$, $\ddot{\mathbf{d}}$	Structural displacement, velocity and acceleration fields
d_i^0, d^i	Cartesian and contravariant components of the displacement field
d^α, d_3	Contravariant components of the displacement field on a surface
$\dot{d}^\alpha$, $\dot{d}_3$	Contravariant components of the velocity on a surface
$\ddot{d}^\alpha$, $\ddot{d}_3$	Contravariant components of the acceleration field on a surface
$\mathbf{d}_\mathrm{h}$	Structural displacement field on a discrete surface
$\mathbf{w}$, w_α	Displacement of surface normal vector and its covariant components
$\mathbf{g}$	Prescribed displacement field along a Dirichlet boundary
$\mathbf{t}$, $\hat{\mathbf{t}}$	Traction vectors on a membrane and on cables

$\mathbf{d}^{(i)}$, $\mathbf{t}^{(i)}$	Displacement and traction vector in $\Omega^{(i)}$
$\mathbf{n}^{\alpha}$	Reaction stress-resultant traction force vector along θ_{α}
$\mathbf{m}^{\alpha}$	Reaction stress-resultant traction moment vector along θ_{α}
$\mathbf{b}$, b^{α}, b_3	Body force vector and its contravariant components
$\mathbf{b}_{\mathrm{g}}$, $\mathbf{b}_{\mathrm{c}}$	Gravitational and centrifugal body force vectors
$\bar{\mathbf{t}}$, $\bar{\mathbf{t}}^{(i,j)}$	Mean interface traction vector along γ_{i} and $\gamma_{\mathrm{i}}^{(i,j)}$
$\mathbf{d}_0$, $\boldsymbol{v}_0$	Initial condition for the structural displacement and velocity fields
$\boldsymbol{\lambda}$, $\boldsymbol{\mu}$	Lagrange Multipliers fields for the displacement and rotation continuity
$\boldsymbol{\lambda}^{(i,j)}$, $\boldsymbol{\mu}^{(i,j)}$	Lagrange Multipliers fields along an interface
$\bar{\mathbf{p}}$	Prescribed stress-resultant traction force along a surface boundary
$\bar{\mathbf{r}}$	Prescribed stress-resultant traction moment along a surface boundary
$\hat{\boldsymbol{\chi}}$, $\hat{\boldsymbol{\chi}}^{(i,j)}$	Interface jump on the displacement field and its restriction on $\gamma_{\mathrm{i}}^{(i,j)}$
$\tilde{\boldsymbol{\chi}}$, $\tilde{\boldsymbol{\chi}}^{(i,j)}$	Interface jump on the rotation field and its restriction on $\gamma_{\mathrm{i}}^{(i,j)}$
$\boldsymbol{v}$, $\boldsymbol{v}^{\mathrm{h}}$	Isogeometric and standard finite element discretizations of a vector field
$\boldsymbol{v}_i^{[j]}$	i-th field in j-th program within a co-simulation
$\mathbf{u}$, u_i	Fluid velocity field and its Cartesian components
$\mathbf{u}^{\mathrm{d}}$, u_i^{d}	Fluid domain velocity field and its Cartesian components
$\tilde{\boldsymbol{v}}$	Prescribed inlet fluid velocity
$\boldsymbol{\mathcal{U}}$	Fluid displacement field on the FSI interface
$\tilde{\mathbf{b}}$, $\tilde{\mathbf{b}}_{\mathrm{h}}$	Structural surface traction field on the exact and the discretized surface
$\tilde{\mathbf{t}}$	Fluid boundary traction field
$\tilde{\boldsymbol{\tau}}$	Prescribed fluid traction field at the outlet
Tensor fields	
$\boldsymbol{\mathcal{S}}$, $\mathcal{S}^0_{ij}$, $\mathcal{S}^{ij}$	PK2 stress, its Cartesian and contravariant components in the continuum
$\mathbf{n}$, $n^{\alpha\beta}$	PK2 stress-resultant force and its contravariant components on a surface
$\mathbf{n}_0$, $n_0^{\alpha\beta}$	PK2 prestress and its contravariant components on a surface
$\mathbf{n}^{(i)}$	PK2 stress-resultant force in $\Omega^{(i)}$
$\mathbf{m}$, $m^{\alpha\beta}$	PK2 stress-resultant moment and its contravariant components on a surface
$\bar{m}^{\alpha\beta}$	PK2 stress-resultant moment components defined over a normalized basis

$\hat{\mathbf{f}}$, $\hat{f}$	PK2 stress-resultant force of cables and its component
$\hat{\mathbf{f}}_0$, $\hat{f}_0$	PK2 prestress and its component for the cables
$\boldsymbol{\sigma}$, σ_{ij}	Cauchy stress tensor and its Cartesian components for the fluid iBVP
$\boldsymbol{\mathcal{C}}$, $\mathcal{C}^{ijkl}$	Material tensor and its contravariant components in the continuum
$\mathcal{C}^{\alpha\beta\gamma\delta}$	Contravariant components of the material tensor on a surface
$\boldsymbol{\mathcal{C}}_{\mathrm{m}}$, $\boldsymbol{\mathcal{C}}_{\mathrm{b}}$	Material tensor for the membrane and the bending stiffness on a surface
$\boldsymbol{\mathcal{A}}$, $\mathcal{A}_{\alpha\beta}$	Metric and its covariant components on a surface
$\alpha_{\alpha\beta}$	Covariant metric components on surface at the current configuration
$\mathcal{A}_{ij}$	Covariant metric components in continuum at reference configuration
$\mathcal{A}^{ij}$	Contravariant metric components in continuum at reference configuration
α_{ij}	Covariant metric components in continuum at the current configuration
$\boldsymbol{\mathcal{B}}$, $\mathcal{B}_{\alpha\beta}$	Curvature tensor and its covariant components at reference configuration
$\beta_{\alpha\beta}$	Covariant components of curvature on surface at the current configuration
$\bar{\mathcal{B}}_{\alpha\beta}$	Normalized covariant curvature components on a surface
$\delta^{\alpha\beta}$, δ^{ij}	Kronecker delta components in two- and three-dimensions
$\boldsymbol{\mathcal{E}}$, $\mathcal{E}_{ij}$	GL strain and its covariant components in the continuum
$\boldsymbol{\varepsilon}$, $\varepsilon_{\alpha\beta}$	GL membrane strain and its covariant components on a surface
$\boldsymbol{\kappa}$, $\kappa_{\alpha\beta}$	GL bending strain and its covariant components on a surface
$\hat{\boldsymbol{\varepsilon}}$, $\hat{\varepsilon}$	GL strain of the cables and its component
$\boldsymbol{\epsilon}$, $\epsilon^{\alpha\zeta}$	Permutation tensor and its contravariant components on a surface
δ_2^{ij}, ϵ_2^{ij}	Kronecker delta and permutation components on the X_1-X_3 plane
$\boldsymbol{\mathit{\Omega}}_2$, $\mathit{\Omega}_2^{ij}$	Rotation in X_1-X_3 plane $\mathit{\Omega}_2^{ij} = -\sin(\omega t)\epsilon_2^{ij} + \cos(\omega t)\delta_2^{ij}$ (anticlockwise)

Spaces

$\mathbb{R}^2$, $\mathbb{R}^3$	Multidimensional Euclidean spaces
D	Subspace of $\mathbb{R}^\alpha$
$C^{\bar{m}}(\mathit{\Omega})$	Space of functions with up to $\bar{m}$-th order continuous derivatives in $\mathit{\Omega}$
$\boldsymbol{\mathcal{L}}^2(\gamma_{\mathrm{i}})$	Space of vector-valued square integrable functions along γ_{i}
$\boldsymbol{\mathcal{H}}^{\bar{m}}(\mathit{\Omega})$	$\bar{m}$-th order Sobolev space of vector-valued functions in $\mathit{\Omega}$
$\boldsymbol{\mathcal{P}}(\mathcal{T}_i)$	Space of vector-valued polynomial functions in $\mathcal{T}_i$

$\boldsymbol{\mathcal{P}}_0\left(\gamma_{\mathrm{i}}^{(i,j)}\right)$	Space of vector-valued piecewise constant functions in $\gamma_{\mathrm{i}}^{(i,j)}$
$\boldsymbol{\mathcal{P}}_\alpha\left(\mathcal{T}_i\right)$	Space of vector-valued linear and bilinear vector functions in $\mathcal{T}_i$
$\boldsymbol{\mathcal{R}}\left(\Omega^{(i)}\right)$	Space of vector-valued rational functions in $\Omega^{(i)}$
$\boldsymbol{\mathcal{V}}$	Admissible solution space of a variational problem
$\boldsymbol{\mathcal{V}}_{\mathrm{k}}$	Kernel of $\boldsymbol{\mathcal{V}}$ with respect to a constraint $\mathbf{c}$
$\boldsymbol{\mathcal{V}}_{\mathrm{h}}$	Finite dimensional admissible solution space of a variational problem
$\boldsymbol{\mathcal{V}}^{(i)}, \boldsymbol{\mathcal{V}}_{\mathrm{h}}^{(i)}$	Admissible solution space in $\Omega^{(i)}$ and its finite dimensional subspace
$\hat{\boldsymbol{\mathcal{V}}}_{\mathrm{h}}, \hat{\boldsymbol{\mathcal{V}}}_{\mathrm{h}}^{(i,j)}$	Lagrange Multipliers finite dimensional spaces (displacement continuity)
$\tilde{\boldsymbol{\mathcal{V}}}_{\mathrm{h}}, \tilde{\boldsymbol{\mathcal{V}}}_{\mathrm{h}}^{(i,j)}$	Lagrange Multipliers finite dimensional spaces (rotation continuity)
$\boldsymbol{\Upsilon}, \boldsymbol{\Upsilon}_{\mathrm{h}}$	Admissible space for isogeometric and finite element solutions

Forms and functionals

L	Functional defined by means of an integral
$\mathcal{J}, \mathcal{J}_{\mathbf{d}}, \mathcal{J}_{\boldsymbol{\nabla}\mathbf{d}}$	A functional and its gradients $(\partial\mathcal{J}/\partial d_i^0)\mathbf{e}_i$ and $(\partial\mathcal{J}/\partial d_{i,j}^0)\mathbf{e}_i\otimes\mathbf{e}_j$
a, l	Form and linear functional of a variational problem

Variations

δL	First variation of a functional L
$\delta\mathbf{d}$	Admissible variation of the displacement field
$\delta\mathbf{c}$	Variation of a constraint
$\delta\boldsymbol{\omega}$	Variation of the rotation vector
$\delta\hat{\boldsymbol{\chi}}, \delta\tilde{\boldsymbol{\chi}}$	Variation of the interface displacement and rotation jump
$\delta\hat{\mathbf{d}}_{\vert\mathscr{S}}$	Variation of the structural DOFs along the FSI interface
$\delta\hat{\boldsymbol{\mathcal{U}}}$	Variation of the fluid FSI interface DOFs
$\delta\boldsymbol{\varepsilon}, \delta\hat{\boldsymbol{\varepsilon}}$	Variation of the GL membrane strain of a surface and the cables
$\delta\boldsymbol{\kappa}$	Variation of the GL bending strain of a surface
$\delta\bar{\mathbf{t}}, \delta\mathbf{t}$	Variation of the mean interface vector and the traction vector itself
$\delta\boldsymbol{\lambda}, \delta\boldsymbol{\mu}$	Variation of the Lagrange Multipliers fields
$\delta\boldsymbol{v}$	Variation of vector field $\boldsymbol{v}$ in isogeometric mortar-based mapping

Basis functions

$N_{\hat{p},i}$	1D scalar-valued B-Spline basis function of order $\hat{p}$

$R_{\hat{p},i}$	1D scalar-valued NURBS basis function of order $\hat{p}$
$N_{\hat{p}_1,\hat{p}_2,i,j}$	2D scalar-valued B-Spline basis functions
$R_{\hat{p}_1,\hat{p}_2,i,j}$	2D scalar-valued NURBS basis functions
$R_{\hat{p}_1,\hat{p}_2,k}$	2D scalar-valued NURBS basis functions sequentially ordered
$R^{(i)}_{\hat{p}_1^{(i)},\hat{p}_2^{(i)},k}$	2D scalar-valued NURBS basis functions in $\mathit{\Omega}^{(i)}$ sequentially ordered
$R^{(i,j)}_{\hat{p},k}$	1D scalar-valued NURBS basis functions along $\gamma_{\mathrm{i}}^{(i,j)}$
$\boldsymbol{\phi}_i$	2D vector-valued basis function for the displacement field
$\boldsymbol{\phi}^{\mathrm{h}}_i$	2D vector-valued standard FEM basis function for the primal field
$\bar{\boldsymbol{\phi}}^{(i)}_j$	2D vector-valued NURBS basis function for the primal field in $\mathit{\Omega}^{(i)}$
$\hat{\boldsymbol{\phi}}^{(i,j)}_k$, $\tilde{\boldsymbol{\phi}}^{(i,j)}_k$	2D vector-valued NURBS basis functions for the Lagrange Multipliers fields

Degrees of Freedom (DOFs)

$\hat{d}_i$	Displacement DOF
$\hat{\mathbf{d}}$, $\dot{\hat{\mathbf{d}}}$, $\ddot{\hat{\mathbf{d}}}$	Vectors of displacement, velocity and acceleration DOFs
$\hat{\mathbf{d}}_{\hat{n}}$, $\dot{\hat{\mathbf{d}}}_{\hat{n}}$, $\ddot{\hat{\mathbf{d}}}_{\hat{n}}$	Vectors of displacement, velocity and acceleration DOFs at given time
$\hat{\mathbf{d}}_{\hat{n},\hat{\imath}}$, $\hat{\mathbf{d}}^{(i)}_{\hat{n},\hat{\imath}}$	Vector of displacement DOFs at given time and iteration in $\mathit{\Omega}$ and in $\mathit{\Omega}^{(i)}$
$\mathit{\Delta}_{\hat{n},\hat{\imath}}\hat{\mathbf{d}}$	Increment of the displacement DOF vector at given time and iteration
$\hat{\mathbf{d}}_{\vert\mathscr{S}}$, $\hat{\mathbf{d}}_{\mathrm{h}\,\vert\mathscr{S}}$	Vector of structural displacement DOFs for IGA and FEM on FSI interface
$\hat{\mathbf{d}}_{\hat{n},\hat{k}}$	Vector of structural DOFs at given time and coupling iteration
$\hat{\mathbf{v}}$, $\hat{\mathbf{v}}_i$	Eigenvectors corresponding to displacement DOFs
$\hat{d}^{(i)}_j$, $\hat{\mathbf{d}}^{(i)}$	Displacement DOF and vector of displacement DOFs in $\mathit{\Omega}^{(i)}$
$\hat{\lambda}^{(i,j)}_k$, $\hat{\mu}^{(i,j)}_k$	Lagrange Multipliers DOFs along $\gamma_{\mathrm{i}}^{(i,j)}$
$\hat{\boldsymbol{\lambda}}^{(i,j)}$, $\hat{\boldsymbol{\mu}}^{(i,j)}$	Vectors of Lagrange Multipliers DOFs along $\gamma_{\mathrm{i}}^{(i,j)}$
$\hat{\boldsymbol{\lambda}}$, $\hat{\boldsymbol{\mu}}$	Vectors of Lagrange Multipliers DOFs along γ_{i}
$\hat{\boldsymbol{\lambda}}_{\hat{n},\hat{\imath}}$, $\hat{\boldsymbol{\mu}}_{\hat{n},\hat{\imath}}$	Vectors of Lagrange Multipliers DOFs for given time step and iteration
$\hat{\upsilon}^{\mathrm{h}}_i$, $\hat{\upsilon}^{(i)}_j$	DOFs on nodes and on control points
$\hat{\boldsymbol{\upsilon}}^{\mathrm{h}}$, $\hat{\boldsymbol{\upsilon}}^{(i)}$, $\hat{\boldsymbol{\upsilon}}$	Vector of DOFs on nodes, control points in $\mathit{\Omega}^{(i)}$ and control points in $\mathit{\Omega}$
$\hat{\boldsymbol{\mathcal{U}}}$	Vector of fluid displacement DOFs on the FSI interface

Discrete matrices and vectors

$\bullet_{(i,j)}, \bullet_{(i)}$	(i,j)-th component of a matrix and i-th component of vector
$\bullet_{\mathrm{v}}$	Tensors in Voigt notation on an orthonormal basis $[\bullet^0_{11} \quad \bullet^0_{22} \quad \bullet^0_{12}]^{\mathrm{T}}$
$\mathbf{K}_0$	Linear stiffness matrix at the start time of the dynamic process
$\mathbf{K}, \mathbf{R}$	Tangent stiffness matrix and steady-state residual force vector
$\mathbf{K}_{\mathrm{d}}, \mathbf{R}_{\mathrm{d}}$	Dynamic tangent stiffness matrix and dynamic residual force vector
$\mathbf{M}, \mathbf{D}$	Mass and damping matrix
$\hat{\mathbf{F}}, \hat{\mathbf{F}}_{\hat{n}}$	External force vector and its instance at given time
$\mathbf{K}_{\mathrm{d}}^{(i)}, \mathbf{R}_{\mathrm{d}}^{(i)}$	Dynamic tangent stiffness and residual force vector in $\Omega^{(i)}$
$\hat{\mathbf{C}}_{\hat{\alpha}}^{(i)}, \hat{\mathbf{C}}_{\hat{\alpha}}^{(i,j)}, \hat{\mathbf{R}}_{\hat{\alpha}}^{(i)}$	Displacement continuity enforcement (Penalty)
$\tilde{\mathbf{C}}_{\tilde{\alpha}}^{(i)}, \tilde{\mathbf{C}}_{\tilde{\alpha}}^{(i,j)}, \tilde{\mathbf{R}}_{\tilde{\alpha}}^{(i)}$	Rotation continuity enforcement (Penalty)
$\bar{\mathbf{C}}_{\bar{\alpha}}^{(i)}, \bar{\mathbf{R}}_{\bar{\alpha}}^{(i)}, \bar{\mathbf{F}}_{\bar{\alpha}}^{(i)}$	Weak Dirichlet boundary conditions (Penalty)
$\boldsymbol{\Lambda}, \boldsymbol{\Lambda}^{(i,j)}$	Displacement continuity enforcement (Lagrange Multipliers)
$\boldsymbol{\mathcal{M}}, \boldsymbol{\mathcal{M}}^{(i,j)}$	Rotation continuity enforcement (Lagrange Multipliers)
$\hat{\mathbf{C}}_{\mathrm{n}}^{(i)}, \hat{\mathbf{C}}_{\mathrm{n}}^{(i,j)}, \hat{\mathbf{R}}_{\mathrm{n}}^{(i)}$	Displacement continuity enforcement (Nitsche)
$\hat{\mathbf{C}}_{\hat{\beta}}^{(i)}, \hat{\mathbf{C}}_{\hat{\beta}}^{(i,j)}, \hat{\mathbf{R}}_{\hat{\beta}}^{(i)}$	Stabilization for displacement continuity enforcement (Nitsche)
$\hat{\mathbf{Q}}_{\mathrm{n}}^{(i,j)}, \hat{\mathbf{Q}}_{\mathrm{n}}^{(i)}, \hat{\mathbf{q}}_{\mathrm{n}}^{(i,j)}$	Stabilization estimation for displacement continuity enforcement (Nitsche)
$\mathbf{K}^{(i,j)}$	Tangent stiffness matrix restricted in patch pair $\Omega^{(i)}$-$\Omega^{(j)}$
$\bar{\mathbf{C}}_{\mathrm{n}}^{(i)}, \bar{\mathbf{R}}_{\mathrm{n}}^{(i)}$	Weak Dirichlet boundary conditions (Nitsche)
$\bar{\mathbf{C}}_{\bar{\beta}}^{(i)}, \bar{\mathbf{R}}_{\bar{\beta}}^{(i)}$	Stabilization for weak Dirichlet boundary conditions (Nitsche)
$\bar{\mathbf{Q}}^{(i)}$	Stabilization estimation for weak Dirichlet boundary conditions (Nitsche)
$\mathbf{D}_{\mathrm{m}}, \mathbf{D}_{\mathrm{b}}$	Material matrices in Voigt notation for membrane and bending stiffness
$\mathbf{C}_{\mathrm{rr}}, \mathbf{C}_{\mathrm{rn}}, \mathbf{C}_{\hat{\alpha},\tilde{\alpha},\bar{\alpha}}$	Mortar-based mapping for transformation of fields on NURBS surfaces
$\mathbf{C}_{\mathrm{rr}}^{(i)}, \mathbf{C}_{\mathrm{rn}}^{(i)}$	Mortar-based mapping for transformation of fields on patch $\Omega^{(i)}$
$\mathbf{C}_{\mathrm{nn}}, \mathbf{C}_{\mathrm{nr}}$	Mortar-based mapping for transformation of fields on Ω_{h}
$\mathbf{B}_{\mathrm{t}}$	B-operator matrix for the rotation field around the tangent vector
$\tilde{\mathbf{F}}_{\mathrm{b}}, \tilde{\mathbf{F}}_{\mathrm{b}}^{(i)}, \tilde{\mathbf{F}}_{\mathrm{b}}^{\mathrm{h}}, \tilde{\mathbf{F}}_{\mathrm{t}}$	Consistent force vectors on FSI interface for IGA, patch $\Omega^{(i)}$, FEM and FVM

Notations and operations

$d_i^0\mathbf{e}_i$	Einstein's summation convention over repeated indices $\sum_{i=1}^{3} d_i^0\mathbf{e}_i$

$d^0_{i,j}$	Partial derivative of d^0_i with respect to X_j, $\partial d^0_i/\partial X_j$
$\mathcal{O}(\bullet)$	Order of magnitude
$\mathbf{V}\circ\hat{\mathbf{C}}$	Composition $\mathbf{V}\left(\hat{\mathbf{C}}(\theta)\right)$
$\boldsymbol{\omega}\cdot\mathbf{e}_\mathrm{t}$	Scalar product $\omega_\alpha e^\alpha_\mathrm{t}$
$\boldsymbol{\mathcal{C}}:\boldsymbol{\mathcal{E}}$	Double contraction between tensors $\mathcal{C}^{ijkl}\mathcal{E}_{kl}\,\mathbf{A}_i\otimes\mathbf{A}_j$
$\partial^\alpha(\bullet)/\partial\theta^\alpha$	Partial derivative of α-th order with respect to θ
$n^{\alpha\beta}\vert_\gamma$	Covariant derivative $\partial n^{\alpha\beta}/\partial\theta_\gamma+n^{\lambda\beta}\Gamma^\alpha_{\gamma\lambda}+n^{\alpha\lambda}\Gamma^\beta_{\gamma\lambda}$
$\hat{\mathbf{e}}_\mathrm{b}\times\hat{\mathbf{e}}_\mathrm{t}$	Cross product
$\mathbf{A}^\alpha\otimes\mathbf{A}^\beta$	Dyadic product
$\dot{\mathbf{d}},\ddot{\mathbf{d}}$	Time derivatives $\partial\mathbf{d}/\partial t$, $\partial^2\mathbf{d}/\partial t^2$
$D\mathbf{u}$	Material derivative $\partial\mathbf{u}/\partial t+\left(\mathbf{u}-\mathbf{u}^\mathrm{d}\right)\cdot\boldsymbol{\nabla}\mathbf{u}$
$\boldsymbol{\nabla}\mathbf{d}$	Gradient of the structural displacement field $\partial d^0_i/\partial X_j\,\mathbf{e}_i\otimes\mathbf{e}_j$
$\boldsymbol{\nabla}\cdot\mathbf{u}$	Divergence of the fluid velocity field $\partial u^0_i/\partial X_i$
$\langle\delta\mathbf{d},\mathbf{d}\rangle_{0,\Omega}$	Inner product in the $\boldsymbol{\mathcal{L}}^2(\Omega)$ space $\int_\Omega\delta d^0_i\,d^0_i\,\mathrm{d}\Omega$
$\lVert\mathbf{X}\rVert_2$	2-norm of vector $\mathbf{X}$, $\left(\sum_{i=1}^3 X_i^2\right)^{1/2}$
$\lVert\bullet\rVert_{\boldsymbol{\mathcal{V}}}$	Norm in space $\boldsymbol{\mathcal{V}}$
$\lVert\mathbf{D}_\mathrm{m}\rVert_\mathrm{F}$	Matrix norm $\left(\sum_i\sum_j D^2_{\mathrm{m}(i,j)}\right)^{1/2}$
$\lVert\mathbf{d}\rVert_{0,\Omega}$	Norm in the $\boldsymbol{\mathcal{L}}^2(\Omega)$ space, $\langle\mathbf{d},\mathbf{d}\rangle^{1/2}_{0,\Omega}$
$\lVert\mathbf{d}\rVert_{1,\Omega}$	Norm in the $\boldsymbol{\mathcal{H}}^1(\Omega)$ space $\left(\int_\Omega\mathbf{d}\cdot\mathbf{d}\,\mathrm{d}\Omega+\int_\Omega\boldsymbol{\nabla}\mathbf{d}:\boldsymbol{\nabla}\mathbf{d}\,\mathrm{d}\Omega\right)^{1/2}$
$\prod_{i=1}^{n_\mathrm{s}}\boldsymbol{\mathcal{V}}^{(i)}_\mathrm{h}$	Product space $\boldsymbol{\mathcal{V}}^{(1)}_\mathrm{h}\times\cdots\times\boldsymbol{\mathcal{V}}^{(n_\mathrm{s})}_\mathrm{h}$
$S^{\alpha\beta}\big\vert_{\theta_3=0}$	Evaluation of $S^{\alpha\beta}$ at $\theta_3=0$
$\mathbf{h}_{\vert\mathcal{T}_i}$	Restriction of field $\mathbf{h}$ in $\mathcal{T}_i$
$\boldsymbol{\Phi}_i$	i-th filter in a co-simulation
$\bullet_\mathrm{h}$, $\bullet^\mathrm{h}$	Numerically computed quantities
$\bullet^\mathrm{T}$	Transpose
$\lceil\bullet\rceil$	Round-up operator

Abbreviations

FSI	Fluid-Structure Interaction
CAD	Computer-Aided Design

List of Symbols and Abbreviations

IGA	Isogeometric Analysis
BVP(s)	Boundary Value Problem(s)
iBVP(s)	initial Boundary Value Problem(s)
NURBS	Non-Uniform Rational B-Spline
FEM	Finite Element Method
B-Rep	Boundary Representation
AiCAD	Analysis in Computer-Aided Design
IBRA	Isogeometric B-Rep Analysis
LBB	Ladyzhenskaya-Babuška-Brezzi
DOF(s)	Degree(s) of Freedom
CP(s)	Control Point(s)
FCM	Finite Cell Method
FVM	Finite Volume Method
ECL	Exact Coupling Layer
URS	Updated Reference Strategy
NREL	National Renewable Energy Laboratory
PDE(s)	Partial Differential Equation(s)
PK2	2nd Piola-Kirchhoff stress measure
GL	Green-Lagrange strain measure
DDM(s)	Domain Decomposition Method(s)
ALE	Arbitrary Lagrangian-Eulerian
CSD	Computational Structural Dynamics
CFD	Computational Fluid Dynamics
GS	Gauss-Seidel
BDF2	Backward Differentiation Formula 2
AMI	Arbitrary Moving Interface
MM	Mortar Mapping
IMM	Isogeometric Mortar Mapping
API	Application Programming Interface
MPI	Message Passing Interface
FI, iFI	Field Integration and inverse FI

Computers are good at following instructions,
but not at reading your mind.

Donald Knuth

Chapter 1

Introduction and Motivation

In this thesis, the partitioned *Fluid-Structure Interaction* (FSI) of thin-walled structures using their exact *Computer-Aided Design* (CAD) representation is detailed. Thin-walled structures of membrane or shell type are for instance stadium roofs and wind turbine blades, see Fig. 1.1. Such structures are typically subject to interaction with wind in addition to other types of external loading (e.g. self-weight, snow, etc.) and they can be modelled by their mid-surface, see in Başar et al. [1]. Their mechanical behaviour is herein predicted directly on their exact CAD representation using *Isogeometric Analysis* (IGA). IGA was firstly introduced in Hughes et al. [2] and Cottrell et al. [3] and it is a modern numerical method for the discretization and numerical approximation of solutions to *Boundary Value Problems* (BVPs) using the exact geometric description. Herein *Non-Uniform Rational B-Spline* (NURBS)-based IGA is considered for the solution of BVPs in multiple, possibly trimmed, surface patches stemming directly from CAD. IGA exhibits two main advantages compared to standard *Finite Element Method* (FEM): The significantly costly meshing step involved in preparing the computational model can be sidestepped since the NURBS basis functions from the geometric parametrization can be directly used for the analysis, see Fig. 1.2. Moreover, the NURBS basis func-

(a) Olympic stadium in Munich, Germany.

(b) Peace and Friendship stadium in Piraeus, Greece.

(c) NREL phase VI wind turbine (Simms et al. [7]).

Figure 1.1: Examples of thin-walled structures.

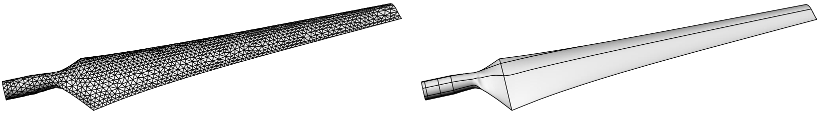

FEM computational model

IGA computational model

Figure 1.2: Faceted FEM (left) versus multipatch NURBS (right) computational models for a wind turbine blade.

tions offer high order smooth approximations of the unknown fields, thus providing higher convergence rates than standard FEM, see also in Buffa et al. [4]. Additionally, IGA enables the numerical discretization of problems with high variational index such as Kirchhoff-Love shells, where the standard C^0-continuous FEM cannot be directly applied. The herein considered structural analysis spans from two-dimensional linear elasticity to geometrically nonlinear membranes and Kirchhoff-Love shells whose mechanical behaviour is predicted numerically, see also in Papadrakakis [5]. Moreover, these kinds of structural problems greatly benefit from IGA given that they are posed on their mid-surface and that geometries stemming directly from CAD are frequently described by their *Boundary Representation* (B-Rep). Therefore, mid-surface reduced structures offer an excellent platform for *Analysis in Computer-Aided Design* (AiCAD) as demonstrated in *Isogeometric B-Rep Analysis* (IBRA) firstly introduced in Breitenberger et al. [6].

The challenge when applying IGA on trimmed multipatch geometries is that the continuity of the solution between the multiple, possibly trimmed, patches has to be ensured along their shared interfaces. Additionally, the application of Dirichlet boundary conditions has to be made weakly given that the patches might be trimmed. In this thesis, multiple methods are considered for treating the aforementioned problems which comprise Penalty, Lagrange Multipliers and Nitsche-type methods. The application of the aforementioned methods is firstly shown in two-dimensional linear elasticity. Subsequently, the Penalty versus the Nitsche-type method and the Penalty versus the Lagrange Multipliers method are elaborated and compared for the membrane and the Kirchhoff-Love shell problem, respectively.

Using the Penalty method, the weak form is extended by quadratic terms which contain Penalty parameters for the imposition of the desirable constraints, see also in Sanders et al. [8]. Provided that the constraints are linear with respect to the unknown fields, the additional Penalty terms are bilinear. As a result, elliptic problems remain elliptic which is highly desirable in terms of existence and uniqueness of solutions to such problems. In addition, the corresponding discrete matrices can be precomputed and used throughout the analysis, thus rendering the method efficient. Typically, smaller convergence rates than for the original problem are expected which depend on the choice of the Penalty parameters, see in Babuška [9]. Moreover, large values for the Penalty parameters may lead to badly conditioned matrices which in some cases can be singular. On the other hand, small values for the Penalty parameters might not be sufficient for the fulfilment of the desirable constraints, see e.g. in Apostolatos et al. [10]. Therefore, an appropriate choice of the Penalty parameters has to be made which is typically problem dependent. Furthermore, the Penalty method is often called *variationally inconsistent* in that an one-to-one correspondence between the strong and the weak forms of the problem cannot be established. This can be observed as a plateau in the convergence graphs as no uniform convergence can be obtained for a fixed Penalty parameter. Therefore the Penalty parameter(s) has(have) to be successively increased, leading in some cases to ill-conditioned systems.

The Lagrange Multipliers method on the other hand makes use of additional fields, the so-called Lagrange Multipliers fields, for the enforcement of the desirable constraints, see also in Babuška [11] and Simeon [12]. As for the Penalty method, the additional Lagrange Multipliers terms are bilinear, given that the desirable constraints are linear with respect to the unknown fields. Therefore, the discrete matrices resulting from the Lagrange Multipliers terms can be also in this case precomputed and used throughout the analysis rendering the method efficient. Additionally, the Lagrange Multipliers method is variationally consistent in contrast to the Penalty method in that it is characterized by uniform convergence. However, the formulation turns into a *saddle point* problem, see also in Apostolatos et al. [10]. The latter means that the *Ladyzhenskaya-Babuška-Brezzi* (LBB) condition needs to be satisfied in order to guarantee a unique solution of the problem, see in Brezzi et al. [13] and Brivadis et al. [14] for more information. This can be shown for particular problems and only for special choices of the finite dimensional spaces, see also in Gresho et al. [15]. Therefore, it is difficult to ensure that any general saddle point formulation has a unique solution. To circumvent this problem, alternative Lagrange Multipliers formulations exist, see also in Teschemacher et al. [16]. Another drawback of the Lagrange Multipliers method in its original form is that the discrete equation system is enlarged by the Lagrange Multipliers *Degrees of Freedom* (DOFs). The latter can be bypassed when alternative *Mortar*-based formulations are considered where the Lagrange Multipliers are condensed out of the equation system, see also in Fritz et al. [17] and Klöppel et al. [18].

Contrary to the aforementioned constraint enforcement methods, the Nitsche-type approach makes use of field fluxes in addition to the unknown fields for the enforcement of the desirable constraints. The method was originally applied in Nitsche [19] to Dirichlet BVPs for which the underlying solution spaces do not have to identically satisfy the boundary conditions. Its application to domain decomposition problems is shown in Sanders et al. [8], Fritz et al. [17], Hansbo et al. [20], Hansbo et al. [21], Sanders et al. [22], and Nguyen et al. [23]. The method was then extended to IGA in Apostolatos et al. [10], Du et al. [24], and Guo et al. [25], while in Ruess et al. [26] its application to the NURBS-embedded *Finite Cell Method* (FCM) (Parvizian et al. [27]) was shown. It is necessary to add Penalty-like stabilization terms in the weak form of the problem in order to maintain coercivity. The underlying stabilization parameters can then be estimated by solving eigenvalue problems whose size is herein significatly smaller than for the original problem since the constraints are applied only along interfaces and boundaries, see in Apostolatos et al. [10], Griebel et al. [28], and Apostolatos et al. [29]. Within the Nitsche-type method, the size of the original discrete equation system remains unchanged and moreover no user interference is needed since the stabilization parameters can be estimated. The additional terms are nonlinear when geometrically nonlinear structural analysis is considered since the fluxes are also herein exploited. This means that the terms accounting for the constraint enforcement have to be be updated at each nonlinear iteration which has the upside that the method dynamically adapts, but it has also the downside that the computational overhead becomes significant. This is especially highlighted in the Kirchhoff-Love shell analysis where the linearization of the shear forces becomes necessary in the context of the Nitsche-type method, which otherwise does not show up in the internal work. Nevertheless, whenever a Nitsche-type method is available it is typically preferred.

Surface coupled problems such as FSI (see also in Breuer et al. [30] and De Nayer et al. [31, 32]), greatly benefit from the smoothness that IGA offers along the common coupling interface, see also in Bazilevs et al. [33]. This is especially important as the quality of the coupling interface plays a decisive role in the overall solution accuracy and robustness for such problems. In this work, the partitioned FSI simulation is extended to IGA on multipatch surfaces for the discretization of the structural equilibrium equations coupled with flow equations discretized by means of the *Finite Volume Method* (FVM) (Ferziger et al. [34]), see also in Wüchner [35]. In particular, the actual CAD geometries are used within isogeometric structural analysis, which are typically described by trimmed NURBS multipatches. Concerning the flow equations, the incompressible Navier-Stokes equations are considered which are discretized using the FVM within open-source software OpenFOAM® (Jasak et al. [36]). The partitioned FSI approach is herein employed as it allows for best-suited specialized solution schemes for each physical field independently, see also in Klöppel et al. [18], Glück et al. [37], and Unger et al. [38]. Accordingly, such fields as displacements and tractions need to be transformed between trimmed multipatch NURBS surfaces representing the structural FSI interface and low order polygonal surfaces representing the fluid FSI interface. For this reason, a novel isogeometric mortar-based mapping method is herein elaborated and assessed,

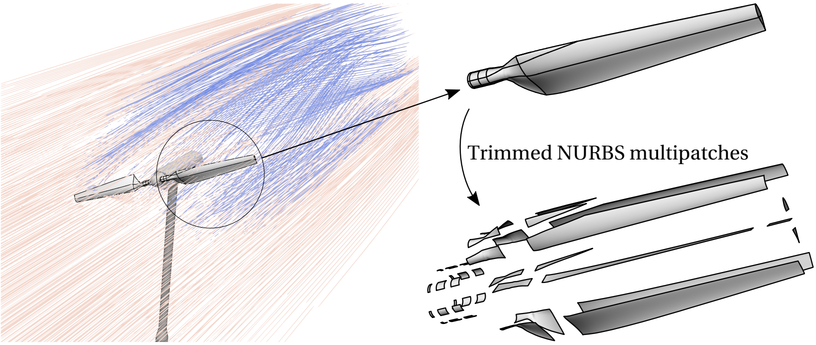

Figure 1.3: Fluid-structure interaction using the exact CAD model in isogeometric structural analysis.

thus extending IGA of thin-walled structures on trimmed multipatch surfaces to FSI, see Fig. 1.3.

Alternatively, the CAD representation (i.e. the trimmed multipatch NURBS representation) of the FSI interface can be used as a mediator surface, herein called the *Exact Coupling Layer* (ECL), for the transformation of fields between two low order discretized surfaces in the context of partitioned FSI with standard FEM discretization of the structural problem. Accordingly, the transformed fields from one low order discretization of the surface to the other are smoothed through the ECL using the isogeometric mortar-based mapping method. This smoothing is especially important as the structural mesh is often coarser than the fluid mesh on the FSI interface. The underlying reason is that the boundary layer and the flow characteristics need typically much finer discretizations, see also in De Nayer et al. [31] and Glück et al. [37].

To enable FSI simulations based on smooth trimmed multipatch NURBS descriptions of thin-walled structures stemming directly from CAD, several developments were accomplished and systematically evaluated. The overall structure of the present thesis is summarized in the following.

CHAPTER 2 sets forth the fundamentals regarding the parametric modelling of curves and surfaces, the principles of variational calculus with special focus on the requirements for the existence and uniqueness of solutions to particular forms of variational problems. These variational problems are then individualized for the case of thin-walled structural analysis using Kirchhoff-Love shell and membrane theory. Especially for the membrane theory, form-finding using the *Updated Reference Strategy* (URS) is discussed. The corresponding content and notions are used in the sequel of this thesis on the one hand for their application in NURBS-based IGA of membrane and Kirchhoff-Love shell structures and on the other hand for their application in isogeometric mortar-based surface coupling on multipatch surfaces.

CHAPTER 3 focuses on the specialization of the parametric description of curves and surfaces to NURBS, as standard in CAD. The notion of trimming is briefly introduced and then the trimmed multipatch NURBS geometries are discussed. Subsequently, three constraint enforcement methods are elaborated and compared for their application to the continuity enforcement between multipatches, namely, a Penalty, a Lagrange Multipliers and a Nitsche-type method. All these methods are then compared in linear static and modal analysis using two benchmark problems in the frame of two-dimensional elasticity.

CHAPTER 4 demonstrates the application of IGA on multipatch surfaces for the geometrically nonlinear structural analysis of membranes. Accordingly, the Penalty and the Nitsche-type methods are elaborated and compared in one benchmark, that of the four-point sail, and two real world engineering applications, those of the middle sail of the Olympic stadium roof in Munich and of a hangar consisting of three connected inflated torus-shaped tubes.

CHAPTER 5 demonstrates the application of IGA on multipatch surfaces for the structural analysis of Kirchhoff-Love shells. Herein, the Penalty and the Lagrange Multipliers methods are elaborated and compared over a series of linear and nonlinear benchmark examples. At the end of this chapter, the application of the aforementioned methodology to the real world engineering example of the NREL phase VI wind turbine with flexible blades is shown. For the latter application, linear static and modal analyses are performed and the solution is compared to a solution obtained using standard FEM.

CHAPTER 6 demonstrates the extension of the isogeometric membrane and Kirchhoff-Love shell analyses on multipatch surfaces to partitioned FSI. Accordingly, a novel isogeometric mortar-based mapping method is elaborated for transformations of fields between a low order discretized surface and a surface consisting of trimmed NURBS multipatches, where implementational aspects are also discussed. A short introduction to the incompressible Navier-Stokes equations is provided along with a discussion on the employed solution schemes within OpenFOAM®. Then, the lid-driven cavity FSI benchmark example is used for the validation and the demonstration of the proposed methodology. Lastly, the FSI simulations of the inflatable hangar and the NREL phase VI wind turbine with flexible blades in numerical wind tunnels are shown and compared to solutions stemming from standard finite element structural discretizations.

The main contributions of this work consist in the elaboration and comparison of various constraint enforcement methods for IGA on multipatch surfaces of thin-walled structures in FSI. Accordingly, a novel isogeometric mortar-based mapping method is herein detailed for the coupling of the structural equations in IGA on multipatches with the flow equations in FVM. The isogeometric mortar-based mapping method is also used for smoothing fields transformed between two low order discretized surfaces taking advantage of the exact CAD description of their common interface. Parts of IGA on multipatch surfaces in linear elasticity briefly discussed in Chap. 3 can be found in Apostolatos et al. [10]. Moreover, parts of IGA on multipatch surfaces detailed in Chap. 4 for membrane structures are available in Apostolatos et al. [29, 39]. Lastly, parts of IGA on multipatch surfaces for Kirchhoff-Love shell problems presented in Chap. 5 are published in Apostolatos et al. [40].

Chapter 2

Foundations

This chapter provides the necessary notions and preliminaries for the sequel of this thesis. At first the differential geometry of curves and surfaces is introduced along with the differential calculus over curvilinear spaces. Subsequently, an introduction to variational calculus is provided where special attention is drawn on the equivalence between strong and weak forms of boundary value problems. Then, the existence and uniqueness of solutions to variational problems and their corresponding mixed formulations are briefly discussed. The structural analysis of Kirchhoff-Love shells and membranes along with form-finding using the *Updated Reference Strategy* (URS) is subsequently introduced. Concerning the time discretization of the dynamic equilibrium, the semidiscretized systems using the *Newmark* method are detailed and then the discrete equation systems resulting from the spatial discretization using the *Finite Element Method* (FEM) are given.

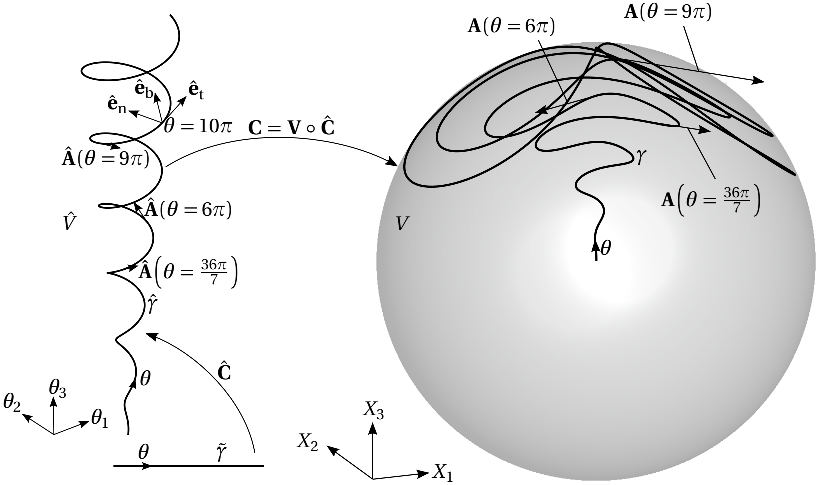

Figure 2.1: Differential geometry of curves: Images of the spiral and its image through a unit ball.

2.1 Introduction to differential geometry

The following section sets forth the fundamentals regarding the differential geometry of curves and surfaces which are later on exploited by specializing the geometric description to *Non-Uniform Rational B-Splines* (NURBS). In the sequel O'Neill [41] is closely followed and $V \subset \mathbb{R}^3$, $\Omega \subset \mathbb{R}^3$ are assumed to be open subspaces of Euclidean space $\mathbb{R}^3$ representing a surface and a volume in Cartesian space with parametric images $\hat{\Omega} \subset \mathbb{R}^2$ and $\hat{V} \subset \mathbb{R}^3$, respectively. Additionally, Latin and Greek indices which are not explicitly defined as variables span from 1 to 3 and from 1 to 2, respectively.

2.1.1 Differential geometry of curves

Let $\hat{\mathbf{C}} : \tilde{\gamma} \to \hat{\gamma}$ be the parametrization of a curve where $\tilde{\gamma} \subset \mathbb{R}$ and $\hat{\gamma} \subset \hat{V}$ are its corresponding parametric and physical spaces, respectively. For the special case of a spiral with increasing radius, where $\tilde{\gamma} = [0, 12\pi]$ and where $\hat{V} \subset \mathbb{R}^3$ is the space defined by the coordinate system θ_1-θ_2-θ_3 (Fig. 2.1), its parametric description reads,

$$\hat{\mathbf{C}}(\theta) = \theta_i \, \hat{\mathbf{A}}_i = \frac{1}{30}\theta \cos\theta \, \hat{\mathbf{A}}_1 + \frac{1}{30}\theta \sin\theta \, \hat{\mathbf{A}}_2 + \frac{3}{10}\theta \, \hat{\mathbf{A}}_3 \,, \tag{2.1}$$

$\hat{\mathbf{A}}_i$, $i = 1, \ldots, 3$ being the orthonormal base vectors in $\hat{V}$ and θ_i the coordinates of any point in that system. The image of the spiral in $\hat{V}$ is depicted in the left of Fig. 2.1. The base (or velocity) vector of curve $\hat{\gamma}$ with parametrization $\hat{\mathbf{C}}$ is defined as the vector $\hat{\mathbf{A}} : \tilde{\gamma} \to \hat{V}$ where,

$$\hat{\mathbf{A}} = \frac{\partial \hat{\mathbf{C}}}{\partial \theta} \,. \tag{2.2}$$

The base vector of the spiral at the parametric locations $\theta = 36\pi/7$, $\theta = 6\pi$ and $\theta = 9\pi$ is also depicted in the left of Fig. 2.1. Additionally, one can define at each parametric location of the curve $\hat{\gamma}$ a convective orthonormal space in $\hat{V}$ spanned by vectors $\hat{\mathbf{e}}_\mathrm{t}$, $\hat{\mathbf{e}}_\mathrm{n}$ and $\hat{\mathbf{e}}_\mathrm{b}$ as,

$$\hat{\mathbf{e}}_\mathrm{t} = \frac{1}{\left\| \frac{\partial \hat{\mathbf{C}}}{\partial \theta} \right\|_2} \frac{\partial \hat{\mathbf{C}}}{\partial \theta} \,, \tag{2.3a}$$

$$\hat{\mathbf{e}}_\mathrm{b} = \frac{1}{\left\| \frac{\partial \hat{\mathbf{C}}}{\partial \theta} \times \frac{\partial^2 \hat{\mathbf{C}}}{\partial \theta^2} \right\|_2} \frac{\partial \hat{\mathbf{C}}}{\partial \theta} \times \frac{\partial^2 \hat{\mathbf{C}}}{\partial \theta^2} \,, \tag{2.3b}$$

$$\hat{\mathbf{e}}_\mathrm{n} = \hat{\mathbf{e}}_\mathrm{b} \times \hat{\mathbf{e}}_\mathrm{t} \,, \tag{2.3c}$$

known as the *Frenet* basis. The Frenet basis is important as vector $\hat{\mathbf{e}}_\mathrm{t}$ (so-called unit velocity vector) remains always tangent to curve $\hat{\gamma}$, vector $\hat{\mathbf{e}}_\mathrm{n}$ (so-called main normal) points in the direction of the curvature of the curve and vector $\hat{\mathbf{e}}_\mathrm{b}$ (so-called binormal) carries information on the torsion of the curve. The Frenet basis at $\theta = 10\pi$ for the case of the spiral geometry is also shown in the left of Fig. 2.1. Consider the transformation $\mathbf{V} : \hat{V} \to V \subset \mathbb{R}^3$,

$$\mathbf{V}\left(\theta_1, \theta_2, \theta_3\right) = \sin\frac{\theta_3}{2\pi}\left(\cos\theta_1 \sin\theta_2 \mathbf{e}_1 + \sin\theta_1 \sin\theta_2 \mathbf{e}_2 + \cos\theta_2 \mathbf{e}_3\right), \tag{2.4}$$

$\mathbf{e}_i$ being the base vectors in the Cartesian space $\mathbb{R}^3$, which transforms domain $\hat{V}$ into the unit ball V,

$$V = \left\{ \mathbf{X} \in \mathbb{R}^3 \,\middle|\, \|\mathbf{X}\|_2 \leq 1 \right\} \,. \tag{2.5}$$

The image of curve $\hat{\gamma}$ through the unit ball parametrization in Eq. (2.4) is then obtained by the parametrization $\mathbf{C} = \mathbf{V} \circ \hat{\mathbf{C}} : \tilde{\gamma} \to \gamma$, see right part of

Fig. 2.1. Accordingly, the tangent vector $\mathbf{A} : \tilde{\gamma} \rightarrow V$ of curve γ is defined by means of the base vector $\hat{\mathbf{A}}$ along $\hat{\gamma}$ using the chain rule,

$$\mathbf{A} = \frac{\partial\, \mathbf{C}}{\partial\, \theta} = \mathbf{A}_i \left(\hat{\mathbf{A}} \cdot \hat{\mathbf{A}}_i \right) , \tag{2.6}$$

where $\hat{\mathbf{A}} \cdot \hat{\mathbf{A}}_i$ are the components of base vector $\hat{\mathbf{A}}$ in $\hat{V}$ and where the Einstein's summation convention over the repeated indices is assumed. Moreover, vectors $\mathbf{A}_i = \partial\, \mathbf{C} / \partial\, \theta_i$ are the base vectors of the geometric parametrization $\mathbf{V}$ of volume V in Eq. (2.4). In the same fashion, base vector $\mathbf{A}$ is depicted for the given parametric locations $\theta = 36\pi/7$, $\theta = 6\pi$ and $\theta = 9\pi$ in the right part of Fig. 2.1 along with the spiral through the unit ball parametrization.

The length of curve $\hat{\gamma}$ in V and of curve γ in $\hat{V}$ are given as,

$$|\hat{\gamma}| = \int_{\hat{\gamma}} \mathrm{d}\hat{\gamma} = \int_{\tilde{\gamma}} \|\hat{\mathbf{A}}\|_2 \, \mathrm{d}\theta \, , \tag{2.7a}$$

$$|\gamma| = \int_{\gamma} \mathrm{d}\gamma = \int_{\tilde{\gamma}} \|\mathbf{A}\|_2 \, \mathrm{d}\theta \, , \tag{2.7b}$$

respectively.

2.1.2 Differential geometry of surfaces

A surface in $\mathbb{R}^3$ is defined by a map $\mathbf{S} : \hat{\Omega} \rightarrow \Omega$, where $\hat{\Omega} \subset \mathbb{R}^2$ and $\Omega \subset \mathbb{R}^3$ stand for the parametric and geometric images of the surface, respectively. As examples, the parametric descriptions of a hemisphere and a hyperbolic paraboloid are given below,

$$\mathbf{S}(\theta_1, \theta_2) = \bar{R}\, \cos\theta_1 \sin\theta_2\, \mathbf{e}_1 + \bar{R}\, \sin\theta_1 \sin\theta_2\, \mathbf{e}_2 + \bar{R}\, \cos\theta_2\, \mathbf{e}_3 \, , \tag{2.8a}$$

$$\mathbf{S}(\theta_1, \theta_2) = \theta_1 \cos\theta_2\, \mathbf{e}_1 + \theta_1 \sin\theta_2\, \mathbf{e}_2 + \theta_1 \left(\cos^2\theta_2 - \sin^2\theta_2 \right) \mathbf{e}_3 \, , \tag{2.8b}$$

in $\hat{\Omega} = [\pi, 2\pi] \times [3\pi, 4\pi]$ and in $\hat{\Omega} = [0, 1/2] \times [0, 2\pi]$, respectively. The corresponding parametric and geometric images are then depicted in Figs. 2.2. A local convective space for each surface Ω may be constructed as follows,

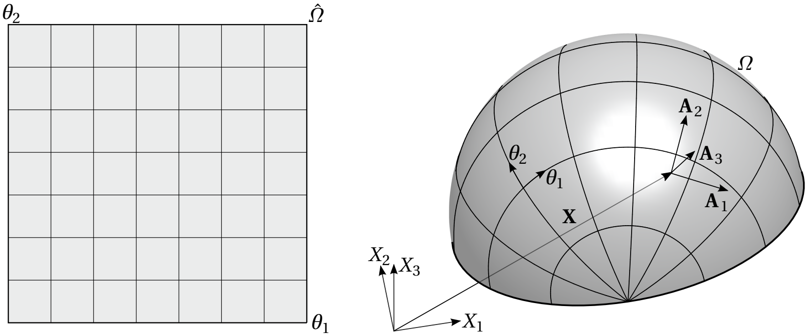

(a) Parametric image of the hemisphere. (b) Geometric image of the hemisphere.

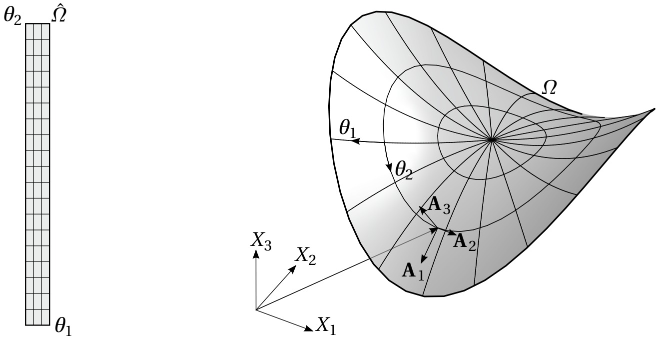

(c) Parametric image of the hyperbolic paraboloid. (d) Geometric image of the hyperbolic paraboloid.

Figure 2.2: Differential geometry of surfaces: Images of the hemisphere and the hyperbolic paraboloid in their parametric and the geometric spaces.

$$\mathbf{A}_\alpha = \frac{\partial \mathbf{S}}{\partial \theta_\alpha}\,, \tag{2.9a}$$

$$\mathbf{A}_3 = \frac{1}{\left\|\mathbf{A}_1 \times \mathbf{A}_2\right\|_2} \mathbf{A}_1 \times \mathbf{A}_2\,, \tag{2.9b}$$

where base vectors $\mathbf{A}_\alpha$ and $\mathbf{A}_3$ are the so-called covariant base vectors of the surface parametrization $\mathbf{S}$. The base vectors of the given parametrizations, that of the hemisphere and the hyperbolic hyperboloid, at given surface points are then shown in Fig. 2.2(b) and Fig. 2.2(d), respectively. Evidently, base vectors $\mathbf{A}_\alpha$ are tangent to surface Ω at any given point and moreover tangent to the Cartesian image of the parametric isolines θ_α, respectively, whereas base vector $\mathbf{A}_3$ corresponds to the surface normal. A contravariant basis $\mathbf{A}^i$ for each surface Ω maybe constructed using the rule $\mathbf{A}_i \cdot \mathbf{A}^j = \delta_i^j$. Since $\mathbf{A}_3$ is perpendicular to both $\mathbf{A}_\alpha$ at each point, it naturally follows that $\mathbf{A}^3 = \mathbf{A}_3$. The second order tensor $\boldsymbol{\mathcal{A}} = \mathcal{A}_{\alpha\beta}\, \mathbf{A}^\alpha \otimes \mathbf{A}^\beta$ with components,

$$\mathcal{A}_{\alpha\beta} = \mathbf{A}_\alpha \cdot \mathbf{A}_\beta \,, \tag{2.10}$$

is called the *metric tensor* or the *first fundamental form* of surface Ω with parametrization $\mathbf{S}$. As opposed to curves, the curvature of a surface is defined by means of the *curvature* second order tensor $\boldsymbol{\mathcal{B}} = \mathcal{B}_{\alpha\beta}\, \mathbf{A}^\alpha \otimes \mathbf{A}^\beta$ whose components are given by,

$$\mathcal{B}_{\alpha\beta} = -\frac{\partial \mathbf{A}_3}{\partial \theta_\alpha} \cdot \mathbf{A}_\beta = -\frac{\partial \mathbf{A}_3}{\partial \theta_\beta} \cdot \mathbf{A}_\alpha = \mathbf{A}_3 \cdot \frac{\partial \mathbf{A}_\alpha}{\partial \theta_\beta} \,, \tag{2.11}$$

which is also known as the *second fundamental form* of surface Ω with parametrization $\mathbf{S}$. Since base vectors $\mathbf{A}_\alpha$ are in general not normalized, values $\mathcal{B}_{\alpha\beta}$ have no direct physical meaning and thus values,

$$\bar{\mathcal{B}}_{\alpha\beta} = \mathcal{B}_{\alpha\beta}\, \|A_\alpha\|_2\, \|A_\beta\|_2 \,. \tag{2.12}$$

can be used instead. At each point on the surface there can be identified a minimum and maximum curvature, denoted by $\bar{k}_1$ and $\bar{k}_2$, respectively, the so-called *principal curvatures*. The corresponding directions where the principal curvatures occur are known as the *principal directions*. The eigenvalues and the corresponding eigenvectors of the generalized eigenvalue problem,

$$\boldsymbol{\mathcal{B}} \cdot \mathbf{v} = \bar{k}\, \boldsymbol{\mathcal{A}} \cdot \mathbf{v} \,, \tag{2.13}$$

are then the principal curvatures $\bar{k}_\alpha$ and principal direction vectors $\mathbf{v}_\alpha$ of surface Ω with parametrization $\mathbf{S}$ at each point, respectively. In Eq. (2.13), the scalar product is defined as $\boldsymbol{\mathcal{B}} \cdot \mathbf{v} = \mathcal{B}_{\alpha\beta}\, v^\beta$, where v^β are the contravariant components of curvature direction vector $\mathbf{v}$ on surface Ω. In this way, the *Gaussian* curvature is obtained by $\bar{K} = \bar{k}_1\, \bar{k}_2$ at each point on surface Ω. Surfaces for which $\bar{K} > 0$ everywhere are called *synclastic* surfaces whereas surfaces for which $\bar{K} < 0$ everywhere are called *anticlastic*.

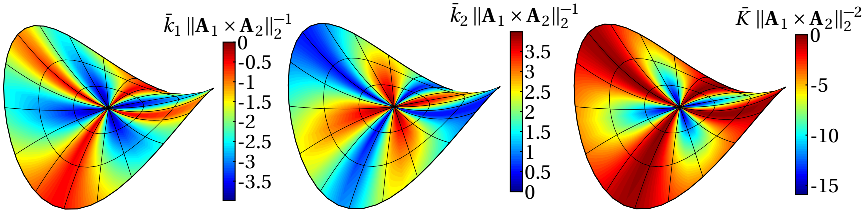

(a) First principal curvature $\bar{k}_1$ normalized by $\|\mathbf{A}_1 \times \mathbf{A}_2\|_2$.

(b) Second principal curvature $\bar{k}_2$ normalized by $\|\mathbf{A}_1 \times \mathbf{A}_2\|_2$.

(c) Gaussian curvature $\bar{K}$ normalized by $\|\mathbf{A}_1 \times \mathbf{A}_2\|_2^2$.

Figure 2.3: Differential geometry of surfaces: Contour of the curvature coefficients for the hyperbolic paraboloid.

Concerning the hemisphere, it is known that the curvature is the same along each parametric direction and thus, the principal curvatures equal the physical normal curvature components, namely, $\bar{k}_1 = \bar{\mathcal{B}}_{11} = \bar{k}_2 = \bar{\mathcal{B}}_{22} = 1/\bar{R}$, whereas component $\bar{\mathcal{B}}_{12}$ is identically zero everywhere. Thus, the Gaussian curvature of the hemisphere equals $\bar{K} = 1/\bar{R}^2 > 0$ and hence, the hemisphere is a synclastic surface. Regarding the hyperbolic paraboloid defined in Eq. (2.8b) it can be firstly observed that $\mathbf{A}_2 = \mathbf{0}$ identically for $\theta_1 = 0$. This is due to the fact that the aforementioned parametrization $\mathbf{S}$ is constructed by squeezing parametric line θ_2 to a point at $\theta_1 = 0$ and revolving θ_2 parametric direction around it. Therefore, surface normal vector $\mathbf{A}_3$ is not well defined at $\theta_1 = 0$. However, the surface normal vector $\mathbf{A}_3$ is well defined everywhere else and by solving eigenvalue problem defined in Eq. (2.13) the principal curvatures $\bar{k}_1$ and $\bar{k}_2$ can be obtained. The various curvature measures concerning the hyperbolic paraboloid are then depicted in Fig. 2.3. The principal curvatures $\bar{k}_1$ and $\bar{k}_2$ are depicted in Figs. 2.3(a) and 2.3(b), respectively, when scaled by $\|\mathbf{A}_1 \times \mathbf{A}_2\|_2$. In this case, it is observed that $\bar{K} < 0$ (Fig. 2.3(c)) for all points but the center $\theta_1 = 0$ where $\mathbf{A}_3$ is undefined and thus the hyperbolic paraboloid belongs to the family of anticlastic surfaces.

2.2 Introduction to variational calculus

Herein a brief introduction to variational calculus is provided, focusing on the aspects which are employed later on in this thesis. Such aspects include the variational formulations of thin-walled structures and the mortar-based surface mapping method posed on multiple domains while being subject to interface and boundary constraints. For laying the underlying formalities, Logan [42] is followed in the sequel. The space of all one-time weakly differentiable vector functions in $\varOmega$ which are identically zero along boundary $\partial\varOmega$ reads,

$$\boldsymbol{\mathcal{V}} = \left\{ \mathbf{h} \in \boldsymbol{\mathcal{H}}^1(\varOmega) | \mathbf{h} = \mathbf{0} \text{ on } \partial\varOmega \right\} , \tag{2.14}$$

where $\boldsymbol{\mathcal{H}}^1(\varOmega)$ is the first order *Sobolev* space of the vector-valued square integrable functions $\mathbf{h} \in \boldsymbol{\mathcal{L}}^2(\varOmega)$ with square integrable derivatives $\partial\mathbf{h}/\partial X_i \in \boldsymbol{\mathcal{L}}^2(\varOmega)$. It is assumed herein that the unknown function fields satisfy a homogeneous *Dirichlet* boundary condition along the whole boundary $\partial\varOmega$, without loss of generality. Accordingly, the admissible spaces for the test and the solution fields are identical as in Eq. (2.14). Alternatively, in case that the unknown function fields satisfy strongly an inhomogeneous Dirichlet boundary condition along $\partial\varOmega$ the admissible space for the unknown solution is different than the admissible space for the test functions which comply strongly with the homogeneous Dirichlet boundary conditions along $\partial\varOmega$. It should be borne in mind that in case the Dirichlet conditions are strongly imposed along a portion of the domain's boundary $\varGamma_\mathrm{d} \subset \partial\varOmega$, the admissible solution spaces do not have to comply with any conditions along the *Neumann* boundary $\varGamma_\mathrm{n} = \partial\varOmega \setminus \varGamma_\mathrm{d}$ where typically the fluxes of the unknown field are weakly imposed. The latter implies that $\varGamma_\mathrm{d} \cap \varGamma_\mathrm{n} = \emptyset$. A functional $L : \boldsymbol{\mathcal{V}} \rightarrow \mathbb{R}$ is a rule that maps each element $\mathbf{h} \in \boldsymbol{\mathcal{V}}$ to a real number. The extension of the derivative notion for real-valued functions to functionals, that of the *Gâteaux derivative* provided below, is essential for defining stationary points of functionals.

Definition 2.1: Gâteaux derivative

Given a functional $L : \boldsymbol{\mathcal{V}} \rightarrow \mathbb{R}$, where $\boldsymbol{\mathcal{V}}$ is a vector space, the *Gâteaux derivative* or *first variation* of L at an element $\mathbf{d} \in \boldsymbol{\mathcal{V}}$ in the direction of $\mathbf{h} \in \boldsymbol{\mathcal{V}}$ is defined as the number,

$$\delta L(\mathbf{d}) = \lim_{\tilde{\epsilon} \to 0} \frac{L(\mathbf{d} + \tilde{\epsilon}\mathbf{h}) - L(\mathbf{d})}{\tilde{\epsilon}} = \frac{\partial}{\partial \tilde{\epsilon}} L(\mathbf{d} + \tilde{\epsilon}\mathbf{h}) \bigg|_{\tilde{\epsilon}=0} . \tag{2.15}$$

It can be easily observed that the Gâteaux derivative closely resembles the notion of the directional derivative for multidimensional functions, where in this case the direction is indicated by vector $\mathbf{h} \in \mathcal{V}$. Function $\tilde{\epsilon}\mathbf{h}$ stands for the corresponding *admissible variation* which is in the sequel denoted as $\delta\mathbf{d}$. In order to motivate the importance of the Gâteaux derivative in the context of structural analysis, in the latter case L, $\mathbf{d}$ and $\delta\mathbf{d}$ stand for the potential energy, the displacement field and its admissible variation, respectively.

2.2.1 Correspondence of strong and weak forms

The *stationary points* of functional L indicate possible locations where L attains its minimum or maximum value which can be either local or global. A vector $\mathbf{d} \in \mathcal{V}$ is said to be a stationary point of functional L if $\delta L(\mathbf{d}) = 0$, where the variation is understood in the sense of Def. 2.1. The aforementioned condition contains information on neither whether that stationary point is local or global nor whether this is a location of minimum or maximum. Whether a functional L attains a unique global or a number local stationary point(s) depends on whether the underlying problem is convex or concave, respectively. On the other hand, whether the stationary point is a location of minimum or maximum also depends on the nature of the underlying problem and corresponding information can be drawn using the second order variation of L defined in a similar fashion as the first variation in Def. 2.1. A fundamental principle of variational calculus, herein presented for vector-valued functions, is provided in Lem. 2.1 below.

Lemma 2.1

Let $\mathbf{F}(\mathbf{X}, \mathbf{d})$ be a continuous vector function in Ω. If the following condition holds true,

$$\int_{\Omega} \mathbf{F}(\mathbf{X}, \mathbf{d}) \cdot \delta\mathbf{d} \, \mathrm{d}\Omega = 0 \,, \tag{2.16}$$

for all admissible variations $\delta\mathbf{d} \in \mathcal{V}$, then $\mathbf{F}(\mathbf{X}, \mathbf{d}) = \mathbf{0}$ identically in Ω.

Concerning Eq. (2.16), derivatives are typically transferred from $\mathbf{F}$ onto the test function $\delta\mathbf{d}$ using integration by parts in order to reduce the continuity requirements on $\mathbf{d}$ and obtain boundary terms which allow the imposition of boundary conditions. Accordingly, the resulting maximum derivative order $\bar{m} \in \mathbb{N}$ on $\delta\mathbf{d}$ in the resulting variational form defines the Sobolev space where variation $\delta\mathbf{d}$ is restricted[1], in other words $\boldsymbol{\mathcal{V}} \subset \boldsymbol{\mathcal{H}}^{\bar{m}}(\Omega)$. Concerning the variational (or weak) forms of the membrane and Kirchhoff-Love shell problems, $\bar{m} = 1$ and $\bar{m} = 2$, respectively (see also Secs. 2.3.3 and 2.3.2). For displacement-based structural analysis problems, where L stands for the potential energy, the corresponding stationary point is the displacement field $\mathbf{d}$ which produces the least potential energy. The *Euler-Lagrange* set of *Partial Differential Equations* (PDEs), introduced in Thm. 2.1, represents the equivalent *strong form* of problem $\delta L = 0$ when functional L has a special integral form.

Theorem 2.1: Euler-Lagrange PDEs

Let $\mathbf{d} \in \boldsymbol{\mathcal{V}}$ be the unknown field and $L : \boldsymbol{\mathcal{V}} \to \mathbb{R}$ a potential of the form,

$$L(\mathbf{d}) = \int_{\Omega} \mathcal{J}(\mathbf{X}, \mathbf{d}, \nabla\mathbf{d})\, \mathrm{d}\Omega\,, \tag{2.17}$$

for a given functional $\mathcal{J} : \boldsymbol{\mathcal{V}} \to \mathbb{R}$. Then, the stationary point $\mathbf{d} \in \boldsymbol{\mathcal{V}}$ of potential L satisfies the Euler-Lagrange PDEs, namely,

$$\mathcal{J}_{\mathbf{d}}(\mathbf{X}, \mathbf{d}, \nabla\mathbf{d}) - \nabla \cdot \mathcal{J}_{\nabla\mathbf{d}}(\mathbf{X}, \mathbf{d}, \nabla\mathbf{d}) = \mathbf{0} \quad \text{in } \Omega, \tag{2.18a}$$

$$\mathbf{d} = \mathbf{0} \quad \text{on } \partial\Omega\,, \tag{2.18b}$$

where $\mathcal{J}_{\mathbf{d}}$ and $\mathcal{J}_{\nabla\mathbf{d}}$ are defined as follows,

$$\mathcal{J}_{\mathbf{d}} = \frac{\partial \mathcal{J}}{\partial d_i^0}\mathbf{e}_i\,, \tag{2.19a}$$

$$\mathcal{J}_{\nabla\mathbf{d}} = \frac{\partial \mathcal{J}}{\partial d_{i,j}^0}\mathbf{e}_i \otimes \mathbf{e}_j\,, \tag{2.19b}$$

with $d_{i,j}^0 = \partial d_i^0 / \partial X_j$ and where $\mathbf{d} = d_i^0 \mathbf{e}_i$ stands for the decomposition of $\mathbf{d}$ in the Cartesian basis.

The expressions in Eqs. (2.18) and (2.19) are written with respect to the Cartesian coordinate system without loss of generality and can be also expressed with respect to a curvilinear coordinate system as introduced in Sec. 2.1.2. The Euler-Lagrange PDEs in Eq. (2.18) are derived by means of

---

[1] Number $\bar{m}$ is also known as the variational index of the corresponding weak form, that is, the highest derivative order on the test function.

the chain rule when computing the first variation of functional $\mathcal{J}$ using Eq. (2.15) for each admissible variation $\delta\mathbf{d} \in \boldsymbol{\mathcal{V}}$ while subsequently using Lem. 2.1. In the context of displacement-based structural analysis, $\mathcal{J}_{\mathbf{d}}$ and $\mathcal{J}_{\nabla\mathbf{d}}$ in Eqs. (2.19) stand for the external body forces and the internal stress tensor field, respectively. As aforementioned, the Euler-Lagrange PDEs in Eq. (2.18) represent the strong form of finding the stationary point $\mathbf{d} \in \boldsymbol{\mathcal{V}}$ of potential L subject to boundary condition in Eq. (2.18b). On the other hand, multiplying Eq. (2.18a) with a $\delta\mathbf{d} \in \boldsymbol{\mathcal{V}}$, integrating over Ω and subsequently performing integration by parts, the so-called *weak* or *variational form* of problem in Eq. (2.18) is obtained, namely: Find $\mathbf{d} \in \boldsymbol{\mathcal{V}}$ such that,

$$\int_{\Omega} \nabla\delta\mathbf{d} : \mathcal{J}_{\nabla\mathbf{d}}(\mathbf{X},\mathbf{d},\nabla\mathbf{d})\,\mathrm{d}\Omega + \int_{\Omega} \delta\mathbf{d}\cdot\mathcal{J}_{\mathbf{d}}(\mathbf{X},\mathbf{d},\nabla\mathbf{d})\,\mathrm{d}\Omega = 0\,, \tag{2.20}$$

for all $\delta\mathbf{d} \in \boldsymbol{\mathcal{V}}$. Weak form in Eq. (2.20) is in general nonlinear and is equivalent to strong form in Eq. (2.18) meaning that the solution of the weak form is the same as for the strong form. As aforementioned, conditions can also be applied onto the fluxes of vector $\mathbf{d}$ along $\Gamma_{\mathrm{n}} \subset \partial\Omega$ which in case of displacement-based structural analysis would stand for externally applied boundary tractions. In the latter case, $\boldsymbol{\mathcal{V}}$ is not subject to the homogeneous boundary conditions along that portion of the boundary.

2.2.2 Existence and uniqueness of solutions to variational problems

As mentioned in Sec. 2.2.1, weak form defined in Eq. (2.20) is equivalent to strong form defined in Eq. (2.18) and thus inherits all properties from the Euler-Lagrange PDEs. The Euler-Lagrange PDEs, depending on the physical problem they describe, might be elliptic (displacement-based structural analysis), parabolic (heat conduction), hyperbolic (incompressible Navier-Stokes flow equations) etc., see in Courant et al. [43] for more information. In this thesis, elliptic Euler-Lagrange PDEs are among others considered which in general govern displacement-based structural analysis problems. For this family of PDEs and their corresponding weak forms, see Eq. (2.20), there may be a unique solution, provided sufficient boundary conditions are applied, when additional conditions are met. Suppose that weak form in Eq. (2.20) can be written as follows: Find $\mathbf{d} \in \boldsymbol{\mathcal{V}}$ such that,

$$a(\delta\mathbf{d},\mathbf{d}) = l(\delta\mathbf{d}) \quad \forall\delta\mathbf{d} \in \boldsymbol{\mathcal{V}}\,, \tag{2.21}$$

where $a : \mathcal{V} \times \mathcal{V} \rightarrow \mathbb{R}$ and $l : \mathcal{V} \rightarrow \mathbb{R}$ is a form and a functional, respectively. The following theorem ensures well-posedness of the weak form in Eq. (2.21) (see in Kikuchi et al. [44] and Ciarlet [45]).

Theorem 2.2: Lax-Milgram theorem

Let $||\bullet||_{\mathcal{V}}$ be a norm in $\mathcal{V}$. Then, if the following conditions are met,

i. Form a is *bilinear*, that is, $a(c\mathbf{h},\mathbf{d}) = a(\mathbf{h},c\mathbf{d}) = c\ a(\mathbf{h},\mathbf{d})$, $a\left(\mathbf{h}_1+\mathbf{h}_2,\mathbf{d}\right) = a\left(\mathbf{h}_1,\mathbf{d}\right) + a\left(\mathbf{h}_2,\mathbf{d}\right)$ and $a\left(\mathbf{h},\mathbf{d}_1+\mathbf{d}_2\right) = a\left(\mathbf{h},\mathbf{d}_1\right) + a\left(\mathbf{h},\mathbf{d}_2\right)$ for all $c \in \mathbb{R}$ and all $\mathbf{h},\mathbf{h}_1,\mathbf{h}_2,\mathbf{d},\mathbf{d}_1,\mathbf{d}_2 \in \mathcal{V}$,

ii. Form a is *continuous*, that is, there exists a real $\bar{C} > 0$ such that, $a(\mathbf{h},\mathbf{d}) \leq \bar{C}\ ||\mathbf{h}||_{\mathcal{V}}\ ||\mathbf{d}||_{\mathcal{V}}$ for all $\mathbf{h},\mathbf{d} \in \mathcal{V}$,

iii. Form a is *coercive* (or *elliptic*), that is, there exists a real $C > 0$ such that, $a(\mathbf{d},\mathbf{d}) \geq C\ ||\mathbf{d}||^2_{\mathcal{V}}$ for all $\mathbf{d} \in \mathcal{V}$,

iv. l is a linear functional, that is, $l(\alpha\mathbf{h}+\mathbf{d}) = \alpha l(\mathbf{h}) + l(\mathbf{d})$ for all real numbers α and for all $\mathbf{h},\mathbf{d} \in \mathcal{V}$,

weak form in Eq. (2.21) has one unique solution $\mathbf{d} \in \mathcal{V}$.

Lax-Milgram Thm. 2.2 is clearly confined to variational problems of the form in Eq. (2.21) where form a is bilinear, continuous and coercive (or elliptic) in $\mathcal{V} \times \mathcal{V}$ and where l is a linear functional in $\mathcal{V}$. For displacement-based structural analysis problems the aforementioned physical interpretation is apparent: Statically determinate linear problems which are typically elliptic attain a unique solution in terms of displacements. However, geometrically nonlinear problems in general may have turning and/or bifurcation points where one unique solution cannot be identified and thus a unique solution for a general nonlinear weak form in Eq. (2.21) is not guaranteed.

Next, suppose that variational problem in Eq. (2.21) is subject to a linear equality vector constraint $\mathbf{c} = \mathbf{c}(\mathbf{d})$ along a subdomain $D \subset \overline{\Omega}$. Then, the constrained problem can be formulated by means of the *Lagrange Multipliers* method, namely: Find $\mathbf{d} \in \mathcal{V}$ and $\boldsymbol{\lambda} \in \mathcal{L}^2(D)$ such that,

$$a(\delta\mathbf{d},\mathbf{d}) + \langle\delta\mathbf{c},\boldsymbol{\lambda}\rangle_{0,D} + \langle\delta\boldsymbol{\lambda},\mathbf{c}\rangle_{0,D} = l(\mathbf{d})\ , \tag{2.22}$$

for all $\delta\mathbf{d} \in \boldsymbol{\mathcal{V}}$ and for all $\delta\boldsymbol{\lambda} \in \boldsymbol{\mathcal{L}}^2(D)$. Scalar product $\langle \bullet, \bullet \rangle_{0,D}$ in Eq. (2.22) is understood as the inner product in the $\boldsymbol{\mathcal{L}}^2(D)$ space, namely,

$$\langle \delta\mathbf{c}, \boldsymbol{\lambda} \rangle_{0,D} = \int_D \delta\mathbf{c} \cdot \boldsymbol{\lambda} \, \mathrm{d}D \, . \tag{2.23}$$

Weak form in Eq. (2.22) is a *mixed* or *saddle-point* formulation. For the latter problem to have a unique solution, additional conditions need to be met which are summarized in Thm. 2.3, see also in Boffi et al. [46].

Theorem 2.3: Ladyzhenskaya-Babuška-Brezzi condition

Let form a be a continuous bilinear form in $\boldsymbol{\mathcal{V}} \times \boldsymbol{\mathcal{V}}$ and l a linear functional in $\boldsymbol{\mathcal{V}}$ as per Thm. 2.2. Let also bilinear form a be coercive in $\boldsymbol{\mathcal{V}}_\mathrm{k} \times \boldsymbol{\mathcal{V}}_\mathrm{k}$ where subspace $\boldsymbol{\mathcal{V}}_\mathrm{k} \subset \boldsymbol{\mathcal{V}}$ is defined as,

$$\boldsymbol{\mathcal{V}}_\mathrm{k} = \left\{ \mathbf{d} \in \boldsymbol{\mathcal{V}} \,\middle|\, \langle \delta\boldsymbol{\lambda}, \mathbf{c} \rangle_{0,D} = 0 \text{ for all } \delta\boldsymbol{\lambda} \in \boldsymbol{\mathcal{L}}^2(D) \right\} \, . \tag{2.24}$$

If in addition the *Ladyzhenskaya-Babuška-Brezzi* (LBB) (or *inf-sup*) condition is satisfied, namely, there exists a constant $\hat{C} > 0$ such that,

$$\inf_{\boldsymbol{\lambda} \in \boldsymbol{\mathcal{L}}^2(D)} \sup_{\mathbf{d} \in \boldsymbol{\mathcal{V}}} \frac{\langle \mathbf{c}, \boldsymbol{\lambda} \rangle_{0,D}}{\|\mathbf{d}\|_{\boldsymbol{\mathcal{V}}} \, \|\boldsymbol{\lambda}\|_{0,D}} \geq \hat{C} \, , \tag{2.25}$$

then mixed formulation in Eq. (2.22) has a unique solution.

It is not a trivial problem for any kind of weak form in Eq. (2.22) to fulfil the LBB condition in Eq. (2.25). One of the most well-known problems of this type is the Stokes problem, see Gresho et al. [15] for more information, for which it can be shown that the LBB condition in Eq. (2.25) is satisfied only for special selections of the discrete subspaces concerning the primal and the Lagrange Multipliers fields, but not for any.

2.3 Continuum mechanics of thin-walled structures

In this section, an introduction to continuum mechanics for thin-walled structures is provided and Başar et al. [1] is closely followed. Starting from the continuum mechanics in the differential volume, the *initial Boundary Value Problems* (iBVPs) for the mid-surface reduced structural models of the Kirchhoff-Love shell and the prestressed membrane are shown.

Then, the corresponding weak formulations of the aforementioned iBVPs are demonstrated and a short introduction to form-finding analysis for prestressed membranes is given.

2.3.1 Preliminaries

This section focuses on the continuum mechanics on curvilinear systems of thin-walled structures including *Kirchhoff-Love shells* and *membranes*. At first, the basics regarding mechanics in 3D space are laid. Therefore, let $V \subset \mathbb{R}^3$ be the continuum's reference geometry consisting of all material points $\mathbf{X}$ defining the continuum. The primal unknown of the problem is the displacement field $\mathbf{d} : V \rightarrow V_t$, where V_t consists of all points $\mathbf{x} = \mathbf{X} + \mathbf{d}$ for each time instance $t \in \mathbb{T}$ in the closed time domain $\mathbb{T} = [T_0, T_\infty]$. A *total Lagrangian description* of the motion is assumed and accordingly all tensors are referred to the reference configuration of the problem. Let $\mathbf{A}_i$ be a curvilinear basis of V which can be computed in a similar fashion as in Eq. (2.9) for a given volume parametrization $\mathbf{V}$. Then, each point of the Cartesian space can be written in terms of either the Cartesian or the curvilinear basis as follows,

$$\mathbf{X} = X_i \mathbf{e}_i = \theta_i \mathbf{A}_i \, , \tag{2.26}$$

X_i and θ_i being the Cartesian and the convective coordinates of position vector $\mathbf{X}$. Accordingly, the displacement field can also be expressed in both the Cartesian and the covariant basis in the same fashion as the position vector in Eq. (2.26), namely,

$$\mathbf{d} = d_i^0 \mathbf{e}_i = d^i \mathbf{A}_i \, . \tag{2.27}$$

Evidently, the base vectors of the current configuration can be expressed similar to the base vectors in the reference configuration, see Eq. (2.9), namely,

$$\mathbf{a}_i = \frac{\partial \mathbf{x}}{\partial \theta_i} = \mathbf{A}_i + \frac{\partial \mathbf{d}}{\partial \theta_i} \, . \tag{2.28}$$

Let $\boldsymbol{\mathcal{S}} = \mathcal{S}_{ij}^0 \mathbf{e}_i \otimes \mathbf{e}_j$ be the *2nd Piola-Kirchhoff* (PK2) stress tensor of the continuum expressed over the Cartesian basis. The stress tensor can be also expressed with respect to the covariant basis of the aforementioned

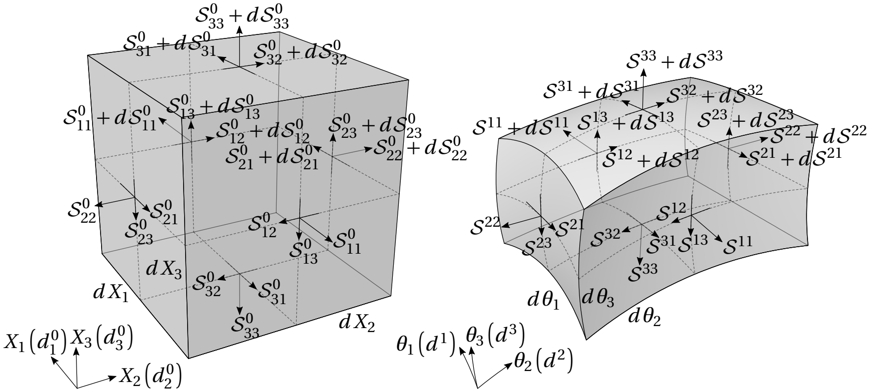

Figure 2.4: Representation of the differential volume in both the Cartesian and a curvilinear coordinate system.

curvilinear space with its contravariant components being,

$$\mathcal{S}^{ij}=\mathcal{S}^0_{kl}\left(\mathbf{A}^i\cdot\mathbf{e}_k\right)\left(\mathbf{A}^j\cdot\mathbf{e}_l\right), \tag{2.29}$$

where $\mathbf{A}^i$ are the contravariant base vectors in 3D, see also Fig. 2.4. In this way, the equilibrium can be posed in either space. Regarding the kinematics, the *Green-Lagrange* (GL) strain tensor $\boldsymbol{\mathcal{E}}=\mathcal{E}_{ij}\mathbf{A}^i\otimes\mathbf{A}^j$ is used, being the energetically conjugate strain measure to the 2nd Piola-Kirchhoff stress measure, whose components in the continuum are defined as,

$$\mathcal{E}_{ij}=\frac{1}{2}\left(\alpha_{ij}-\mathcal{A}_{ij}\right), \tag{2.30}$$

$\mathcal{A}_{ij}$ and α_{ij} being the metric tensor coefficients of the continuum for the reference and the current configuration, respectively, defined similar to metric coefficients of a surface in Eq. (2.10). In terms of the material law, the linear *Hooke's* law (*St. Venant Kirchhoff* material model) is employed which is defined with the aid of the material tensor $\boldsymbol{\mathcal{C}}=\mathcal{C}^{ijkl}\mathbf{A}_i\otimes\mathbf{A}_j\otimes\mathbf{A}_k\otimes\mathbf{A}_l$, whose components read,

$$\mathcal{C}^{ijkl}=\frac{E}{2(1+\nu)}\left(\mathcal{A}^{ik}\mathcal{A}^{jl}+\mathcal{A}^{il}\mathcal{A}^{jk}+\frac{2\nu}{1-2\nu}\mathcal{A}^{ij}\mathcal{A}^{kl}\right), \tag{2.31}$$

E and ν being the *Young's modulus* and the *Poisson's ratio* of the elastic structure. Moreover, $\mathcal{A}^{ik}=\mathbf{A}^i\cdot\mathbf{A}^k$ in Eq. (2.31) are the contravariant metric

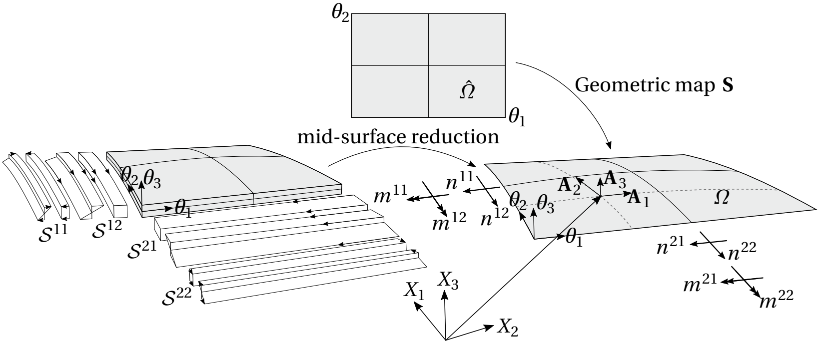

Figure 2.5: Continuum mechanics for thin-walled structures: Mid-surface reduction.

coefficients. Then, the stress-strain relation in the continuum reads,

$$\boldsymbol{\mathcal{S}} = \boldsymbol{\mathcal{C}} : \boldsymbol{\mathcal{E}}\,, \tag{2.32}$$

which is valid for large deformations but small strains. Lastly, inertial and damping forces are considered, which are of the form $\rho\ddot{\mathbf{d}}$ and $c\dot{\mathbf{d}}$, respectively, where ρ, c, $\dot{\mathbf{d}}$ and $\ddot{\mathbf{d}}$ stand for the structural density, the damping coefficient, the velocity and the acceleration vectors, respectively. As aforementioned, in this thesis thin-walled structures of Kirchhoff-Love shell or membrane type are considered. Therefore, it is assumed that the structure is only represented by its mid-surface Ω, whereas the out-of-plane strain and stress components $\mathcal{E}_{i3}$, $\mathcal{E}_{3i}$, $\mathcal{S}^{i3}$, $\mathcal{S}^{3i}$ identically vanish, as it is explained in Sec. 2.3.2. The latter assumptions are valid for thin shells and membranes where $\bar{h}/\bar{R} \ll 20$, $\bar{R}$ and $\bar{h}$ being the radius of curvature (Eq. (2.11)) and the thickness of the structure which is herein considered constant, respectively. In the next sections a brief introduction to structural analysis of Kirchhoff-Love shells and membranes is provided.

2.3.2 Structural analysis of Kirchhoff-Love shells

Let the continuum's geometry V, described in Sec. 2.3.1, be thin in θ_3-direction, see Fig. 2.5. Following the thin structure assumption in Sec. 2.3.1, a reduction to the mid-surface Ω can be performed and in this way each point on the continuum's space described in Eq. (2.26) can be expressed as follows,

$$\mathbf{X} = \theta_\alpha \mathbf{A}_\alpha + \theta_3 \mathbf{A}_3 \,, \tag{2.33}$$

for all $(\theta_1, \theta_2) \in \hat{\Omega}$ and all $\theta_3 \in [-\bar{h}/2, \bar{h}/2]$, where the covariant base vectors $\mathbf{A}_\alpha$ and $\mathbf{A}_3$ are given in Eqs. (2.9). The displacement field $\mathbf{d}$ is then also restricted on the mid-surface and can then be expressed by its in-plane and out-of-plane components on the covariant space of the surface, namely,

$$\mathbf{d} = d^\alpha \mathbf{A}_\alpha + d_3 \mathbf{A}_3 \,. \tag{2.34}$$

Accordingly, the current configuration is only represented by the mid-surface Ω_t for each time instance $t \in \mathbb{T}$. In this way, the continuum's GL strain components can be expressed as,

$$\mathcal{E}_{\alpha\beta} = \varepsilon_{\alpha\beta} + \kappa_{\alpha\beta}\theta_3 + \mathcal{O}\left(\theta_3^2\right) \,, \tag{2.35a}$$

$$\varepsilon_{\alpha\beta} = \frac{1}{2}\left(\alpha_{\alpha\beta} - \mathcal{A}_{\alpha\beta}\right) \,, \tag{2.35b}$$

$$\kappa_{\alpha\beta} = \left(\mathcal{B}_{\alpha\beta} - \beta_{\alpha\beta}\right) \,, \tag{2.35c}$$

where $\boldsymbol{\varepsilon} = \varepsilon_{\alpha\beta}\mathbf{A}^\alpha \otimes \mathbf{A}^\beta$ and $\boldsymbol{\kappa} = \kappa_{\alpha\beta}\mathbf{A}^\alpha \otimes \mathbf{A}^\beta$ are the resulting membrane and bending strain tensors, respectively, and where $\mathcal{A}_{\alpha\beta}$ and $\alpha_{\alpha\beta}$ stand for the metric tensor coefficients of the mid-surface Ω defined in Eq. (2.10) in the reference and current configuration, respectively, see also in Kiendl et al. [47]. In addition, $\mathcal{B}_{\alpha\beta}$ and $\beta_{\alpha\beta}$ stand for the curvature coefficients defined in Eq. (2.11) in the reference and the current configuration, respectively, meaning that the bending strain $\boldsymbol{\kappa}$ is the change of the curvature between the reference and the current configuration. Warping and other high-order effects along the thickness are neglected (see Eq. (2.35a) where high order terms with respect to θ_3 are assumed negligible), which is a valid assumption for thin-walled structures. In this way, cross sections normal to the mid-surface are assumed to remain normal to the mid-surface and planar after the deformation. In addition, cross sections normal to the mid-surface remain normal to the mid-surface after deformation, with the implication that no out-of-plane shear deformation may occur. Hooke's law defined in Eq. (2.32) is then also reduced to the mid-surface and the out-of-plane stress components are assumed negligible, that is, $\mathcal{S}^{i3} = \mathcal{S}^{3i} = 0$ as a result of the elimination of the out-of-plane strain components. Additionally, the stress components $\mathcal{S}^{\alpha\beta}$ are linearly distributed along the thickness as a result of the linear distribution of the strain components along the thickness, see Eq. (2.35). In this way, the constant part of the stress components results into a membrane in-plane stress-resultant force tensor $\mathbf{n} = n^{\alpha\beta}\,\mathbf{A}_\alpha \otimes \mathbf{A}_\beta$ whereas the remaining linear symmetric with respect to the $\theta_3 = 0$ axis part results in a stress-resultant moment tensor $\mathbf{m} = m^{\alpha\beta}\,\mathbf{A}_\alpha \otimes \mathbf{A}_\beta$, see Fig. 2.5. These resulting stress-resultant force and moment tensors are obtained by pre-integration of the stress components $\mathcal{S}^{\alpha\beta}$ along the thickness θ_3-direction, namely,

$$n^{\alpha\beta} = \int_{-\bar{h}/2}^{\bar{h}/2} \mathcal{S}^{\alpha\beta}\, \mathrm{d}\theta_3 = \mathcal{S}^{\alpha\beta}|_{\theta_3=0}\, \bar{h}\,, \tag{2.36a}$$

$$m^{\alpha\beta} = \int_{-\bar{h}/2}^{\bar{h}/2} \mathcal{S}^{\alpha\beta}\, \theta_3\, \mathrm{d}\theta_3 = \mathcal{S}^{\alpha\beta}|_{\theta_3=0}\, \frac{\bar{h}^3}{12}\,, \tag{2.36b}$$

where $\mathcal{S}^{\alpha\beta}|_{\theta_3=0} = \mathcal{S}^{\alpha\beta}\left(\theta_3 = 0\right)$, see also in Gross et al. [48]. Therefore, reducing the three-dimensional continuum down to a surface has the implication of generating moments. Linear Hooke's law in Eq. (2.32) can then be split to account separately for the membrane and the bending parts of the stress, namely,

$$\mathbf{n} = \boldsymbol{\mathcal{C}}_\mathrm{m} : \boldsymbol{\varepsilon}\,, \tag{2.37a}$$

$$\mathbf{m} = \boldsymbol{\mathcal{C}}_\mathrm{b} : \boldsymbol{\kappa}\,, \tag{2.37b}$$

where,

$$\boldsymbol{\mathcal{C}}_\mathrm{m} = \bar{h}\, \mathcal{C}^{\alpha\beta\gamma\delta}\mathbf{A}_\alpha \otimes \mathbf{A}_\beta \otimes \mathbf{A}_\gamma \otimes \mathbf{A}_\delta\,, \tag{2.38a}$$

$$\boldsymbol{\mathcal{C}}_\mathrm{b} = \frac{\bar{h}^3}{12}\, \mathcal{C}^{\alpha\beta\gamma\delta}\mathbf{A}_\alpha \otimes \mathbf{A}_\beta \otimes \mathbf{A}_\gamma \otimes \mathbf{A}_\delta\,, \tag{2.38b}$$

respectively, taking into consideration only the in-plane components of the material tensor $\boldsymbol{\mathcal{C}}$ defined in Eq. (2.31). Let $\mathbf{w} = w_\alpha \mathbf{A}^\alpha = \mathbf{a}_3 - \mathbf{A}_3$ be the difference of the surface normal vector between the current and the reference configuration, respectively, see Fig. 2.6. Assuming small strains, it can be shown (Başar et al. [1]) that the covariant components of vector $\mathbf{w}$ are given by,

$$w_\alpha = -\left(\frac{\partial d_3}{\partial \theta_\alpha} + d^\gamma \mathcal{B}_{\gamma\alpha}\right), \tag{2.39}$$

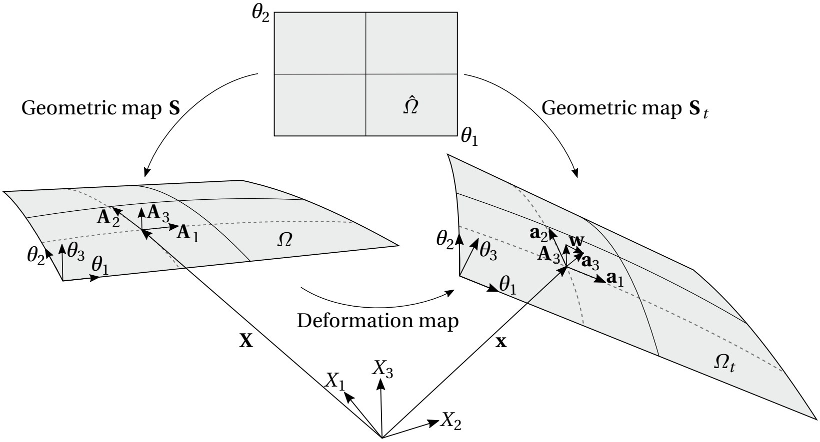

Figure 2.6: Continuum mechanics for thin-walled structures: Deformation of the mid-surface at time $t \in \mathbb{T}$.

where $\mathcal{B}_{\gamma\alpha}$ stand for the covariant components of the curvature tensor, see Eq. (2.11), in the reference configuration. In this way, the rotation vector $\boldsymbol{\omega}$ at a given location $\mathbf{X}$ is defined with the aid of $\mathbf{w}$, namely,

$$\boldsymbol{\omega} = \mathbf{A}_3 \times \mathbf{w} = \omega^{\varsigma} \mathbf{A}_{\zeta} \, , \tag{2.40a}$$

$$\omega^{\varsigma} = -\left(\frac{\partial d_3}{\partial \theta_\alpha} + d^{\gamma} \mathcal{B}_{\gamma\alpha} \right) \epsilon^{\alpha\zeta} \, , \tag{2.40b}$$

$\boldsymbol{\epsilon} = \epsilon^{\alpha\zeta} \mathbf{A}_\alpha \otimes \mathbf{A}_\zeta$ being the permutation second order tensor. Thus, the rotation is a linear differential operator over the displacement field $\mathbf{d}$. Accordingly, the rotation vector can be defined along any curve on surface Ω. Let $\gamma \subset \Omega$ be a curve along which the rotation vector is to be determined. Let also $\hat{\mathbf{e}}_{\mathrm{t}} = \hat{e}^{\alpha}_{\mathrm{t}} \mathbf{A}_\alpha$ and $\hat{\mathbf{e}}_{\mathrm{n}} = \hat{e}^{\alpha}_{\mathrm{n}} \mathbf{A}_\alpha$ be the tangent and the normal to curve γ unit vectors on the tangent space of surface Ω where $\boldsymbol{\epsilon} \cdot \hat{\mathbf{e}}_{\mathrm{t}} = -\hat{\mathbf{e}}_{\mathrm{n}}$ and $\boldsymbol{\epsilon} \cdot \hat{\mathbf{e}}_{\mathrm{n}} = \hat{\mathbf{e}}_{\mathrm{t}}$. In this way, a local orthonormal basis $(\hat{\mathbf{e}}_{\mathrm{t}}, \hat{\mathbf{e}}_{\mathrm{n}}, \mathbf{A}_3)$ is constructed. The rotation vector can be split into its bending and its twisting components namely,

$$\boldsymbol{\omega} = \omega_{\mathrm{t}} \hat{\mathbf{e}}_{\mathrm{t}} + \omega_{\mathrm{n}} \hat{\mathbf{e}}_{\mathrm{n}} \, , \tag{2.41a}$$

$$\omega_{\mathrm{t}} = \boldsymbol{\omega} \cdot \hat{\mathbf{e}}_{\mathrm{t}} = \left(\frac{\partial d_3}{\partial \theta_\alpha} + d^\gamma \mathcal{B}_{\gamma\alpha} \right) \hat{e}^\alpha_{\mathrm{n}} \,, \tag{2.41b}$$

$$\omega_{\mathrm{n}} = \boldsymbol{\omega} \cdot \hat{\mathbf{e}}_{\mathrm{n}} = -\left(\frac{\partial d_3}{\partial \theta_\alpha} + d^\gamma \mathcal{B}_{\gamma\alpha} \right) \hat{e}^\alpha_{\mathrm{t}} \,. \tag{2.41c}$$

Subsequently, displacement and/or rotation Dirichlet boundary conditions are prescribed along a portion of the body's boundary $\Gamma_{\mathrm{d}} \subset \partial\Omega$, confining ourselves to homogeneous Dirichlet boundary conditions without loss of generality. Forces $\bar{\mathbf{p}}$ and/or moments $\bar{\mathbf{r}}$ are applied over another portion of the shell's boundary $\Gamma_{\mathrm{n}} \subset \partial\Omega$ forming the *Neumann* boundary conditions. Finally, it is also assumed that the elastic body is subject to body forces denoted by $\mathbf{b} = b^\alpha \mathbf{A}_\alpha + b_3 \mathbf{A}_3$. Then, the Kirchhoff-Love iBVP reads:

$$\rho \ddot{d}^\beta + c\, \dot{d}^\beta + n^{\alpha\beta}|_\alpha - q^\alpha \mathcal{B}^\beta_\alpha + b^\beta = 0 \,, \quad \text{in } \Omega \times \mathbb{T} \,, \tag{2.42a}$$

$$\rho \ddot{d}_3 + c\, \dot{d}_3 + n^{\alpha\beta} \mathcal{B}_{\alpha\beta} + q^\alpha|_\alpha + b_3 = 0 \,, \quad \text{in } \Omega \times \mathbb{T} \,, \tag{2.42b}$$

$$m^{\alpha\beta}|_\alpha - q^\beta = 0 \,, \quad \text{in } \Omega \times \mathbb{T} \,, \tag{2.42c}$$

$$\mathbf{d} = \mathbf{d}_0 \,, \text{ in } \Omega \text{ at } t = T_0 \,, \tag{2.42d}$$

$$\dot{\mathbf{d}} = \boldsymbol{v}_0 \,, \text{ in } \Omega \text{ at } t = T_0 \,, \tag{2.42e}$$

$$\mathbf{d} = \mathbf{0} \,, \quad \text{on } \subset \Gamma_{\mathrm{d}} \times \mathbb{T} \,, \tag{2.42f}$$

$$\boldsymbol{\omega} = \mathbf{0} \,, \quad \text{on } \subset \Gamma_{\mathrm{d}} \times \mathbb{T} \,, \tag{2.42g}$$

$$\mathbf{n}^\alpha \hat{e}_\alpha = \bar{\mathbf{p}} \,, \quad \text{on } \subset \Gamma_{\mathrm{n}} \times \mathbb{T} \,, \tag{2.42h}$$

$$\mathbf{m}^\alpha \hat{e}_\alpha = \bar{\mathbf{r}} \,, \quad \text{on } \subset \Gamma_{\mathrm{n}} \times \mathbb{T} \,, \tag{2.42i}$$

where $\hat{\mathbf{e}} = \hat{e}_\alpha \mathbf{A}^\alpha$ stands for the normal to the Neumann boundary Γ_{n}. The stress-resultant traction force and the stress-resultant traction moment vectors are given by,

$$\mathbf{n}^\alpha = n^{\alpha\beta} \mathbf{A}_\beta + q^\alpha \mathbf{A}_3 \,, \tag{2.43a}$$

$$\mathbf{m}^\alpha = m^{\alpha\beta} \mathbf{A}_\beta \,, \tag{2.43b}$$

respectively. Moreover, the covariant derivative with respect to θ_α, the first and the second time derivatives are denoted by $\bullet|_\alpha$, $\dot{\bullet}$ and $\ddot{\bullet}$, respectively. Additionally, q^α stand for the contravariant components of the shear force vector. Eqs. (2.42a), (2.42b) and (2.42c) represent the in-plane, the out-of-plane and the moment equilibrium, respectively. Eqs. (2.42d) and (2.42e) stand for the initial conditions of the displacement and the velocity fields, respectively. Eqs. (2.42f) and (2.42g) stand for the Dirichlet boundary conditions on the displacement and rotation fields along Γ_{d}, respectively, whereas Eqs. (2.42h) and (2.42i) stand for the Neumann boundary conditions along Γ_{n}. For the placement of the weak form of the Kirchhoff-Love BVP, solution space $\boldsymbol{\mathcal{V}}$ defined in Eq. (2.14) needs to be redefined in order to account for twice weakly differentiable functions which satisfy also the rotation Dirichlet boundary conditions, that is,

$$\boldsymbol{\mathcal{V}} = \left\{ \mathbf{h} \in \left(\boldsymbol{\mathcal{H}}^2(\Omega)\right)^3 \middle| \mathbf{h} = \mathbf{0} \text{ and } \boldsymbol{\omega}(\mathbf{h}) = \mathbf{0} \text{ along } \subset \Gamma_{\mathrm{d}} \right\} . \tag{2.44}$$

The additional derivative requirement comes from the presence of second order derivatives on the displacement field through the bending strain defined in Eq. (2.35c). As it is mentioned in Sec. 2.3.2, the problem can be formulated by enforcing weakly the Dirichlet boundary conditions, rendering the admissible space $\boldsymbol{\mathcal{V}}$ free from complying with the Dirichlet boundary conditions along Γ_{d}. The weak form of the Kirchhoff-Love shell iBVP defined in Eqs. (2.42) for each time instance $t \in \mathbb{T}$ reads: Find $\mathbf{d} \in \boldsymbol{\mathcal{V}}$ such that:

$$\left\langle \delta\mathbf{d}, \rho\bar{h}\ddot{\mathbf{d}} \right\rangle_{0,\Omega} + \left\langle \delta\mathbf{d}, c\bar{h}\dot{\mathbf{d}} \right\rangle_{0,\Omega} + a(\delta\mathbf{d}, \mathbf{d}) = l(\delta\mathbf{d}) \quad \forall \delta\mathbf{d} \in \boldsymbol{\mathcal{V}}, \tag{2.45}$$

where form $a : \boldsymbol{\mathcal{V}} \times \boldsymbol{\mathcal{V}} \rightarrow \mathbb{R}$ and linear functional $l : \boldsymbol{\mathcal{V}} \rightarrow \mathbb{R}$ in Eq. (2.45) are defined as follows,

$$a(\delta\mathbf{d}, \mathbf{d}) := \int_{\Omega} \delta\boldsymbol{\varepsilon} : \mathbf{n} \, \mathrm{d}\Omega + \int_{\Omega} \delta\boldsymbol{\kappa} : \mathbf{m} \, \mathrm{d}\Omega , \tag{2.46a}$$

$$l(\delta\mathbf{d}) := \langle \delta\mathbf{d}, \mathbf{b} \rangle_{0,\Omega} + \left\langle \delta\mathbf{d}, \bar{\mathbf{p}} \right\rangle_{0,\Gamma_{\mathrm{n}}} + \langle \delta\boldsymbol{\omega}, \bar{\mathbf{r}} \rangle_{0,\Gamma_{\mathrm{n}}} . \tag{2.46b}$$

It can be shown that for linear kinematics, problem in Eq. (2.45) has a unique solution as per Lax-Milgram theorem in Thm. 2.2, see also in Noels et al. [49].

2.3.3 Structural analysis of membranes

Membranes can be generally derived from shells by neglecting the bending stiffness and the shear deformation. This kind of structures can only withstand tensile stresses when no stabilization is considered because significant amount of compressive stresses might result in wrinkling which in principle represents zero energy modes (static indeterminacy). In order to attain a static equilibrium configuration, also internal prestress $\mathbf{n}_0 = n_0^{\alpha\beta}\mathbf{A}_\alpha \otimes \mathbf{A}_\beta$ needs to be applied, in addition to a stabilizing body force field $\mathbf{b}$ (pneumatic structures). As a result of the applied internal prestress, the boundaries need either to be fully supported with a given condition $\mathbf{d} = \mathbf{g}$ on $\varGamma_\mathrm{d}$ or cables need to be embedded, see also in Philipp et al. [50–53] and Bauer et al. [54]. Let the set of boundary embedded cables be geometrically defined by $\mathbf{C} : \hat{\varGamma}_\mathrm{c} \to \varGamma_\mathrm{c} \subset \partial\varOmega$ which are also prestressed with prestress $\hat{\mathbf{f}}_0 = \hat{f}_0\mathbf{A}\otimes\mathbf{A}$, where $\mathbf{A}$ stands for the base vector of the parametrization $\mathbf{C}$, see Eq. (2.6). The kinematics of the embedded cables are defined via the GL strain tensor $\hat{\boldsymbol{\varepsilon}} = \hat{\varepsilon}\,\tilde{\mathbf{A}}\otimes\tilde{\mathbf{A}}$ similar to Eq. (2.35a), whose component write,

$$\hat{\varepsilon} = \mathbf{a}\cdot\mathbf{a} - \mathbf{A}\cdot\mathbf{A}\,, \tag{2.47}$$

where $\tilde{\mathbf{A}} = \|\mathbf{A}\|_2^{-2}\,\mathbf{A}$ stands for the contravariant base vector of the cables' convective space. Additionally, $\mathbf{A}$ and $\mathbf{a}$ stand for the base vectors of the reference and the current configuration of the cables, respectively. Similar to the definition in Eq. (2.32), the 2nd Piola-Kirchhoff force field $\hat{\mathbf{f}} = \hat{f}\,\mathbf{A}\otimes\mathbf{A}$ for the set of cables is defined through the constitutive material law as,

$$\hat{f} = \hat{E}\,\hat{A}\,\hat{\varepsilon}\,, \tag{2.48}$$

for all $\mathbf{X} \in \varGamma_\mathrm{c}$ where $\hat{E}$ and $\hat{A}$, stand for the Young's modulus and the cross sectional area of the cables, respectively. Then, the strong form of the membrane iBVP reads,

$$\rho\,\ddot{d}^\beta + c\,\dot{d}^\beta + \left(n^{\alpha\beta} + n_0^{\alpha\beta}\right)|_\alpha + b^\beta = 0 \quad \text{in } \varOmega\times\mathbb{T}\,, \tag{2.49a}$$

$$\rho\,\ddot{d}_3 + c\,\dot{d}_3 + \left(n^{\alpha\beta} + n_0^{\alpha\beta}\right)\mathcal{B}_{\alpha\beta} + b_3 = 0 \quad \text{in } \varOmega\times\mathbb{T}\,, \tag{2.49b}$$

$$\hat{\rho}\ddot{\mathbf{d}} + \hat{c}\dot{\mathbf{d}} + \mathbf{t} + \hat{\mathbf{t}} = \mathbf{0} \quad \text{on } \varGamma_\mathrm{c}\times\mathbb{T}\,, \tag{2.49c}$$

$$\mathbf{d} = \mathbf{d}_0 \text{ in } \varOmega \text{ at } t = T_0\,, \tag{2.49d}$$

$$\dot{\mathbf{d}} = \boldsymbol{v}_0 \text{ in } \varOmega \text{ at } t = T_0\,, \tag{2.49e}$$

$$\mathbf{d} = \mathbf{g} \quad \text{on } \varGamma_\mathrm{d}\times\mathbb{T}\,, \tag{2.49f}$$

$$\mathbf{t} = \bar{\mathbf{p}} \quad \text{on } \varGamma_\mathrm{n}\times\mathbb{T}\,, \tag{2.49g}$$

where $\hat{\rho}$ and $\hat{c}$ stand for the density and the damping coefficient of the cables. In contrast to shells, membrane problems can only be formulated by means of nonlinear strain measures so that they are rendered statically determinate. Eqs. (2.49a) and (2.49b) stand for the in-plane and out-of-plane dynamic equilibrium, respectively. Eq. (2.49c) stands for the dynamic equilibrium along the boundaries where cables are embedded. The initial conditions on the displacement and velocity fields are given in Eqs. (2.49d) and (2.49e), respectively. Then, Eqs. (2.49f) and (2.49g) represent the Dirichlet and the Neumann boundary conditions, respectively. Concerning the traction vectors appearing in Eq. (2.49c), they are defined by means of the *Cauchy* stress tensor, namely,

$$\mathbf{t} = \left(n^{\alpha\beta} + n_0^{\alpha\beta} \right) \hat{e}_\alpha \mathbf{a}_\beta \,, \tag{2.50a}$$

$$\hat{\mathbf{t}} = \left(\hat{f} + \hat{f}_0 \right) \|\mathbf{A}\|_2 \mathbf{a} \,, \tag{2.50b}$$

respectively, see also in Başar et al. [1]. Note that the traction vector along the boundary of the membrane defined in Eq. (2.50a) is defined similar to Eq. (2.43a) by neglecting the shear force and adding the prestress. For the weak form of the membrane iBVP one-time weakly differentiable functions are enough and thus, the space defined in Eq. (2.14) is in this case valid. Therefore, the weak form of the membrane iBVP reads: Find $\mathbf{d} \in \boldsymbol{\mathcal{V}}$ such that,

$$\begin{aligned} \left\langle \delta\mathbf{d}, \rho \bar{h} \ddot{\mathbf{d}} \right\rangle_{0,\Omega} + \left\langle \delta\mathbf{d}, c \bar{h} \dot{\mathbf{d}} \right\rangle_{0,\Omega} + \left\langle \delta\mathbf{d}, \hat{\rho} \hat{A} \ddot{\mathbf{d}} \right\rangle_{0,\Gamma_\mathrm{c}} + \left\langle \delta\mathbf{d}, \hat{c} \hat{A} \dot{\mathbf{d}} \right\rangle_{0,\Gamma_\mathrm{c}} & \\ + a\left(\delta\mathbf{d}, \mathbf{d}\right) = l\left(\delta\mathbf{d}\right) \quad \forall \delta\mathbf{d} \in \boldsymbol{\mathcal{V}}, & \end{aligned} \tag{2.51}$$

where form $a : \boldsymbol{\mathcal{V}} \times \boldsymbol{\mathcal{V}} \rightarrow \mathbb{R}$ and linear functional $l : \boldsymbol{\mathcal{V}} \rightarrow \mathbb{R}$ in Eq. (2.51) are defined as follows,

$$a\left(\delta\mathbf{d}, \mathbf{d}\right) := \int_\Omega \delta\boldsymbol{\varepsilon} : \left(\mathbf{n} + \mathbf{n}_0 \right) \, \mathrm{d}\Omega + \int_{\Gamma_\mathrm{c}} \delta\hat{\boldsymbol{\varepsilon}} : \left(\hat{\mathbf{f}} + \hat{\mathbf{f}}_0 \right) \, \mathrm{d}\Gamma \,, \tag{2.52a}$$

$$l\left(\delta\mathbf{d}\right) := \left\langle \delta\mathbf{d}, \mathbf{b} \right\rangle_{0,\Omega} + \left\langle \delta\mathbf{d}, \bar{\mathbf{p}} \right\rangle_{0,\Gamma_\mathrm{n}} \,. \tag{2.52b}$$

Given that no significant wrinkling due to excessive compressive forces develops throughout the analysis, problem in Eq. (2.51) is well-defined.

2.3.4 Form-finding analysis

Being typical for membrane structures, prestress is applied frequently in conjunction with a stabilizing surface traction field, chosen in such a way that the membrane can withstand the occurring load cases without damage and significant wrinkling. Thus, the structure is in static equilibrium before the loading process (e.g. by external loads due to snow, wind, live load or earthquakes) begins. The latter means that the displacement field resulting from zero external tractions and without root point excitation (inhomogeneous Dirichlet boundary conditions) equals zero. It should be borne in mind that not any free-form surface Ω representing a membrane structure is in static equilibrium given the prescribed Dirichlet/Neumann boundary conditions, the embedded cables and the corresponding prestress fields, see Sec. 2.3.3, as opposed to other structures, such as plates, shells etc. This is due to the fact that membrane theory requires the internal forces to be tangential to the structure's surface, which results in a direct coupling between overall forces, state and shape. Thus, the challenge is to find the specific equilibrium shape for a given prestress distribution (possibly extended by some external follower force terms in case of inflatable structures) since this constitutes an inverse problem with all the associated difficulties for numerical solution schemes. More specifically, the discrete solution is non-unique with respect to the tangential movements of the geometric parametrization. Therefore, a large variety of so-called form-finding methods was developed which use different strategies to regularize the inherent singularity in the discrete equations for the computation of equilibrium shapes of membranes subject to prescribed prestress fields. One approach is the *Dynamic Relaxation* method, see in Day [55], Barnes [56], and Wakefield [57], where a fictitious transient analysis of the membrane structure is performed considering significant damping which finally reaches the static equilibrium configuration representing the sought membrane shape under prestress. Another class of solution procedures is based on the idea of the so-called *Force Densities* which was introduced in Linkwitz et al. [58] and Linkwitz [59]. An extension of this to a consistent formulation in the frame of large deformation continuum mechanics was realized through the *Updated Reference Strategy* (URS) introduced in Bletzinger et al. [60] which extends the originally non-solvable weak form, written in terms of Cauchy stresses in the current configuration, by a stabilization term formulated in terms of the 2nd Piola-Kirchhoff stress state in a step-wise updated reference configuration based on a homotopy mapping. Enhancements and adaptations of the URS can be found in Wüchner et al. [61] and Dieringer et al. [62] amongst others. Due to its generality regarding the type of structural model (cable, membrane or any combinations of them) and especially the flexibility to employ any suitable set of basis functions, see also in Philipp et al. [52], this is the numerical solution approach used within the present work. The extended functional for the form-finding analysis based on the URS is provided in Eq. (34) on page 152 of the original publication in Wüchner et al. [61]. In this thesis the URS is used when considering only the stabilization term, that is the term related to the 2nd Piola-Kirchhoff force tensor.

2.4 Space and time discretization

The iBVPs and their corresponding weak forms for the Kirchhoff-Love shells and the membranes in Secs. 2.3.2 and 2.3.3, respectively, are discretized separately in space and in time. For the space discretization, the *Buvnov-Galerkin finite element* discretization is employed which is later on extended to account for IGA.

2.4.1 Semidiscretization

Consider a partition $\mathcal{T}_{\mathrm{h}}$ of Ω consisting of a set of finite elements $\mathcal{T}_i$, $i = 1, \dots, n_{\mathrm{e}} \in \mathbb{N}$. For a standard FEM approach this triangulation results in a faceted representation Ω_{h} of Ω which is not the case for IGA. However, the discrete equation systems within both numerical approaches have identical forms and therefore are presented herein unified. Let space $\mathcal{V}_{\mathrm{h}}$ be a finite dimensional subspace of $\mathcal{V}$, such that,

$$\mathcal{V}_{\mathrm{h}} = \left\{ \mathbf{h} \in \mathcal{V} \,\middle|\, \mathbf{h}_{|\mathcal{T}_i} \in \mathcal{P}(\mathcal{T}_i) \text{ for all } i = 1, \dots, n_{\mathrm{e}} \right\} , \tag{2.53}$$

where $\mathcal{P}(\mathcal{T}_i)$ stands for the space of all polynomial vector functions in element $\mathcal{T}_i$. Subsequently, let $\boldsymbol{\phi}_i$, $i = 1, \dots, \dim \mathcal{V}_{\mathrm{h}}$ be a basis of $\mathcal{V}_{\mathrm{h}}$. Then, for each element $\mathbf{d} \in \mathcal{V}_{\mathrm{h}}$ there exists reals $\hat{d}_i$ such that,

$$\mathbf{d} = \sum_{i=1}^{\dim \mathcal{V}_{\mathrm{h}}} \boldsymbol{\phi}_i \hat{d}_i \, , \tag{2.54}$$

at a given time instance $t \in \mathbb{T}$. Reals $\hat{d}_i$ are the so-called *Degrees of Freedom* (DOFs) and can be grouped into a vector, namely,

$$\hat{\mathbf{d}} = \begin{bmatrix} \hat{d}_1 & \cdots & \hat{d}_{\dim \mathcal{V}_{\mathrm{h}}} \end{bmatrix}^{\mathrm{T}} , \tag{2.55}$$

to ease the set-up of the discrete equations systems. In this way, projection of either variational form in Eq. (2.45) or in Eq. (2.51) onto $\mathcal{V}_\mathrm{h} \times \mathcal{V}_\mathrm{h}$ yields a nonlinear equation system, which in dynamic residual form writes,

$$\mathbf{R}_\mathrm{d}(\hat{\mathbf{d}}) := \mathbf{M}\ddot{\hat{\mathbf{d}}} + \mathbf{D}\dot{\hat{\mathbf{d}}} + \mathbf{R}(\hat{\mathbf{d}}) - \hat{\mathbf{F}} \,, \tag{2.56}$$

where $\hat{\mathbf{d}}$, $\dot{\hat{\mathbf{d}}}$ and $\ddot{\hat{\mathbf{d}}}$ stand for the discrete vectors of the displacement, the velocity and the acceleration DOFs, respectively, whereas $\hat{\mathbf{F}}$ stands for the externally applied force vector. The mass matrix $\mathbf{M}$ in Eq. (2.56) for the Kirchhoff-Love and the membrane problem has entries,

$$M_{(i,j)} = \left\langle \boldsymbol{\phi}_i, \rho \boldsymbol{\phi}_j \right\rangle_\Omega \,, \tag{2.57a}$$

$$M_{(i,j)} = \left\langle \boldsymbol{\phi}_i, \rho \boldsymbol{\phi}_j \right\rangle_\Omega + \left\langle \boldsymbol{\phi}_i, \hat{\rho} \boldsymbol{\phi}_j \right\rangle_{\Gamma_\mathrm{c}} \,, \tag{2.57b}$$

respectively. The components of the steady-state residual vector $\mathbf{R}$ in Eq. (2.56) on the other hand for the Kirchhoff-Love and the membrane problem are given by,

$$R_{(i)} = \int_\Omega \frac{\partial \boldsymbol{\varepsilon}}{\partial \hat{d}_i} : \mathbf{n} \,\mathrm{d}\Omega + \int_\Omega \frac{\partial \boldsymbol{\kappa}}{\partial \hat{d}_i} : \mathbf{m} \,\mathrm{d}\Omega \tag{2.58a}$$

$$R_{(i)} = \int_\Omega \frac{\partial \boldsymbol{\varepsilon}}{\partial \hat{d}_i} : (\mathbf{n} + \mathbf{n}_0) \,\mathrm{d}\Omega + \int_{\Gamma_\mathrm{c}} \frac{\partial \hat{\boldsymbol{\varepsilon}}}{\partial \hat{d}_i} : (\hat{\mathbf{f}} + \hat{\mathbf{f}}_0) \,\mathrm{d}\Gamma \,, \tag{2.58b}$$

as per the definitions of the corresponding forms in Eqs. (2.46a) and (2.52a), respectively. In this way, the entries of the steady-state tangent stiffness matrix $\mathbf{K}$ for the Kirchhoff-Love and membrane problem are given by $K_{(i,j)} = \partial R_{(i)} / \partial \hat{d}_j$, namely,

$$\begin{aligned} K_{(i,j)} = &\int_\Omega \frac{\partial \boldsymbol{\varepsilon}}{\partial \hat{d}_i} : \frac{\partial \mathbf{n}}{\partial \hat{d}_j} \,\mathrm{d}\Omega + \int_\Omega \frac{\partial^2 \boldsymbol{\varepsilon}}{\partial \hat{d}_i \partial \hat{d}_j} : \mathbf{n} \,\mathrm{d}\Omega + \\ &\int_\Omega \frac{\partial \boldsymbol{\kappa}}{\partial \hat{d}_i} : \frac{\partial \mathbf{m}}{\partial \hat{d}_j} \,\mathrm{d}\Omega + \int_\Omega \frac{\partial^2 \boldsymbol{\kappa}}{\partial \hat{d}_i \partial \hat{d}_j} : \mathbf{m} \,\mathrm{d}\Omega \,, \end{aligned} \tag{2.59a}$$

$$\begin{aligned} K_{(i,j)} = &\int_\Omega \frac{\partial \boldsymbol{\varepsilon}}{\partial \hat{d}_i} : \frac{\partial \mathbf{n}}{\partial \hat{d}_j} \,\mathrm{d}\Omega + \int_\Omega \frac{\partial^2 \boldsymbol{\varepsilon}}{\partial \hat{d}_i \partial \hat{d}_j} : (\mathbf{n} + \mathbf{n}_0) \,\mathrm{d}\Omega + \\ &\int_{\Gamma_\mathrm{c}} \frac{\partial \hat{\boldsymbol{\varepsilon}}}{\partial \hat{d}_i} : \frac{\partial \hat{\mathbf{f}}}{\partial \hat{d}_j} \,\mathrm{d}\Gamma + \int_{\Gamma_\mathrm{c}} \frac{\partial^2 \hat{\boldsymbol{\varepsilon}}}{\partial \hat{d}_i \partial \hat{d}_j} : (\hat{\mathbf{f}} + \hat{\mathbf{f}}_0) \,\mathrm{d}\Gamma \,, \end{aligned} \tag{2.59b}$$

respectively. Lastly, the entries of the force vector $\hat{\mathbf{F}}$ are given by,

$$\hat{F}_{(i)} = \left\langle \boldsymbol{\phi}_i, \mathbf{b} \right\rangle_{0,\varOmega} + \left\langle \boldsymbol{\phi}_i, \bar{\mathbf{p}} \right\rangle_{0,\varGamma_\mathrm{n}} + \left\langle \frac{\partial \boldsymbol{\omega}}{\partial \hat{d}_i}, \bar{\mathbf{r}} \right\rangle_{0,\varGamma_\mathrm{n}} , \tag{2.60a}$$

$$\hat{F}_{(i)} = \left\langle \boldsymbol{\phi}_i, \mathbf{b} \right\rangle_{0,\varOmega} + \left\langle \boldsymbol{\phi}_i, \bar{\mathbf{p}} \right\rangle_{0,\varGamma_\mathrm{n}} , \tag{2.60b}$$

for the Kirchhoff-Love shell and the membrane problem, respectively.

2.4.2 Time discretization and discrete equation system

Having defined the semi-discrete equation system in Eq. (2.56), the *Newmark* method is employed for the time discretization. That is because it is unconditionally stable for linear problems, second order in time and it is associated with the least numerical damping, see in Newmark [63]. The forthcoming derivations can be however easily exploited for any desirable time integration method. In this way, assumed is that the continuous time domain $\mathbb{T}$ is discretized in time steps $t_{\hat{n}}$ with constant time step size $\varDelta t = t_{\hat{n}} - t_{\hat{n}-1}$. Let $\hat{\mathbf{d}}_{\hat{n}} = \hat{\mathbf{d}}(t_{\hat{n}})$ stand for the discrete vector of DOFs at time step $t_{\hat{n}} \in \mathbb{T}$. Following Newmark [63], the assumptions below on the displacement, the velocity and the dynamic residual at $t_{\hat{n}}$ are made,

$$\hat{\mathbf{d}}_{\hat{n}} = \hat{\mathbf{d}}_{\hat{n}-1} + \varDelta t\, \dot{\hat{\mathbf{d}}}_{\hat{n}-1} + (\varDelta t)^2 \left(\frac{1}{2} - \beta_\mathrm{n} \right) \ddot{\hat{\mathbf{d}}}_{\hat{n}-1} + (\varDelta t)^2 \beta_\mathrm{n}\, \ddot{\hat{\mathbf{d}}}_{\hat{n}} , \tag{2.61a}$$

$$\dot{\hat{\mathbf{d}}}_{\hat{n}} = \dot{\hat{\mathbf{d}}}_{\hat{n}-1} + \varDelta t \left(1 - \gamma_\mathrm{n} \right) \ddot{\hat{\mathbf{d}}}_{\hat{n}-1} + \varDelta t \gamma_\mathrm{n}\, \ddot{\hat{\mathbf{d}}}_{\hat{n}} , \tag{2.61b}$$

$$\mathbf{R}_\mathrm{d}(\hat{\mathbf{d}}_{\hat{n}}) = \mathbf{M}\, \ddot{\hat{\mathbf{d}}}_{\hat{n}} + \mathbf{D}\, \dot{\hat{\mathbf{d}}}_{\hat{n}} + \mathbf{R}(\hat{\mathbf{d}}_{\hat{n}}) - \hat{\mathbf{F}}_{\hat{n}} , \tag{2.61c}$$

where β_n and γ_n are the so-called Newmark parameters and where $\hat{\mathbf{F}}_{\hat{n}} = \hat{\mathbf{F}}(t_{\hat{n}})$. Substituting Eqs. (2.61a) and (2.61b) in Eq. (2.61c), Eq. (2.56) can be written solely depending on the displacement field of time step $t_{\hat{n}}$ namely,

$$\begin{aligned} \mathbf{R}_\mathrm{d}(\hat{\mathbf{d}}_{\hat{n}}) = & \left(\frac{1}{\beta_\mathrm{n} (\varDelta t)^2} \mathbf{M} + \frac{\gamma_\mathrm{n}}{\beta_\mathrm{n} \varDelta t} \mathbf{D} \right) \hat{\mathbf{d}}_{\hat{n}} + \mathbf{R}(\hat{\mathbf{d}}_{\hat{n}}) - \hat{\mathbf{F}}_{\hat{n}} - \\ & \left(\frac{1}{\beta_\mathrm{n}} \mathbf{M} + \frac{\gamma_\mathrm{n}}{\beta_\mathrm{n} \varDelta t} \mathbf{D} \right) \hat{\mathbf{d}}_{\hat{n}-1} - \left(\frac{1}{\beta_\mathrm{n} \varDelta t} \mathbf{M} - \frac{\beta_\mathrm{n} - \gamma_\mathrm{n}}{\beta_\mathrm{n}} \right) \dot{\hat{\mathbf{d}}}_{\hat{n}-1} - \\ & \left(\frac{1 - 2\beta_\mathrm{n}}{2\beta_\mathrm{n}} \mathbf{M} - \varDelta t \frac{2\beta_\mathrm{n} - \gamma_\mathrm{n}}{2\beta_\mathrm{n}} \mathbf{D} \right) \ddot{\hat{\mathbf{d}}}_{\hat{n}-1} . \end{aligned} \tag{2.62}$$

The iterative *Newton-Raphson* method is subsequently employed for solving the nonlinear equation system in Eq. (2.62) at each time step $t_{\hat{n}} \in \mathbb{T}$. In this way, the linearized equation system to be solved at the $\hat{\imath}$-th Newton-Raphson iteration writes,

$$\mathbf{K}_{\mathrm{d}}(\hat{\mathbf{d}}_{\hat{n},\hat{\imath}})\,\Delta_{\hat{n},\hat{\imath}}\,\hat{\mathbf{d}} = -\mathbf{R}_{\mathrm{d}}(\hat{\mathbf{d}}_{\hat{n},\hat{\imath}})\,, \tag{2.63}$$

$\hat{\mathbf{d}}_{\hat{n},\hat{\imath}}$ being the discrete vector of DOFs at $\hat{\imath}$-th nonlinear iteration within $\hat{n}$-th time step and where the displacement increment is defined as,

$$\Delta_{\hat{n},\hat{\imath}}\,\hat{\mathbf{d}} := \hat{\mathbf{d}}_{\hat{n},\hat{\imath}+1} - \hat{\mathbf{d}}_{\hat{n},\hat{\imath}}\,. \tag{2.64}$$

The effective tangent stiffness matrix $\mathbf{K}_{\mathrm{d}}$ is then given by,

$$\mathbf{K}_{\mathrm{d}}(\hat{\mathbf{d}}_{\hat{n},\hat{\imath}}) = \left(\frac{1}{\beta_{\mathrm{n}}(\Delta t)^2}\mathbf{M} + \frac{\gamma_{\mathrm{n}}}{\beta_{\mathrm{n}}\Delta t}\mathbf{D} \right) + \mathbf{K}(\hat{\mathbf{d}}_{\hat{n},\hat{\imath}})\,. \tag{2.65}$$

2.4.3 Modal analysis and Rayleigh damping approach

It is possible for a structure with a linear strain measure and linear material law, to decompose its dynamic response into a number of linearly independent modes using the so-called *modal analysis.* These modes are called *eigenmode shapes* and the corresponding frequencies *eigenfrequencies* or *natural frequencies.* To obtain the eigenvalue problem which governs the modal decomposition of the dynamic system, firstly the damping matrix and the external loading are neglected from residual equation system in Eq. (2.56). Then, it is assumed that the discrete vector of DOFs is decomposed on its space-time dependence as,

$$\hat{\mathbf{d}} = \hat{\mathbf{v}}\,\sin(\hat{\omega}\,t)\,, \tag{2.66}$$

$\hat{\mathbf{v}}$ being the time invariant set of DOFs. Additionally, since also nonlinear strain measures are considered within this thesis, a first order linearization of the steady-state residual $\mathbf{R}(\hat{\mathbf{d}})$ in Eq. (2.56) is performed, that is,

$$\mathbf{R}(\hat{\mathbf{d}}) \approx \mathbf{K}_0\hat{\mathbf{d}}\,, \tag{2.67}$$

where $\mathbf{K}_0 = \mathbf{K}(\hat{\mathbf{d}}_{0,0})$ stands for the linear stiffness matrix, that is, the tangent stiffness matrix evaluated at $t = T_0$ and at the first nonlinear iteration. In this way, residual equation system in Eq. (2.56) becomes,

$$-\hat{\omega}^2\mathbf{M}\hat{\mathbf{v}} + \mathbf{K}_0\hat{\mathbf{v}} = \mathbf{0}\,, \tag{2.68}$$

which is an eigenvalue problem to be solved for the eigenmode shapes $\hat{\mathbf{v}}_i$ and the corresponding eigenfrequencies $f_i = \hat{\omega}_i/2\pi$, $i = 1,\dots,\dim \boldsymbol{\mathcal{V}}_\mathrm{h}$.

Regarding the damping matrix $\mathbf{D}$, the *Rayleigh* damping approach (see in Clough et al. [64] and Thomsen et al. [65]) is employed, that is,

$$\mathbf{D} = \alpha_\mathrm{r}\mathbf{M} + \beta_\mathrm{r}\mathbf{K}_0\,, \tag{2.69}$$

$\alpha_\mathrm{r}, \beta_\mathrm{r} \in \mathbb{R}^{\star}_{+}$ being the Rayleigh damping parameters. In a similar manner as in Chowdhury et al. [66], given two significant frequencies f_i, f_j with $i, j = 1,\dots,\dim \boldsymbol{\mathcal{V}}_\mathrm{h}$ of the problem and their corresponding damping ratios ζ_i, ζ_j, respectively, the Rayleigh parameters can be estimated as follows,

$$\alpha_\mathrm{r} = \frac{2\hat{\omega}_i\hat{\omega}_j}{\hat{\omega}_j^2 - \hat{\omega}_i^2}\left(\hat{\omega}_j\zeta_i - \hat{\omega}_i\zeta_j\right)\,, \tag{2.70a}$$

$$\beta_\mathrm{r} = \frac{2\hat{\omega}_i\hat{\omega}_j}{\hat{\omega}_j^2 - \hat{\omega}_i^2}\left(-\frac{\zeta_i}{\hat{\omega}_j} + \frac{\zeta_j}{\hat{\omega}_i}\right)\,, \tag{2.70b}$$

respectively.

Chapter 3

Isogeometric Analysis on Multipatch Surfaces

In this chapter the preliminaries concerning NURBS-based IGA on trimmed multipatches are laid which are used in the sequel of this thesis and studies Apostolatos et al. [10] and Breitenberger et al. [6] are closely followed. Given the parametric description of curves and surfaces demonstrated in Chap. 2, this chapter starts with the NURBS-based parametric description of curves and surfaces. Subsequently, the trimmed multipatch representation of surfaces in *Computer-Aided Design* (CAD) is shown and the methodology for handling trimmed surface NURBS multipatches within isogeometric analysis is subsequently discussed. Concerning the continuity enforcement across the multipatches, the Penalty, the Lagrange Multipliers and the Nitsche-type methods are formulated and elaborated. These methods are then compared in the static analysis of an infinite plate with a hole subject to tension and in the modal analysis of a circular plate within two-dimensional linear elasticity.

3.1 Parametric modelling using non-uniform rational b-splines

In the following, the NURBS parametrized curves and surfaces are introduced along with the underlying basis functions. The NURBS basis functions consist of piecewise rational polynomial functions constructed using the piecewise polynomial b-spline basis functions and a set of weights. In turn, the b-spline basis functions originate from the Bernstein polynomial basis functions used for constructing Bézier curves and surfaces which constitute the origins of modern CAD modelling. More information on the subject can be found in Piegl et al. [67].

3.1.1 Non-uniform rational b-spline curves

In this section the NURBS curves are introduced. Let the curve's parametric space $\hat{\gamma}$ be defined via a knot vector $\boldsymbol{\Theta}$ consisting of a set of knots $\hat{\theta}_i \in \boldsymbol{\Theta}$, with $i = 1, \ldots, m \in \mathbb{N}$ in ascending order. Given also a polynomial order $\hat{p}$, the NURBS basis functions $R_{\hat{p},i}$, with $i = 1, \ldots, n \in \mathbb{N}$, are constructed by means of the b-spline basis functions $N_{\hat{p},i}$ in $\hat{\gamma}$ as,

$$R_{\hat{p},i}(\theta) = \frac{\hat{w}_i \, N_{\hat{p},i}(\theta)}{\sum_{j=1}^{n} \hat{w}_j \, N_{\hat{p},j}(\theta)} \,, \quad \forall \theta \in \hat{\gamma} \,, \tag{3.1}$$

where $\hat{w}_i$ stand for the weights of the NURBS basis functions in $\boldsymbol{\Theta}$. The number of knots, the number of the basis functions and the polynomial order of the basis functions are related via $m = n + \hat{p} + 1$. Then, the b-spline basis functions $N_{\hat{p},i}$ are constructed by means of the *Cox-De Boor* recursion formula, that is,

$$N_{\hat{q},i}(\theta) = \frac{\theta - \hat{\theta}_i}{\hat{\theta}_{i+\hat{q}} - \hat{\theta}_i} \, N_{\hat{q}-1,i}(\theta) + \frac{\hat{\theta}_{i+\hat{q}+1} - \theta}{\hat{\theta}_{i+\hat{q}+1} - \hat{\theta}_{i+1}} \, N_{\hat{q}-1,i+1}(\theta) \,, \; \forall \theta \in \hat{\gamma} \,, \tag{3.2}$$

where $\hat{q} = 0, \ldots, \hat{p}$. Thus, the b-spline basis functions $N_{\hat{p},i}$ are obtained by a recursive construction $\hat{q} = 0, \ldots, \hat{p}$ where $N_{0,i}(\theta) = 1$ for $\theta \in [\hat{\theta}_i, \hat{\theta}_{i+1}[$ while $N_{0,i}(\theta) = 0$ identically elsewhere concerning the constant basis functions. Moreover, the definition $0/0 = 0$ is also assumed in Eq. (3.2). The b-spline and subsequently the NURBS basis functions attain C^{∞}-continuity within each knot span $]\hat{\theta}_i, \hat{\theta}_{i+1}[\subset \hat{\gamma}$ and $C^{\hat{p}-\hat{k}_i}$-continuity across knots $\hat{\theta}_i$, $\hat{k}_i$ being the multiplicity of knot $\hat{\theta}_i$ in $\boldsymbol{\Theta}$. In this way, given a set of *Control Points* (CPs) $\hat{\mathbf{X}}_i$, $i = 1, \ldots, n \in \mathbb{N}$ in $\mathbb{R}^\alpha$ Euclidean space, known as the *Control Polygon*, the corresponding NURBS curve $\mathbf{C} : \hat{\gamma} \rightarrow \mathbb{R}^\alpha$ is defined as follows,

$$\mathbf{C}(\theta) = \sum_{i=1}^{n} R_{\hat{p},i}(\theta)\ \hat{\mathbf{X}}_i\,, \tag{3.3}$$

at each parametric location $\theta \in \hat{\gamma}$. Within this thesis, open knot vectors $\boldsymbol{\Theta}$ are considered, namely, the first and the last knots, $\hat{\theta}_1, \hat{\theta}_m \in \boldsymbol{\Theta}$ respectively, have $\hat{p}+1$-multiplicity so that the curve is interpolated by the control polygon at the beginning and at the end. In the sequel, saying that a NURBS basis $R_{\hat{p},i}$, $i = 1, \ldots, n$ is of polynomial order $\hat{p}$ implies that its underlying b-spline basis $N_{\hat{p},i}$ attains polynomial order $\hat{p}$.

3.1.2 Non-uniform rational b-spline surfaces

The two-dimensional NURBS basis functions $R_{\hat{p}_1,\hat{p}_2,i,j}$, with $i = 1, \ldots, m_1 \in \mathbb{N}$ and $j = 1, \ldots, m_2 \in \mathbb{N}$, are constructed by means of the two-dimensional b-spline basis functions $N_{\hat{p}_1,\hat{p}_2,i,j}$ in a similar fashion as the NURBS curves in Eq. (3.1), that is,

$$R_{\hat{p}_1,\hat{p}_2,i,j}\left(\theta_1,\theta_2\right) = \frac{\hat{w}_{i,j} N_{\hat{p}_1,\hat{p}_2,i,j}\left(\theta_1,\theta_2\right)}{\sum_{k=1}^{n_1}\sum_{l=1}^{n_2} \hat{w}_{k,l} N_{\hat{p}_1,\hat{p}_2,k,l}\left(\theta_1,\theta_2\right)} \quad \forall\left(\theta_1,\theta_2\right) \in \hat{\Omega}\,, \tag{3.4}$$

$\hat{p}_\alpha$, m_α and n_α standing for the polynomial orders, the number of knots at each knot vector $\boldsymbol{\Theta}_\alpha$ and the number of one-dimensional b-spline basis functions in θ_α-parametric direction, respectively. Surface's parametric domain $\hat{\Omega}$ is then defined by the square domain spanned in θ_α-direction by knot vector $\boldsymbol{\Theta}_\alpha$. Additionally, $\hat{w}_{i,j}$ stands for the weight associated with NURBS basis function $R_{\hat{p}_1,\hat{p}_2,i,j}$. The two-dimensional b-spline basis functions $N_{\hat{p}_1,\hat{p}_2,i,j}$ in turn are constructed as a tensor product of the underlying one-dimensional b-spline basis functions, that is,

$$N_{\hat{p}_1,\hat{p}_2,i,j}\left(\theta_1,\theta_2\right) = N_{\hat{p}_1,i}\left(\theta_1\right) N_{\hat{p}_2,j}\left(\theta_2\right)\,, \quad \forall\left(\theta_1,\theta_2\right) \in \hat{\Omega}\,. \tag{3.5}$$

In this way, given a net of points $\hat{\mathbf{X}}_{i,j}$ in $\mathbb{R}^3$ known as the *Control Point Net*, the corresponding NURBS surface $\mathbf{S} : \hat{\Omega} \rightarrow \Omega \subset \mathbb{R}^3$ is given by,

$$\mathbf{S}\left(\theta_1,\theta_2\right) = \sum_{i=1}^{n_1}\sum_{j=1}^{n_2} R_{\hat{p}_1,\hat{p}_2,i,j}\left(\theta_1,\theta_2\right) \hat{\mathbf{X}}_{i,j}\,, \quad \forall\left(\theta_1,\theta_2\right) \in \hat{\Omega}\,. \tag{3.6}$$

Since open knot vectors $\boldsymbol{\Theta}_\alpha$ are herein considered, see Sec. 3.1.1, surface Ω interpolates the four corners of the control point net. The latter property along with the affine covariance of the NURBS basis functions allows for the application of strong Dirichlet boundary conditions at boundaries of untrimmed patches within NURBS-based IGA. In the sequel, assumed is an one-to-one a map $(i, j) \rightarrow k$ such that $R_{\hat{p}_1,\hat{p}_2,i,j} \rightarrow R_{\hat{p}_1,\hat{p}_2,k}$ with $k = 1, \ldots, n_1 n_2$ for a sequential ordering of the NURBS (or b-spline) basis functions which is necessary for the construction of the discrete equation systems.

3.1.3 Refinement

Given a NURBS-based geometric model, a refinement can be performed in order to enhance the underlying NURBS basis functions and obtain a more flexible CAD model. For NURBS curves and surfaces, see Secs. 3.1.1 and 3.1.2 respectively, the so-called knot insertion and order elevation refinement strategies are available, see in Piegl et al. [67] for more information. These naturally extend to NURBS volumes which however are not part of this thesis. Within the aforementioned refinement strategies, a new refined NURBS basis is constructed. Additionally, the geometric space spanned by the original NURBS basis is a subspace of the geometric space spanned by the newly constructed one, thus allowing for preserving the geometric model unchanged while having more flexibility. This is especially important in CAD modelling as it is often desirable to create local features on a given geometric model which the initial NURBS parametrization may not allow for. In terms of IGA this step is essential as the initial CAD model might not be analysis suitable in terms of approximation power and thus refinement may eventually be necessary. The two main refinement strategies are summarized in Fig. 3.1. As an example, the hemisphere described in Sec. 2.1.2 is herein used, constructed this time using a NURBS parametrization, see Fig. 3.1(a), where the knot lines, the control polygon and the CPs are denoted by solid lines, dashed lines and circles, respectively. Within knot insertion, new knots $\hat{\theta}_i$ are added into the parametric space $\hat{\Omega}$, see Fig. 3.1(b) and accordingly the newly generated control polygon approaches the hemisphere. On the other hand, when order elevation is employed the polynomial order of the NURBS basis functions is increased, see Fig. 3.1(c), where evidently the corresponding refined control polygon keeps a larger distance from the actual geometry when compared to knot insertion. The latter can be attributed to the higher

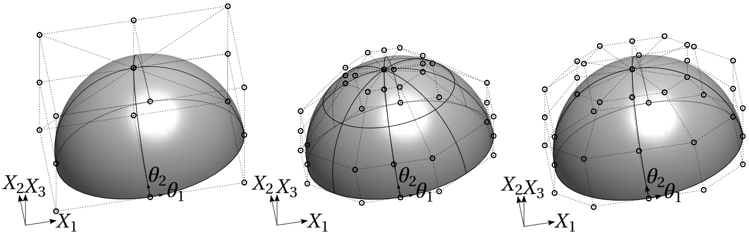

(a) NURBS model. (b) h-refinement. (c) p-refinement.

Figure 3.1: Refinement: NURBS modelling of a hemisphere along with the h-(knot insertion) and p-(order elevation) refined models.

order basis functions obtained by order elevation provided that all control point weights are strictly positive. Nevertheless, in both cases more CPs are generated and thus more flexibility is added into the model. These refinement strategies are also used for refining the NURBS-based IGA computational models. The knot insertion resembles the h-refinement in standard FEM where more elements are added in the model, whereas the order elevation resembles the p-refinement in high-order FEM where the order of the basis functions is increased. Moreover, an hp-refinement technique can be used in NURBS-based IGA where a combination of the h- and p- refinement is employed such that the continuity of the basis functions is kept unchanged. Additionally, a k-refinement strategy is also available where both elements are added while increasing the polynomial order of the basis, see in Hughes et al. [2] for more information. Thus, the refinement in NURBS-based IGA can be efficiently performed using existing highly efficient algorithms from CAD as opposed to standard FEM where the mesh generation may be a bottleneck.

3.2 Computer-aided geometric description of surfaces

It is typical for any kind of three-dimensional geometry in CAD to be described by its bounding surface, known as *Boundary-Representation* (B-Rep) description of the geometry. This is mainly due to the complexity of generating a volume parametrization for any arbitrary three-dimensional geometry which is typically not needed in CAD. Therefore, mid-surface reduced structural models, such as shells and membranes, which are described in CAD using trimmed multipatch surfaces within their B-Rep representation benefit from *Analysis in Computer Aided Design* AiCAD as demonstrated firstly in Breitenberger et al. [6].

3.2.1 Trimmed surfaces

A trimmed NURBS surface $\varOmega$ is obtained using a set of trimming curves $\hat{\mathbf{C}}_i : \tilde{\gamma}_i \rightarrow \hat{\gamma}_i \subset \hat{\varOmega}$, with $i = 1, \ldots, n_\mathrm{t} \in \mathbb{N}$ which define a closed bounded subset of the surface's original square parametric space $\hat{\varOmega}$, see Sec. 3.1.2. It is clear that trimming curves have three images: The parametric one $\tilde{\gamma}_i$, the physical one $\hat{\gamma}_i$ which is obtained using the map $\hat{\mathbf{C}}_i$ and the geometric one obtained by the composed map $\mathbf{C}_i = \mathbf{S} \circ \hat{\mathbf{C}}_i$, see also in Sec. 2.1.1. In this way, multiple bounded subsets of $\hat{\varOmega}$ may be defined and thus also surfaces with holes can be elegantly constructed. Trimming curves $\hat{\mathbf{C}}_i$ are in general NURBS curves, see Eq. (3.3), whose physical image is a subset of the surface's parametric image $\hat{\varOmega}$. Additionally, these curves have a representation on the Cartesian space, $\gamma_i \subset \varOmega$, via the transformation $\mathbf{C}_i = \mathbf{S} \circ \hat{\mathbf{C}}_i : \tilde{\gamma}_i \rightarrow \gamma_i$, $\mathbf{S}$ being the NURBS parametrization of surface $\varOmega$ in Eq. (3.6). The parametric space of an example trimming curve $\tilde{\gamma}_4$, the surface's parametric space $\hat{\varOmega}$, the surface's geometric space $\varOmega$ and the corresponding transformations are shown in Fig. 3.2. The aforementioned trimming technique is highly beneficial in that the parametrization $\mathbf{S}$ of surface $\varOmega$ remains unchanged and in that re-trimming can be efficiently performed by defining only a new set of trimming curves in $\hat{\varOmega}$.

3.2.2 Trimmed multipatch surfaces

The trimming procedure described in Sec. 3.2.1 provides a lot of flexibility in describing arbitrary shapes in Euclidean space originating from generic models. However, in real world engineering practice, multiple trimmed surfaces are considered to accurately describe large scale models, such as cars, ships, airplanes, etc. Let $\varOmega^{(i)}$, with $i = 1, \ldots, n_\mathrm{s} \in \mathbb{N}$, be a *non-overlapping domain decomposition* of $\varOmega$, meaning that,

$$\bigcup_{i=1}^{n_\mathrm{s}} \overline{\varOmega^{(i)}} = \overline{\varOmega} \,, \tag{3.7a}$$

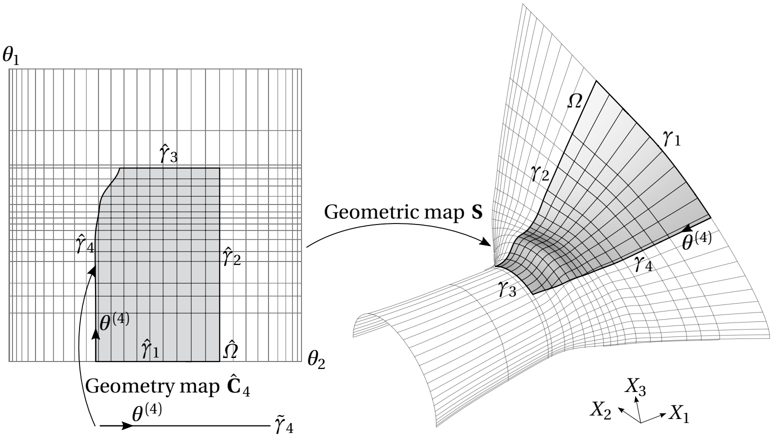

Figure 3.2: Computer-aided description of surfaces: Trimming operation for NURBS surfaces.

$$\bigcup_{i=1}^{n_\mathrm{s}} \Omega^{(i)} = \Omega_\mathrm{d} \,, \tag{3.7b}$$

$$\Omega^{(i)} \cap \Omega^{(j)} = \emptyset \quad \forall (i,j) \in \mathcal{I} \,, \tag{3.7c}$$

$$\overline{\Omega^{(i)}} \cap \overline{\Omega^{(j)}} = \gamma_\mathrm{i}^{(i,j)} \quad \forall (i,j) \in \mathcal{I} \,, \tag{3.7d}$$

$$\bigcup_{(i,j)\in\mathcal{I}} \gamma_\mathrm{i}^{(i,j)} = \gamma_\mathrm{i} \,, \tag{3.7e}$$

$\mathcal{I}$ being the set of all pairs (i,j) where $i,j = 1,\dots,n_\mathrm{s}$ with $i \neq j$ and let $n_\mathrm{i} \in \mathbb{N}$ be the number of non-empty sets $\gamma_\mathrm{i}^{(i,j)}$. Each of the surface patch subdomain $\Omega^{(i)}$ has a NURBS parametrization $\mathbf{S}^{(i)} : \hat{\Omega}^{(i)} \to \Omega^{(i)}$ as per Eq. (3.6) and a set of trimming curves $\hat{\gamma}_j^{(i)}$, with parametrizations $\hat{\mathbf{C}}_j^{(i)}$ as per Eq. (3.3), for $j = 1,\dots,n_\mathrm{t}^{(i)} \in \mathbb{N}$, $n_\mathrm{t}^{(i)}$ being the number of curves trimming patch $\Omega^{(i)}$. An example of a trimmed multipatch geometry is depicted in Fig. 3.3 along with the distinct patch parametric spaces and the corresponding trimming curves. In terms of CAD, each interface $\gamma_\mathrm{i}^{(i,j)}$ has a unique representation from each of the neighbouring patches, namely, $\hat{\gamma}_j^{(i)}$ and $\hat{\gamma}_i^{(j)}$ in the parametric spaces of patches $\Omega^{(i)}$ and $\Omega^{(j)}$, respectively. For real world engineering applications, this distinct representation of the patch inter-

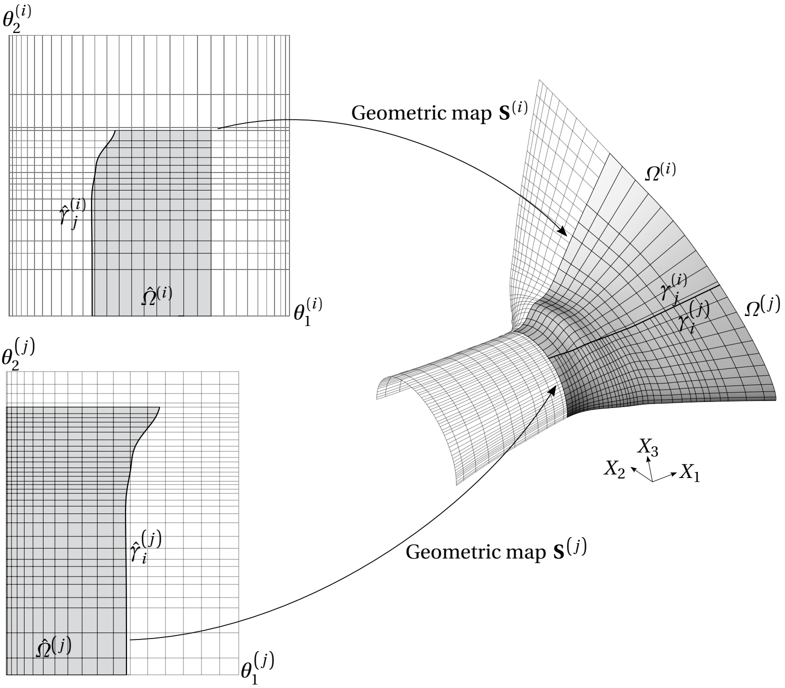

Figure 3.3: Computer-aided description of surfaces: Trimmed NURBS multipatch surfaces.

faces is in general not identical in the physical space, that is, $\gamma_j^{(i)} \cap \gamma_i^{(j)} \neq \gamma_{\mathrm{i}}^{(i,j)}$. The accuracy of the interface parametrization from each neighbouring patch is then controlled by a tolerance which in most CAD software is user defined. However, when applying IGA on trimmed NURBS multipatches, it is important that the trimming curves $\gamma_j^{(i)}$ and $\gamma_i^{(j)}$ representing the interface $\gamma_{\mathrm{i}}^{(i,j)}$ are identified so that the evaluation of the interface integrals, accounting for the continuity enforcement across the multipatches, can be performed. Most CAD software provide this identification of the patch interfaces through a *sew* option where the topological information of the geometry is generated.

3.3 Isogeometric analysis on multipatch surfaces

In this section various methods are studied concerning the continuity enforcement of the solution across mutlipatches within IGA on multipatch surfaces. This is very important as strong enforcement of the interface conditions is restrictive and cannot be applied on arbitrarily trimmed multipatch models directly stemming from CAD, see for example in Kiendl et al. [68]. These methods comprise Penalty, Lagrange Multipliers and Nitsche-type formulations. The two-dimensional linear plane stress problem is herein employed as model problem and the methods are then selectively extended to account for the three-dimensional geometrically linear and nonlinear Kirchhoff-Love shells and membranes. However, the introduction of IGA on trimmed patches is skipped as its application has been successfully demonstrated within *Isogeometric B-Rep Analysis* (IBRA) in Breitenberger et al. [6].

3.3.1 Model problem – Two-dimensional elasticity

The two-dimensional plane stress analysis is chosen as model problem for the demonstration of the methods concerning the continuity enforcement of the solution between multipatches. Accordingly, the strong and the weak formulation of the two-dimensional plane stress analysis is equivalent to that of the membrane analysis, see Eqs. (2.49) and (2.51), when restricted into the two-dimensional space $\mathbb{R}^2$ by neglecting the prestress and the cables. The aforementioned problem is depicted in Fig. 3.4 where only two neighbouring patches, $\Omega^{(i)}$ and $\Omega^{(j)}$ are considered for the sake of clarity and $\hat{\mathbf{e}}_{\mathrm{n}}^{(i)}$ stands for the outward normal to boundary $\partial\Omega^{(i)}$ vector. In the sequel, the restriction of any field within subdomain $\Omega^{(i)}$ is indicated by a superscript, e.g. for the displacement field $\mathbf{d}_{|_{\Omega^{(i)}}} = \mathbf{d}^{(i)}$. The interface Dirichlet and Neumann compatibility conditions then read,

$$\mathbf{d}^{(i)} - \mathbf{d}^{(j)} = \mathbf{0}\,, \tag{3.8a}$$

$$\mathbf{t}^{(i)} + \mathbf{t}^{(j)} = \mathbf{0}\,, \tag{3.8b}$$

respectively, along the common interface $\gamma_{\mathrm{i}}^{(i,j)}$. In the sequel, the displacement jump across interface γ_{i} is indicated by $\hat{\boldsymbol{\chi}}$ where $\mathbf{d}^{(i)} - \mathbf{d}^{(j)} = \hat{\boldsymbol{\chi}}^{(i,j)} = \hat{\boldsymbol{\chi}}_{|_{\gamma_i^{(i,j)}}}$. The problem is then posed on the decomposition of domain Ω defined in Eqs. (3.7) and thus the solution space defined in Eq. (2.53) may be

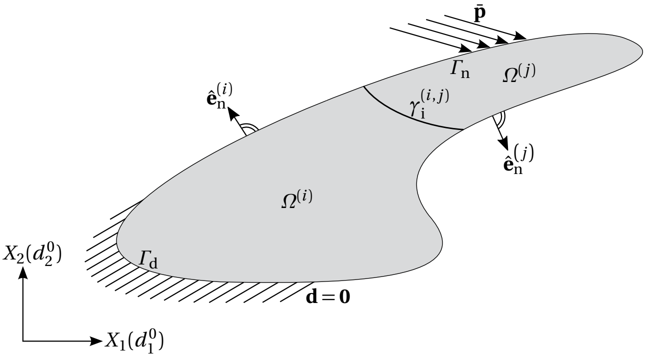

Figure 3.4: Isogeometric analysis on multipatch surfaces: Model problem-two dimensional plane stress analysis.

constructed as a product space which is discontinuous between the subdomains $\Omega^{(i)}$, $i=1,\ldots,n_\mathrm{s}$, namely, $\mathcal{V}=\prod_{i=1}^{n_\mathrm{s}}\mathcal{V}^{(i)}$. In this way, no continuity of the solution across the multipatches is assumed, which is considered in the following by means of the various *Domain Decomposition Methods* DDMs, see also in Toselli et al. [69].

3.3.2 Isogeometric discretization

Concerning the discretization of the aforementioned weak forms, IGA on multipatch surfaces is employed. In this way, the finite dimensional subspace $\mathcal{V}_\mathrm{h}\subset\mathcal{V}$ is constructed using the parametric description of each patch $\Omega^{(i)}$ as $\mathcal{V}_\mathrm{h}=\prod_{i=1}^{n_\mathrm{s}}\mathcal{V}_\mathrm{h}^{(i)}$ where,

$$\mathcal{V}_\mathrm{h}^{(i)}=\left\{\mathbf{d}^{(i)}\in\mathcal{V}^{(i)}\,\middle|\,\mathbf{d}^{(i)}\in\mathcal{R}\left(\Omega^{(i)}\right)\,\forall i=1,\ldots,n_\mathrm{s}\text{ with }\mathbf{d}=\mathbf{0}\text{ on }\Gamma_\mathrm{d}\right\}, \quad (3.9)$$

$\mathcal{R}(\Omega^{(i)})$ being the space of all vector-valued piecewise rational polynomials for which the NURBS basis functions of the geometric parametrization constitute a basis in each patch $\Omega^{(i)}$. Although functions from space in Eq. (3.9) identically satisfy the Dirichlet boundary conditions, it is shown in Chaps. 4, 5 and 6 how these conditions can also be weakly applied in the corresponding variational forms. Let $\bar{\boldsymbol{\phi}}_j^{(i)}$, with $j=1,\ldots,\dim\mathcal{V}_\mathrm{h}^{(i)}$, be a basis of $\mathcal{V}_\mathrm{h}^{(i)}$ for all $i=1,\ldots,n_\mathrm{s}$. Then, there exist reals $\hat{d}_j^{(i)}$, the so-called

Degrees of Freedom (DOFs), such that for each $\mathbf{d} \in \boldsymbol{\mathcal{V}}_\mathrm{h}$ it holds,

$$\mathbf{d} = \sum_{i=1}^{n_\mathrm{s}} \sum_{j=1}^{\dim \boldsymbol{\mathcal{V}}_\mathrm{h}^{(i)}} \bar{\boldsymbol{\phi}}_j^{(i)} \hat{d}_j^{(i)} . \tag{3.10}$$

Herein, the vector-valued NURBS basis functions are constructed as,

$$\bar{\boldsymbol{\phi}}_r^{(i)} = R_{\hat{p}_1^{(i)}, \hat{p}_2^{(i)}, k}^{(i)} \mathbf{e}_l , \tag{3.11}$$

where $k = \lceil r/3 \rceil$ and $l = r - 3\lceil r/3 \rceil + 3$ for all $r = 1, \dots \dim \boldsymbol{\mathcal{V}}_\mathrm{h}^{(i)}$ stand for the indices of the CPs and the Cartesian directions, respectively. Additionally, $R_{\hat{p}_1^{(i)}, \hat{p}_2^{(i)}, k}^{(i)}$ and $n_\alpha^{(i)}$, stand for the scalar-valued NURBS basis functions in patch $\Omega^{(i)}$ with polynomial orders $\hat{p}_1^{(i)}$ and $\hat{p}_2^{(i)}$ and the number of CPs of patch $\Omega^{(i)}$ in $\theta_\alpha^{(i)}$-parametric direction, respectively, see Sec. 3.1.2. The latter implies that $\dim \boldsymbol{\mathcal{V}}_\mathrm{h}^{(i)} = 3 n_1^{(i)} n_2^{(i)}$. These DOFs do not represent physical values since they are defined on the CPs which in general do not interpolate the geometry. In the same way, the admissible space of the Lagrange Multipliers field can be constructed as $\hat{\boldsymbol{\mathcal{V}}}_\mathrm{h} = \prod_{(i,j) \in \mathcal{I}} \hat{\boldsymbol{\mathcal{V}}}_\mathrm{h}^{(i,j)} \subset \boldsymbol{\mathcal{L}}^2(\gamma_\mathrm{i})$, where $\hat{\boldsymbol{\mathcal{V}}}_\mathrm{h}^{(i,j)} \subset \boldsymbol{\mathcal{R}}\left(\gamma_\mathrm{i}^{(i,j)}\right)$ and where $\boldsymbol{\mathcal{R}}\left(\gamma_\mathrm{i}^{(i,j)}\right)$ stands for the space of all vector-valued rational polynomials along $\gamma_\mathrm{i}^{(i,j)}$ of a given NURBS interface parametrization. Similar to Eq. (3.10), let $\hat{\boldsymbol{\phi}}_k^{(i,j)}$, with $k = 1, \dots, \dim \hat{\boldsymbol{\mathcal{V}}}_\mathrm{h}^{(i,j)}$ be a basis for each $\hat{\boldsymbol{\mathcal{V}}}_\mathrm{h}^{(i,j)}$. Then, for each $\boldsymbol{\lambda} \in \hat{\boldsymbol{\mathcal{V}}}_\mathrm{h}$ there exist reals $\hat{\lambda}_k^{(i,j)}$, the so-called Lagrange Multipliers DOFs, such that,

$$\boldsymbol{\lambda} = \sum_{(i,j) \in \mathcal{I}} \sum_{r=1}^{\dim \hat{\boldsymbol{\mathcal{V}}}_\mathrm{h}^{(i,j)}} \hat{\boldsymbol{\phi}}_r^{(i,j)} \hat{\lambda}_r^{(i,j)} , \tag{3.12}$$

where the vector-valued NURBS basis functions $\hat{\boldsymbol{\phi}}_r^{(i,j)}$ are constructed similar to Eq. (3.11), namely, $\hat{\boldsymbol{\phi}}_r^{(i,j)} = R_{\hat{p},k}^{(i,j)} \mathbf{e}_l$ where $R_{\hat{p},k}^{(i,j)}$ stand for the scalar-valued NURBS basis functions defined in Eq. (3.1) on curve $\gamma_\mathrm{i}^{(i,j)}$ and where $k = \lceil r/3 \rceil$ and $l = r - 3\lceil r/3 \rceil + 3$ for all $r = 1, \dots \dim \hat{\boldsymbol{\mathcal{V}}}_\mathrm{h}^{(i,j)}$. For the sake of simplicity, the displacement and the Lagrange Multipliers DOFs are grouped into vectors accounting for each patch $\Omega^{(i)}$ and each interface

$\gamma_{\mathrm{i}}^{(i,j)}$, namely,

$$\hat{\mathbf{d}}^{(i)} = \begin{bmatrix} \hat{d}_1^{(i)} & \cdots & \hat{d}_{\dim \mathcal{V}_{\mathrm{h}}^{(i)}}^{(i)} \end{bmatrix}^{\mathrm{T}} , \tag{3.13a}$$

$$\hat{\boldsymbol{\lambda}}^{(i,j)} = \begin{bmatrix} \hat{\lambda}_1^{(i,j)} & \cdots & \hat{\lambda}_{\dim \hat{\mathcal{V}}_{\mathrm{h}}^{(i,j)}}^{(i,j)} \end{bmatrix}^{\mathrm{T}} . \tag{3.13b}$$

The following discrete equation systems are presented for the general geometrically nonlinear problem and are used in the sequel of this thesis. The linearized equilibrium equation in Eq. (2.63) at time step $t_{\hat{n}}$ and at Newton-Raphson iteration $\hat{i}$ for the multipatch setting reads,

$$\begin{bmatrix} \mathbf{K}_{\mathrm{d}}^{(1)} & \cdots & \mathbf{0} \\ \vdots & \ddots & \vdots \\ \mathbf{0} & \cdots & \mathbf{K}_{\mathrm{d}}^{(n_{\mathrm{s}})} \end{bmatrix} \Delta_{\hat{n},\hat{i}} \begin{bmatrix} \hat{\mathbf{d}}^{(1)} \\ \vdots \\ \hat{\mathbf{d}}^{(n_{\mathrm{s}})} \end{bmatrix} = - \begin{bmatrix} \mathbf{R}_{\mathrm{d}}^{(1)} \\ \vdots \\ \mathbf{R}_{\mathrm{d}}^{(n_{\mathrm{s}})} \end{bmatrix} , \tag{3.14}$$

where $\mathbf{K}_{\mathrm{d}}^{(i)}$, $\mathbf{R}_{\mathrm{d}}^{(i)}$ and $\Delta_{\hat{n},\hat{i}}\, \hat{\mathbf{d}}^{(i)} = \hat{\mathbf{d}}_{\hat{n},\hat{i}+1} - \hat{\mathbf{d}}_{\hat{n},\hat{i}}^{(i)}$ stand for the dynamic tangent stiffness matrix in Eq. (2.65), the dynamic residual vector in Eq. (2.56) and the displacement increment in Eq. (2.64) at patch $\Omega^{(i)}$, respectively. The extensions of the discrete equation system in Eq. (3.14) with the coupling terms stemming from each DDM are shown in the following sections.

3.3.3 Penalty method

Let $\hat{\alpha} : \gamma_{\mathrm{i}} \rightarrow \mathbb{R}_{+}^{\star}$ be the Penalty parameter defined along the interface γ_{i}, $\mathbb{R}_{+}^{\star}$ being the set of strictly positive real numbers. Accordingly, the variational form of the problem using Penalty writes: Find $\mathbf{d} \in \mathcal{V}$ with $\hat{\boldsymbol{\chi}} \in \mathcal{L}^2(\gamma_{\mathrm{i}})$ such that,

$$\left\langle \delta\mathbf{d}, \rho\, \bar{h}\, \ddot{\mathbf{d}} \right\rangle_{0,\Omega} + \left\langle \delta\mathbf{d}, c\, \bar{h}\, \dot{\mathbf{d}} \right\rangle_{0,\Omega} + a\left(\delta\mathbf{d}, \mathbf{d}\right) + \left\langle \delta\hat{\boldsymbol{\chi}}, \hat{\alpha}\, \hat{\boldsymbol{\chi}} \right\rangle_{0,\gamma_{\mathrm{i}}} = l\left(\delta\mathbf{d}\right) , \tag{3.15}$$

for all $\delta\mathbf{d} \in \mathcal{V}$ with $\delta\hat{\boldsymbol{\chi}} \in \mathcal{L}^2(\gamma_{\mathrm{i}})$. The Penalty parameter is chosen piecewise constant along each interface as $\hat{\alpha}|_{\gamma_{\mathrm{i}}^{(i,j)}} = \hat{\alpha}^{(i,j)}$. As typical for the Penalty methods, the Penalty term added in Eq. (3.15) is bilinear and coercive, see Lax-Milgram Thm. 2.2, since the imposed condition is linear with respect to the displacement field. Therefore, variational problem in Eq. (3.15) preserves the properties of the original problem in terms of existence and uniqueness of the solution. Projecting weak form in Eq. (3.15) onto $\mathcal{V}_\mathrm{h} \times \mathcal{V}_\mathrm{h}$ yields the following discrete equation system,

$$\begin{bmatrix} \mathbf{K}_\mathrm{d}^{(1)} + \hat{\mathbf{C}}_{\hat{\alpha}}^{(1)} & \cdots & \hat{\mathbf{C}}_{\hat{\alpha}}^{(1,n_\mathrm{s})} \\ \vdots & \ddots & \vdots \\ \hat{\mathbf{C}}_{\hat{\alpha}}^{(n_\mathrm{s},1)} & \cdots & \mathbf{K}_\mathrm{d}^{(n_\mathrm{s})} + \hat{\mathbf{C}}_{\hat{\alpha}}^{(n_\mathrm{s})} \end{bmatrix} \Delta_{\hat{n},\hat{\imath}} \begin{bmatrix} \hat{\mathbf{d}}^{(1)} \\ \vdots \\ \hat{\mathbf{d}}^{(n_\mathrm{s})} \end{bmatrix} = - \begin{bmatrix} \mathbf{R}_\mathrm{d}^{(1)} + \hat{\mathbf{R}}_{\hat{\alpha}}^{(1)} \\ \vdots \\ \mathbf{R}^{(n_\mathrm{s})} + \hat{\mathbf{R}}_{\hat{\alpha}}^{(n_\mathrm{s})} \end{bmatrix} \tag{3.16}$$

where the entries of the additional Penalty matrices $\hat{\mathbf{C}}_{\hat{\alpha}}^{(i)}$, $\hat{\mathbf{C}}_{\hat{\alpha}}^{(i,j)}$ and the residual vectors $\hat{\mathbf{R}}_{\hat{\alpha}}^{(i)}$ are given by,

$$\hat{C}_{\hat{\alpha}(k,r)}^{(i)} = \sum_{j=1,j\neq i}^{n_\mathrm{s}} \left\langle \bar{\boldsymbol{\phi}}_k^{(i)}, \hat{\alpha}^{(i,j)} \bar{\boldsymbol{\phi}}_r^{(i)} \right\rangle_{0,\gamma_\mathrm{i}^{(i,j)}} , \tag{3.17a}$$

$$\hat{C}_{\hat{\alpha}(k,r)}^{(i,j)} = - \left\langle \bar{\boldsymbol{\phi}}_k^{(i)}, \hat{\alpha}^{(i,j)} \bar{\boldsymbol{\phi}}_r^{(j)} \right\rangle_{0,\gamma_\mathrm{i}^{(i,j)}} , \tag{3.17b}$$

$$\hat{\mathbf{R}}_{\hat{\alpha}}^{(i)} = \hat{\mathbf{C}}_{\hat{\alpha}}^{(i)} \hat{\mathbf{d}}_{\hat{n},\hat{\imath}}^{(i)} + \sum_{j=1,j\neq i}^{n_\mathrm{s}} \hat{\mathbf{C}}_{\hat{\alpha}}^{(i,j)} \hat{\mathbf{d}}_{\hat{n},\hat{\imath}}^{(j)} . \tag{3.17c}$$

The shortcoming of the Penalty method lies in that correspondence between the strong and the weak form cannot be established, see Sec. 2.2.1, and thus the Penalty method is often called *variationally inconsistent.* The latter has the implication that a uniform convergence to the solution cannot be guaranteed for a constant Penalty parameter. On the other hand, increasing the Penalty parameter might result in badly conditioned systems which may lead to inaccurate solutions and render iterative solvers inapplicable, see also in Babuška [11] for more information. Since the additional Penalty terms of the weak form in Eq. (3.15) are linear in terms of the displacement field, matrices in Eqs. (3.17) are constant and thus, can be precomputed and used throughout the analysis which in addition to the positive definiteness of equation system in Eq. (3.16) leads to an efficient and stable methodology for IGA on multipatches. The magnitude of the Penalty parameters is problem dependent and it is discussed in the corresponding sections.

3.3.4 Lagrange Multipliers method

Another popular method for the constraint enforcement is the Lagrange Multipliers method within which an additional Lagrange Multipliers field $\boldsymbol{\lambda}$ is introduced. Then, the corresponding weak formulation of the problem by means of the Lagrange Multipliers method writes: Find $\mathbf{d} \in \boldsymbol{\mathcal{V}}$ and $\boldsymbol{\lambda} \in \boldsymbol{\mathcal{L}}^2(\gamma_\mathrm{i})$ such that,

$$\begin{aligned} \left\langle \delta\mathbf{d}, \rho\,\bar{h}\,\ddot{\mathbf{d}} \right\rangle_{0,\Omega} + \left\langle \delta\mathbf{d}, c\,\bar{h}\,\dot{\mathbf{d}} \right\rangle_{0,\Omega} + a\,(\delta\mathbf{d}, \mathbf{d}) + \left\langle \delta\hat{\boldsymbol{\chi}}, \boldsymbol{\lambda} \right\rangle_{0,\gamma_\mathrm{i}} + \left\langle \delta\boldsymbol{\lambda}, \hat{\boldsymbol{\chi}} \right\rangle_{0,\gamma_\mathrm{i}} & \\ = l\,(\delta\mathbf{d}), & \end{aligned} \tag{3.18}$$

for all $\delta\mathbf{d} \in \boldsymbol{\mathcal{V}}$ with $\delta\hat{\boldsymbol{\chi}} \in \boldsymbol{\mathcal{L}}^2(\gamma_\mathrm{i})$ and for all $\delta\boldsymbol{\lambda} \in \boldsymbol{\mathcal{L}}^2(\gamma_\mathrm{i})$. The additional Lagrange Multipliers terms in Eq. (3.18) turn the problem into a saddle point formulation, see Sec. 2.2.2, meaning that the *Ladyzhenskaya-Babuška-Brezzi* (LBB) condition defined in Thm. 2.3 needs to be satisfied so that a unique solution to the problem can be guaranteed. It is required to take into consideration the additional Lagrange Multipliers discretization in Eq. (3.12) for the statement of the discrete equation system corresponding to the Lagrange Multipliers method. Projection of weak form in Eq. (3.18) onto $\boldsymbol{\mathcal{V}}_\mathrm{h} \times \boldsymbol{\mathcal{V}}_\mathrm{h} \times \hat{\boldsymbol{\mathcal{V}}}_\mathrm{h}$ yields,

$$\begin{aligned} & \begin{bmatrix} \mathbf{K}_\mathrm{d}^{(1)} & \cdots & \mathbf{0} & \\ \vdots & \ddots & \vdots & \boldsymbol{\Lambda} \\ \mathbf{0} & \cdots & \mathbf{K}_\mathrm{d}^{(n_\mathrm{s})} & \\ & \boldsymbol{\Lambda}^\mathrm{T} & & \mathbf{0} \end{bmatrix} \Delta_{\hat{n},\hat{\imath}} \begin{bmatrix} \hat{\mathbf{d}}^{(1)} \\ \vdots \\ \hat{\mathbf{d}}^{(n_\mathrm{s})} \\ \hat{\boldsymbol{\lambda}} \end{bmatrix} = \\ & \quad - \begin{bmatrix} \mathbf{R}_\mathrm{d}^{(1)} + \sum_{(1,j)\in\mathcal{I}} \boldsymbol{\Lambda}^{(1,j)} \hat{\boldsymbol{\lambda}}_{\hat{n},\hat{\imath}}^{(1,j)} \\ \vdots \\ \mathbf{R}_\mathrm{d}^{(n_\mathrm{s})} + \sum_{(n_\mathrm{s},j)\in\mathcal{I}} \boldsymbol{\Lambda}^{(n_\mathrm{s},j)} \hat{\boldsymbol{\lambda}}_{\hat{n},\hat{\imath}}^{(n_\mathrm{s},j)} \\ \boldsymbol{\Lambda}^\mathrm{T}\,\hat{\mathbf{d}}_{\hat{n},\hat{\imath}} \end{bmatrix}, \end{aligned} \tag{3.19}$$

where $\hat{\mathbf{d}}_{\hat{n},\hat{\imath}}$ stands for the complete vector of displacement DOFs $\hat{\mathbf{d}}$ on the entire multipatch geometry, namely,

$$\hat{\mathbf{d}} = \begin{bmatrix} \hat{\mathbf{d}}^{(1)} & \cdots & \hat{\mathbf{d}}^{(n_\mathrm{s})} \end{bmatrix}^\mathrm{T}, \tag{3.20}$$

at $\hat{n}$-th time step and $\hat{\imath}$-th nonlinear iteration. Additionally, $\hat{\boldsymbol{\lambda}}_{\hat{n},\hat{\imath}}^{(i,j)}$ stands for the Lagrange Multiplier DOFs along $\gamma_{\mathrm{i}}^{(i,j)}$ at time step $\hat{n}$ and nonlinear iteration $\hat{\imath}$. The Lagrange Multipliers matrix $\boldsymbol{\Lambda}$ and the assembled Lagrange Multipliers vector of DOFs $\hat{\boldsymbol{\lambda}}$, respectively, read,

$$\boldsymbol{\Lambda} = \begin{bmatrix} \ddots & \boldsymbol{\Lambda}^{(1,n_{\mathrm{s}})} & \iddots \\ \cdots & \vdots & \cdots \\ \iddots & \boldsymbol{\Lambda}^{(n_{\mathrm{s}},1)} & \ddots \end{bmatrix} , \tag{3.21a}$$

$$\hat{\boldsymbol{\lambda}} = \begin{bmatrix} \cdots & \hat{\boldsymbol{\lambda}}^{(1,n_{\mathrm{s}})} & \cdots \end{bmatrix}^{\mathrm{T}} . \tag{3.21b}$$

Moreover, the additional Lagrange Multipliers matrices $\boldsymbol{\Lambda}^{(i,j)}$ in Eq. (3.21a) have entries,

$$\Lambda_{(k,r)}^{(i,j)} = \pm \left\langle \hat{\boldsymbol{\phi}}_{k}^{(i,j)}, \bar{\boldsymbol{\phi}}_{r}^{(i)} \right\rangle_{0,\gamma_{\mathrm{i}}^{(i,j)}} , \tag{3.22}$$

for all pairs $(i,j) \in \mathcal{I}$, where the ± sign depends on the ordering of patches $\Omega^{(i)}$ and $\Omega^{(j)}$ in the definition of Eq. (3.8a). The saddle point nature of the Lagrange Multipliers method is revealed in its discrete form from the zero block at the lower right bottom of the system's matrix, see Eq. (3.19). The discrete subspace $\hat{\boldsymbol{\mathcal{V}}}_{\mathrm{h}}$ has to be so chosen as to satisfy the *Ladyzhenskaya-Babuška-Brezzi* (LBB) condition in Thm. 2.3 in the discrete level, but this problem is not trivial for any arbitrary isogeometric discretization, see also in Brivadis et al. [14]. Although the saddle point formulation offered by the Lagrange Multipliers method is variationally consistent as opposed to Penalty method, the resulting equation system needs not to be positive definite with zeros in the main diagonal, rendering also in this case iterative solvers inapplicable. In addition, the problem is not guaranteed to have a unique solution which greatly depends on the selection of the discrete subspaces and thus the linear equation system resulting from the field discretizations may be singular. Thus, the Lagrange Multipliers discretization is problem dependent and is chosen in such a way that the discrete equation system in Eq. (3.19) is not singular, whenever possible. Similar to Penalty method, also in this case the additional Lagrange Multipliers matrices are constant and can be precomputed rendering the methodology efficient, yet not necessarily stable due to its saddle point nature.

The Lagrange Multipliers field can be condensed out for special types of problems including plane stress analysis, resulting in the so-called *Mortar* formulation leading to a well-posed problem, see also in Klöppel et al. [18].

3.3.5 Nitsche-type method

An alternative to the Penalty and the Lagrange Multipliers methods is offered by the Nitsche-type method, firstly introduced in Nitsche [19] for the solution of Dirichlet BVPs where the corresponding solution spaces do not identically satisfy the Dirichlet boundary conditions. The method is herein employed for the continuity enforcement across the multipatches. The mean interface traction vector $\bar{\mathbf{t}}$ along the interface γ_{i} needs to be introduced, whose restriction at each interface $\gamma_{\mathrm{i}}^{(i,j)}$ reads,

$$\bar{\mathbf{t}}^{(i,j)} = \bar{\mathbf{t}}_{|_{\gamma_{\mathrm{i}}^{(i,j)}}} = \frac{1}{2}\left(\mathbf{t}^{(i)} - \mathbf{t}^{(j)}\right) , \tag{3.23}$$

and where $\mathbf{t}^{(i)} = \hat{\mathbf{e}}_{\mathrm{n}}^{(i)} \cdot \mathbf{n}^{(i)}$ stands for the traction vector along $\partial \Omega^{(i)}$, $\mathbf{n}^{(i)}$ being the restriction of the 2nd Piola Kirchhoff force tensor at subdomain $\Omega^{(i)}$ as per Eq. (2.36a). By also introducing a stabilization parameter $\hat{\beta} : \gamma_{\mathrm{i}} \rightarrow \mathbb{R}_{+}^{\star}$ which is defined piecewise constant along γ_{i} similar to the Penalty parameter in Sec. 3.3.3, the weak form of the problem with Nitsche writes: Find $\mathbf{d} \in \boldsymbol{\mathcal{V}}$ with $\hat{\boldsymbol{\chi}}, \bar{\mathbf{t}} \in \boldsymbol{\mathcal{L}}^2(\gamma_{\mathrm{i}})$ such that,

$$\begin{aligned} &\left\langle \delta \mathbf{d}, \rho \bar{h} \ddot{\mathbf{d}} \right\rangle_{0,\Omega} + \left\langle \delta \mathbf{d}, c \bar{h} \dot{\mathbf{d}} \right\rangle_{0,\Omega} + a(\delta \mathbf{d}, \mathbf{d}) \\ -&\left\langle \delta \hat{\boldsymbol{\chi}}, \bar{\mathbf{t}} \right\rangle_{0,\gamma_{\mathrm{i}}} - \left\langle \delta \bar{\mathbf{t}}, \hat{\boldsymbol{\chi}} \right\rangle_{0,\gamma_{\mathrm{i}}} + \left\langle \delta \hat{\boldsymbol{\chi}}, \hat{\beta} \hat{\boldsymbol{\chi}} \right\rangle_{0,\gamma_{\mathrm{i}}} = l(\delta \mathbf{d}) , \end{aligned} \tag{3.24}$$

for all $\delta \mathbf{d} \in \boldsymbol{\mathcal{V}}$ with $\delta \hat{\boldsymbol{\chi}}, \delta \bar{\mathbf{t}} \in \boldsymbol{\mathcal{L}}^2(\gamma_{\mathrm{i}})$. The Penalty-like stabilization term in Eq. (3.24) is necessary for maintaining coercivity of the weak form. It can be shown that if there exist constants $\hat{C}^{(i,j)} > 0$ such that,

$$||\bar{\mathbf{t}}^{(i,j)}||_{0,\gamma_{\mathrm{i}}^{(i,j)}}^2 \leq \hat{C}^{(i,j)} a(\mathbf{d}, \mathbf{d}) \quad \forall \mathbf{d} \in \boldsymbol{\mathcal{V}} , \tag{3.25}$$

along each interface boundary $\gamma_{\mathrm{i}}^{(i,j)}$, then the extended bilinear form in Eq. (3.24) remains coercive as per Lax-Milgram Thm. 2.2 whereas it maintains its symmetry and boundedness, see also in Apostolatos et al. [10] and Griebel et al. [28]. Condition in Eq. (3.25) results in an estimate for the stabilization parameter along each interface, namely $\hat{\beta}^{(i,j)} = \hat{\beta}_{|_{\gamma_{\mathrm{i}}^{(i,j)}}}$, which is obtained by solving a set of interface eigenvalue problems. In a similar fashion as in Sec. 3.3.3, projecting weak form in Eq. (3.24) onto $\mathcal{V}_\mathrm{h} \times \mathcal{V}_\mathrm{h}$ results in the following discrete equation system,

$$\begin{bmatrix} \mathbf{K}_\mathrm{d}^{(1)} + \hat{\mathbf{C}}_\mathrm{n}^{(1)} + \hat{\mathbf{C}}_{\hat{\beta}}^{(1)} & \cdots & \hat{\mathbf{C}}_\mathrm{n}^{(1,n_\mathrm{s})} + \hat{\mathbf{C}}_{\hat{\beta}}^{(1,n_\mathrm{s})} \\ \vdots & \ddots & \vdots \\ \hat{\mathbf{C}}_\mathrm{n}^{(n_\mathrm{s},1)} + \hat{\mathbf{C}}_{\hat{\alpha}}^{(n_\mathrm{s},1)} & \cdots & \mathbf{K}_\mathrm{d}^{(n_\mathrm{s})} + \hat{\mathbf{C}}_\mathrm{n}^{(n_\mathrm{s})} + \hat{\mathbf{C}}_{\hat{\beta}}^{(n_\mathrm{s})} \end{bmatrix} \Delta_{\hat{n},\hat{\imath}} \begin{bmatrix} \hat{\mathbf{d}}^{(1)} \\ \vdots \\ \hat{\mathbf{d}}^{(n_\mathrm{s})} \end{bmatrix} = - \begin{bmatrix} \mathbf{R}_\mathrm{d}^{(1)} + \hat{\mathbf{R}}_\mathrm{n}^{(1)} + \hat{\mathbf{R}}_{\hat{\beta}}^{(1)} \\ \vdots \\ \mathbf{R}_\mathrm{d}^{(n_\mathrm{s})} + \hat{\mathbf{R}}_\mathrm{n}^{(n_\mathrm{s})} + \hat{\mathbf{R}}_{\hat{\beta}}^{(n_\mathrm{s})} \end{bmatrix}, \tag{3.26}$$

where the entries of the additional Nitsche matrices $\hat{\mathbf{C}}_\mathrm{n}^{(i)}$, $\hat{\mathbf{C}}_\mathrm{n}^{(i,j)}$ and residual vectors $\hat{\mathbf{R}}_\mathrm{n}^{(i)}$ are given by,

$$\hat{C}_{\mathrm{n}(k,r)}^{(i)} = -\frac{1}{2} \sum_{j=1, j\neq i}^{n_\mathrm{s}} \left(\left\langle \left. \frac{\partial \mathbf{t}^{(i)}}{\partial \hat{d}_k^{(i)}} \right|_{\hat{\mathbf{d}}_{\hat{n},\hat{\imath}}^{(i)}}, \bar{\boldsymbol{\phi}}_r^{(i)} \right\rangle_{0,\gamma_\mathrm{i}^{(i,j)}} + \left\langle \bar{\boldsymbol{\phi}}_k^{(i)}, \left. \frac{\partial \mathbf{t}^{(i)}}{\partial \hat{d}_r^{(i)}} \right|_{\hat{\mathbf{d}}_{\hat{n},\hat{\imath}}^{(i)}} \right\rangle_{0,\gamma_\mathrm{i}^{(i,j)}} \pm \left\langle \left. \frac{\partial^2 \mathbf{t}^{(i)}}{\partial \hat{d}_k^{(i)} \partial \hat{d}_r^{(i)}} \right|_{\hat{\mathbf{d}}_{\hat{n},\hat{\imath}}^{(i)}}, \mathbf{d}_{\hat{n},\hat{\imath}}^{(i)} - \mathbf{d}_{\hat{n},\hat{\imath}}^{(j)} \right\rangle_{0,\gamma_\mathrm{i}^{(i,j)}} \right), \tag{3.27a}$$

$$\hat{C}_{\mathrm{n}(k,r)}^{(i,j)} = -\frac{1}{2} \left(\left\langle \left. \frac{\partial \mathbf{t}^{(i)}}{\partial \hat{d}_k^{(i)}} \right|_{\hat{\mathbf{d}}_{\hat{n},\hat{\imath}}^{(i)}}, \bar{\boldsymbol{\phi}}_r^{(j)} \right\rangle_{0,\gamma_\mathrm{i}^{(i,j)}} + \left\langle \bar{\boldsymbol{\phi}}_k^{(i)}, \left. \frac{\partial \mathbf{t}^{(j)}}{\partial \hat{d}_r^{(j)}} \right|_{\hat{\mathbf{d}}_{\hat{n},\hat{\jmath}}^{(i)}} \right\rangle_{0,\gamma_\mathrm{i}^{(i,j)}} \right), \tag{3.27b}$$

$$\hat{R}_{\mathrm{n}(k)}^{(i)} = \pm \frac{1}{2} \sum_{j=1, j\neq i}^{n_\mathrm{s}} \left(\left\langle \bar{\boldsymbol{\phi}}_k^{(i)}, \left. \mathbf{t}^{(i)} \right|_{\hat{\mathbf{d}}_{\hat{n},\hat{\imath}}^{(i)}} - \left. \mathbf{t}^{(j)} \right|_{\hat{\mathbf{d}}_{\hat{n},\hat{\imath}}^{(j)}} \right\rangle_{0,\gamma_\mathrm{i}^{(i,j)}} + \left\langle \left. \frac{\partial \mathbf{t}^{(i)}}{\partial \hat{d}_k^{(i)}} \right|_{\hat{\mathbf{d}}_{\hat{n},\hat{\imath}}^{(i)}}, \mathbf{d}_{\hat{n},\hat{\imath}}^{(i)} - \mathbf{d}_{\hat{n},\hat{\imath}}^{(j)} \right\rangle_{0,\gamma_\mathrm{i}^{(i,j)}} \right). \tag{3.27c}$$

The signs ± in Eqs. (3.27a) and (3.27c) depend on the ordering of the patch pairs in $\mathcal{I}$ with respect to the definition of the interface jump in Eq. (3.8a) and the definition of the mean interface traction in Eq. (3.23). Moreover, $\mathbf{d}^{(i)}_{\hat{n},\hat{\imath}}$ stands for the actual displacement field at time step $t_{\hat{n}}$ and at $\hat{\imath}$-th Newton-Raphson iteration in patch $\Omega^{(i)}$. Matrices $\hat{\mathbf{C}}^{(i)}_{\hat{\beta}}$, $\hat{\mathbf{C}}^{(i,j)}_{\hat{\beta}}$ and residual vectors $\hat{\mathbf{R}}^{(i)}_{\hat{\beta}}$ related to the Penalty-like stabilization terms are defined as in Eqs. (3.17). The discrete form of the condition in Eq. (3.25) which leads to coercivity may be written in terms of the generalized eigenvalue problem,

$$\det\left(\hat{\mathbf{Q}}^{(i,j)}_{\mathrm{n}} - \hat{C}^{(i,j)}\mathbf{K}^{(i,j)}\right) = 0\,, \tag{3.28}$$

which is solved for the corresponding eigenvalues $\hat{C}^{(i,j)}_r$ along each non-empty interface $\gamma^{(i,j)}_{\mathrm{i}}$. Auxiliary matrices $\hat{\mathbf{Q}}^{(i,j)}$ and $\mathbf{K}^{(i,j)}$ are defined as,

$$\hat{\mathbf{Q}}^{(i,j)}_{\mathrm{n}} = \begin{bmatrix} \hat{\mathbf{Q}}^{(i)}_{\mathrm{n}} & \hat{\mathbf{q}}^{(i,j)}_{\mathrm{n}} \\ \hat{\mathbf{q}}^{(j,i)}_{\mathrm{n}} & \hat{\mathbf{Q}}^{(j)}_{\mathrm{n}} \end{bmatrix}, \tag{3.29a}$$

$$\mathbf{K}^{(i,j)} = \begin{bmatrix} \mathbf{K}^{(i)}|_{\gamma^{(i,j)}_{\mathrm{i}}} & \mathbf{0} \\ \mathbf{0} & \mathbf{K}^{(j)}|_{\gamma^{(i,j)}_{\mathrm{i}}} \end{bmatrix}, \tag{3.29b}$$

where $\mathbf{K}^{(i)}|_{\gamma^{(i,j)}_{\mathrm{i}}}$ stands for the restriction of the tangent stiffness matrix $\mathbf{K}^{(i)}$ on the DOFs along the interface $\gamma^{(i,j)}_{\mathrm{i}}$. Moreover, The entries of matrices $\hat{\mathbf{Q}}^{(i)}_{\mathrm{n}}$ and $\hat{\mathbf{q}}^{(i,j)}_{\mathrm{n}}$ are given by,

$$\begin{aligned} \hat{Q}^{(i)}_{\mathrm{n}(k,r)} = \frac{1}{4}\sum_{j=1,j\neq i}^{n_{\mathrm{s}}} \Bigg(& \left\langle \left.\frac{\partial \mathbf{t}^{(i)}}{\partial \hat{d}^{(i)}_k}\right|_{\hat{\mathbf{d}}^{(i)}_{\hat{n},\hat{\imath}}}, \left.\frac{\partial \mathbf{t}^{(i)}}{\partial \hat{d}^{(i)}_r}\right|_{\hat{\mathbf{d}}^{(i)}_{\hat{n},\hat{\imath}}} \right\rangle_{0,\gamma^{(i,j)}_{\mathrm{i}}} \pm \\ & \left\langle \left.\frac{\partial^2 \mathbf{t}^{(i)}}{\partial \hat{d}^{(i)}_k \partial \hat{d}^{(i)}_r}\right|_{\hat{\mathbf{d}}^{(i)}_{\hat{n},\hat{\imath}}}, \mathbf{t}^{(i)}|_{\hat{\mathbf{d}}^{(i)}_{\hat{n},\hat{\imath}}} - \mathbf{t}^{(j)}|_{\hat{\mathbf{d}}^{(j)}_{\hat{n},\hat{\imath}}} \right\rangle_{0,\gamma^{(i,j)}_{\mathrm{i}}} \Bigg), \end{aligned} \tag{3.30a}$$

$$\hat{q}^{(i,j)}_{\mathrm{n}(k,r)} = -\frac{1}{4}\left\langle \left.\frac{\partial \mathbf{t}^{(i)}}{\partial \hat{d}^{(i)}_{k}}\right|_{\hat{\mathbf{d}}^{(i)}_{\hat{n},\hat{\imath}}}, \left.\frac{\partial \mathbf{t}^{(j)}}{\partial \hat{d}^{(j)}_{r}}\right|_{\hat{\mathbf{d}}^{(j)}_{\hat{n},\hat{\imath}}} \right\rangle_{0,\gamma^{(i,j)}_{\mathrm{i}}}, \tag{3.30b}$$

where also here the sign ± in Eq. (3.30a) depends on the ordering of patches $\Omega^{(i)}$ and $\Omega^{(j)}$ in patch pair $(i,j) \in \mathcal{I}$. Eq. (3.28) is posed on the beginning of each time step $t_{\hat{n}}$ so that the stabilization parameters are estimated once every time step $t_{\hat{n}}$, thus maintaining the quadratic convergence of the Newton-Raphson nonlinear scheme. Then, the estimation of the stabilization parameter needs to be chosen as

$$\hat{\beta}^{(i,j)} \geq 2 n_{\mathrm{i}} \max_{r} \hat{C}^{(i,j)} . \tag{3.31}$$

This is an approximation and it is only used for obtaining an estimation of the stabilization parameters at each time step. For geometrically linear problems, the terms containing second derivatives with respect to the DOFs vanish and problem in Eq. (3.28) is by construction linear. Since relation in Eq. (3.31) only provides an estimation, higher values can be chosen in case coarse time step sizes are considered so that the extended by Nitsche problem remains coercive. However, only the lower bounds of the stabilization parameters in (3.31) are used in this thesis.

3.3.6 Numerical integration

In this section, the procedure for the numerical integration along the patch interfaces $\gamma^{(i,j)}_{\mathrm{i}}$ is presented and accordingly the *Gauss integration* rule is assumed, see also in Hughes et al. [70, 71]. Let $\hat{\gamma}^{(i)}_{j}$ and $\hat{\gamma}^{(j)}_{i}$ be the images of interface $\gamma^{(i,j)}_{\mathrm{i}}$ in the parametric spaces of patches $\Omega^{(i)}$ and $\Omega^{(j)}$, respectively, see Fig. 3.3. Let the intersections of all knot lines in $\hat{\Omega}^{(j)}$ with $\hat{\gamma}^{(j)}_{i}$ be denoted by $\boldsymbol{\theta}^{(j)}_{i,r} \in \hat{\Omega}^{(j)}$ with $r = 1, \ldots, \hat{n}^{(j)}_{i}$, $\hat{\Omega}^{(j)}$ being the parametric space of patch $\Omega^{(j)}$, see Sec. 3.1.2. Their projection $\mathrm{proj}_{\hat{\gamma}^{(i)}_{j}} \boldsymbol{\theta}^{(j)}_{i,r}$ on curve $\hat{\gamma}^{(i)}_{j}$ via the geometric space onto patch $\hat{\Omega}^{(i)}$ is given by,

$$\mathrm{proj}_{\hat{\gamma}^{(i)}_{k}} \boldsymbol{\theta}^{(j)}_{i,r} = \left(\left(\mathbf{S}^{(i)} \right)^{-1} \circ \mathbf{S}^{(j)} \right) \left(\boldsymbol{\theta}^{(j)}_{i,r} \right), \tag{3.32}$$

where $\mathbf{S}^{(i)}$ and $\mathbf{S}^{(j)}$ stand for the geometric maps of patches $\Omega^{(i)}$ and $\Omega^{(j)}$, respectively, see Eq. (3.6). The aforementioned projection is in general nonlinear and is herein computed using the Newton-Raphson iteration method. Given also the intersections of all knot lines in patch $\Omega^{(i)}$ with $\gamma_j^{(i)}$, namely $\boldsymbol{\theta}_{j,s}^{(i)} \in \gamma_j^{(i)}$ with $s = 1, \ldots, \hat{n}_j^{(i)}$, all points $\{\mathrm{proj}_{\hat{\gamma}_j^{(i)}} \boldsymbol{\theta}_{i,r}^{(j)}, \boldsymbol{\theta}_{j,s}^{(i)}\}$ are then sorted along the trimming curve $\hat{\gamma}_j^{(i)}$, namely, $\bar{\boldsymbol{\theta}}_{j,q}^{(i)}$, $q = 1, \ldots, \bar{n}_j^{(i)} \in \mathbb{N}$. In this way, the Gauss integration takes place at each interval $]\tilde{\theta}_{j,q}^{(i)}, \tilde{\theta}_{j,q+1}^{(i)}[\subset \tilde{\gamma}_j^{(i)}$, $q = 1, \ldots, \bar{n}_j^{(i)} - 1$, where

$$\tilde{\theta}_{j,q}^{(i)} = \left(\hat{\mathbf{C}}_j^{(i)}\right)^{-1} \left(\bar{\boldsymbol{\theta}}_{j,q}^{(i)}\right), \tag{3.33}$$

given the map $\hat{\mathbf{C}}_j^{(i)}$ and parametric space of the trimming curve $\tilde{\gamma}_j^{(i)}$ see also Fig. 3.2, thus ensuring that the integrands are C^{∞}-continuous. Similarly, for the numerical integration along boundaries $\Gamma_{\mathrm{d}}^{(i)} = \partial \Omega^{(i)} \cap \Gamma_{\mathrm{d}}$, whenever the application of weak Dirichlet boundary conditions is considered, let $\hat{\gamma}_{\mathrm{d}}^{(i)}$ stand for the parametric description of the trimming curve representing $\Gamma_{\mathrm{d}}^{(i)}$ in patch $\Omega^{(i)}$. Then, once more the intersections $\boldsymbol{\theta}_{\mathrm{d},s}^{(i)}$, $s = 1, \ldots, \hat{n}_{\mathrm{d}}^{(i)} \in \mathbb{N}$, of the knot lines of parametric space $\hat{\Omega}^{(i)}$ with the trimming curve $\hat{\gamma}_{\mathrm{d}}^{(i)}$ are computed and sorted along $\hat{\gamma}_{\mathrm{d}}^{(i)}$ so that the Gauss integration can be performed at each interval $]\tilde{\theta}_{\mathrm{d},s}^{(i)}, \tilde{\theta}_{\mathrm{d},s+1}^{(i)}[\subset \tilde{\gamma}_{\mathrm{d}}^{(i)}$, $s = 1, \ldots, \hat{n}_{\mathrm{d}}^{(i)} - 1$, once more ensuring that the integrands are C^{∞}-continuous, where $\tilde{\theta}_{\mathrm{d},s}^{(i)}$ is computed similar to Eq. (3.33). The number of the Gauss points is then dependent on the polynomial order of the integrand which may vary depending on the underlying weak formulation and the employed constraint enforcement method. Given that the images of trimming curves $\hat{\gamma}_j^{(i)}$ and $\hat{\gamma}_i^{(j)}$ in the geometric space, namely $\gamma_j^{(i)}$ and $\gamma_i^{(j)}$, are a good approximation of the interface curve $\gamma_{\mathrm{i}}^{(i,j)}$, inversion of the aforementioned projection from patch $\Omega^{(i)}$ onto patch $\Omega^{(j)}$ is equivalently valid.

3.4 Numerical examples

Next, two geometrically linear problems are considered to demonstrate the application of NURBS-based IGA on multipatches in both static and modal analysis. For both problems the same material properties are used, that is, Young's modulus and Poisson ratio equal to $E = 10^5$ Pa and $\nu = 0$, respectively. The Penalty parameter is then chosen as a scaling of the Young's

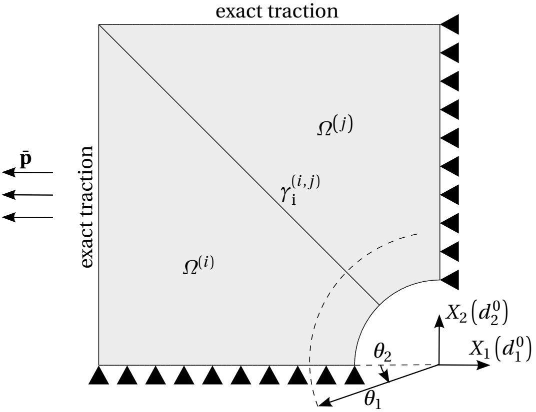

Figure 3.5: Infinite plate with a hole under tension: Problem placement.

modulus, that is, $\hat{\alpha}^{(i,j)} = E \times 10^3$. The Lagrange Multipliers discretization is chosen based on the coarsest discretization from the neighbouring patches. For the sake of clarity, numerically computed values are indicated by either a subscript $\bullet_{\mathrm{h}}$ or superscript $\bullet^{\mathrm{h}}$ to distinguish them from the reference solutions.

3.4.1 Infinite elastic plate with circular hole in tension

Herein a comparison of the DDMs described in Secs. 3.3.3-3.3.5 is provided on the problem of an infinite elastic plate with circular hole, which is subject to tensional loading at $X_1 = \pm\infty$. The plate is modelled using its one quarter by applying symmetry boundary conditions, roller supports, as well as exact tractions at its upper and right edge, see Fig. 3.5. The rectangular plate has length size equal to $\bar{L} = 4$ m and radius of its hole equal to $\bar{R} = 1$ m. Exact solution in terms of both the displacements and stresses can be obtained via analytical methods as explained in Barber [72]. Moreover, the problem's domain is decomposed into two patches, herein denoted by $\Omega^{(i)}$ and $\Omega^{(j)}$, sharing a common interface $\gamma_{\mathrm{i}}^{(i,j)}$.

Then, the deformation and normal force distribution n^{11} is depicted in Figs. 3.6 for a given refinement level also when using the Nitsche-type method, see Eq. (3.24), for the continuity enforcement of the displacement field across $\gamma_{\mathrm{i}}^{(i,j)}$. Patch $\Omega^{(i)}$ is parametrized using 16 elements with $\hat{p}_1^{(i)} = 4$ and $\hat{p}_2^{(i)} = 3$ polynomial orders of the corresponding NURBS basis functions whereas patch $\Omega^{(j)}$ is parametrized using 121 elements and corresponding polynomial orders of the underlying NURBS basis functions $\hat{p}_2^{(j)} = 1$ and $\hat{p}_2^{(j)} = 2$, see Sec. 3.1.2. For the given parametrization of patches $\Omega^{(i)}$ and $\Omega^{(j)}$, interface $\gamma_{\mathrm{i}}^{(i,j)}$ is aligned with the $\theta_1^{(i)}$ and the $\theta_2^{(j)}$ parametric lines in the parametric spaces of patches $\Omega^{(i)}$ and $\Omega^{(j)}$, respectively. Therefore, the solutions $\mathbf{d}^{(i)}$ and $\mathbf{d}^{(j)}$ are piecewise quartic C^3-continuous and piecewise linear C^0-continuous along $\gamma_{\mathrm{i}}^{(i,j)}$, respectively. This has the implication of oscillating discontinuous force components across the interface $\gamma_{\mathrm{i}}^{(i,j)}$ from patch $\Omega^{(j)}$ resembling standard piecewise C^0-continuous finite elements whereas the fourth order smooth NURBS interpolation of the displacement field from patch $\Omega^{(j)}$ results in an excellent approximation of the interface force components when compared to the analytical force distributions, see Figs. 3.7, highlighting the superiority of IGA to standard FEM in terms of approximation power.

Concluding, the DDMs are compared within refinement studies using the relative interface error of the displacements in $\mathcal{H}^1\left(\gamma_{\mathrm{i}}^{(i,j)}\right)$-norm and the relative interface traction field in $\mathcal{L}^2\left(\gamma_{\mathrm{i}}^{(i,j)}\right)$-norm, see Figs. 3.8 and 3.9, respectively. For the convergence graphs, a low and a high order NURBS basis is used. For the low order NURBS basis, the underlying polynomial orders are chosen as $\hat{p}_1^{(i)} = 1$, $\hat{p}_2^{(i)} = 2$, $\hat{p}_1^{(j)} = 3$ and $\hat{p}_2^{(j)} = 2$, whereas for the high order NURBS basis the underlying polynomial orders are chosen as $\hat{p}_1^{(i)} = 3$, $\hat{p}_2^{(i)} = 4$, $\hat{p}_1^{(j)} = 5$ and $\hat{p}_2^{(j)} = 4$. The convergence studies suggest superiority of the Lagrange Multipliers and Nitsche methods against the Penalty method for which a fixed Penalty parameter is chosen. On the other hand, a suitable Lagrange Multipliers discretization needs to be found for the Lagrange Multipliers method and accordingly an enlarged by additional DOFs, non-positive definite equation system needs to be solved. This is not the case for the Nitsche-type method, where the system properties do not differ from the original one and no problem specific parameter

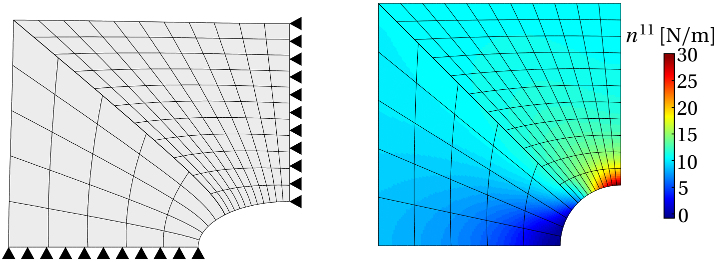

(a) Deformation scaled by 2000.

(b) Contour of the force field n^{11}.

Figure 3.6: Infinite plate with a hole under tension: Deformation scaled by 2000 and contour of the force field n^{11} along the multipatch geometry using Nitsche.

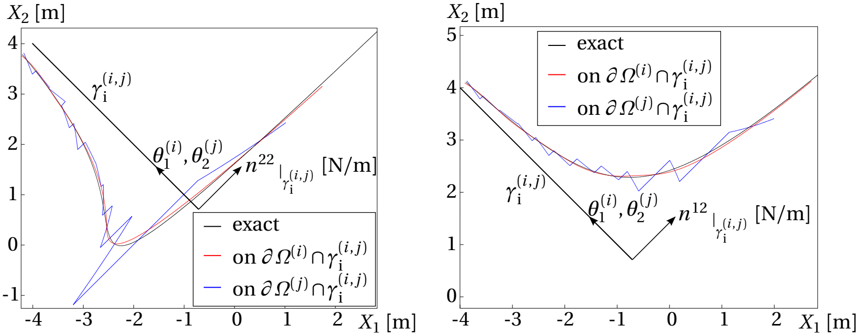

(a) Interface force component n^{22}.

(b) Interface force component n^{12}.

Figure 3.7: Infinite plate with a hole under tension: Interface force distribution from both neighbouring patches against the analytical solution using Nitsche.

or discretization need to be selected. Nevertheless, all aforementioned DDMs provide highly accurate results in the context of NURBS-based IGA on multipatches for linear elasticity thus extending IGA to multipatches for this kind of problems.

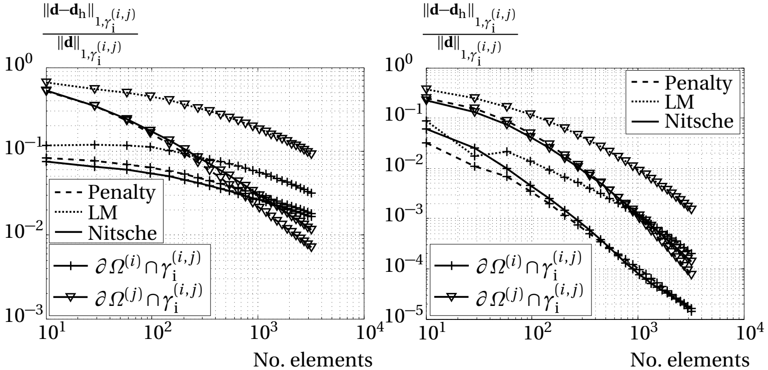

(a) Low polynomial order NURBS basis. (b) High polynomial order NURBS basis.

Figure 3.8: Infinite plate with a hole under tension: Relative error in the $\mathcal{H}^1\left(\gamma_i^{(i,j)}\right)$-norm of the displacement field for the low and high order polynomial NURBS bases.

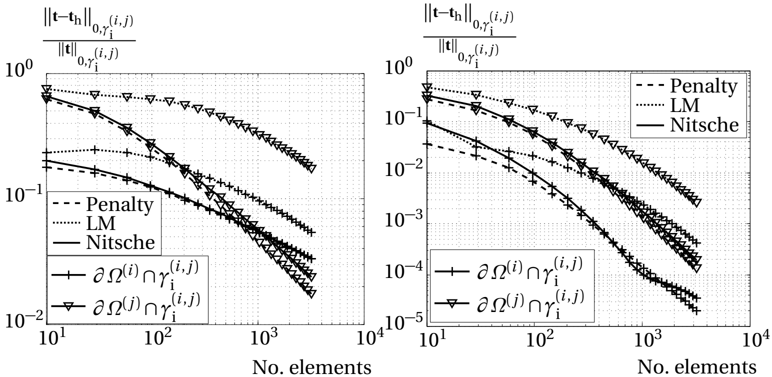

(a) Low polynomial order NURBS basis. (b) High polynomial order NURBS basis.

Figure 3.9: Infinite plate with a hole under tension: Relative error in the $\mathcal{L}^2\left(\gamma_i^{(i,j)}\right)$-norm of the traction field for the low and high order polynomial NURBS bases.

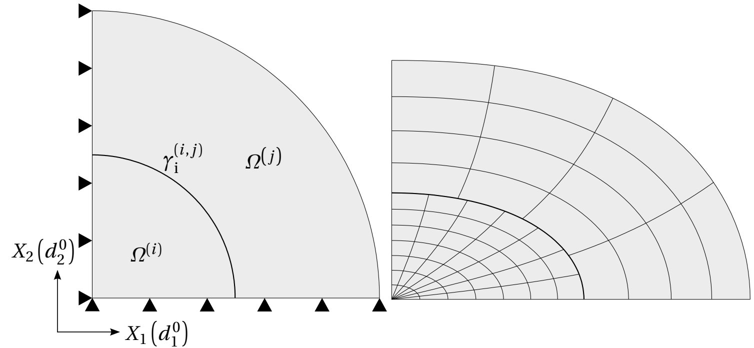

(a) Problem placement. (b) First eigenmode shape.

Figure 3.10: Modal analysis of a circular plate: Problem placement and first eigenmode shape of the multipatch geometry using Nitsche.

3.4.2 Modal analysis of a circular plate

Lastly, the modal analysis of a circular plate is herein considered to demonstrate the extension of IGA to multipatches in the context of structural dynamics, see Fig. 3.10. Accordingly, the problem setting and the first eigenmode shape when using Nitsche is depicted in Fig. 3.10(a) and Fig. 3.10(b), respectively. As reference solution a single patch solution using 3600 elements with polynomial orders of the NURBS basis $\hat{p}_1 = 17$ and $\hat{p}_2 = 16$ is employed. As in Sec. 3.4.1 the plate is modelled only by its one quarter when applying symmetry conditions and the problem's domain is decomposed into two patches $\Omega^{(i)}$ and $\Omega^{(j)}$ sharing a curved interface $\gamma_i^{(i,j)}$, see Fig. 3.10(a). The first eigenmode shape (Eq. (2.68)), which is obtained using Nitsche, is depicted in Fig. 3.10(b). Subsequently, a refinement study for a low and a high polynomial order of the underlying NURBS basis is performed based on the relative error in the first and in the fifth eigenfrequencies of the problem, see Figs. 3.11. The low polynomial orders of the NURBS basis are chosen as $\hat{p}_1^{(i)} = 2$, $\hat{p}_1^{(i)} = 1$, $\hat{p}_1^{(j)} = 3$, $\hat{p}_2^{(j)} = 2$ whereas the high polynomial orders are chosen one order higher in each parametric direction. It is evident that the Penalty method for a fixed Penalty parameter levels off at a given accuracy level, whereas the Lagrange Multipliers and the Nitsche methods converge uniformly to the solution. However, the

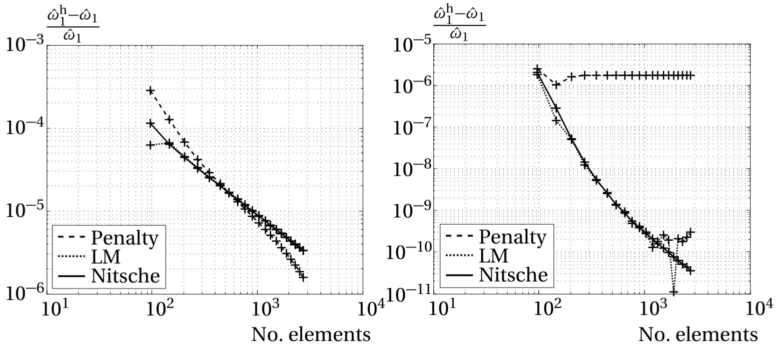

(a) First eigenfrequency corresponding to the low polynomial NURBS basis.

(b) First eigenfrequency corresponding to the high polynomial NURBS basis.

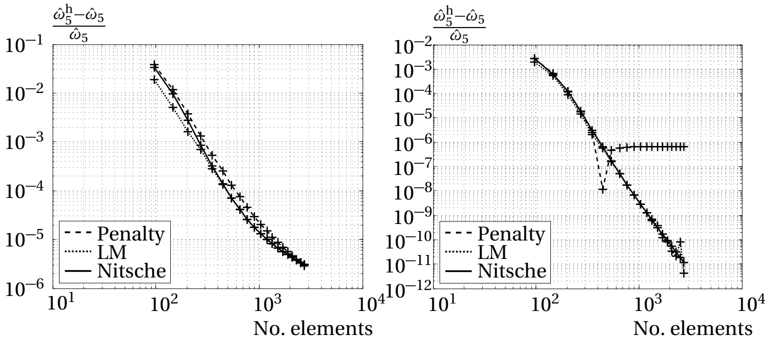

(c) Fifth eigenfrequency corresponding to the low polynomial NURBS basis.

(d) Fifth eigenfrequency corresponding to the high polynomial NURBS basis.

Figure 3.11: Modal analysis of a circular plate: Convergence graphs for the first and the fifth eigenfrequencies using Nitsche for a low and a high order NURBS polynomial basis of the multipatch geometry.

Lagrange Multipliers method is associated with an oscillatory convergence behaviour, typical for saddle point problems for which the LBB condition in Thm. 2.3 is not guaranteed. Contrary, the Nitsche method is associated with uniform convergence for which no problem dependent parameters need to be adjusted. It can be concluded that the proposed methods extend naturally IGA to multipatches in the context of structural dynamics.

3.5 Concluding remarks

In this chapter the preliminaries and the formalities for performing isogeometric analysis on multipatches are laid. Accordingly, the geometric parametrization of surfaces using NURBS, as standard in CAD, is shown. Then, the trimmed multipatch representation of NURBS surfaces is illustrated and the isogeometric discretization of fields over such surfaces is highlighted. In addition, the Penalty, the Lagrange Multipliers and Nitsche-type methods for the enforcement of the interface constraints are shown along with their application to the two-dimensional plane stress problem in both linear statics and dynamics. In the following chapters, these methods are selectively chosen for their application to three dimensional prestressed membranes, Kirchhoff-Love shells and to the isogeometric mortar-based mapping method. The general procedure for isogeometric analysis on multipatches described in this chapter is subsequently followed throughout the thesis.

Chapter 4

Isogeometric Membrane Analysis on Multipatches

Membranes are widely used in engineering practice as their inherently optimal load carrying behaviour and their architectural free-form shapes result in high-end modern engineering structures. Typically, membranes are subject to prestress in addition to prestressed cables which might be embedded into their geometry. Therefore, form-finding analysis is necessary for obtaining the desirable configuration of static equilibrium for this kind of structures, see Sec. 2.3.4. Isogeometric analysis on multipatch surfaces offers an optimal platform for closing the circle design – form-finding – structural analysis – design as demonstrated in Philipp et al. [52]. In this chapter the Penalty and the Nitsche-type methods presented in Secs. 3.3.3 and 3.3.5, respectively, are elaborated and compared for the multipatch coupling and the application of weak Dirichlet boundary conditions in the context of form-finding, modal and geometrically nonlinear transient analysis for membrane structures. In the sequel of this chapter, studies in Apostolatos et al. [29, 39] are closely followed.

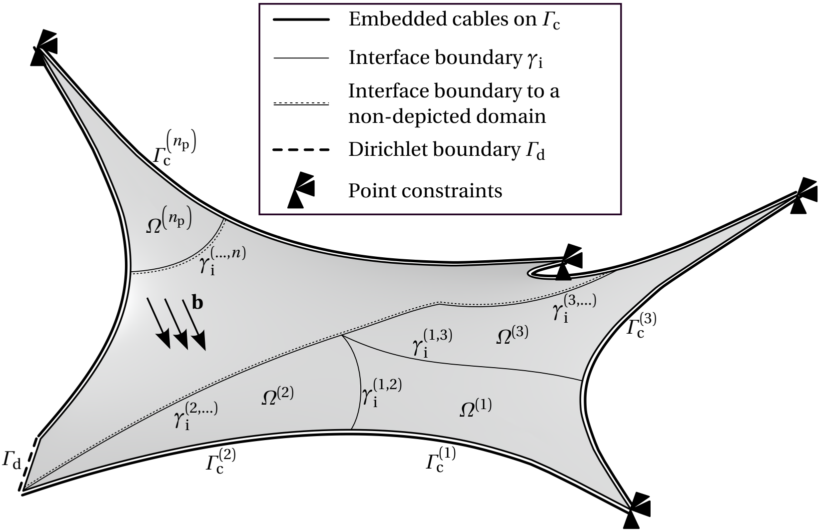

Figure 4.1: Problem placement: Decomposition of the membrane's surface in multiple domains with boundary embedded cables.

4.1 Theory

In this section the extensions of the Penalty and Nitsche-type methods for the multipatch coupling presented in Secs. 3.3.3 and 3.3.5, respectively, to account also for weak Dirichlet boundary conditions in the context of isogeometric analysis of membrane structures on multipatches are shown. The *Updated Reference Strategy* (URS) is used for the form-finding analysis, as discussed in Sec. 2.3.4. Accordingly, only the displacement continuity condition defined in Eq. (3.8a) along with the inhomogeneous Dirichlet boundary condition defined in Eq. (2.49f) need to be enforced in the weak form of the problem.

4.1.1 Problem placement

Herein surface Ω represents a flexible surface whose kinematics are governed by the membrane theory, see Sec. 2.3.3. The governing iBVP and weak form of the membrane problem are shown in Eqs. (2.49) and in Eq. (2.51), respectively, which define the structural behaviour of each patch $\Omega^{(i)}$ assuming as in Sec. 5.1.1 the non-overlapping decomposition of domain Ω defined in Eqs. (3.7). The corresponding problem setting of a membrane structure on multipatches subject to Dirichlet and Neumann boundary conditions along with boundary embedded cables is shown in Fig. 4.1. In the following sections, the Penalty and the Nitsche-type methods are elaborated for the isogeometric analysis of membrane structures on multipatch surfaces. The theory is complemented by three examples. Moreover, Dirichlet conditions at discrete points are enforced strongly, whereas Dirichlet conditions along Γ_{d} are enforced weakly. Clearly, $\Gamma_{\mathrm{d}}^{(i)} = \emptyset$ if patch $\Omega^{(i)}$ does not have any intersection with Γ_{d}. Let in the sequel $n_{\mathrm{d}} \in \mathbb{N}$ to be the number of non-empty boundary segments $\Gamma_{\mathrm{d}}^{(i)}$.

4.1.2 Penalty method

Let $\bar{\alpha} : \Gamma_{\mathrm{d}} \rightarrow \mathbb{R}_{+}^{\star}$ be the Penalty parameter associated with the application of weak Dirichlet boundary conditions along Γ_{d}. Then, the extension of weak form in Eq. (3.15) to account for isogeometric analysis of membrane structures, see (2.51), on multipatches accounting weakly for the application of the Dirichlet boundary conditions reads: Find the displacement field $\mathbf{d} \in \boldsymbol{\mathcal{V}} \cup \boldsymbol{\mathcal{L}}^2(\Gamma_{\mathrm{d}})$ for each time instance $t \in \mathbb{T}$ with $\hat{\boldsymbol{\chi}} \in \boldsymbol{\mathcal{L}}^2(\gamma_{\mathrm{i}})$ such that,

$$\begin{aligned}\left\langle \delta\mathbf{d}, \rho\,\bar{h}\,\ddot{\mathbf{d}} \right\rangle_{0,\Omega_{\mathrm{d}}} + \left\langle \delta\mathbf{d}, c\,\bar{h}\,\dot{\mathbf{d}} \right\rangle_{0,\Omega_{\mathrm{d}}} + \left\langle \delta\mathbf{d}, \hat{\rho}\hat{A}\ddot{\mathbf{d}} \right\rangle_{0,\Gamma_{\mathrm{c}}} + \left\langle \delta\mathbf{d}, \hat{c}\hat{A}\dot{\mathbf{d}} \right\rangle_{0,\Gamma_{\mathrm{c}}} + \\ a\left(\delta\mathbf{d}, \mathbf{d}\right) + \left\langle \delta\hat{\boldsymbol{\chi}}, \hat{\alpha}\,\hat{\boldsymbol{\chi}} \right\rangle_{0,\gamma_{\mathrm{i}}} + \langle \delta\mathbf{d}, \bar{\alpha}\mathbf{d} \rangle_{0,\Gamma_{\mathrm{d}}} = l\left(\delta\mathbf{d}\right) + \left\langle \delta\mathbf{d}, \bar{\alpha}\mathbf{g} \right\rangle_{0,\Gamma_{\mathrm{d}}}\,,\end{aligned} \tag{4.1}$$

for all $\delta\mathbf{d} \in \boldsymbol{\mathcal{V}} \cup \boldsymbol{\mathcal{L}}^2(\Gamma_{\mathrm{d}})$ with $\delta\hat{\boldsymbol{\chi}} \in \boldsymbol{\mathcal{L}}^2(\gamma_{\mathrm{i}})$. The definition of the displacement jump $\hat{\boldsymbol{\chi}}$ is given in Sec. 3.3.1. Since the additional terms appear only on the Dirichlet boundary which can be decomposed between the patches, namely, $\Gamma_{\mathrm{d}}^{(i)} = \partial\Omega^{(i)} \cap \Gamma_{\mathrm{d}}$ for all $i = 1, \ldots, n_{\mathrm{s}}$, the coupling components of the equation system in Eq. (3.16) are not affected and hence the coupled system becomes,

$$\begin{bmatrix} \mathbf{K}_{\mathrm{d}}^{(1)} + \hat{\mathbf{C}}_{\hat{\alpha}}^{(1)} + \bar{\mathbf{C}}_{\bar{\alpha}}^{(1)} & \cdots & \hat{\mathbf{C}}_{\hat{\alpha}}^{(1,n_{\mathrm{s}})} \\ \vdots & \ddots & \vdots \\ \hat{\mathbf{C}}_{\hat{\alpha}}^{(n_{\mathrm{s}},1)} & \cdots & \mathbf{K}_{\mathrm{d}}^{(n_{\mathrm{s}})} + \hat{\mathbf{C}}_{\hat{\alpha}}^{(n_{\mathrm{s}})} + \bar{\mathbf{C}}_{\bar{\alpha}}^{(n_{\mathrm{s}})} \end{bmatrix} \Delta_{\hat{n},\hat{\imath}} \begin{bmatrix} \hat{\mathbf{d}}^{(1)} \\ \vdots \\ \hat{\mathbf{d}}^{(n_{\mathrm{s}})} \end{bmatrix} = -\begin{bmatrix} \mathbf{R}_{\mathrm{d}}^{(1)} + \hat{\mathbf{R}}_{\hat{\alpha}}^{(1)} + \bar{\mathbf{R}}_{\bar{\alpha}}^{(1)} \\ \vdots \\ \mathbf{R}_{\mathrm{d}}^{(n_{\mathrm{s}})} + \hat{\mathbf{R}}_{\hat{\alpha}}^{(n_{\mathrm{s}})} + \bar{\mathbf{R}}_{\bar{\alpha}}^{(n_{\mathrm{s}})} \end{bmatrix}, \tag{4.2}$$

where the additional residual vectors $\bar{\mathbf{R}}_{\bar{\alpha}}^{(i)}$ are given by,

$$\bar{\mathbf{R}}_{\bar{\alpha}}^{(i)} = \bar{\mathbf{C}}_{\bar{\alpha}}^{(i)} \hat{\mathbf{d}}_{\hat{n},\hat{\imath}}^{(i)} - \bar{\mathbf{F}}_{\bar{\alpha}}^{(i)} \, . \tag{4.3}$$

The additional matrices $\bar{\mathbf{C}}_{\bar{\alpha}}^{(i)}$ and force vectors $\bar{\mathbf{F}}_{\bar{\alpha}}^{(i)}$ due to the weak enforcement of the Dirichlet boundary conditions have entries,

$$\bar{C}_{\bar{\alpha}(j,k)}^{(i)} = \left\langle \bar{\boldsymbol{\phi}}_{j}^{(i)}, \bar{\alpha}^{(i)} \bar{\boldsymbol{\phi}}_{k}^{(i)} \right\rangle_{0,\Gamma_{\mathrm{d}}^{(i)}} \, , \tag{4.4a}$$

$$\bar{F}_{\bar{\alpha}(j)}^{(i)} = \left\langle \bar{\boldsymbol{\phi}}_{j}^{(i)}, \bar{\alpha}^{(i)} \mathbf{g} \right\rangle_{0,\Gamma_{\mathrm{d}}^{(i)}} \, , \tag{4.4b}$$

where the Penalty parameter $\bar{\alpha}^{(i)} = \bar{\alpha}_{|_{\Gamma_{\mathrm{d}}^{(i)}}}$ is chosen piecewise constant along each boundary $\Gamma_{\mathrm{d}}^{(i)}$. The Penalty method offers herein also an efficient and straightforward approach for handling both the multipatch coupling and the application of weak Dirichlet boundary conditions. The shortcoming of the Penalty method lies in that the underlying Penalty parameters need to be increased with the refinement so that a uniform convergence to the solution can be obtained due to the variational inconsistency of the method itself, see Sec. 3.3.3. Herein the Penalty parameters are chosen as a scaling of the material matrix norm $\|\mathbf{D}_{\mathrm{m}}\|_{\mathrm{F}}$ times the inverse of the minimum element area and the maximum polynomial order along each Dirichlet boundary $\Gamma_{\mathrm{d}}^{(i)}$ and each interface $\gamma_{\mathrm{i}}^{(i,j)}$ for $\hat{\alpha}^{(i,j)}$ and $\bar{\alpha}^{(i)}$, respectively.

4.1.3 Nitsche-type method

As an alternative to the aforementioned Penalty method in Sec. 4.1.2, a Nitsche-type method is herein proposed, see also in Sec. 3.3.5, for the multipatch coupling and the application of weak Dirichlet boundary conditions in the context of isogeometric membrane analysis on multipatches. Let $\bar{\beta} : \gamma_\mathrm{i} \rightarrow \mathbb{R}^\star_+$ be the stabilization parameter associated with the weak enforcement of the Dirichlet boundary conditions in Eq. (2.49f). In this way, the extension of the weak form in Eq. (3.24) to account for isogeometric analysis of membrane structures on multipatches with weak Dirichlet boundary conditions reads: Find the displacement field $\mathbf{d} \in \boldsymbol{\mathcal{V}} \cup \boldsymbol{\mathcal{H}}^1(\mathit{\Gamma}_\mathrm{d})$ for each time instance $t \in \mathbb{T}$ with $\hat{\boldsymbol{\chi}}, \bar{\mathbf{t}} \in \boldsymbol{\mathcal{L}}^2(\gamma_\mathrm{i})$ such that,

$$\begin{aligned} &\left\langle \delta \mathbf{d}, \rho \bar{h} \ddot{\mathbf{d}} \right\rangle_{0,\mathit{\Omega}_\mathrm{d}} + \left\langle \delta \mathbf{d}, c \bar{h} \dot{\mathbf{d}} \right\rangle_{0,\mathit{\Omega}_\mathrm{d}} + \left\langle \delta \mathbf{d}, \hat{\rho} \hat{A} \ddot{\mathbf{d}} \right\rangle_{0,\mathit{\Gamma}_\mathrm{c}} + \left\langle \delta \mathbf{d}, \hat{c} \hat{A} \dot{\mathbf{d}} \right\rangle_{0,\mathit{\Gamma}_\mathrm{c}} \\ &\quad + a(\delta \mathbf{d}, \mathbf{d}) - \left\langle \delta \hat{\boldsymbol{\chi}}, \bar{\mathbf{t}} \right\rangle_{0,\gamma_\mathrm{i}} - \left\langle \delta \bar{\mathbf{t}}, \hat{\boldsymbol{\chi}} \right\rangle_{0,\gamma_\mathrm{i}} + \left\langle \delta \hat{\boldsymbol{\chi}}, \hat{\beta} \hat{\boldsymbol{\chi}} \right\rangle_{0,\gamma_\mathrm{i}} - \langle \delta \mathbf{d}, \mathbf{t} \rangle_{0,\mathit{\Gamma}_\mathrm{d}} \\ &\quad - \langle \delta \mathbf{t}, \mathbf{d} \rangle_{0,\mathit{\Gamma}_\mathrm{d}} + \left\langle \delta \mathbf{d}, \bar{\beta} \mathbf{d} \right\rangle_{0,\mathit{\Gamma}_\mathrm{d}} = l(\delta \mathbf{d}) - \left\langle \delta \mathbf{t}, \mathbf{g} \right\rangle_{0,\mathit{\Gamma}_\mathrm{d}} + \left\langle \delta \mathbf{d}, \bar{\beta} \mathbf{g} \right\rangle_{0,\mathit{\Gamma}_\mathrm{d}} \, , \end{aligned} \tag{4.5}$$

for all $\mathbf{d} \in \boldsymbol{\mathcal{V}} \cup \boldsymbol{\mathcal{H}}^1(\mathit{\Gamma}_\mathrm{d})$ with $\delta \hat{\boldsymbol{\chi}}, \delta \bar{\mathbf{t}} \in \boldsymbol{\mathcal{L}}^2(\gamma_\mathrm{i})$. Moreover, $\bar{\mathbf{t}}$ stands for the mean interface traction defined in Eq. (3.23) and $\mathbf{t}$ for the traction vector defined in Eq. (2.50a) for the membrane problem. As for the Penalty parameter in Sec. 4.1.2, the stabilization parameter is defined piecewise constant along each boundary $\mathit{\Gamma}_\mathrm{d}^{(i)}$, namely, $\bar{\beta}^{(i)} = \bar{\beta}_{|_{\mathit{\Gamma}_\mathrm{d}^{(i)}}}$. Equivalent to Nitsche-type method for the multipatch coupling introduced in Sec. 3.3.5 the necessary condition for coercivity due to the additional terms along the Dirichlet boundary in Eq. (4.5) is the existence of constants $\bar{C}^{(i)} > 0$ such that,

$$||\mathbf{t}^{(i)}||^2_{0,\mathit{\Gamma}_\mathrm{d}^{(i)}} \leq \bar{C}^{(i)} a(\mathbf{d}, \mathbf{d}) \quad \forall \mathbf{d} \in \boldsymbol{\mathcal{V}} \, , \tag{4.6}$$

along each Dirichlet boundary $\mathit{\Gamma}_\mathrm{d}^{(i)}$. In this way, the equation system in Eq. (3.26) in this case becomes,

$$\begin{bmatrix} \mathbf{K}_\mathrm{d}^{(1)} + \hat{\mathbf{C}}_\mathrm{n}^{(1)} + \hat{\mathbf{C}}_{\hat{\beta}}^{(1)} + \bar{\mathbf{C}}_\mathrm{n}^{(1)} + \bar{\mathbf{C}}_{\bar{\beta}}^{(1)} & \cdots & \hat{\mathbf{C}}_\mathrm{n}^{(1,n_\mathrm{s})} + \hat{\mathbf{C}}_{\hat{\beta}}^{(1,n_\mathrm{s})} \\ \vdots & \ddots & \vdots \\ \hat{\mathbf{C}}_\mathrm{n}^{(n_{\mathrm{s},1})} + \hat{\mathbf{C}}_{\bar{\beta}}^{(n_\mathrm{s},1)} & \cdots & \mathbf{K}_\mathrm{d}^{(n_\mathrm{s})} + \hat{\mathbf{C}}_\mathrm{n}^{(n_\mathrm{s})} + \hat{\mathbf{C}}_{\hat{\beta}}^{(n_\mathrm{s})} + \bar{\mathbf{C}}_\mathrm{n}^{(n_\mathrm{s})} + \bar{\mathbf{C}}_{\bar{\beta}}^{(n_\mathrm{s})} \end{bmatrix}$$

$$\mathit{\Delta}_{\hat{n},\hat{\imath}} \begin{bmatrix} \hat{\mathbf{d}}^{(1)} \\ \vdots \\ \hat{\mathbf{d}}^{(n_\mathrm{s})} \end{bmatrix} = - \begin{bmatrix} \mathbf{R}^{(1)}_\mathrm{d} + \hat{\mathbf{R}}^{(1)}_\mathrm{n} + \hat{\mathbf{R}}^{(1)}_{\hat{\beta}} + \bar{\mathbf{R}}^{(1)}_\mathrm{n} + \bar{\mathbf{R}}^{(1)}_{\bar{\beta}} \\ \vdots \\ \mathbf{R}^{(n_\mathrm{s})}_\mathrm{d} + \hat{\mathbf{R}}^{(n_\mathrm{s})}_\mathrm{n} + \hat{\mathbf{R}}^{(n_\mathrm{s})}_{\hat{\beta}} + \bar{\mathbf{R}}^{(n_\mathrm{s})}_\mathrm{n} + \bar{\mathbf{R}}^{(n_\mathrm{s})}_{\bar{\beta}} \end{bmatrix}, \tag{4.7}$$

where the additional Nitsche matrices $\bar{\mathbf{C}}^{(i)}_\mathrm{n}$ and residual vectors $\bar{\mathbf{R}}^{(i)}_\mathrm{n}$ have entries,

$$\begin{aligned} \bar{C}^{(i)}_{\mathrm{n}(j,k)} = & - \left\langle \left. \frac{\partial \mathbf{t}^{(i)}}{\partial \hat{d}^{(i)}_j} \right|_{\hat{\mathbf{d}}^{(i)}_{\hat{n},\hat{\imath}}}, \bar{\boldsymbol{\phi}}^{(i)}_k \right\rangle_{0,\mathit{\Gamma}^{(i)}_\mathrm{d}} - \left\langle \bar{\boldsymbol{\phi}}^{(i)}_j, \left. \frac{\partial \mathbf{t}^{(i)}}{\partial \hat{d}^{(i)}_k} \right|_{\hat{\mathbf{d}}^{(i)}_{\hat{n},\hat{\imath}}} \right\rangle_{0,\mathit{\Gamma}^{(i)}_\mathrm{d}} - \\ & \left\langle \left. \frac{\partial^2 \mathbf{t}^{(i)}}{\partial \hat{d}^{(i)}_j \partial \hat{d}^{(i)}_k} \right|_{\hat{\mathbf{d}}^{(i)}_{\hat{n},\hat{\imath}}}, \mathbf{d}^{(i)}_{\hat{n},\hat{\imath}} \right\rangle_{0,\mathit{\Gamma}^{(i)}_\mathrm{d}}, \end{aligned} \tag{4.8a}$$

$$\bar{R}^{(i)}_{\mathrm{n}(j)} = - \left\langle \left. \frac{\partial \mathbf{t}^{(i)}}{\partial \hat{d}^{(i)}_j} \right|_{\hat{\mathbf{d}}^{(i)}_{\hat{n},\hat{\imath}}}, \mathbf{d}^{(i)}_{\hat{n},\hat{\imath}} - \mathbf{g} \right\rangle_{0,\mathit{\Gamma}^{(i)}_\mathrm{d}} - \left\langle \bar{\boldsymbol{\phi}}^{(i)}_j, \left. \mathbf{t}^{(i)} \right|_{\hat{\mathbf{d}}^{(i)}_{\hat{n},\hat{\imath}}} \right\rangle_{0,\mathit{\Gamma}^{(i)}_\mathrm{d}}. \tag{4.8b}$$

Matrices $\bar{\mathbf{C}}^{(i)}_{\bar{\beta}}$ and vectors $\bar{\mathbf{R}}^{(i)}_{\bar{\beta}}$ related to the stabilization terms in Eq. (4.7) are defined as the corresponding discrete matrices and vectors resulting from the Penalty method in Eqs. (4.3) and (4.4), respectively. Moreover, the discrete form of the necessary condition for coercivity in Eq. (4.6) can be formulated as a generalized eigenvalue problem similar to Eq. (3.28),

$$\det \left(\bar{\mathbf{Q}}^{(i)} - \bar{C}^{(i)} \left. \mathbf{K}^{(i)} \right|_{\mathit{\Gamma}^{(i)}_\mathrm{d}} \right) = 0\,, \tag{4.9}$$

which is solved for the corresponding eigenvalues $\bar{C}^{(i)}_r$ along each non-empty boundary $\mathit{\Gamma}^{(i)}_\mathrm{d}$. The components of matrices $\bar{\mathbf{Q}}^{(i)}$ in Eq. (4.9) are defined as,

$$\begin{aligned}\bar{Q}^{(i)}_{(j,k)} = & \left\langle \left. \frac{\partial \mathbf{t}^{(i)}}{\partial \hat{d}^{(i)}_j} \right|_{\hat{\mathbf{d}}^{(i)}_{\hat{n}},\hat{\imath}} , \left. \frac{\partial \mathbf{t}^{(i)}}{\partial \hat{d}^{(i)}_k} \right|_{\hat{\mathbf{d}}^{(i)}_{\hat{n}},\hat{\imath}} \right\rangle_{0,\Gamma^{(i)}_{\mathrm{d}}} + \\ & \left\langle \left. \frac{\partial^2 \mathbf{t}^{(i)}}{\partial \hat{d}^{(i)}_j \partial \hat{d}^{(i)}_k} \right|_{\hat{\mathbf{d}}^{(i)}_{\hat{n}},\hat{\imath}} , \left. \mathbf{t}^{(i)} \right|_{\hat{\mathbf{d}}^{(i)}_{\hat{n}},\hat{\imath}} \right\rangle_{0,\Gamma^{(i)}_{\mathrm{d}}} .\end{aligned} \tag{4.10}$$

Additionally, $\mathbf{K}^{(i)}|_{\Gamma^{(i)}_{\mathrm{d}}}$ stands for the restriction of tangent stiffness matrix $\mathbf{K}^{(i)}$ of patch $\Omega^{(i)}$ at the DOFs along the Dirichlet boundary $\Gamma^{(i)}_{\mathrm{d}}$. Applying the Nitsche-type method for the interface continuity and the application of weak Dirichlet boundary conditions the estimates for the stabilization parameters $\hat{\beta}^{(i,j)}$ and $\bar{\beta}^{(i)}$ become,

$$\hat{\beta}^{(i,j)} \geq 4 n_{\mathrm{i}} \max_r \hat{C}^{(i,j)}_r , \tag{4.11a}$$

$$\bar{\beta}^{(i)} \geq 4 n_{\mathrm{d}} \max_r \bar{C}^{(i)}_r , \tag{4.11b}$$

respectively.

4.2 Numerical examples

Next, three examples are used for the demonstration of the aforementioned methods in the context of isogeometric membrane analysis on multipatches. The first one is the well-established benchmark of the four-point sail, see in Wüchner [35]. For this example, form-finding analysis is used to obtain the shape of static equilibrium and subsequently modal and geometrically nonlinear transient analysis given a live load are performed. Subsequently, the middle sail of the Olympic stadium roof in Munich is considered in the context of practically relevant applications. Accordingly, form-finding, modal and transient analyses are performed. Lastly, another example of practical relevance, that of an inflatable hangar consisting of three inflatable torus-shaped tubes, is used in order to show the application of the aforementioned methods on real world engineering problems. For all aforementioned numerical examples, the initial conditions for the

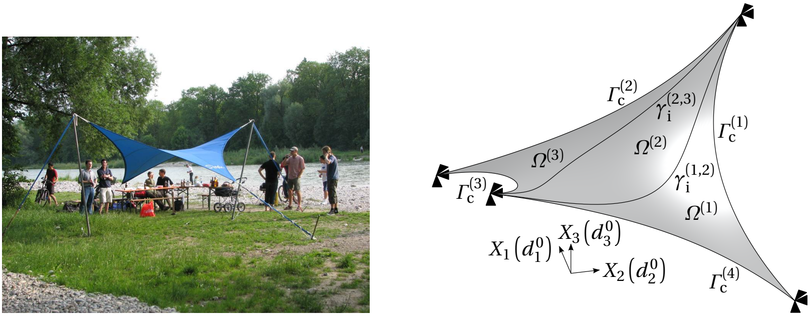

(a) Example of a four-point sail.

(b) Multipatch geometry.

Figure 4.2: Four-point sail: Problem setting.

displacement and the velocity fields are chosen as $\mathbf{d}_0 = \mathbf{0}$ and $\boldsymbol{v}_0 = \mathbf{0}$, respectively, in the context of transient analysis. As reference solution, a single patch solution or a standard finite element solution within `Carat++` software (Fischer [73]) is used.

4.2.1 Four-point sail

The first numerical example consists of the form-finding and subsequently modal and geometrically nonlinear transient analysis of a four-point sail, see Fig. 4.2. A picture of the four-point sail and the corresponding problem setting are shown in Figs. 4.2(a) and 4.2(b), respectively. This membrane structure has been extensively used as a demonstrator for the URS method discussed in Sec. 2.3.4. For the case set-up, the work in Wüchner [35] is followed. The sail and the definition of its underlying multipatch geometry consisting of three patches with two interfaces is shown in Fig. 4.2(b), where four cables are attached to all four external edges. The Young's modulus, the Poisson's ratio, the density and the thickness of the membrane structure are defined as $E = 8 \times 10^8$ Pa, $\nu = 0.4$, $\rho = 800$ Kg/m^3 and $\bar{h} = 10^{-3}$ m, respectively. Additionally, the sail is subject to isotropic prestress, with the normal components equal to $n_0^{11} = n_o^{22} = n_0 = 3 \times 10^3$ N/m and the shear components set to zero. Regarding the cables, the Young's modulus, the density and the diameter of their circular cross sections these are set as $\hat{E} = 1.6 \times 10^{11}$ Pa, $\hat{\rho} = 8300$ Kg/m^3 and $\hat{D} = 12 \times 10^{-3}$ m, respectively.

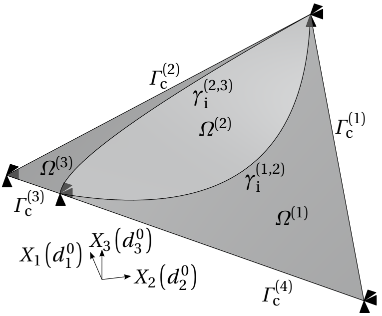

Figure 4.3: Four-point sail: Problem setting for the form-finding analysis.

Moreover, all cables are subject to the same prestress condition with magnitude $\hat{f}_0 = 6 \times 10^4$ N.

At first, the geometry of static equilibrium for the four-point sail is sought. The problem setting for the form-finding analysis is depicted in Fig. 4.3, where the reference geometry consists of planar patches. However, their interfaces are chosen curved and the underlying parametrizations attain singularities. Especially for patch $\Omega^{(2)}$, two parametric singularities at its fixed ends exist. The expected solution of the URS consists of radii of curvature at each $\Gamma_c^{(i)}$ equal to $\bar{R} = \hat{f}_0 / n_0 = 20$ m, in this case, see in Bletzinger et al. [60]. For the refinement study, patches $\Omega^{(1)}$, $\Omega^{(2)}$ and $\Omega^{(3)}$ are parametrized using $\lceil 14\, i_r/9 \rceil$, $\lceil 2\, i_r/3 \rceil$ and $\lceil 3\, i_r/2 \rceil$ elements, respectively, where $i_r = 1, \ldots, 22$ is the refinement index. The respective patch parametrizations of three refinement levels are shown in Fig. 4.4. In addition, two polynomial order settings are considered: The low polynomial order setting where patches $\Omega^{(1)}$ and $\Omega^{(3)}$ are parametrized using biquadratic b-spline bases and patch $\Omega^{(2)}$ is parametrized using a bicubic b-spline basis. On the other hand, the fine polynomial order setting consists of parametrizing patches $\Omega^{(1)}$ and $\Omega^{(3)}$ using bicubic b-spline bases and patch $\Omega^{(2)}$ with a biquartic b-spline basis. As reference the solution of a single patch parametrization using a bicubic b-spline basis and 2500 elements is used. For the form-finding analysis, 20 form-finding iterations are used for both methods and the form-finding iterations are also halted if the norm of displacement incre-

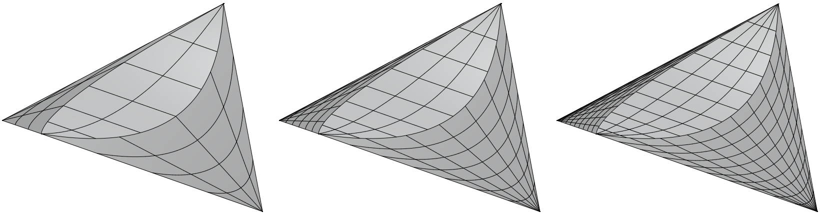

(a) Refinement level $i_\mathrm{r} = 1$. (b) Refinement level $i_\mathrm{r} = 3$. (c) Refinement level $i_\mathrm{r} = 5$.

Figure 4.4: Four-point sail: Parametrizations for three different refinement levels concerning the form-finding analysis.

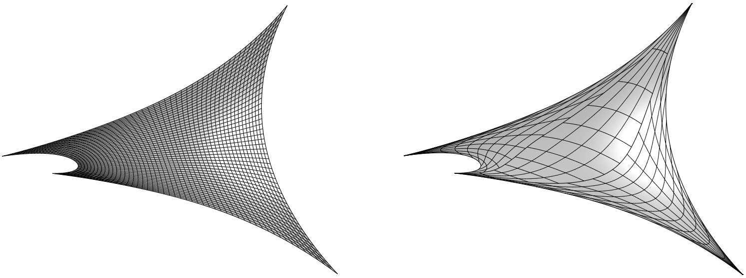

(a) Single patch. (b) IGA on multipatches with Penalty.

Figure 4.5: Four-point sail: Form-finding results using the Penalty method at refinement level $i_\mathrm{r} = 5$ for the high polynomial order setting against the single patch solution.

ment from one form-finding iteration to another is smaller or equal to 10^{-4}. The form-found geometries for the reference single patch and three-patch geometry using the Penalty method at refinement step $i_\mathrm{r} = 5$ corresponding to the high polynomial order setting are shown in Fig. 4.5 demonstrating excellent accordance between each other. One can observe an excellent qualitative match of the results when using IGA on multipatches compared to the single patch solution. For the quantitative discussion of the results, convergence graphs are used. At first, the relative error of the form-finding analysis in the $\mathcal{L}^2(\Omega)$-norm is shown in Fig. 4.6 for both the low and the high polynomial order settings in case of increasing h-refinement of the

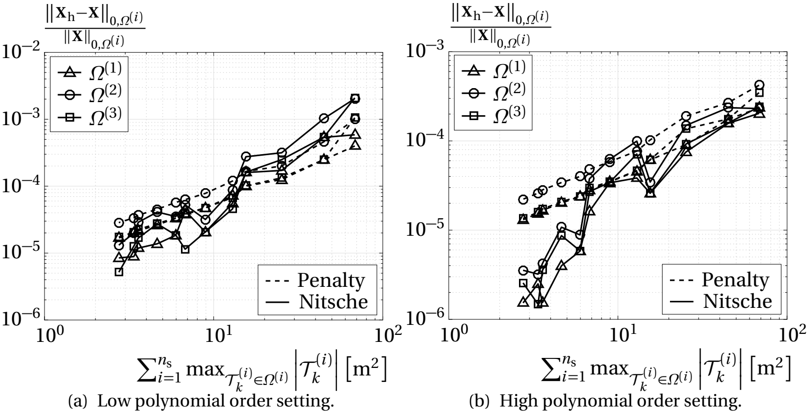

(a) Low polynomial order setting.

(b) High polynomial order setting.

Figure 4.6: Four-point sail: Relative error of the form-finding results in each patch.

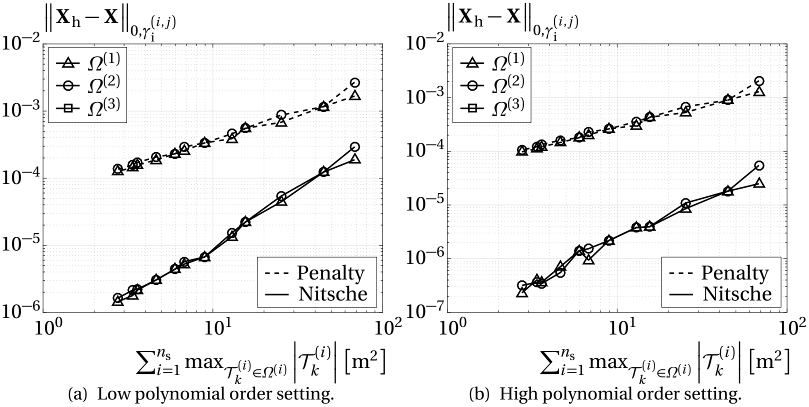

(a) Low polynomial order setting.

(b) High polynomial order setting.

Figure 4.7: Four-point sail: Error in the interface conditions of the form-finding results.

parametrization (knot insertion) where clearly the Nitsche outperforms the Penalty method in both settings. Then, the error in the $\mathcal{L}^2(\gamma_\mathrm{i})$-norm is shown in Fig. 4.7 once more for both the low and the high polynomial order settings, where the Nitsche-type method achieves a higher accuracy

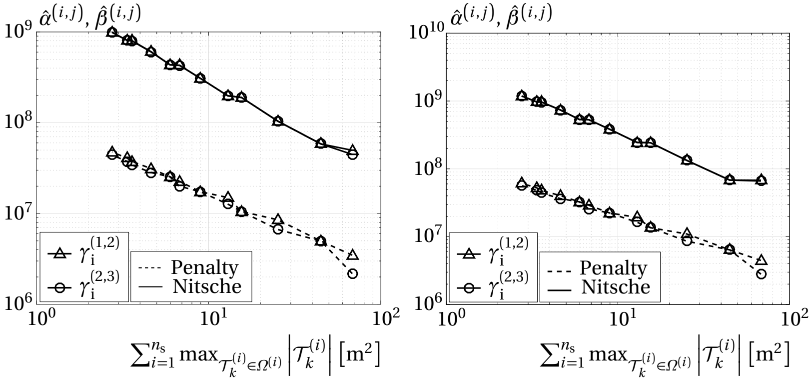

(a) Low polynomial order study.
(b) High polynomial order study.

Figure 4.8: Four-point sail: Evolution of the Penalty and the stabilization parameters for each interface through refinement.

by two and three orders of magnitude than the Penalty method.

Subsequently, the evolution of the Penalty and the stabilization parameters for the Penalty and the Nitsche-type methods are shown in the set of Figs. 4.8 for both polynomial order settings. The estimated stabilization parameters for the Nitsche-type method are one order of magnitude larger than the Penalty parameters for the Penalty method but the rate of increase as the element size goes to zero is the same for both. Furthermore, in set of Figs. 4.9, the evolution of the stabilization parameters for the Nitsche-type method is shown for both the low and the high polynomial order settings for three selected refinement levels and for each interface. As expected, the stabilization parameters increase with the form-finding iterations as the shape of the membrane is changing but at the convergence region the stabilization parameters obtain also their converged values.

For the modal and the transient analyses (Fig. 4.11), two representative settings are considered: One coarse and one fine setting. The coarse setting uses the low polynomial order as described before and the refinement level $i_{\mathrm{r}} = 6$. The fine setting is characterized by using the high polynomial order and refinement level $i_{\mathrm{r}} = 12$. The corresponding reference configurations

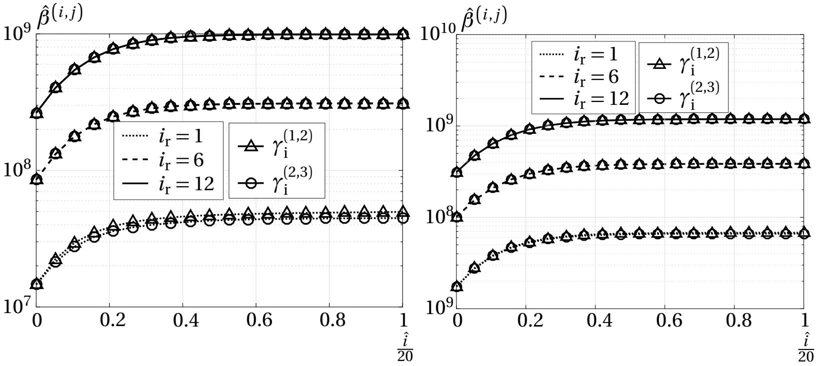

(a) Low polynomial order study.

(b) High polynomial order study.

Figure 4.9: Four-point sail: Evolution of the stabilization parameters corresponding to Nitsche-type method for each interface through form-finding iterations.

of static equilibrium under the prestress state are obtained using the URS and the Nitsche-type method for the multipatch coupling. In Fig. 4.10 three mode shapes corresponding to eigenfrequencies f_1, f_4 and f_{20} are depicted for the single patch reference isogeometric discretization and the isogeometric discretization on multipatches when using the Penalty method. As before, the qualitative results show excellent agreement between isogeometric analysis on single and multiple patches. As quantitative study of the eigenfrequency analysis, Fig. 4.11(a) shows the computed eigenfrequency spectrum for the coarse and fine setting scaled by the numerical spectrum of the reference single patch solution corresponding to the first 400 eigenfrequencies. As expected, the finer the discretization becomes the closer the results get to the reference solution, where both the Penalty and the Nitsche-type methods yield highly accurate results.

For the transient analysis of the four-point sail, the time span $\mathbb{T} = [0, 1]$ s is chosen. As mentioned at the beginning of this section, the considered dynamic load is defined as,

$$\mathbf{b}(t) = -0.05 \left| \sin(6\pi t) \right| \mathbf{e}_3 \, [\mathrm{Pa}] \, , \text{ for all } t \in \mathbb{T} \, . \tag{4.12}$$

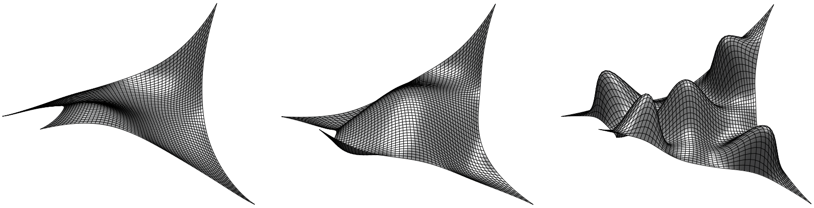

(a) $f_1 = 4.65$ Hz (single patch).

(b) $f_4 = 5.22$ Hz (single patch).

(c) $f_{20} = 11.21$ Hz (single patch).

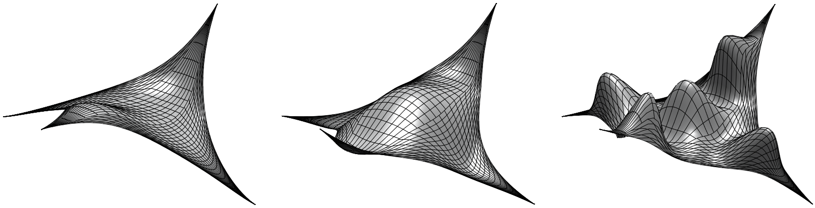

(d) $f_1^{\mathrm{h}} = 4.65$ Hz (IGA on multipatches with Penalty).

(e) $f_4^{\mathrm{h}} = 5.22$ Hz (IGA on multipatches with Penalty).

(f) $f_{20}^{\mathrm{h}} = 11.23$ Hz (IGA on multipatches with Penalty).

Figure 4.10: Four-point sail: Comparison between the single and multipatch mode shapes (Penalty).

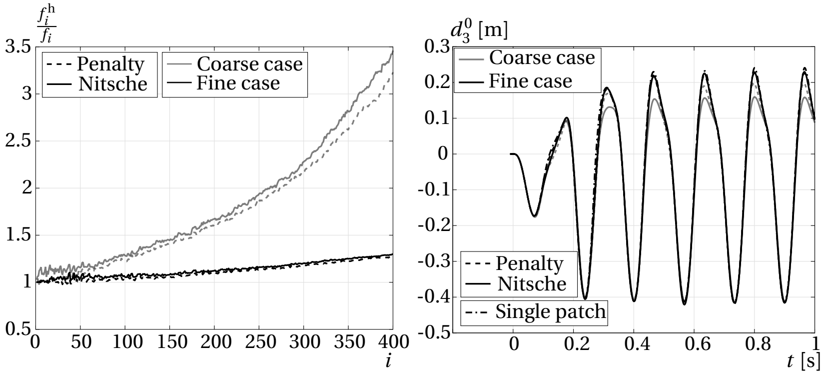

(a) Relative error in the computed eigenfrequencies.

(b) Time-displacement curves.

Figure 4.11: Four-point sail: Relative error in the computed eigenfrequencies and time-displacement curves.

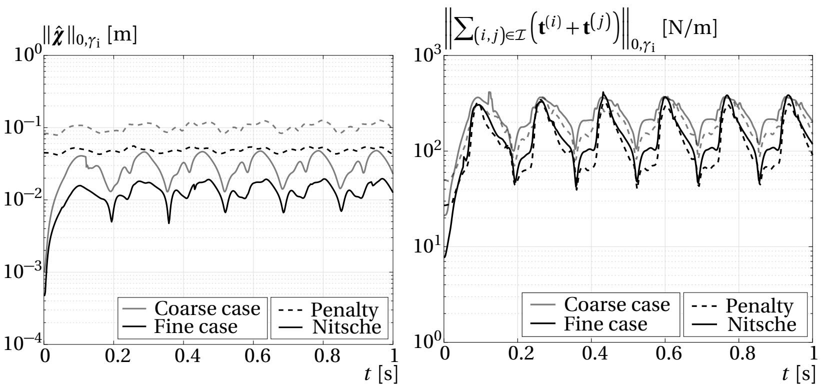

(a) Evolution of the error in the displacement interface condition.

(b) Evolution of the error in the traction interface condition.

Figure 4.12: Four-point sail: Evolution of the error in the displacement and traction interface condition throughout the time.

For the estimation of the Rayleigh damping parameters, eigenfrequencies $f_1 = 4.6568$ Hz and $f_{10} = 8.9537$ Hz from the reference single patch solution are used, see Sec. 2.4.3. By substituting them in Eqs. (2.70), the specific Rayleigh damping parameters $\alpha_\mathrm{r} = 3.8497\ \mathrm{s}^{-1}$ and $\beta_\mathrm{r} = 0.0023$ s are obtained. For the single patch, the coarse and the fine settings, the same time step size for the Newmark time integration scheme is chosen as $\Delta t = 2\times10^{-3}$ s. The corresponding time-displacement curves for the d_3^0 component of the displacement field at the middle of the sail is shown in Fig. 4.11(b) for both the coarse and the fine settings and for both methods against the single patch solution. For the coarse setting the Nitsche-type method does not accurately predict the amplitude of the oscillation, however when refining the spatial discretization both methods deliver highly accurate results.

Furthermore, the error in the interface conditions along γ_i throughout the time is investigated, see Fig. 4.12. The evolution of the error in the interface Dirichlet condition in Eq. (3.8a) in the $\mathcal{L}^2(\gamma_\mathrm{i})$-norm for both methods is shown in Fig. 4.12(a). The Nitsche-type method outperforms the Penalty method in both the coarse and fine polynomial order settings. Fig. 4.12(b)

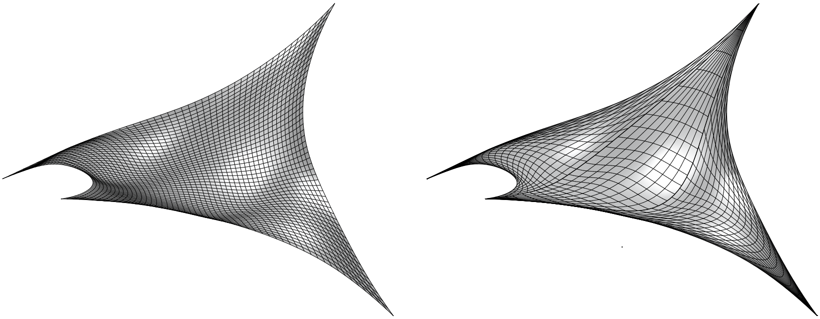

(a) Single patch.

(b) IGA on multipatches with Penalty.

Figure 4.13: Four-point sail: Deformation at $t = 0.36$ s scaled by 10 for both the single and the multipatch model (Penalty).

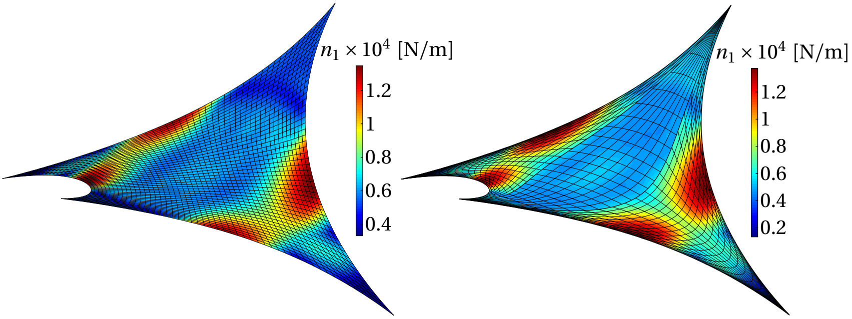

(a) First principal force n_1 contour at time $t = 0.81$ s (single patch).

(b) First principal force n_1 contour at time $t = 0.81$ s (IGA on multipatches with Penalty).

Figure 4.14: Four-point sail: Principal force n_1 contour at $t = 0.81$ s for both the single and multipatch models.

then shows the evolution of the error in the interface Neumann condition in Eq. (3.8b) in the $\mathcal{L}^2(\gamma_\mathrm{i})$-norm for both methods and for both polynomial order settings demonstrating high accuracy especially for the high polynomial order setting.

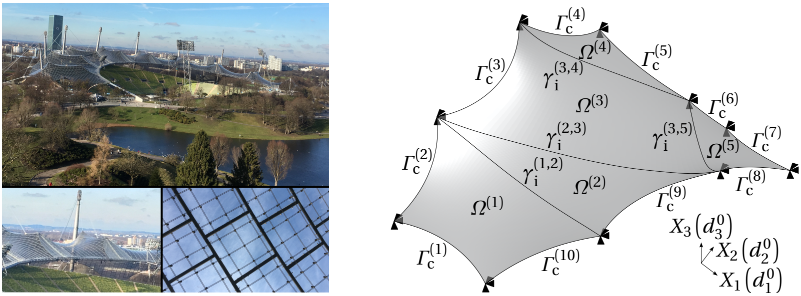

(a) Impression of the Munich's Olympic stadium and the middle sail of its roof.

(b) Multipatch geometry of the middle sail of the Olympic stadium roof in Munich.

Figure 4.15: Middle sail of the Olympic stadium roof in Munich: Problem setting.

Figs. 4.13 and 4.14 depict the deformation at time $t = 0.36$ s scaled by 10 and the contour of the first principal force field at time $t = 0.81$ s, respectively, for the reference single patch solution and the solution obtained using isogeometric analysis on multipatches with Penalty. The results show excellent agreement indicating the successful performance of both methods for these kinds of problems with emphasis on the Nitsche-type method.

4.2.2 Middle sail of the Olympic stadium roof in Munich

In this section the middle sail of the Olympic stadium roof in Munich is investigated, see Fig. 4.15. The roof of the Olympic stadium in Munich consists of nine sail-like structures. These are connected to each other on fixed locations at their boundaries which in turn are attached to pillars (Otto [74]). These pillars are herein assumed to be rigid and thus no interaction between the sails is expected. Therefore, only the middle sail's structural behaviour of this roof is herein considered. The prestressed middle sail consists of a cable net out of steel where plexiglas plates are mounted on it (detailed view is shown on bottom picture in Fig. 4.15(a)). The corresponding geometric model of the middle sail using five b-spline patches is shown in Fig. 4.15(b). For the assessment of the global structural behaviour, the very detailed structure is assumed to behave like a homogenized, prestressed membrane and this can be modelled by respective homogenized structural properties of a prestressed membrane roof with boundary embedded cables (Dieringer [75] and Philipp [76]). In this way, the plexiglas plates are assumed to have thickness $\bar{h}_{\text{plexiglas}} = 7 \times 10^{-3}$ m whereas they do not contribute to the structural stiffness of the prestressed roof but only to the mass with density $\rho_{\text{plexiglas}} = 500$ Kg/m^3. It is assumed that each of the inner cables has diameter equal to $\hat{D}_{\text{inner}} = 1.4 \times 10^{-2}$ m corresponding to cross sectional area $\hat{A}_{\text{inner}} = \pi\, \hat{D}^2_{\text{inner}}/4 = 4.9\, \pi \times 10^{-5}$ m^2. For each square of characteristic length $\bar{l} = 75 \times 10^{-2}$ m of the structure, four inner cables (two along each side of the characteristic square) are included. In this way, the homogenized thickness of the structure is given by $\bar{h} = \bar{h}_{\text{plexiglas}} + 2\, \hat{A}_{\text{inner}}/\bar{l}$. All steel cables are assumed to have Young's modulus and density of $E_{\text{steel}} = 210 \times 10^9$ Pa and $\rho_{\text{steel}} = 7850$ Kg/m^3, respectively. Then, the density of the membrane is homogenized by $\rho = 1.15(\rho_{\text{plexiglas}}\, \bar{h}_{\text{plexiglas}}\, \bar{l}^2 + 4\rho_{\text{steel}}\, \hat{A}_{\text{inner}}\, \bar{l})$, where 15% additional mass due to the hinges and other welding material is added. With respect to the stiffness of the sail, the homogenized Young's modulus of the sail is given as $E = 2\, E_{\text{steel}}\, \hat{A}_{\text{inner}}/(\bar{l}\, \bar{h})$. The cable net itself can be assumed having a negligible Poisson effect and as the plexiglas plates do not contribute to the structural stiffness of the sail, the Poisson's ratio is assumed to be zero. To obtain the desirable shape of equilibrium of the prestressed sail, the ratio between the area of the boundary cables and the thickness of the membrane is set to 10, that is, the boundary cables have cross sectional area of $\hat{A} = 10\bar{h}$. The diameter of the boundary cables is assumed to be $\hat{D}_{\text{outer}} = 5\, \hat{D}_{\text{inner}}$, that is, five times the diameter of the inner cables. However, this is not in accordance with the chosen value for the cross sectional area of the boundary cables and for this reason the Young's modulus and the density of the boundary cables are scaled with the ratio between the actual and the assigned value of the cross sectional area that is $\hat{E} = E_{\text{steel}}\, \pi\, \hat{D}^2_{\text{outer}}/(4\, \hat{A})$ and $\hat{\rho} = \rho_{\text{steel}}\, \pi\, \hat{D}^2_{\text{outer}}/(4\, \hat{A})$, respectively. To conclude, the homogenized membrane has Young's modulus, Poisson's ratio, density and thickness of $E = 1.1632 \times 10^{10}$ Pa, $\nu = 0$, $\rho = 1543.2968$ Kg/m^3 and $\bar{h} = 0.0074$ m, respectively. On the other hand, the boundary cables have Young's modulus, density and cross sectional area of $\hat{E} = 1.0905 \times 10^{10}$ Pa, $\hat{\rho} = 407.6693$ Kg/m^3 and $\hat{A} = 0.074$ m^2, respectively. The choice for the values of the prestresses for the membrane $n_0^{11} = n_0^{22} = n_0$ ($n_0^{12} = 0$) and the boundary cables $\hat{f}_0^{(i)}$ for obtaining the sail geometry as in Philipp [76] is

$n_0\,[\mathrm{N/m}]$	$\hat{f}_0^{(1)}$	$\hat{f}_0^{(2)}$	$\hat{f}_0^{(3)}$	$\hat{f}_0^{(4)}$	$\hat{f}_0^{(5)}$
2×10^8	$1680\hat{f}_0$	$1730\hat{f}_0$	$1595\hat{f}_0$	$1690\hat{f}_0$	$1350\hat{f}_0$
$n_0\,[\mathrm{N/m}]$	$\hat{f}_0^{(6)}$	$\hat{f}_0^{(7)}$	$\hat{f}_0^{(8)}$	$\hat{f}_0^{(9)}$	$\hat{f}_0^{(10)}$
2×10^8	$1250\hat{f}_0$	$1250\hat{f}_0$	$1575\hat{f}_0$	$1550\hat{f}_0$	$1845\hat{f}_0$

Table 4.1: Middle sail of the Olympic stadium roof in Munich: Definition of the prestress for the membrane and the boundary cables.

shown in Table 4.1 where $\hat{f}_0 = 4\times10^5$ N is a constant scaling of all prestress values for the boundary cables.

As accurate reference solution for the form-finding, the modal and the transient analysis, the solution of the same problem using 30312 linear triangular elements and the standard FEM is used. In Fig. 4.16(a) the reference configuration of the form-finding problem is shown.

Concerning the refinement study $\lceil 11\left(i_{\mathrm{r}}+4\right)/5\rceil$, $\lceil 7\left(i_{\mathrm{r}}+4\right)/5\rceil$, $\lceil 14\left(i_{\mathrm{r}}+4\right)/5\rceil$, $\lceil 3\left(i_{\mathrm{r}}+4\right)/5\rceil$ and $\lceil 12\left(i_{\mathrm{r}}+4\right)/5\rceil$ elements for patches $\Omega^{(1)}$, $\Omega^{(2)}$, $\Omega^{(3)}$, $\Omega^{(4)}$ and $\Omega^{(5)}$ are used, where the refinement index ranges as $i_{\mathrm{r}} = 1,\dots,12$. Accordingly, the discretizations and the form-found geometries along with the corresponding geometric errors for three selected refinements are depicted in Fig. 4.16. The corresponding parametrizations of the refinement sequence are depicted in Figs. 4.16(b)-4.16(d). As it can be seen at the corresponding figures, patches $\Omega^{(2)}$, $\Omega^{(4)}$ and $\Omega^{(5)}$ attain parametrization singularities as the corresponding patches are degenerated to triangles. Two polynomial order settings are accordingly used: The low polynomial order setting within which patches $\Omega^{(1)}$, $\Omega^{(3)}$, $\Omega^{(5)}$ are parametrized using piecewise C^0-continuous bilinear b-spline basis functions and patches $\Omega^{(2)}$, $\Omega^{(4)}$ using C^1-continuous biquadratic b-spline basis functions and the high polynomial order setting within which patches $\Omega^{(1)}$, $\Omega^{(3)}$, $\Omega^{(5)}$ are parametrized using piecewise C^1-continuous biquadratic b-spline basis functions and patches $\Omega^{(2)}$, $\Omega^{(4)}$ using C^2-continuous bicubic b-spline basis functions.

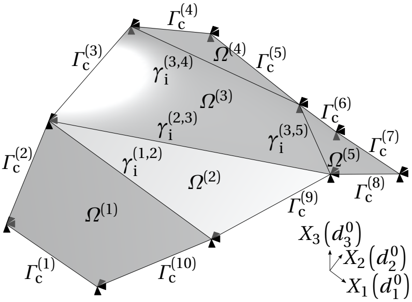

(a) Problem setting for the reference configuration of the form-finding analysis.

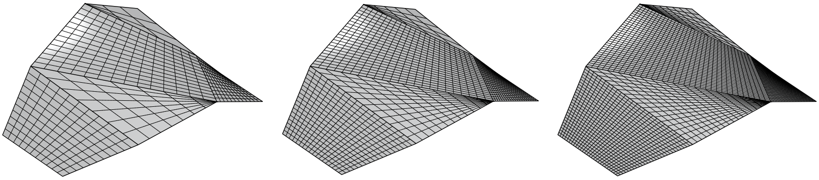

(b) Parametrization for refinement level $i_r = 1$. (c) Parametrization for refinement level $i_r = 4$. (d) Parametrization for refinement level $i_r = 8$.

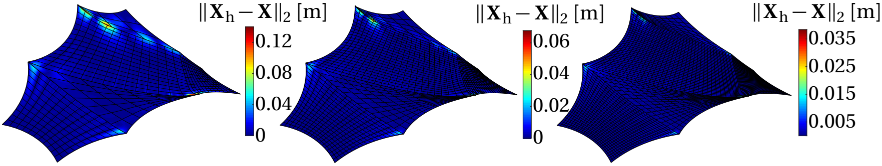

(e) Form-found multipatch geometry and error for $i_r = 1$. (f) Form-found multipatch geometry and error for $i_r = 4$. (g) Form-found multipatch geometry and error for $i_r = 8$.

Figure 4.16: Middle sail of the Olympic stadium roof in Munich: Problem setting for the form-finding analysis along with three selected NURBS parametrizations of three different refinement levels and the corresponding form-found geometries when using the Nitsche-type method.

In Figs. 4.16(e)- 4.16(g) the error distribution of the form-finding results is shown for three selected refinement levels when the Nitsche-type method is used. Clearly, the error decreases as the element size goes to zero and it can be observed that the highest levels of error are concentrated along the patch interfaces and, in particular, at the singularity locations, as ex-

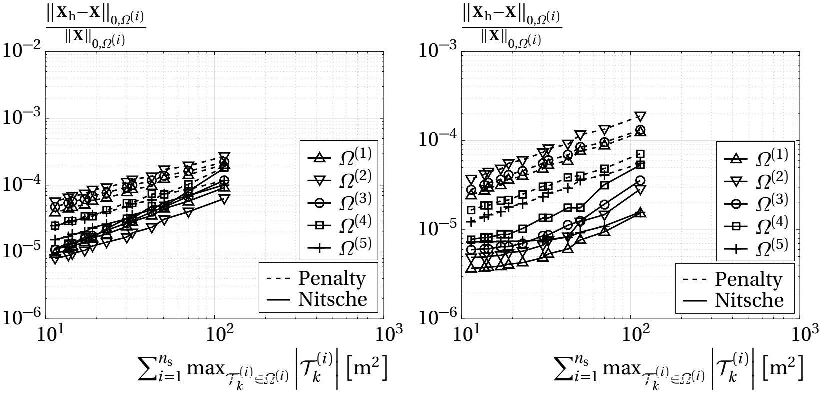

(a) Low polynomial order case.
(b) High polynomial order case.

Figure 4.17: Middle sail of the Olympic stadium roof in Munich: Relative error of the form-finding analysis for each patch.

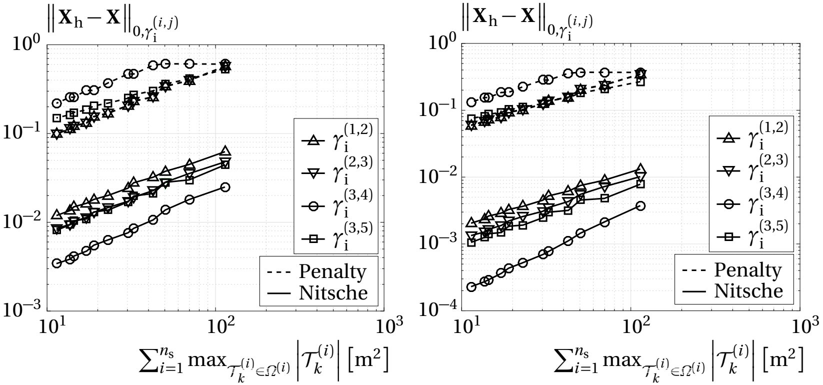

(a) Low polynomial order case.
(b) High polynomial order case.

Figure 4.18: Middle sail of the Olympic stadium roof in Munich: Error in the interface conditions of the form-finding analysis for individual patch interfaces.

pected. In Fig. 4.17 and Fig. 4.18, the relative error in the $\mathcal{L}^2\left(\Omega^{(i)}\right)$-norm for each patch and the absolute error along each patch interface in the $\mathcal{L}^2\left(\gamma_\mathrm{i}^{(i,j)}\right)$-norm is shown against the maximum element area for every

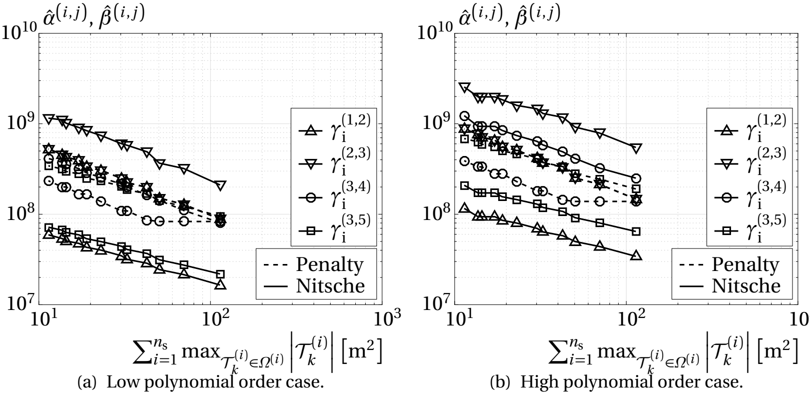

(a) Low polynomial order case. (b) High polynomial order case.

Figure 4.19: Middle sail of the Olympic stadium roof in Munich: Evolution of the Penalty and the stabilization parameters for each interface throughout refinement.

refinement level, respectively. Regarding the relative error in each patch, the Nitsche-type method outperforms the Penalty method in both the low and the high polynomial order settings. Concerning the absolute error along the interfaces, it can be seen that the Nitsche-type method once more outperforms the Penalty method for both the coarse and the fine settings.

In Fig. 4.19 the evolution of the Penalty and stabilization parameters for the Penalty and the Nitsche-type methods is shown for both the low and high polynomial order settings. Notwithstanding that the order of magnitude for the Penalty and the stabilization parameters concerning the Penalty and the Nitsche-type method, respectively, is of the same order, the Nitsche-type method provides significantly more accurate results than the Penalty method in terms of both the relative error in each patch and the absolute interface error. This confirms the superiority of Nitsche against the Penalty method in terms of accuracy for this kind of problems.

In Fig. 4.20 the evolution of the stabilization parameters of the Nitsche-type method for two selected refinement levels throughout the form-finding

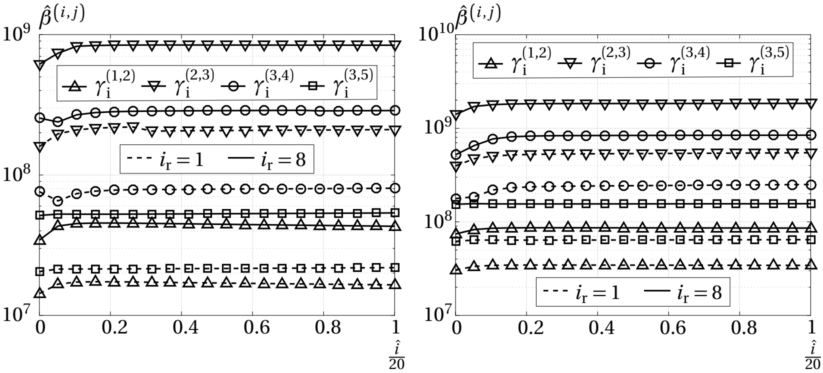

(a) Low polynomial order case. (b) High polynomial order case.

Figure 4.20: Middle sail of the Olympic stadium roof in Munich: Evolution of the stabilization parameters in Nitsche's method for each interface throughout form-finding iterations.

iterations is shown for both the low and the high polynomial order settings. It can be deduced that at the beginning of the form-finding iterations, where the shape of the sail is strongly modified, there is a notable change of the stabilization parameters which mostly tend to increase smoothly. It can be seen that as the form-finding iterations converge to a form-found shape, the corresponding stabilization parameters also converge to a constant value, which is expected.

Next, two multipatch isogeometric discretizations are chosen for the modal and the transient analysis (Fig. 4.22). Regarding the coarse setting, the h-refinement level $i_{\mathrm{r}} = 5$ and the low polynomial order setting is chosen whereas for the fine setting the h-refinement level $i_{\mathrm{r}} = 10$ and the high polynomial order setting as described above is chosen. The reference geometry of all isogeometric discretizations is computed using the URS form-finding method whereas the Nitsche-type method is employed for the multipatch coupling.

A modal analysis is performed based on the FEM mesh, the coarse and the fine isogeometric settings. The eigenmode shapes of eigenfrequencies f_1,

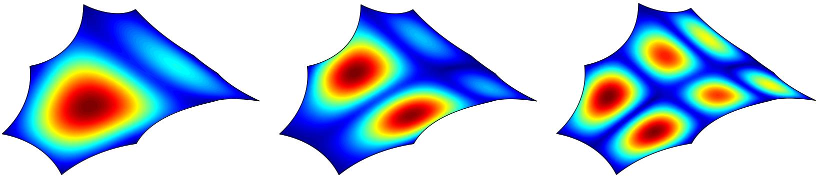

(a) $f_1 = 6.40$ Hz (FEM).

(b) $f_4 = 8.52$ Hz (FEM).

(c) $f_7 = 10.53$ Hz (FEM).

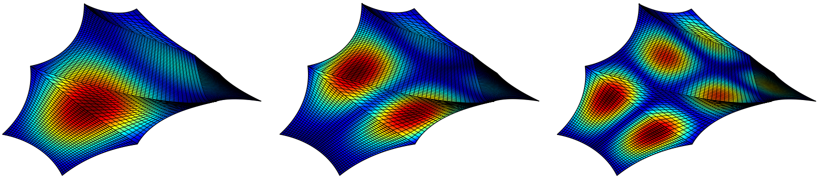

(d) $f_1^{\mathrm{h}} = 6.40$ Hz (IGA on multipatches with Nitsche).

(e) $f_4^{\mathrm{h}} = 8.52$ Hz (IGA on multipatches with Nitsche).

(f) $f_7^{\mathrm{h}} = 10.53$ Hz (IGA on multipatches with Nitsche).

Figure 4.21: Middle sail of the Olympic stadium roof in Munich: Mode shapes for the finite element discretization (upper row) and for the isogeometric analysis on multipatch surfaces using the Nitsche-type method (lower row) corresponding to refinement level $i_{\mathrm{r}} = 10$ and to the high polynomial order setting.

f_4 and f_7 for the FEM mesh and the multipatch isogeometric discretizations using Nitsche are shown in Fig. 4.21 using contours of the displacement field corresponding to each modal shape. The results show excellent agreement between the standard FEM and the isogeometric analysis on multipatch surfaces.

Fig. 4.22(a) shows the computed eigenfrequencies of the coarse and the fine isogeometric settings when using both methods scaled by the eigenfrequencies computed with the reference FEM model. The Nitsche-type method provides less accurate results than the Penalty method for the coarse case, a fact which is however corrected in the fine setting where the results of both methods match accurately the expected FEM solution.

Next, a geometrically nonlinear transient analysis of the prestressed sail with edge cables is performed. Concerning the transient analysis, the structure is left unloaded and its own weight is also considered negligible. Then,

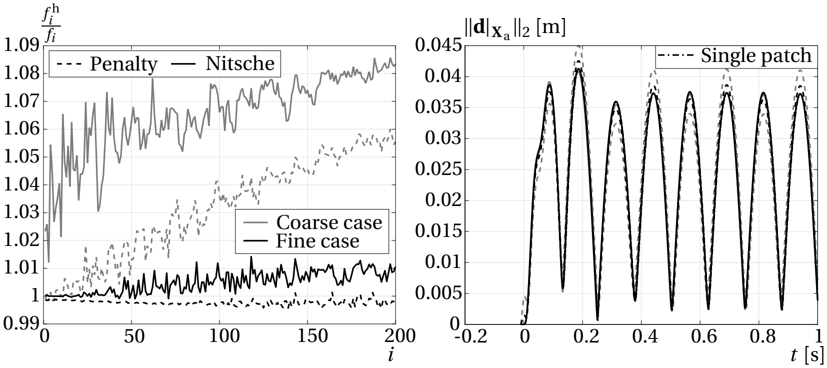

(a) Relative Error in the frequency spectrum.

(b) Time-displacement curves.

Figure 4.22: Middle sail of the Olympic stadium roof in Munich: Relative error in the computed eigenfrequencies and time-displacement curves.

a root point excitation of the structure is assumed for which the motion of all fixed corners is imposed as,

$$\mathbf{g}(t) = 0.03\sin(8\pi t)\,\mathbf{e}_2\,[\mathrm{m}]\,,\ \text{for all } t \in \mathbb{T}, \tag{4.13}$$

where the time span for this problem is chosen as $\mathbb{T} = [0, 1]$ s. The time step size for the coarse and the fine settings is chosen as $\varDelta t = 0.0013$ s and $\varDelta t = 0.001$ s, respectively. The time step size $\varDelta t = 0.001$ s is also chosen for the time discretization of the reference FEM solution. Since the imposition of the inhomogeneous Dirichlet boundary conditions is done strongly in this case, the admissible solution spaces for the test and unknown fields are not the same but the unknown displacement field needs to be chosen in such a way as to identically satisfy the motion at all fixed corners, see Hughes et al. [70] for more information. For the estimation of the Rayleigh damping parameters according to Eqs. (2.70) the eigenfrequencies $f_1 = 6.403$ Hz and $f_2 = 7.209$ Hz from the reference FEM model are used resulting in $\alpha_{\mathrm{r}} = 4.2616\ \mathrm{s}^{-1}$ and $\beta_{\mathrm{r}} = 0.0023$ s for the Rayleigh damping parameters. As inspection point, the material point with coordinates $\mathbf{X}_{\mathrm{a}} = 47.9297\,\mathbf{e}_1 + 121.3484\,\mathbf{e}_2 + 35.1936\,\mathbf{e}_3$ [m] is used. This point is chosen as a node in the FEM mesh which is subsequently projected onto both isogeometric multipatch settings in order to get the closest point

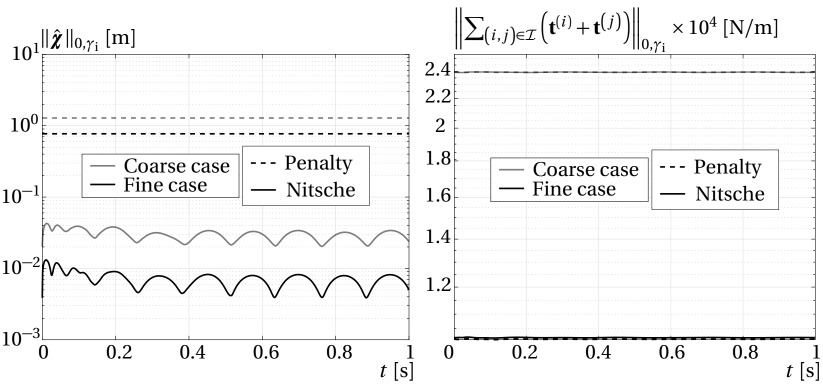

(a) Evolution of the error in the displacement interface condition.

(b) Evolution of the error in the traction interface condition.

Figure 4.23: Middle sail of the Olympic stadium roof in Munich: Evolution of the error in the Dirichlet and Neumann interface conditions over the simulation time.

projections as the FEM and the multipatch isogeometric models are not identical in the form-found state.

The 2-norm of the displacement $\|\mathbf{d}|_{\mathbf{X}_{\mathrm{a}}}\|_2$ is then computed and compared throughout the simulation time between each isogeometric multipatch setting and the FEM reference mesh and the results are summarized in Fig. 4.22(b). The legends are the same as in Fig. 4.22(a) and are not repeated in Fig. 4.22(b) not to overshadow the time-displacement curves. For the coarse setting, it can be seen that the Nitsche-type method is significantly more accurate than the Penalty method. The time-displacement curve corresponding to the Nitsche-type method overlaps with the finite element solution for the fine setting. The Penalty method on the other hand overestimates the displacement magnitude at the inspection point for the coarse setting. However, the corresponding results are considerably improved for the fine setting concerning the Penalty method, which are however still less accurate as for the Nitsche-type method.

Furthermore, Fig. 4.23 shows the evolution of the error in the Dirichlet and Neumann interface conditions in the $\mathcal{L}^2(\gamma_{\mathrm{i}})$-norm (Eqs. (3.8a) and (3.8b),

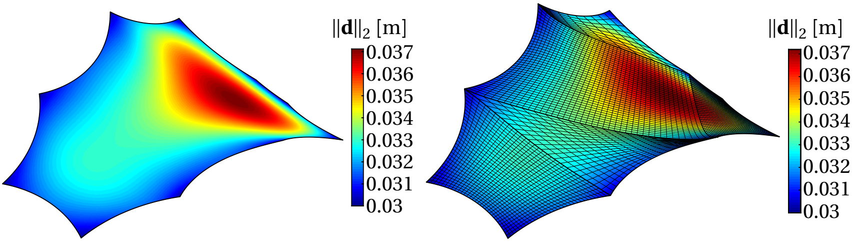

(a) Displacement norm (FEM).

(b) Displacement norm (IGA on multipatches with Nitsche).

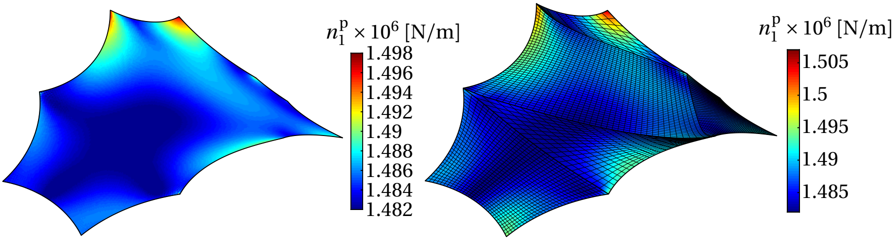

(c) First principal force (FEM).

(d) First principal force (IGA on multipatches with Nitsche).

Figure 4.24: Middle sail of the Olympic stadium roof in Munich: Displacement norm and first principal stress-resultant force contour at $t = 0.44$ s for the FEM and IGA multipatch models.

respectively) against the time. Concerning the evolution of the error in the interface Dirichlet condition, the Nitsche-type method clearly outperforms the Penalty method for both settings. Concerning the interface Neumann condition, the Nitsche-type method delivers more accurate results than the Penalty method.

In Fig. 4.24 the contour of the displacement 2-norm $\|\mathbf{d}\|_2$ and the distribution of the first principal stress-resultant force field n_1^{p} in the local Cartesian space is shown at the time instance $t = 0.44$ s using FEM and isogeometric analysis on multipatch surfaces with Nitsche. As it can be deduced from the illustration, the results are highly accurate in terms of both the displacement field itself and the stress-resultant force field.

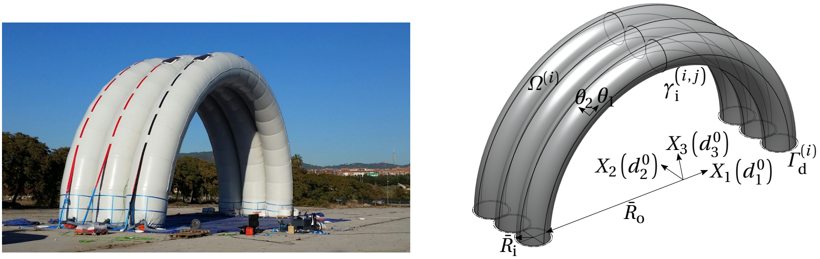

(a) Picture of an inflatable hangar `www.cimne.com/websasp/ulites/news.asp` (online on 31.01.2019).

(b) Multipatch geometry.

Figure 4.25: Inflatable hangar: Problem setting.

4.2.3 Inflatable hangar

Lastly, an inflatable hangar is considered in the context of practically relevant applications. The structure consists of three semi-torus shaped tubes, see Fig. 4.25. A picture of the hangar and its underlying CAD model with boundary conditions are shown in Figs. 4.25(a) and 4.25(b), respectively. Each tube is connected to its neighbouring tube(s) through the shared interface making the structure coherent. The tubes are coming into contact tangentially to each other, thus sharing a common curved interface. For each semi-torus tube, the inner and the overall radii are given as $\bar{R}_{\mathrm{i}} = 1.25$ m and $\bar{R}_{\mathrm{o}} = 10$ m, respectively. The Young's modulus, the Poisson's ratio, the density and the thickness of the membrane are given as $E = 3.1 \times 10^8$ Pa, $\nu = 0.3$, $\rho = 1250$ Kg/m^3 and $\bar{h} = 6 \times 10^{-4}$ m, respectively (Wüchner et al. [77]). The inner pressure for keeping the inflated structure in equilibrium is modelled by a follower load $\mathbf{b} = \mathbf{a}_3$ [KPa], where $\mathbf{a}_3$ stands for the outward surface normal vector in the current configuration. The corresponding NURBS multipatch CAD model consists of 24 patches $\Omega^{(i)}$ with 24 Dirichlet boundaries $\Gamma_{\mathrm{d}}^{(i)}$ at the ground and 52 interface boundaries $\gamma_{\mathrm{i}}^{(i)}$. The torus structure needs an inhomogeneous anisotropic prestress state with zero shear stress components due to its different radii of curvature along its principal curvature directions. Therefore, the prestress values which need to be applied such that the structure remains in equilibrium under the

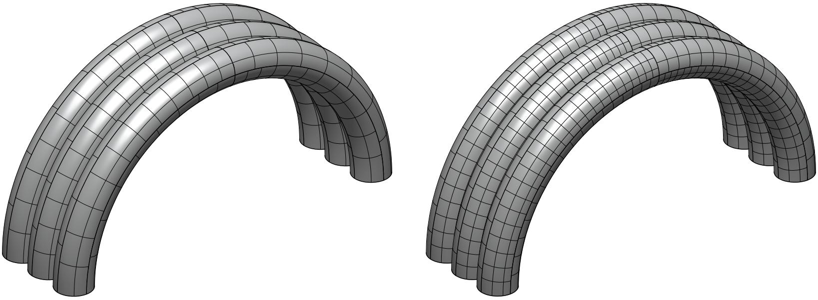

(a) Coarse isogeometric discretization. (b) Fine isogeometric discretization.

Figure 4.26: Inflatable hangar: Coarse and fine multipatch NURBS parametrizations.

given internal pressure are,

$$n_0^{11} = \frac{\|\mathbf{b}\|_2 \bar{R}_\mathrm{i}}{2\bar{h}}\,, \tag{4.14a}$$

$$n_0^{22} = n_0^{11} \frac{2\bar{R} + \bar{R}_\mathrm{i} \sin\theta_2}{\bar{R} + \bar{R}_\mathrm{i} \sin\theta_2}\,, \tag{4.14b}$$

and $n_0^{12} = 0$, see in Fryer et al. [78], where $(\theta_1, \theta_2) \in [0, \pi] \times [0, 2\pi]$ stands for the principal curvature directions of the half torus-shaped tubes depicted in Fig. 4.25(b) and $\bar{R} = \bar{R}_\mathrm{o} + \bar{R}_\mathrm{i}$. Prestress components n_0^{11}, n_0^{22} are defined along the principal curvature directions θ_1 and θ_2, respectively.

For this example, no form-finding analysis is performed as the reference equilibrium configuration is obtained using the aforementioned values for the prestress and the exact geometry of the inflated half torus-shaped tubes which represent the inflatable hangar. Similar to the previous numerical examples, two isogeometric discretizations are considered and the corresponding results are compared against the reference FEM solution when the same roof structure is solved using C^0-continuous bilinear elements. Two isogeometric computational models are herein considered, see Fig. 4.26. For both settings adjacent patches are parametrized using different polynomial orders for the corresponding NURBS basis functions. The coarse setting in Fig. 4.26(a) consists of patches with C^1-continuous

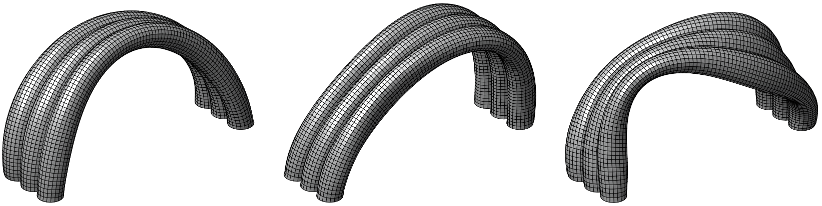

(a) $f_1 = 1.74$ Hz (FEM). (b) $f_2 = 2.05$ Hz (FEM). (c) $f_4 = 3.5$ Hz (FEM).

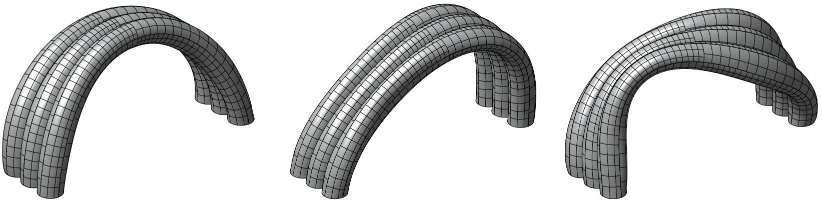

(d) $f_1^{\mathrm{h}} = 1.74$ Hz (IGA on multipatches with Nitsche). (e) $f_2^{\mathrm{h}} = 2.07$ Hz (IGA on multipatches with Nitsche). (f) $f_4^{\mathrm{h}} = 3.52$ Hz (IGA on multipatches with Nitsche).

Figure 4.27: Inflatable hangar: Comparison of selected mode shapes between the reference FEM solution and the NURBS multipatch solution using the Nitsche-type method.

biquadratic NURBS basis functions for all patches and the fine setting in Fig. 4.26(b) consists of patches with C^1-continuous biquadratic and C^2-continuous bicubic NURBS basis functions.

As in the previous examples, also here modal and transient analyses are performed (Fig. 4.28). The modal analysis is performed for both the coarse and the fine settings of the isogeometric multipatch discretizations and for the reference finite element solution. The corresponding mode shapes of eigenfrequencies f_1, f_2 and f_4 for the reference FEM solution and the fine setting using the Nitsche-type method are shown in Fig. 4.27, where excellent agreement of the results between the isogeometric analysis on multipatch surfaces and the reference FEM solution is exhibited. The computed eigenfrequencies of the coarse and the fine settings scaled by the eigenfrequencies of the reference FEM solution are shown in Fig. 4.28(a). The Penalty method outperforms the Nitsche-type method for the coarse setting, whereas both methods provide satisfactory results of comparable

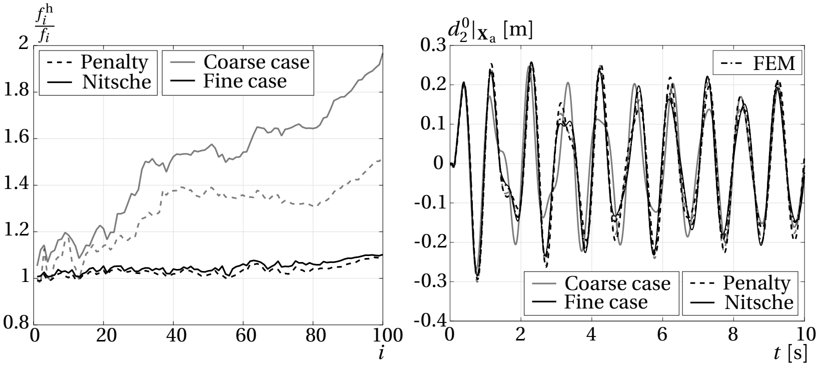

(a) Relative error in the frequency spectrum.

(b) Time-displacement curves.

Figure 4.28: Inflatable hangar: Relative error in the computed eigenfrequencies and time-displacement curves.

accuracy for the fine setting.

In the same manner as for the previous numerical examples, a transient analysis of the inflated structure is performed. Concerning the Rayleigh damping, the values $\alpha_r = 0.1177$ and $\beta_r = 0.0014$ are assigned (Wüchner et al. [77]). The time span of the simulation is $\mathbb{T} = [0, 10]$ s and a root point excitation of the structure is considered. In this way a motion along Γ_d is imposed as,

$$\mathbf{g}(t) = 10^{-3} \sin(10\pi t)\, \mathbf{e}_1 + 10^{-1} \sin(2\pi t)\, \mathbf{e}_2 + 10^{-4} \sin(5\pi t)\, \mathbf{e}_3\,. \quad (4.15)$$

The time step size for the reference finite element mesh, the coarse and the fine settings are chosen as $\Delta t = 10^{-3}$ s, $\Delta t = 0.00125$ s and $\Delta t = 0.01$ s, respectively. An inspection point on the structure is chosen $\mathbf{X}_a = 0.3655\mathbf{e}_1 + -1.18882\mathbf{e}_2 + 11.63053\mathbf{e}_3$ $[m]$ and the displacement component along the X_2-Cartesian axis is investigated. In Fig. 4.28(b) it is shown the displacement component $d_2^0|_{\mathbf{X}_a}$ for the coarse and the fine setting of the multipatch isogeometric discretization and the FEM mesh. The results show highly satisfactory agreement with the reference solution while the finer the discretization becomes the better the results are. However, also in this example, the results from the isogeometric analysis on multipatches with Penalty were found to be worse in terms of the amplitude when compared

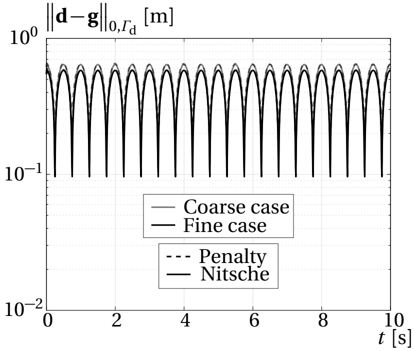

(a) Evolution of the Dirichet condition.

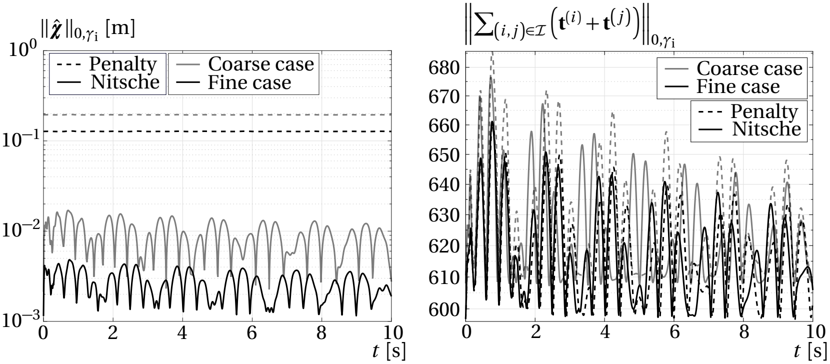

(b) Evolution of the displacement interface condition.

(c) Evolution of the traction interface condition.

Figure 4.29: Inflatable hangar: Evolution of the Dirichlet and interface conditions throughout the time.

with Nitsche especially for the coarse setting. Subsequently, the error in the Dirichlet and in the interface conditions along $\mathit{\Gamma}_\mathrm{d}$ and γ_i, respectively, is studied, see Fig. 4.29. The evolution of the error in the Dirichlet condition along $\mathit{\Gamma}_\mathrm{d}$, the patch interface Dirichlet condition and the patch interface Neumann condition throughout the simulation time are depicted in Fig. 4.29(a), Fig. 4.29(b) and Fig. 4.29(c), respectively. Concerning the error along the Dirichlet boundary $\mathit{\Gamma}_\mathrm{d}$ the Penalty and the Nitsche-type methods perform similarly. The Nitsche-type method produces more accurate results with respect to the satisfaction of the patch interface Dirichlet and

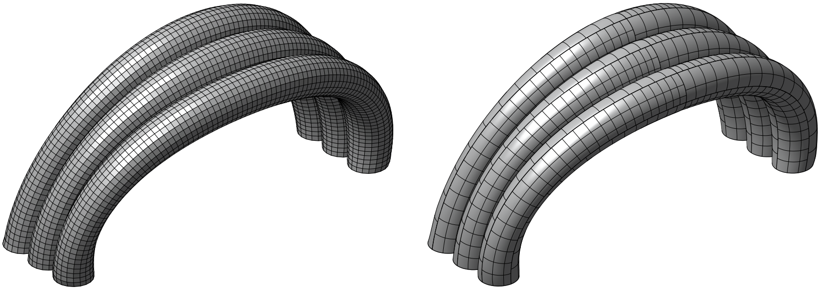

(a) FEM. (b) IGA on multipatches with Nitsche.

Figure 4.30: Inflatable hangar: Scaled by 20 deformation at at time $t = 2.65$ s for both the FEM and the multipatch isogeometric computational models.

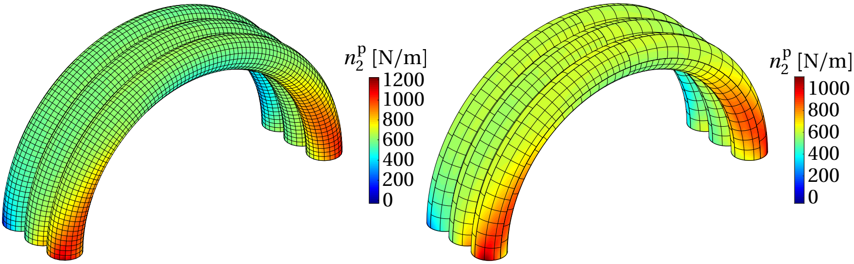

(a) FEM. (b) IGA on multipatches with Nitsche.

Figure 4.31: Inflatable hangar: 2nd principal force n_2 contour at different time $t = 6.23$ s for both the FEM and the multipatch isogeometric computational models.

Neumann conditions in both the coarse and the fine settings compared to the Penalty method.

Figs. 4.30 and 4.31 show the scaled by 20 deformation at time $t = 2.65$ s and the contour of the second principal stress-resultant force n_2^p at time $t = 6.23$ s, respectively, for both the finite element and the IGA on multipatches with Nitsche models. The results of the isogeometric analysis on multipatches show excellent agreement to the reference FEM solution.

4.3 Concluding remarks

In this chapter, the application of the Penalty and Nitsche-type methods for the multipatch coupling and enforcement of weak Dirichlet boundary conditions in the context of isogeometric membrane analysis on multipatches is demonstrated. At first, the extensions of the weak forms introduced in Sec. 3.3 to account for weak Dirichlet boundary conditions is shown for the two chosen methods. Subsequently, three examples are used as demonstration: One well-established benchmark example, that of the four-point, where a full framework consisting of form-finding using the URS on the CAD model, modal analysis and subsequently geometrically nonlinear transient analysis is performed. The results are compared to a single patch solution. Lastly, the practically relevant examples of the middle sail of the Olympic stadium roof in Munich and an inflatable hangar are used for the demonstration of the applicability of the proposed methods in the context of real world engineering problems. The Nitsche-type method was found to be superior as compared to the Penalty method for this kind of problems for all analyses herein considered.

Chapter 5

Isogeometric Kirchhoff-Love Shell Analysis on Multipatches

Kirchhoff-Love shell structures constitute an important category of thin shells, their main benefit being that the underlying formulation is purely displacement-based. The latter comes in the price that the variational index of the corresponding weak form raises to two, in other words at least C^1-continuous functions for the discretization are needed, see in Başar et al. [1]. Isogeometric analysis is then perfectly suited for the numerical approximation of such problems as the underlying NURBS basis functions are typically smooth. The underlying CAD geometry typically comprises multiple trimmed patches, see Chap. 3, and thus the continuity of the solution across neighbouring patches needs to be addressed. Moreover, parametric singularities and locations with C^0-continuity (e.g. kinks in the geometry) need to be also addressed. The Penalty and the Lagrange Multipliers methods are chosen for the multipatch coupling following Apostolatos et al. [40]. Then, a series of benchmark examples are used and the NREL Phase VI wind turbine with two flexible blades, see in Simms et al. [7], is chosen for demonstrating the extension of the proposed methodology in industrial scale applications.

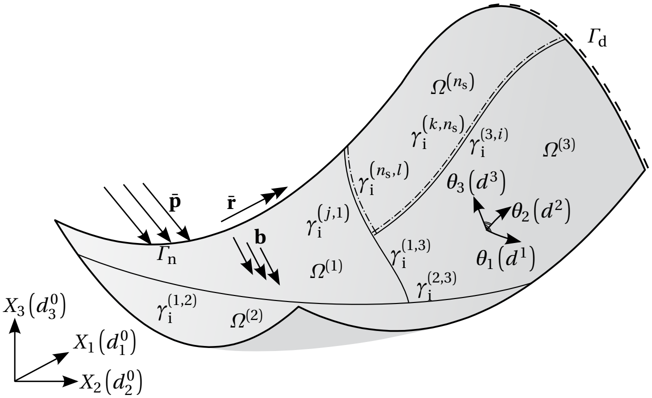

Figure 5.1: Problem placement: Domain decomposition of the shell's surface.

5.1 Theory

The *initial Boundary Value Problem* (iBVP) and the corresponding weak form of equilibrium for the Kirchhoff-Love shell problem is discussed in Sec. 2.3.2 whereas IGA on multipatches is demonstrated in Sec. 3.3. Therefore, this chapter discusses only the extensions of the weak forms and the corresponding discrete equation systems arising from the application of the Penalty and the Lagrange Multipliers methods for the multipatch coupling for this type of problems.

5.1.1 Problem placement

Herein Ω represents a flexible surface whose mechanical behaviour is governed by the Kirchhoff-Love shell theory, see Sec. 2.3.2. Assuming the decomposition of Ω defined in Eqs. (3.7), iBVP in Eqs. (2.42) holds at each patch $\Omega^{(i)}$. Therefore, also the rotation field in Eq. (2.40) needs to be continuous across the neighbouring patches $\Omega^{(i)}$ and $\Omega^{(j)}$ in addition to the displacement continuity in Eq. (3.8a), that is,

$$\boldsymbol{\omega}^{(i)} + \boldsymbol{\omega}^{(j)} = \mathbf{0}\,, \tag{5.1}$$

along $\gamma_{\mathrm{i}}^{(i,j)}$ for all $(i, j) \in \mathcal{I}$. It is important to note that the rotation continuity condition in Eq. (5.1) implies that the interface tangent and normal to boundaries $\partial\Omega^{(i)}\cap\gamma_{\mathrm{i}}^{(i,j)}$ and $\partial\Omega^{(j)}\cap\gamma_{\mathrm{i}}^{(i,j)}$ vectors in Eqs. (2.3.2), namely $\hat{\mathbf{e}}_{\mathrm{n}}^{(i)},\hat{\mathbf{e}}_{\mathrm{t}}^{(i)}$ and $\hat{\mathbf{e}}_{\mathrm{n}}^{(j)},\hat{\mathbf{e}}_{\mathrm{t}}^{(j)}$, respectively, have opposite to each other directions. Evidently, the interface normal and the tangent vectors to the interface boundaries from the neighbouring patches in industrial CAD geometries are not necessarily aligned since the physical images of the interface boundaries are not necessarily identical, see Sec. 3.2.2. However, this causes no problem to the proposed methodology as it is shown in Breitenberger et al. [6] where ‘‘dirty’’ CAD geometries are successfully dealt with. The aforementioned problem is depicted in Fig. 5.1 along with the corresponding Dirichlet and Neumann boundary conditions. In the sequel, the interface rotation jump is denoted by $\tilde{\boldsymbol{\chi}}$, that is, $\boldsymbol{\omega}^{(i)}+\boldsymbol{\omega}^{(j)}=\tilde{\boldsymbol{\chi}}^{(i,j)}=\tilde{\boldsymbol{\chi}}|_{\gamma_{\mathrm{i}}^{(i,j)}}$, similar to the displacement jump defined in Sec. 3.3.

5.1.2 Penalty method

The weak form of the Penalty method defined in Eq. (3.15) is extended by an additional Penalty term with associated Penalty parameter $\tilde{\alpha}:\gamma_{\mathrm{i}}\rightarrow\mathbb{R}_{+}^{\star}$ and the corresponding weak form of equilibrium in Eq. (2.45) for the Kirchhoff-Love shell analysis, becomes: Find the displacement field $\mathbf{d}\in\boldsymbol{\mathcal{V}}$ for each time instance $t\in\mathbb{T}$ with $\hat{\boldsymbol{\chi}},\tilde{\boldsymbol{\chi}}\in\boldsymbol{\mathcal{L}}^2(\gamma_{\mathrm{i}})$ such that,

$$\begin{gathered}\left\langle\delta\mathbf{d},\rho\bar{h}\ddot{\mathbf{d}}\right\rangle_{0,\Omega_{\mathrm{d}}}+\left\langle\delta\mathbf{d},c\bar{h}\dot{\mathbf{d}}\right\rangle_{0,\Omega_{\mathrm{d}}}+\\ a(\delta\mathbf{d},\mathbf{d})+\left\langle\delta\hat{\boldsymbol{\chi}},\hat{\alpha}\,\hat{\boldsymbol{\chi}}\right\rangle_{0,\gamma_{\mathrm{i}}}+\left\langle\delta\tilde{\boldsymbol{\chi}},\tilde{\alpha}\,\tilde{\boldsymbol{\chi}}\right\rangle_{0,\gamma_{\mathrm{i}}}=l(\delta\mathbf{d})\,,\end{gathered}\tag{5.2}$$

for all $\delta\mathbf{d}\in\boldsymbol{\mathcal{V}}$ with $\delta\hat{\boldsymbol{\chi}},\delta\tilde{\boldsymbol{\chi}}\in\boldsymbol{\mathcal{L}}^2(\gamma_{\mathrm{i}})$. In this way, the corresponding discrete equation system with Penalty (Eq. (3.16)) becomes,

$$\begin{gathered}\begin{bmatrix}\mathbf{K}_{\mathrm{d}}^{(1)}+\hat{\mathbf{C}}_{\hat{\alpha}}^{(1)}+\tilde{\mathbf{C}}_{\tilde{\alpha}}^{(1)} & \cdots & \hat{\mathbf{C}}_{\hat{\alpha}}^{(1,n_{\mathrm{s}})}+\tilde{\mathbf{C}}_{\tilde{\alpha}}^{(1,n_{\mathrm{s}})}\\ \vdots & \ddots & \vdots\\ \hat{\mathbf{C}}_{\hat{\alpha}}^{(n_{\mathrm{s}},1)}+\tilde{\mathbf{C}}_{\tilde{\alpha}}^{(n_{\mathrm{s}},1)} & \cdots & \mathbf{K}_{\mathrm{d}}^{(n_{\mathrm{s}})}+\hat{\mathbf{C}}_{\hat{\alpha}}^{(n_{\mathrm{s}})}+\tilde{\mathbf{C}}_{\tilde{\alpha}}^{(n_{\mathrm{s}})}\end{bmatrix}\Delta_{\hat{n},\hat{\imath}}\begin{bmatrix}\hat{\mathbf{d}}^{(1)}\\ \vdots\\ \hat{\mathbf{d}}^{(n_{\mathrm{s}})}\end{bmatrix}=\\ \begin{bmatrix}\mathbf{R}_{\mathrm{d}}^{(1)}+\hat{\mathbf{R}}_{\hat{\alpha}}^{(1)}+\tilde{\mathbf{R}}_{\tilde{\alpha}}^{(1)}\\ \vdots\\ \mathbf{R}_{\mathrm{d}}^{(n_{\mathrm{s}})}+\hat{\mathbf{R}}_{\hat{\alpha}}^{(n_{\mathrm{s}})}+\tilde{\mathbf{R}}_{\tilde{\alpha}}^{(n_{\mathrm{s}})}\end{bmatrix},\end{gathered}\tag{5.3}$$

where $\tilde{\alpha}^{(i,j)} = \tilde{\alpha}_{|_{\gamma_\mathrm{i}^{(i,j)}}}$. Matrices $\tilde{\mathbf{C}}_{\tilde{\alpha}}^{(i)}, \tilde{\mathbf{C}}_{\tilde{\alpha}}^{(i,j)}$ and vectors $\tilde{\mathbf{R}}_{\tilde{\alpha}}^{(i)}$ are given similar to Eqs. (3.17), namely,

$$\tilde{C}_{\tilde{\alpha}(k,r)}^{(i)} = \sum_{j=1, j\neq i}^{n_\mathrm{s}} \left\langle \boldsymbol{\omega}^{(i)}\left(\bar{\boldsymbol{\phi}}_k^{(i)}\right), \tilde{\alpha}^{(i,j)} \boldsymbol{\omega}^{(i)}\left(\bar{\boldsymbol{\phi}}_r^{(i)}\right)\right\rangle_{0,\gamma_\mathrm{i}^{(i,j)}}, \tag{5.4a}$$

$$\tilde{C}_{\tilde{\alpha}(k,r)}^{(i,j)} = \left\langle \boldsymbol{\omega}^{(i)}\left(\bar{\boldsymbol{\phi}}_k^{(i)}\right), \tilde{\alpha}^{(i,j)} \boldsymbol{\omega}^{(j)}\left(\bar{\boldsymbol{\phi}}_r^{(j)}\right)\right\rangle_{0,\gamma_\mathrm{i}^{(i,j)}}, \tag{5.4b}$$

$$\tilde{\mathbf{R}}_{\tilde{\alpha}}^{(i)} = \tilde{\mathbf{C}}_{\tilde{\alpha}}^{(i)} \hat{\mathbf{d}}_{\hat{n},\hat{\imath}}^{(i)} + \sum_{j=1, j\neq i}^{n_\mathrm{s}} \tilde{\mathbf{C}}_{\tilde{\alpha}}^{(i,j)} \hat{\mathbf{d}}_{\hat{n},\hat{\imath}}^{(j)}. \tag{5.4c}$$

This straightforward extension of weak form in Eq. (3.16) to account for the continuity requirements within Kirchhoff-Love shell analysis proves highly beneficial since the original problem remains coercive provided that not too large values for the Penalty parameters are chosen. Herein, the Penalty parameters $\hat{\alpha}$ and $\tilde{\alpha}$ are chosen as a scaling of the matrix norms $||\mathbf{D}_\mathrm{m}||_\mathrm{F}$ and $||\mathbf{D}_\mathrm{b}||_\mathrm{F}$ corresponding to the material matrices for the membrane and the bending stiffness of the Kirchhoff-Love shell, respectively (see Appx. A).

5.1.3 Lagrange Multipliers method

The application of the Lagrange Multipliers method for the continuity enforcement in isogeometric Kirchhoff-Love shell analysis on multipatches is herein performed using an additional Lagrange Multipliers field $\boldsymbol{\mu}$ across the interface boundary γ_i. In this way, weak form in Eq. (3.18) combined with the weak form of equilibrium of the Kirchhoff-Love shell in Eq. (2.45) results in: Find $\mathbf{d} \in \boldsymbol{\mathcal{V}}$ with $\hat{\boldsymbol{\chi}}, \tilde{\boldsymbol{\chi}} \in \boldsymbol{\mathcal{L}}^2(\gamma_\mathrm{i})$ and $\boldsymbol{\lambda}, \boldsymbol{\mu} \in \boldsymbol{\mathcal{L}}^2(\gamma_\mathrm{i})$ such that,

$$\begin{gathered} \left\langle \delta\mathbf{d}, \rho \bar{h} \ddot{\mathbf{d}} \right\rangle_{0,\Omega_\mathrm{d}} + \left\langle \delta\mathbf{d}, c \bar{h} \dot{\mathbf{d}} \right\rangle_{0,\Omega_\mathrm{d}} + a(\delta\mathbf{d}, \mathbf{d}) \\ + \left\langle \delta\hat{\boldsymbol{\chi}}, \boldsymbol{\lambda} \right\rangle_{0,\gamma_\mathrm{i}} + \left\langle \delta\boldsymbol{\lambda}, \hat{\boldsymbol{\chi}} \right\rangle_{0,\gamma_\mathrm{i}} + \left\langle \delta\tilde{\boldsymbol{\chi}}, \boldsymbol{\mu} \right\rangle_{0,\gamma_\mathrm{i}} + \left\langle \delta\boldsymbol{\mu}, \tilde{\boldsymbol{\chi}} \right\rangle_{0,\gamma_\mathrm{i}} = l(\delta\mathbf{d}), \end{gathered} \tag{5.5}$$

for all $\delta\mathbf{d} \in \boldsymbol{\mathcal{V}}$ with $\delta\hat{\boldsymbol{\chi}}, \delta\tilde{\boldsymbol{\chi}} \in \boldsymbol{\mathcal{L}}^2(\gamma_\mathrm{i})$ and for all $\delta\boldsymbol{\lambda}, \delta\boldsymbol{\mu} \in \boldsymbol{\mathcal{L}}^2(\gamma_\mathrm{i})$. Let $\tilde{\boldsymbol{\mathcal{V}}}_\mathrm{h} \subset \boldsymbol{\mathcal{L}}^2(\gamma_\mathrm{i})$ be the finite dimensional space for Lagrange Multipliers field $\boldsymbol{\mu}$. Similar to space $\hat{\boldsymbol{\mathcal{V}}}_\mathrm{h}$ defined in Sec. 3.3.4, space $\tilde{\boldsymbol{\mathcal{V}}}_\mathrm{h}$ is also constructed as $\tilde{\boldsymbol{\mathcal{V}}}_\mathrm{h} = \prod_{(i,j)\in\mathcal{I}} \tilde{\boldsymbol{\mathcal{V}}}_\mathrm{h}^{(i,j)}$ where $\boldsymbol{\mu}^{(i,j)} = \boldsymbol{\mu}_{|_{\gamma_\mathrm{i}^{(i,j)}}} \in \tilde{\boldsymbol{\mathcal{V}}}_\mathrm{h}^{(i,j)}$ and moreover the choice $\hat{\boldsymbol{\mathcal{V}}}_\mathrm{h}, \tilde{\boldsymbol{\mathcal{V}}}_\mathrm{h} \subset \boldsymbol{\mathcal{P}}_0\left(\gamma_\mathrm{i}^{(i,j)}\right)$ is herein employed, $\boldsymbol{\mathcal{P}}_0\left(\gamma_\mathrm{i}^{(i,j)}\right)$ being the space of all constant vector functions along $\gamma_{\mathrm{i}}^{(i,j)}$. In this way, given a basis of each $\tilde{\boldsymbol{\mathcal{V}}}_{\mathrm{h}}^{(i,j)}$, namely, $\tilde{\boldsymbol{\phi}}_{k}^{(i,j)}$ with $k=1,\ldots,\dim\tilde{\boldsymbol{\mathcal{V}}}_{\mathrm{h}}^{(i,j)}$ one has,

$$\boldsymbol{\mu}=\sum_{(i,j)\in\mathcal{I}}\;\sum_{k=1}^{\dim\tilde{\boldsymbol{\mathcal{V}}}_{\mathrm{h}}^{(i,j)}}\tilde{\boldsymbol{\phi}}_{k}^{(i,j)}\hat{\mu}_{k}^{(i,j)}\,, \tag{5.6}$$

$\hat{\mu}_{k}^{(i,j)}$ being the DOFs of the additional Lagrange Multipliers discretization. It is important to note that spaces $\hat{\boldsymbol{\mathcal{V}}}_{\mathrm{h}}^{(i,j)}$ and $\tilde{\boldsymbol{\mathcal{V}}}_{\mathrm{h}}^{(i,j)}$ are not necessarily the same but may differ thus allowing for different Lagrange Multipliers discretizations for $\boldsymbol{\lambda}$ and $\boldsymbol{\mu}$. In this way, the discrete equation system in Eq. (3.19) becomes,

$$\begin{bmatrix} \mathbf{K}_{\mathrm{d}}^{(1)} & \cdots & \mathbf{0} & & \\ \vdots & \ddots & \vdots & \boldsymbol{\Lambda} & \boldsymbol{\mathcal{M}} \\ \mathbf{0} & \cdots & \mathbf{K}_{\mathrm{d}}^{(n_{\mathrm{s}})} & & \\ & \boldsymbol{\Lambda}^{\mathrm{T}} & & \mathbf{0} & \mathbf{0} \\ & \boldsymbol{\mathcal{M}}^{\mathrm{T}} & & \mathbf{0} & \mathbf{0} \end{bmatrix} \Delta_{\hat{n},\hat{\imath}} \begin{bmatrix} \hat{\mathbf{d}}^{(1)} \\ \vdots \\ \hat{\mathbf{d}}^{(n_{\mathrm{s}})} \\ \hat{\boldsymbol{\lambda}} \\ \hat{\boldsymbol{\mu}} \end{bmatrix} = \\ -\begin{bmatrix} \mathbf{R}_{\mathrm{d}}^{(1)}+\sum_{(1,j)\in\mathcal{I}}\left(\boldsymbol{\Lambda}^{(1,j)}\hat{\boldsymbol{\lambda}}_{\hat{n},\hat{\imath}}^{(1,j)}+\boldsymbol{\mathcal{M}}^{(1,j)}\hat{\boldsymbol{\mu}}_{\hat{n},\hat{\imath}}^{(1,j)}\right) \\ \vdots \\ \mathbf{R}_{\mathrm{d}}^{(n_{\mathrm{s}})}+\sum_{(n_{\mathrm{s}},j)\in\mathcal{I}}\left(\boldsymbol{\Lambda}^{(n_{\mathrm{s}},j)}\hat{\boldsymbol{\lambda}}_{\hat{n},\hat{\imath}}^{(n_{\mathrm{s}},j)}+\boldsymbol{\mathcal{M}}^{(n_{\mathrm{s}},j)}\hat{\boldsymbol{\mu}}_{\hat{n},\hat{\imath}}^{(n_{\mathrm{s}},j)}\right) \\ \boldsymbol{\Lambda}^{\mathrm{T}}\,\hat{\mathbf{d}}_{\hat{n},\hat{\imath}} \\ \boldsymbol{\mathcal{M}}^{\mathrm{T}}\,\hat{\mathbf{d}}_{\hat{n},\hat{\imath}} \end{bmatrix}. \tag{5.7}$$

The additional matrices and vectors associated with the new Lagrange Multipliers field $\boldsymbol{\mu}$ in Eq. (5.7) are then given in a similar to Eqs. (3.21), namely,

$$\boldsymbol{\mathcal{M}}=\begin{bmatrix} \ddots & \boldsymbol{\mathcal{M}}^{(1,n_{\mathrm{s}})} & \iddots \\ \cdots & \vdots & \cdots \\ \iddots & \boldsymbol{\mathcal{M}}^{(n_{\mathrm{s}},1)} & \ddots \end{bmatrix}, \tag{5.8a}$$

$$\hat{\boldsymbol{\mu}} = \begin{bmatrix} \cdots & \hat{\boldsymbol{\mu}}^{(1,n_\mathrm{s})} & \cdots \end{bmatrix}^\mathrm{T} , \tag{5.8b}$$

once more $\hat{\boldsymbol{\mu}}^{(i,j)}_{\hat{n},\hat{i}}$ standing for the complete vector of Lagrange Multipliers DOFs for $\boldsymbol{\mu}$ along $\gamma_\mathrm{i}^{(i,j)}$ at time step $t_{\hat{n}}$ and nonlinear iteration $\hat{i}$. Moreover, submatrices $\boldsymbol{\mathcal{M}}^{(i,j)}$ in Eq. (5.8a) have entries,

$$\mathcal{M}^{(i,j)}_{(k,r)} = \left\langle \tilde{\boldsymbol{\phi}}^{(i,j)}_{k}, \boldsymbol{\omega}\left(\bar{\boldsymbol{\phi}}^{(i)}_{r}\right)\right\rangle_{0,\gamma_\mathrm{i}^{(i,j)}} , \tag{5.9}$$

for all pairs $(i,j) \in \mathcal{I}$, similar to Eq. (3.22). As aforementioned, a constant discontinuous Lagrange Multipliers discretization is chosen for both $\boldsymbol{\lambda}$ and $\boldsymbol{\mu}$. In addition, field $\boldsymbol{\lambda}|_{\gamma_\mathrm{i}^{(i,j)}}$ is discretized using as many elements $\hat{n}^{(i,j)}$ as the coarsest of the neighbouring patches $\Omega^{(i)}$ and $\Omega^{(j)}$ has whereas field $\boldsymbol{\mu}|_{\gamma_\mathrm{i}^{(i,j)}}$ is discretized with $\tilde{n}^{(i,j)} = \lceil \hat{n}^{(i,j)}/2 \rceil$ number of elements.

5.2 Numerical examples

In the following sections, three benchmark examples and one practically relevant case are chosen as demonstration. For the benchmark examples, one geometrically linear and two geometrically nonlinear problems are considered where the Penalty and the Lagrange Multipliers methods are systematically evaluated and compared. Lastly, the Penalty method is chosen for its application to geometrically linear and modal analysis of the NREL phase VI wind turbine with flexible blades, see in Simms et al. [7], due to its modularity and robustness especially needed for large scale engineering problems.

5.2.1 Scordelis-Lo roof

The first chosen benchmark example is that of the geometrically linear Scordelis-Lo roof, studied firstly in Scordelis et al. [79]. For this example, the Young's modulus, the Poisson ratio and the thickness are chosen as $E = 4.32 \times 10^5$ Pa, $\nu = 0$ and $\bar{h} = 25$ cm, respectively. The geometry is a part of a cylinder whose axis lies along the X_1-coordinate with length $\bar{L} = 50$ m whereas its radius and arc equals $\bar{R} = 25$ m and $\bar{\phi} = 4\pi/9$, respectively. The structure is supported at $X_1 = \pm\bar{L}/2$ with diaphragms, meaning that

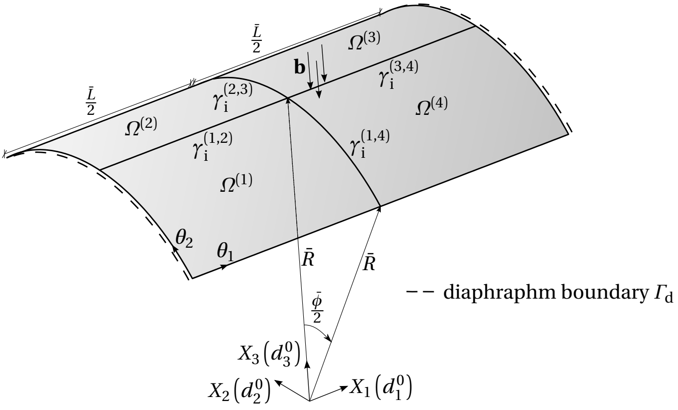

Figure 5.2: Scordelis-Lo roof: Problem placement.

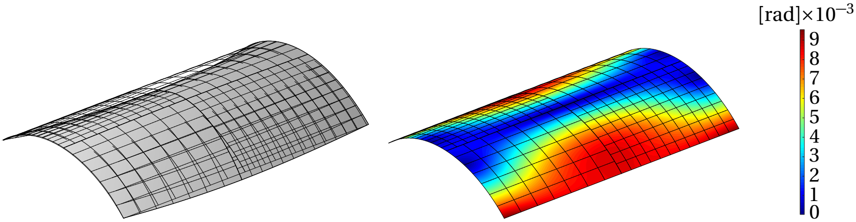

(a) Deformation scaled by 7.

(b) 2-norm of the rotation field $\|\boldsymbol{\omega}\|_2$.

Figure 5.3: Scordelis-Lo roof: Postprocessing (Lagrange Multipliers). Setting corresponding to refinement level $i_{\mathrm{r}} = 5$. Patches $\Omega^{(1)}$, $\Omega^{(2)}$, $\Omega^{(3)}$, $\Omega^{(4)}$ modelled using 49, 132, 48 and 108 elements, respectively, whereas pairs $\Omega^{(1)}$,$\Omega^{(3)}$ and $\Omega^{(2)}$,$\Omega^{(4)}$ have biquartic and bicubic bases, respectively.

the motion of the shell is confined in X_2- and X_3-directions. Since no symmetry reduction is herein employed, the original geometry is treated as a whole, while symmetrically dividing it into four patches and fixing corner with coordinates $(-\bar{L}/2, -\bar{R}\sin(\bar{\phi}/2), \bar{R}\cos(\bar{\phi}/2))$ to prevent rigid body movements. Additionally, a uniform constant dead load $\mathbf{b} = 0.09\,\mathbf{e}_3$ KPa is

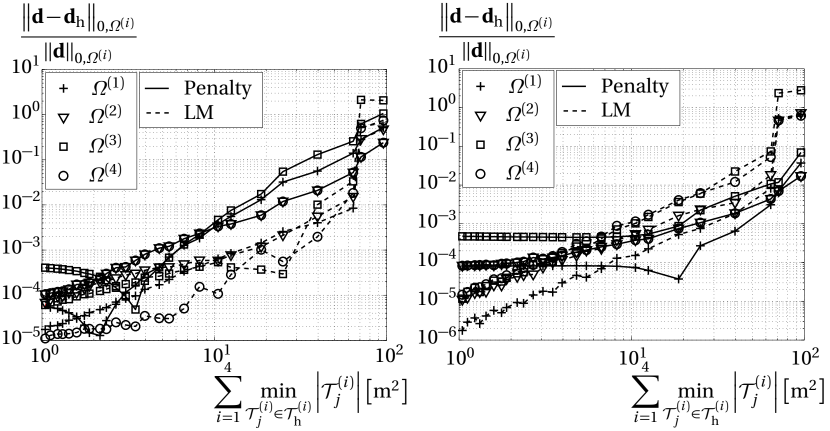

(a) $\Omega^{(1)}$, $\Omega^{(3)}$ bicubic and $\Omega^{(2)}$, $\Omega^{(4)}$ biquadratic bases.

(b) $\Omega^{(1)}$, $\Omega^{(3)}$ biquartic and $\Omega^{(2)}$, $\Omega^{(4)}$ bicubic bases.

Figure 5.4: Scordelis-Lo roof: Convergence study. Relative displacement error in the L^2-norm at each subdomain against the sum of the minimum element areas for the multipatch geometry.

applied over the whole surface of the structure, see Fig. 5.2. Subsequently, a convergence study for the displacement, the force and moment field is performed, where as reference solution a single patch solution using 2400 bidecic basis is used. Two polynomial order settings are herein considered: A low order setting where patch pairs $\Omega^{(1)}$, $\Omega^{(3)}$ and $\Omega^{(2)}$, $\Omega^{(4)}$ are modelled using bicubic and biquadratic bases, respectively, and a high order setting within which patch pairs $\Omega^{(1)}$, $\Omega^{(3)}$ and $\Omega^{(2)}$, $\Omega^{(4)}$ are modelled using biquartic and bicubic bases, respectively. Regarding the h-refinement, see Sec. 3.1.3, patches $\Omega^{(1)}$, $\Omega^{(2)}$, $\Omega^{(3)}$ and $\Omega^{(4)}$ are refined using $\lceil 4i_\mathrm{r}/3\rceil \times \lceil 4i_\mathrm{r}/3\rceil$, $\lceil 7i_\mathrm{r}/4+2\rceil \times \lceil 7i_\mathrm{r}/4+3\rceil$, $\lceil 6i_\mathrm{r}/4\rceil \times \lceil 6i_\mathrm{r}/4-2\rceil$ and $\lceil 8i_\mathrm{r}/5+4\rceil \times \lceil 8i_\mathrm{r}/5+1\rceil$ elements in θ_1- and in θ_2-parametric directions, respectively. The scaling of the Penalty parameters is chosen constant throughout the refinement as 10^3 and 0.25×10^3 for $\hat{\alpha}$ and $\tilde{\alpha}$, respectively. The scaled deformation and the contour of the rotation field $\boldsymbol{\omega}$ is depicted in Fig. 5.3. Since the Penalty parameters are chosen constant, the Penalty method levels off at a given accuracy level in all convergence graphs associated with the high order setting, see Figs. 5.4 and 5.5. On the contrary, the Lagrange

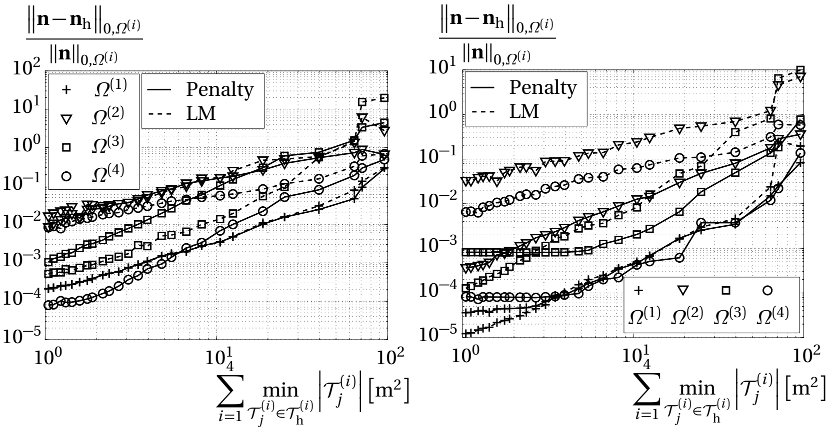

(a) $\Omega^{(1)}$, $\Omega^{(3)}$ bicubic and $\Omega^{(2)}$, $\Omega^{(4)}$ biquadratic bases.

(b) $\Omega^{(1)}$, $\Omega^{(3)}$ biquartic and $\Omega^{(2)}$, $\Omega^{(4)}$ bicubic bases.

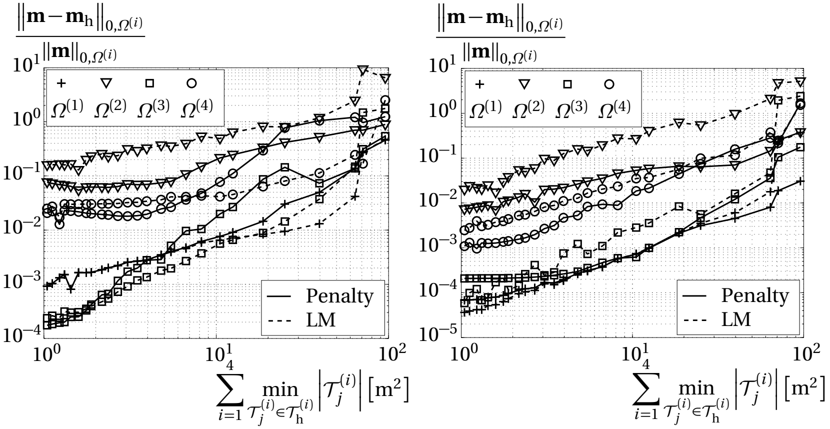

(c) $\Omega^{(1)}$, $\Omega^{(3)}$ bicubic and $\Omega^{(2)}$, $\Omega^{(4)}$ biquadratic bases.

(d) $\Omega^{(1)}$, $\Omega^{(3)}$ biquartic and $\Omega^{(2)}$, $\Omega^{(4)}$ bicubic bases.

Figure 5.5: Scordelis-Lo roof: Convergence study. Relative error in the force and moment tensors at each subdomain against the sum of the minimum element areas for the multipatch geometry.

Multipliers method demonstrates uniform convergence to the solution since the Lagrange Multipliers fields are refined also uniformly following

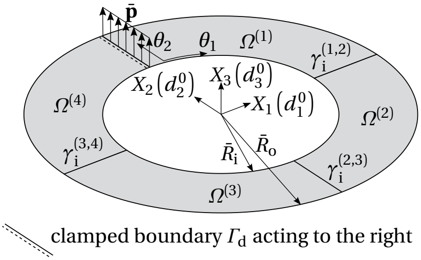

Figure 5.6: Slit annular plate subject to tip lifting line force: Problem placement.

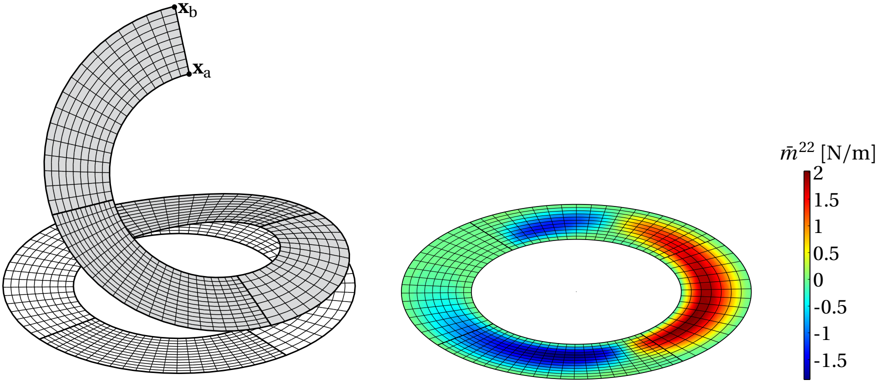

(a) Ultimate deformation.

(b) Ultimate moment field $\bar{m}^{22}$.

Figure 5.7: Slit annular plate subject to tip lifting line force: Postprocessing (Penalty). Results corresponding to the fine setting.

the rule described in Sec. 5.1.3.

5.2.2 Slit annular plate subject to tip lifting line force

In this section, the geometrically nonlinear benchmark problem of a slit annular plate subject to tip lifting force is studied, see in Sze et al. [80]. The Young's modulus and the Poisson ratio are accordingly chosen as $E = 21 \times 10^3$ Pa and $\nu = 0$, respectively. The inner radius, the outer radius, the thickness of the shell and the load magnitude are chosen as $\bar{R}_i = 6$ m,

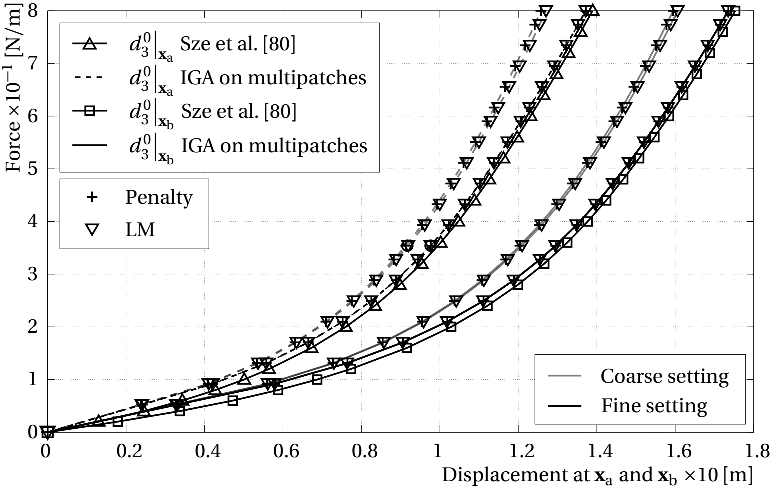

Figure 5.8: Slit annular plate subject to tip lifting line force: Load-displacement curves.

$\bar{R}_o = 10$ m, $\bar{h} = 3$ cm, and $\bar{\mathbf{p}} = 8 \times 10^{-1}\,\mathbf{e}_3$ [N/m], respectively. The problem is subsequently decomposed into four patches, see Fig. 5.6. Two settings are chosen for this case: The coarse setting for which patches $\Omega^{(1)}$, $\Omega^{(2)}$, $\Omega^{(3)}$ and $\Omega^{(4)}$ are parametrized using thirty-six, eighteen, twenty-eight and ten elements, respectively, all having C^1-continuous biquadratic bases. On the other hand, the fine setting consists in parametrizing patches $\Omega^{(1)}$, $\Omega^{(2)}$, $\Omega^{(3)}$ and $\Omega^{(4)}$ with two hundred-nine, one-hundred five, two hundred seventy-three and one hundred fifty-three elements, respectively, where patches $\Omega^{(1)}$ and $\Omega^{(3)}$ have a C^1-continuous biquadratic basis and patches $\Omega^{(2)}$ and $\Omega^{(4)}$, a C^2-continuous bicubic basis. The scaling of the Penalty parameters is chosen as 10^2 and 10^3 for $\hat{\alpha}$ and $\tilde{\alpha}$, respectively. For the solution of the nonlinear problem, sixty-one load steps are used with Newton-Raphson tolerance equal to 10^{-6} in the residual forces. The ultimate shell's deformation and the distribution of the physical moment component $\bar{m}^{22} = m^{22}\|\mathbf{A}_2\|_2^2$ across the shell's surface for the fine setting and when using the Penalty method is depicted in Fig. 5.7. Lastly, the load-displacement curves corresponding to the d_3^0 component of the displacements at points with current position vectors $\mathbf{x}_a$ and $\mathbf{x}_b$ (see Fig. 5.7(a)) for both the coarse

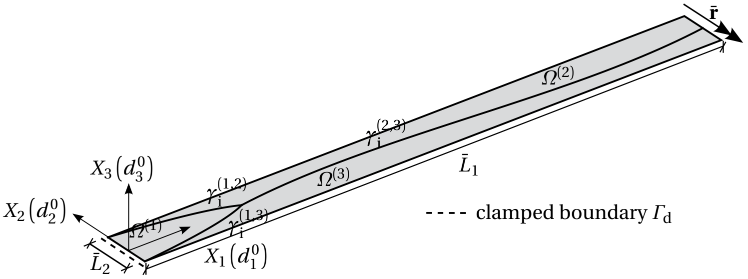

Figure 5.9: Cantilever subjected to end moment: Problem placement.

and the fine settings against the reference solution provided in Sze et al. [80] are depicted in Fig. 5.8. It is worth mentioning that the reference solution corresponds to a Reissner-Mindlin shell formulation and therefore the reference load-displacement curves cannot be identical with the ones provided by the isogeometric analysis on multipatch surfaces for a Kirchhoff-Love shell. However, the problem considers a relatively thin structure and thus the results from both theories are very close to each other when the fine setting is considered, as expected.

5.2.3 Cantilever subjected to end moment

The second geometrically nonlinear problem herein considered is that of a cantilever subject to an end moment. The material properties of the cantilever, that is, the Young's modulus and Poisson ratio are equal to $E = 1.2 \times 10^3$ Pa and $\nu = 0$, respectively. Accordingly, the length, the width and thickness of the cantilever are chosen as $\bar{L}_1 = 12$ m, $\bar{L}_2 = 1$ m and $\bar{h} = 10$ cm, respectively. The end bending moment is chosen as $\bar{\mathbf{r}} = -(2\pi E I_\mathrm{i}/\bar{L}_1)\,\mathbf{e}_2$, where $I_\mathrm{i} = \bar{L}_2\bar{L}_1^3/12$ is the cantilever's moment of inertia. It is known that under this loading, the cantilever bends into a circle of radius $\bar{R} = E I_\mathrm{i}/\|\mathbf{r}\|_2$, see in Sze et al. [80] and Kiendl [81]. The computational domain is decomposed into three patches, see Fig. 5.9. These patches are neighbouring through three interfaces which are chosen in this example curved. Quadratic Bézier curves (see in Piegl et al. [67]) are chosen for the geometric description of interfaces $\gamma_\mathrm{i}^{(1,2)}$ and $\gamma_\mathrm{i}^{(1,3)}$ whereas a cubic Bézier curve is

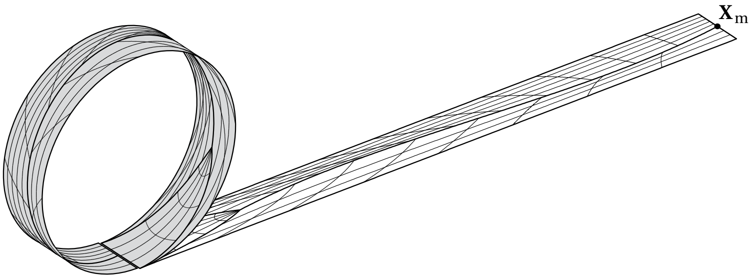

(a) Ultimate cantilever's deformation.

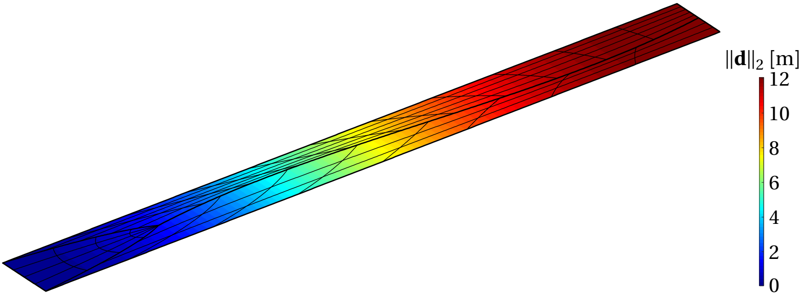

(b) The 2-norm of the ultimate displacement field $\|\mathbf{d}\|_2$.

Figure 5.10: Cantilever subjected to end moment: Postprocessing (Lagrange Multipliers). Results corresponding to the fine setting.

chosen for the geometric description of the interface $\gamma_\mathrm{i}^{(2,3)}$. Important is to note that within this decomposition of the cantilever, patch $\Omega^{(1)}$ attains a parametric singularity on its boundary point $\gamma_\mathrm{i}^{(1,2)} \cap \gamma_\mathrm{i}^{(1,3)}$ as its rectangular parametric space is degenerated into a triangle in the geometric space, see Sec. 3.2 for the geometric description of NURBS patches. For this numerical example the tolerance in the 2-norm of the residual forces within the Newton-Raphson scheme is chosen as 10^{-5} and twenty load steps are employed. The scaling of the Penalty parameters $\hat{\alpha}$ and $\tilde{\alpha}$ is chosen as 10^2 and 10^{-2}, respectively. As in the previous examples, one coarse and one fine setting are considered: The coarse setting consists of parametrizing patches

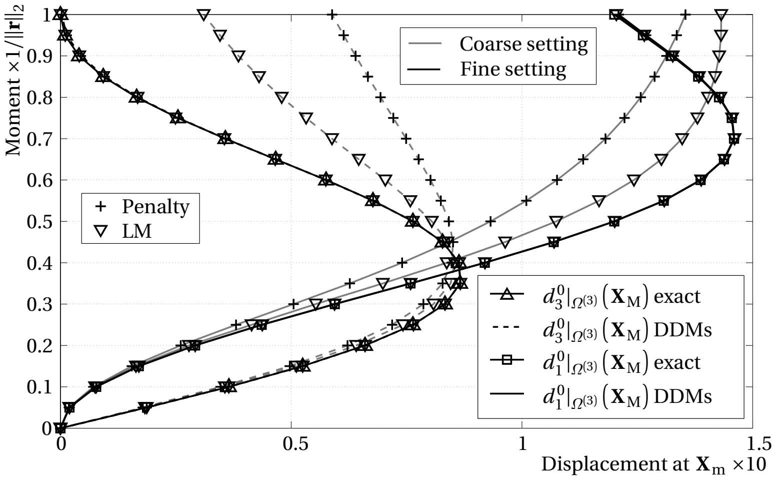

Figure 5.11: Cantilever subjected to end moment: Load-displacement curves.

$\Omega^{(1)}$, $\Omega^{(2)}$ and $\Omega^{(3)}$ using four, ten and twenty-one elements, respectively, all attaining C^2-continuous bicubic polynomial bases. Concerning the fine setting, patches $\Omega^{(1)}$, $\Omega^{(2)}$ and $\Omega^{(3)}$ are parametrized with sixteen, twenty-four and fifty-five elements, respectively, all attaining C^3-continuous bi-quartic polynomial bases. The ultimate cantilever's deformation and the ultimate displacement field in the 2-norm using the Lagrange Multipliers method and corresponding to the fine setting is shown in Fig. 5.10. As expected, the cantilever is bent into a circle of the expected radius while both the Penalty and the Lagrange Multipliers methods are proven to handle pointwise singularities even when these appear on the interface γ_i. Subsequently, the load-displacement curves for the $d_3^0|_{\mathbf{X}_\mathrm{m}}$ and $d_1^0|_{\mathbf{X}_\mathrm{m}}$ components of the displacement field of the mid-point at the tip of the cantilever $\mathbf{X}_\mathrm{m}$ along $\partial\Omega^{(3)}$, see Fig. 5.10(a), are depicted in Fig. 5.11 for both the Penalty and the Lagrange Multipliers methods. The results obtained using both methods are highly accurate as shown in the corresponding load-displacement curves where the curves overlap with the reference solution proposed in Sze et al. [80] for the fine setting.

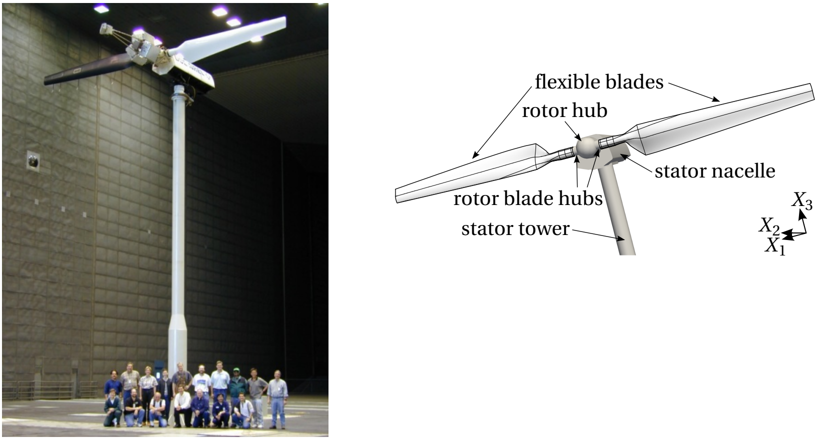

(a) Picture of the NREL phase VI wind turbine Simms et al. [7].

(b) Trimmed multipatch blade geometry.

Figure 5.12: NREL phase VI wind turbine: Problem setting.

5.2.4 NREL phase VI wind turbine with flexible blades

In this section, the NREL phase VI wind turbine with flexible blades (Simms et al. [7]) is employed as demonstration of isogeometric analysis on multipatch surfaces in industrial scale applications, see Fig. 5.12. A picture of the actual turbine can be seen in Fig. 5.12(a). The corresponding CAD model consisting of rigid parts and the two flexible blades whose stiffness is enhanced using two longitudinal spars along the longitudinal trimming curves on the blades' surfaces, is shown in Fig. 5.12(b). The Penalty method is accordingly chosen for this application. The Lagrange Multipliers method is not herein considered because its discrete equation system is enlarged by the Lagrange Multipliers DOFs and because of its saddle point nature, see in Eq. (5.7), which render the method inapplicable in its original form. However, an alternative form of the Lagrange Multipliers method for Kirchhoff-Love shells proposed in Teschemacher et al. [16] can

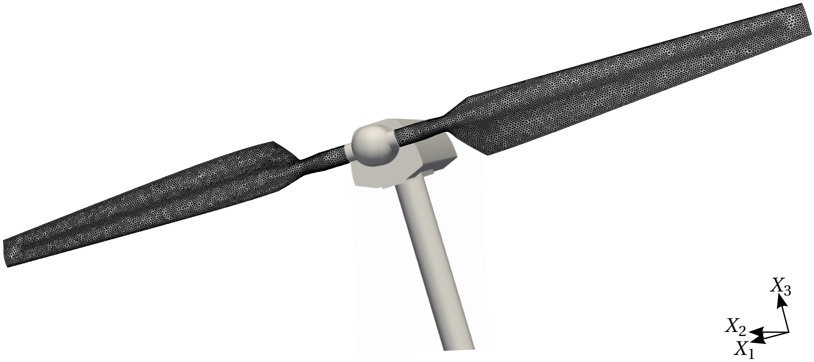

(a) Standard finite element mesh.

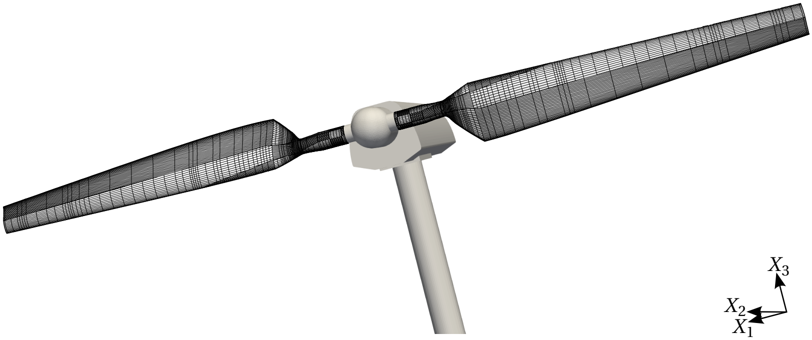

(b) B-rep computational model.

Figure 5.13: NREL phase VI wind turbine: Standard finite element and IGA on multipatch surfaces computational models for the flexible blades.

be used for large scale engineering applications instead.

The original computational model in Sicklinger et al. [82] involves a composite material model with varying thickness by analyzing the data provided in Simms et al. [7]. Herein a simplified model is used with a Saint-Venant Kirchhoff material model. The homogenized Young's modulus, density and thickness of the flexible blades are obtained by a calibration using a geometrically linear static and a modal analysis against the maximum

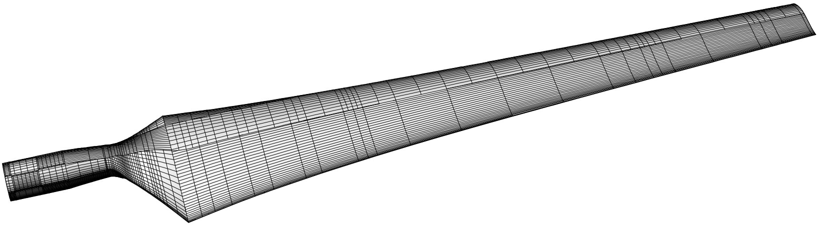

(a) Right blade.

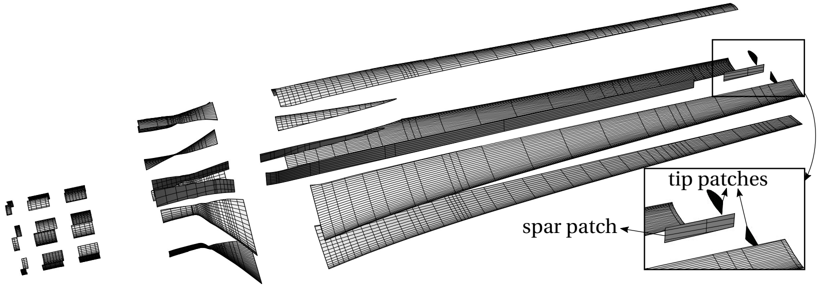

(b) Right blade exploded.

Figure 5.14: NREL phase VI wind turbine: Right blade of the NREL Phase VI wind turbine, both complete and decomposed into its underlying trimmed patches.

displacement and the first eigenfrequency, respectively, computed in Sicklinger et al. [82]. In this way, the Young's modulus, the density and the thickness of the flexible blades are assumed to be $E = 6 \times 10^{10}$ Pa, $\rho = 1.515 \times 10^3$ Kg/m^3 and $\bar{h} = 7$ mm, respectively. The Poisson ratio is then chosen as $\nu = 0.2$. Regarding the static analysis, the flexible blades are subject to their self-weight, namely, $\mathbf{b} = -\rho\,\bar{h}\,\mathbf{e}_3$. The results of IGA on multipatches for this example are compared with the results obtained using a standard finite element discretization of the flexible blades, see Fig. 5.13. Accordingy, the FEM model consists of 48630 triangular elements (Fig. 5.13(a)) based on a shell model with Reissner-Mindlin kinematics within software `Carat++`. Then, the corresponding h-refined multipatch NURBS computational model of the flexible blades is shown in Fig. 5.13(b). Subsequently, the NURBS computational model of the right blade is shown both intact

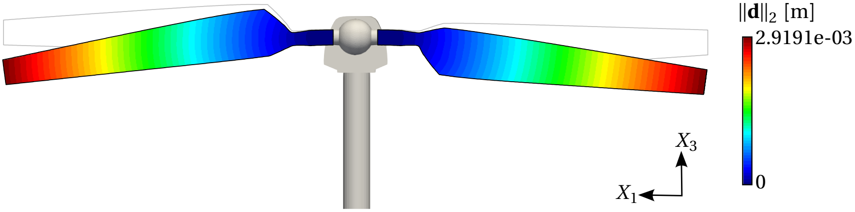

(a) Contour of the 2-norm of the displacement field $\|\mathbf{d}\|_2$ (FEM).

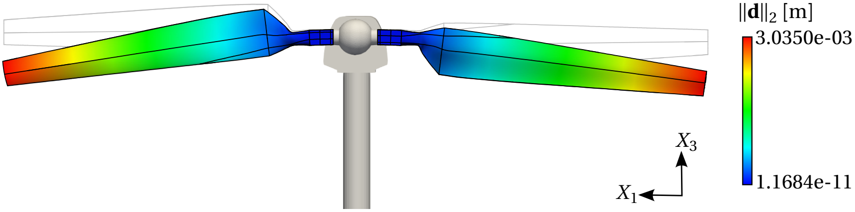

(b) Contour of the 2-norm of the displacement field $\|\mathbf{d}\|_2$ (IGA on multipatches with Penalty).

Figure 5.15: NREL phase VI wind turbine: Contour of the 2-norm of the displacement fields under the self-weight of the wind turbine blades for both the FEM and IGA models over the scaled by 200 current configuration.

and decomposed into its underlying trimmed patches in Fig. 5.14 where the geometric complexity and the large number of the underlying trimmed NURBS multipatches comprising the geometry is highlighted. It is worth mentioning that the spars and the tip of the NURBS computational model are connected to the rest of the blades' skin with a C^0-parametric continuity forming geometric kinks, thus adding another complexity to the NURBS multipatch model. Each blade consists of 37 trimmed patches with 170 interface boundaries of highly diverse sizes and parametrizations. Moreover, since the NURBS patches connecting the blades to the rigid rotor blade hubs are heavily trimmed, no strong boundary conditions can be applied. Therefore, weak application of the Dirichlet boundary conditions along 12 boundaries has to be used in this case, which can be achieved by enhancing weak form in Eq. (5.2) with boundary terms as shown in Sec. 4.1.2 for the membrane problem. The rule for the choice of the additional Penalty parameter $\bar{\alpha}$ follows the aforementioned rule for $\hat{\alpha}$ discussed in Sec. 5.1.2. A rotational Dirichlet boundary condition could also be ap-

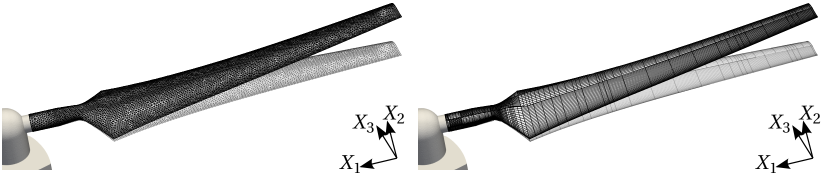

(a) 1st mode shape (FEM) corresponding to eigenfrequency $f_1 = 8.876031$ Hz (1st flapwise).

(b) 1st mode shape (IGA) corresponding to eigenfrequency $f_1^{\mathrm{h}} = 8.799294$ Hz (1st flapwise).

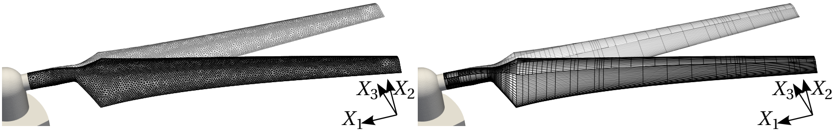

(c) 2nd mode shape (FEM) corresponding to eigenfrequency $f_2 = 12.17649$ Hz (1st edgewise).

(d) 2nd mode shape (IGA) corresponding to eigenfrequency $f_2^{\mathrm{h}} = 11.91276$ Hz (1st edgewise).

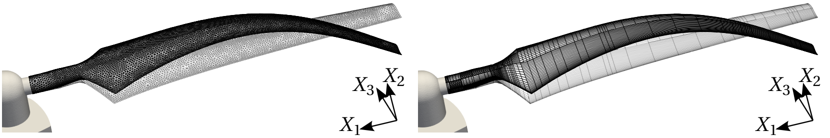

(e) 3rd mode shape (FEM) corresponding to eigenfrequency $f_3 = 41.42258$ Hz (2nd flapwise).

(f) 3rd mode shape (IGA) corresponding to eigenfrequency $f_3^{\mathrm{h}} = 41.17361$ Hz (2nd flapwise).

Figure 5.16: NREL phase VI wind turbine: Three first mode shapes with their corresponding eigenfrequencies for both the FEM and IGA on multipatches with Penalty models.

plied in the same way as the displacement Dirichlet boundary condition using another Penalty term in Eq. (5.2) if needed, see also in Breitenberger et al. [6]. The scaling associated to the Penalty parameters is then chosen as the inverse of the minimum element edge size along each interface and Dirichlet boundary (see Sec. 3.3.6) for $\hat{\alpha}, \tilde{\alpha}$ and $\bar{\alpha}$, respectively.

The contour of the 2-norm of the displacement field $||\mathbf{d}||_2$ across the blades in the current configuration due to self-weight for both the standard FEM and IGA on multipatches is shown in Fig. 5.15 demonstrating excellent accordance of the results. Moreover, an eigenfrequency analysis for both models is performed (Eq. (2.68)) and the first three eigenfrequencies of both the standard FEM and IGA models are shown in Fig. 5.16 demonstrating an excellent accordance of the results also in structural dynamics.

5.3 Concluding remarks

This chapter demonstrates the extension of the isogeometric Kirchhoff-Love shell analysis firstly introduced in Kiendl et al. [47] to multipatches using the Penalty and the Lagrange Multipliers methods. The application of the proposed methodology in a real world engineering example, that of the NREL phase VI wind turbine with flexible blades, shows the relevance of the proposed methodology to geometries stemming directly from CAD where the Penalty method can be beneficially used for both the continuity enforcement of the solution across the multipatches and the application of weak Dirichlet boundary conditions, see also in Breitenberger et al. [6]. In addition, the handling of parametric singularities and C^0-continuities can be treated without additional effort in the frame of the proposed methodology, see Secs. 5.2.3 and 5.2.4, respectively. The results suggest that isogeometric analysis on multipatches for Kirchhoff-Love shell analysis naturally extends to trimmed multipatches accounting for geometries stemming directly CAD also for real world engineering models.

Chapter 6

Fluid-Structure Interaction using the Isogeometric Mortar Method

This chapter presents the extension of *Fluid-Structure Interaction* (FSI) to account for thin-walled structures of membrane and Kirchhoff-Love shell type in isogeometric analysis on multipatches, see Chaps. 4 and 5 respectively. Firstly, the isogeometric mortar-based mapping method is introduced and elaborated. This is essential as fields need to be transformed between a trimmed multipatch NURBS surface representing the structural FSI interface and a low order surface discretization representing the fluid FSI interface, as the fluid iBVP is herein spatially discretized by means of the *Finite Volume Method* (FVM), see also in Bazilevs et al. [33]. Subsequently, the Navier-Stokes equations are briefly discussed in an *Arbitrary Lagrangian-Eulerian* (ALE) description of the motion and the partitioned FSI approach is introduced. Then, the lid-driven cavity FSI benchmark is used for the demonstration and the validation of the methodology. Lastly, the fluid-structure interaction of the inflatable hangar and the NREL phase VI wind turbine with flexible blades in numerical wind tunnels is shown, thus extending isogeometric analysis on multipatch surfaces to multiphysics problems of fluid-structure interaction type.

6.1 Isogeometric mortar-based mapping for surfaces

In this section the isogeometric mortar-based mapping method is described where fields are transformed between a low order faceted discretization and a NURBS multipatch description of a surface. Additionally, the NURBS multipatch description of the surface can be used as a mediator *Exact Coupling Layer* (ECL). The ECL can be used to smooth the transformed fields between two low order representations of the FSI interface and it is represented using the exact CAD model of the common interface. In the sequel of this chapter it is assumed that Ω and Ω_{h} are the exact surface representation stemming from CAD as described in Chap. 3 and a low order faceted representation of the surface with a finite number of C^0-continuous low order elements, respectively.

6.1.1 Theory

This section presents the problem placement along with the weak formulation and the discrete equation system governing the isogeometric mortar-based mapping method. All formulas are provided for the special case where fields are transformed between a low order discretized and a multipatch NURBS surface, however the following principles might well apply for any mortar-based mapping method. Accordingly, let $\mathcal{T}_i$, $i = 1, \dots, n_{\mathrm{e}} \in \mathbb{N}$ stand for the set of standard low order finite elements in Ω_{h}. Let $\boldsymbol{v}^{\mathrm{h}} \in \boldsymbol{\Upsilon}_{\mathrm{h}}$ be a field defined isoparametrically on the low order discretized surface Ω_{h} where,

$$\boldsymbol{\Upsilon}_{\mathrm{h}} = \left\{ \boldsymbol{v}^{\mathrm{h}} \in \boldsymbol{\mathcal{L}}^2\left(\Omega_{\mathrm{h}}\right) \middle| \, \boldsymbol{v}^{\mathrm{h}}{}_{|\mathcal{T}_i} \in \boldsymbol{\mathcal{P}}_{\alpha}\left(\mathcal{T}_i\right) \text{ for all } \mathcal{T}_i \in \Omega_{\mathrm{h}} \right\} , \tag{6.1}$$

and where $\boldsymbol{\mathcal{P}}_{\alpha}\left(\mathcal{T}_i\right)$ stands for the linear ($\alpha = 1$) or bilinear ($\alpha = 2$) polynomial vector-valued functions in each finite element $\mathcal{T}_i$. Let also $\Omega^{(i)}$, $i = 1, \dots, n_{\mathrm{s}}$ be a non-overlapping decomposition of Ω as defined in Eqs. (3.7). The goal is to find that field $\boldsymbol{v} \in \boldsymbol{\mathcal{L}}^2\left(\Omega_{\mathrm{d}}\right)$ which is the closest to $\boldsymbol{v}^{\mathrm{h}}$ in the $\boldsymbol{\mathcal{L}}^2(\Omega_{\mathrm{d}})$-space, namely,

$$\boldsymbol{v} = \arg \min_{\boldsymbol{v} \in \boldsymbol{\mathcal{L}}^2\left(\Omega_{\mathrm{d}}\right)} \|\boldsymbol{v}^{\mathrm{h}} - \boldsymbol{v}\|_{0,\Omega_{\mathrm{d}}} , \tag{6.2}$$

where field $\boldsymbol{v}$ is discontinuous along the interface γ_{i} and where Ω_{d} is defined in Eq. (3.7b). The problem in Eq. (6.2) might herein also be subject

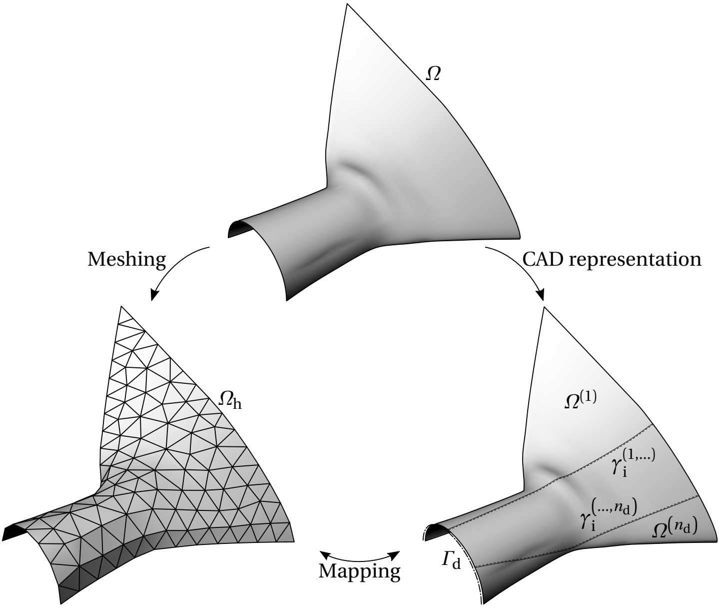

Figure 6.1: Problem placement: Low order FEM discretization and CAD representation of a surface Ω.

to the following interface and boundary conditions,

$$\boldsymbol{v} = \mathbf{0} \quad \text{on } \Gamma_\mathrm{d}\,, \tag{6.3a}$$

$$\boldsymbol{v}^{(i)} - \boldsymbol{v}^{(j)} = \mathbf{0} \quad \text{on each } \gamma_\mathrm{i}^{(i,j)}\,, \tag{6.3b}$$

$$\omega_\mathrm{t}^{(i)} + \omega_\mathrm{t}^{(j)} = 0 \quad \text{on each } \gamma_\mathrm{i}^{(i,j)}\,, \tag{6.3c}$$

where $\boldsymbol{v}^{(i)} = \boldsymbol{v}_{|_{\Omega^{(i)}}}$ and $\omega_\mathrm{t}^{(i)} = \omega_\mathrm{t}\left(\boldsymbol{v}^{(i)}\right)$ using only the rotation around the tangent to each boundary $\gamma_\mathrm{i}^{(i,j)}$ vector following the definition introduced in Eq. (2.41b), see Fig. 6.1. Let $\hat{\boldsymbol{\chi}}$ and $\tilde{\boldsymbol{\chi}}$ be the interface jump on $\boldsymbol{v}$ and its rotation around the tangent to the interface vector $\omega_\mathrm{t}(\boldsymbol{v})$, respectively, see also Secs. 3.3.1 and 5.1.1. With the aforementioned conditions in Eqs. (6.3) one can restrict the transformed field along Γ_d while simultaneously maintaining a solution in $\boldsymbol{\mathcal{H}}^1\left(\gamma_\mathrm{i}\right)$. The solution of problem in Eq. (6.2) subject to the interface and boundary conditions in Eqs. (6.3) can be obtained by the minimization of the augmented with Penalty terms functional $L : \boldsymbol{\Upsilon} \rightarrow \mathbb{R}$,

$$L(\boldsymbol{v}) = \frac{1}{2}\left(\|\boldsymbol{v}^{\mathrm{h}} - \boldsymbol{v}\|^2_{0,\Omega_{\mathrm{d}}} + \|\hat{\alpha}\hat{\boldsymbol{\chi}}\|^2_{0,\gamma_{\mathrm{i}}} + \|\tilde{\alpha}\tilde{\boldsymbol{\chi}}\|^2_{0,\gamma_{\mathrm{i}}} + \|\bar{\alpha}\boldsymbol{v}\|^2_{0,\Gamma_{\mathrm{d}}}\right) , \tag{6.4}$$

where space $\boldsymbol{\Upsilon}$ of the admissible variations herein reads,

$$\boldsymbol{\Upsilon} = \left\{ \boldsymbol{v} \in \prod_{i=1}^{n_{\mathrm{s}}} \boldsymbol{\mathcal{R}}\left(\Omega^{(i)}\right) \subset \boldsymbol{\mathcal{L}}^2\left(\Omega_{\mathrm{d}}\right) \middle| \hat{\boldsymbol{\chi}}, \tilde{\boldsymbol{\chi}} \in \boldsymbol{\mathcal{L}}^2\left(\gamma_{\mathrm{i}}\right) \text{ and } \boldsymbol{v} \in \boldsymbol{\mathcal{L}}^2\left(\Gamma_{\mathrm{d}}\right) \right\} , \tag{6.5}$$

since field $\boldsymbol{v}$ is isogeometrically defined over Ω_{d} and where $\boldsymbol{\mathcal{R}}\left(\Omega^{(i)}\right)$ stands for the space of all rational vector-valued polynomials in patch $\Omega^{(i)}$ for which the NURBS basis functions from the geometric parametrization of Ω_{d} form a basis, see also Sec. 3.3.2. In this way, the corresponding weak form of the aforementioned problem reads: Given a $\boldsymbol{v}^{\mathrm{h}} \in \boldsymbol{\Upsilon}_{\mathrm{h}}$, find a $\boldsymbol{v} \in \boldsymbol{\Upsilon}$, such that,

$$a(\delta\boldsymbol{v}, \boldsymbol{v}) = l(\delta\boldsymbol{v}) , \quad \text{for all } \delta\boldsymbol{v} \in \boldsymbol{\Upsilon} . \tag{6.6}$$

The bilinear form $a : \boldsymbol{\Upsilon} \times \boldsymbol{\Upsilon} \rightarrow \mathbb{R}$ and the linear functional $l : \boldsymbol{\Upsilon} \rightarrow \mathbb{R}$ in Eq. (6.6) are defined as follows,

$$\begin{aligned} a(\delta\boldsymbol{v}, \boldsymbol{v}) := \langle \delta\boldsymbol{v}, \boldsymbol{v} \rangle_{0,\Omega_{\mathrm{d}}} + \left\langle \delta\hat{\boldsymbol{\chi}}, \hat{\alpha}\hat{\boldsymbol{\chi}} \right\rangle_{0,\gamma_{\mathrm{i}}} + \left\langle \delta\tilde{\boldsymbol{\chi}}, \tilde{\alpha}\tilde{\boldsymbol{\chi}} \right\rangle_{0,\gamma_{\mathrm{i}}} + \\ \langle \delta\boldsymbol{v}, \bar{\alpha}\boldsymbol{v} \rangle_{0,\Gamma_{\mathrm{d}}} , \end{aligned} \tag{6.7a}$$

$$l(\delta\boldsymbol{v}) := \left\langle \delta\boldsymbol{v}, \boldsymbol{v}^{\mathrm{h}} \right\rangle_{0,\Omega_{\mathrm{d}}} . \tag{6.7b}$$

The weak form in Eq. (6.6) has a unique solution since bilinear form in Eq. (6.7a) is coercive and continuous whereas functional in Eq. (6.7b) is linear in $\boldsymbol{\Upsilon}$, see Thm. 2.2. However, the quality of the solution depends on the choice of the Penalty parameters as typical for the Penalty methods, see also in Babuška [9]. Let the subdomains $\Omega^{(i)}$ be represented by a set of trimmed NURBS patches within a surface CAD model, see Sec. 3.2.2. In this way, spaces $\boldsymbol{\Upsilon}_{\mathrm{h}}$ and $\boldsymbol{\Upsilon}$ are by construction finite dimensional and therefore given the vector-valued standard finite element and NURBS basis functions at each patch $\Omega^{(i)}$, $\boldsymbol{\phi}^{\mathrm{h}}_i$, $i = 1, \ldots, \dim \boldsymbol{\Upsilon}_{\mathrm{h}}$ and $\bar{\boldsymbol{\phi}}^{(i)}_j$, $j = 1, \ldots, \dim \boldsymbol{\mathcal{R}}\left(\Omega^{(i)}\right)$, respectively, one has,

$$\boldsymbol{v}^{\mathrm{h}} = \sum_{i=1}^{\dim \boldsymbol{\Upsilon}_{\mathrm{h}}} \boldsymbol{\phi}_i^{\mathrm{h}} \hat{v}_i^{\mathrm{h}} \,, \tag{6.8a}$$

$$\boldsymbol{v} = \sum_{i=1}^{n_{\mathrm{s}}} \sum_{j=1}^{\dim \boldsymbol{\mathcal{R}}\left(\Omega^{(i)}\right)} \bar{\boldsymbol{\phi}}_j^{(i)} \hat{v}_j^{(i)} \,, \tag{6.8b}$$

where $\hat{v}_j^{\mathrm{h}}$ and $\hat{v}_j^{(i)}$ stand for the DOFs of the finite element and the isogeometric discretization within each patch $\Omega^{(i)}$, respectively. These can be grouped into vectors similar to Eq. (3.13a), that is,

$$\hat{\boldsymbol{v}}^{\mathrm{h}} = \begin{bmatrix} \hat{v}_1^{\mathrm{h}} & \cdots & \hat{v}_{\dim \boldsymbol{\Upsilon}_{\mathrm{h}}}^{\mathrm{h}} \end{bmatrix}^{\mathrm{T}} \,, \tag{6.9a}$$

$$\hat{\boldsymbol{v}}^{(i)} = \begin{bmatrix} \hat{v}_1^{(i)} & \cdots & \hat{v}_{\dim \boldsymbol{\Upsilon}}^{(i)} \end{bmatrix}^{\mathrm{T}} \,. \tag{6.9b}$$

Accordingly, the discrete equation system corresponding to the weak form in Eq. (6.6) reads,

$$\left(\mathbf{C}_{\mathrm{rr}} + \mathbf{C}_{\hat{\alpha},\tilde{\alpha},\bar{\alpha}}\right) \hat{\boldsymbol{v}} = \mathbf{C}_{\mathrm{rn}} \hat{\boldsymbol{v}}^{\mathrm{h}} \,, \tag{6.10}$$

where,

$$\mathbf{C}_{\mathrm{rr}} = \begin{bmatrix} \mathbf{C}_{\mathrm{rr}}^{(1)} & \cdots & \mathbf{0} \\ \vdots & \ddots & \vdots \\ \mathbf{0} & \cdots & \mathbf{C}_{\mathrm{rr}}^{(n_{\mathrm{s}})} \end{bmatrix} \,, \tag{6.11a}$$

$$\mathbf{C}_{\mathrm{rn}} = \begin{bmatrix} \mathbf{C}_{\mathrm{rn}}^{(1)} & \cdots & \mathbf{0} \\ \vdots & \ddots & \vdots \\ \mathbf{0} & \cdots & \mathbf{C}_{\mathrm{rn}}^{(n_{\mathrm{s}})} \end{bmatrix} \,, \tag{6.11b}$$

$$\mathbf{C}_{\hat{\alpha},\tilde{\alpha},\bar{\alpha}} = \begin{bmatrix} \hat{\mathbf{C}}_{\hat{\alpha}}^{(1)} + \tilde{\mathbf{C}}_{\tilde{\alpha}}^{(1)} + \bar{\mathbf{C}}_{\bar{\alpha}}^{(1)} & \cdots & \hat{\mathbf{C}}_{\hat{\alpha}}^{(1,n_{\mathrm{s}})} + \tilde{\mathbf{C}}_{\tilde{\alpha}}^{(1,n_{\mathrm{s}})} \\ \vdots & \ddots & \vdots \\ \hat{\mathbf{C}}_{\hat{\alpha}}^{(n_{\mathrm{s}},1)} + \tilde{\mathbf{C}}_{\tilde{\alpha}}^{(n_{\mathrm{s}},1)} & \cdots & \hat{\mathbf{C}}_{\hat{\alpha}}^{(n_{\mathrm{s}})} + \tilde{\mathbf{C}}_{\tilde{\alpha}}^{(n_{\mathrm{s}})} + \bar{\mathbf{C}}_{\bar{\alpha}}^{(n_{\mathrm{s}})} \end{bmatrix} \,, \tag{6.11c}$$

$$\hat{\boldsymbol{v}} = \begin{bmatrix} \hat{\boldsymbol{v}}^{(1)} & \cdots & \hat{\boldsymbol{v}}^{(n_{\mathrm{s}})} \end{bmatrix}^{\mathrm{T}} \,. \tag{6.11d}$$

Penalty matrices $\hat{\mathbf{C}}_{\hat{\alpha}}^{(i)}$ and $\hat{\mathbf{C}}_{\hat{\alpha}}^{(i,j)}$ are defined as per Eqs. (3.17a) and (3.17b), respectively, in Sec. 3.3.3, and are used for the imposition of the field's continuity across $\gamma_{\mathrm{i}}^{(i,j)}$. On the other hand, Penalty matrix $\bar{\mathbf{C}}_{\bar{\alpha}}^{(i)}$ is defined in Eq. (4.4a), see Sec. 4.1.2, and is used for the imposition of a homogeneous boundary condition along the Dirichlet boundary $\Gamma_{\mathrm{d}}^{(i)}$. Moreover, Penalty matrices $\tilde{\mathbf{C}}_{\tilde{\alpha}}^{(i)}$, $\tilde{\mathbf{C}}_{\tilde{\alpha}}^{(i,j)}$ are given similar to Eqs. (5.4a) and (5.4b), respectively, where instead of the total rotation of field $\boldsymbol{\omega}(\boldsymbol{v})$, the rotation around the tangent to boundary γ_{i}, namely $\omega_{\mathrm{t}}(\boldsymbol{v})$ defined in Eq. (2.41b), is herein considered. These can be used for the imposition of the rotation continuity across $\gamma_{\mathrm{i}}^{(i,j)}$ and are herein only used when the displacement is transformed onto the multipatch geometry. Additionally, the entries of matrices $\mathbf{C}_{\mathrm{rr}}^{(i)}$, $\mathbf{C}_{\mathrm{rn}}^{(i)}$ are given by,

$$C_{\mathrm{rr}(j,k)}^{(i)} = \left\langle \bar{\boldsymbol{\phi}}_{j}^{(i)}, \bar{\boldsymbol{\phi}}_{k}^{(i)} \right\rangle_{0,\Omega^{(i)}} , \tag{6.12a}$$

$$C_{\mathrm{rn}\,(\mathrm{j,k})}^{(i)} = \left\langle \bar{\boldsymbol{\phi}}_{j}^{(i)}, \boldsymbol{\phi}_{k}^{\mathrm{h}} \right\rangle_{0,\Omega^{(i)}} , \tag{6.12b}$$

The matrix containing the Penalty terms, namely, $\mathbf{C}_{\hat{\alpha},\tilde{\alpha},\bar{\alpha}}$ in Eq. (6.11c), is optional and can be selectively used. In case some of the corresponding Penalty contributions are not considered, the corresponding Penalty parameter at the subscript of $\mathbf{C}_{\hat{\alpha},\tilde{\alpha},\bar{\alpha}}$ is replaced by zero. Its application depends on the numerical example, see Sec. 6.4. As aforementioned, problem in Eq. (6.10) is well defined provided that the corresponding Penalty parameters are carefully chosen. Herein, the following choice of the Penalty parameters is made,

$$\hat{\alpha}^{(i,j)} = \hat{p}_{\max}^{(i,j)} \left(h_{\mathrm{i}}^{(i,j)} \right)^{-1} \tag{6.13a}$$

$$\tilde{\alpha}^{(i,j)} = \hat{\alpha}^{(i,j)} \, ||\mathbf{B}_{\mathrm{t}}||_{\mathrm{F}}^{-1} , \tag{6.13b}$$

$$\bar{\alpha}^{(i)} = \hat{p}_{\max}^{(i)} \left(h_{\mathrm{d}}^{(i)} \right)^{-1} , \tag{6.13c}$$

where $\hat{p}_{\max}^{(i,j)}$ stands for the maximum polynomial order of the NURBS parametrizations $\mathbf{S}^{(i)}$, $\mathbf{S}^{(j)}$ for patches $\Omega^{(i)}$ and $\Omega^{(j)}$, respectively. Similarly, $\hat{p}_{\max}^{(i)}$ stands for the maximum polynomial order of the NURBS parametrization $\Omega^{(i)}$. Then, $h_{\mathrm{i}}^{(i,j)}$ and $h_{\mathrm{d}}^{(i)}$ in Eqs. (6.13a) and (6.13c) are given by,

$$h_{\mathrm{i}}^{(i,j)} = \min_{s=1,\ldots,\bar{n}_j^{(i)}-1} \left| \gamma_j^{(i)} \big|_{]\tilde{\theta}_{j,s}^{(i)},\tilde{\theta}_{j,s+1}^{(i)}[} \right| , \tag{6.14a}$$

$$h_{\mathrm{d}}^{(i)} = \min_{s=1,\ldots,\hat{n}_{\mathrm{d}}^{(i)}-1} \left| \gamma_{\mathrm{d}}^{(i)} \big|_{]\tilde{\theta}_{\mathrm{d},s}^{(i)},\tilde{\theta}_{\mathrm{d},s+1}^{(i)}[} \right| , \tag{6.14b}$$

respectively, where $\bar{n}_j^{(i)}$ and $\hat{n}_{\mathrm{d}}^{(i)}$ stand for the number of intersections of trimming curve $\gamma_{\mathrm{i}}^{(i,j)}$ with the knot lines in patches $\Omega^{(i)}$, $\Omega^{(j)}$ and the number of intersections of trimming curve $\Gamma_{\mathrm{d}}^{(i)}$ with the knot lines in patch $\Omega^{(i)}$, see Sec. 3.3.6. Curves $\gamma_j^{(i)}$ and $\gamma_{\mathrm{d}}^{(i)}$ stand for the geometric representation of trimming curves $\hat{\gamma}_j^{(i)}$ and $\hat{\gamma}_{\mathrm{d}}^{(i)}$, respectively, and the definitions of $\hat{\gamma}_j^{(i)}$, $\hat{\gamma}_{\mathrm{d}}^{(i)}$, $\tilde{\theta}_{j,s}^{(i)}$ and $\tilde{\theta}_{\mathrm{d},s}^{(i)}$ can be found in Sec. 3.3.6. Additionally, $\gamma_{\mathrm{d}}^{(i)} \big|_{]\tilde{\theta}_{\mathrm{d},s}^{(i)},\tilde{\theta}_{\mathrm{d},s+1}^{(i)}[}$, $|\gamma_j^{(i)}|$ and $||\mathbf{B}_{\mathrm{t}}||_{\mathrm{F}}$ stand for the restriction of the trimming curve $\gamma_{\mathrm{d}}^{(i)}$ in $]\tilde{\theta}_{\mathrm{d},s}^{(i)},\tilde{\theta}_{\mathrm{d},s+1}^{(i)}[$, the length of curve $\gamma_j^{(i)}$ and the matrix norm of the B-operator matrix of the rotation field ω_{t} (see Appx. A), respectively. Thus, the Penalty parameters for the enforcement of the field continuity constraints and the weak Dirichlet boundary conditions are chosen as the inverse of the minimum element edge sizes along the corresponding trimming curves whereas for the enforcement of the interface rotation continuity of the field, the corresponding Penalty parameter is scaled with the matrix norm of the B-operator matrix associated with the rotation field.

For the mortar-based transformation of a field $\boldsymbol{v}$ defined isogeometrically on a multipatch NURBS surface to a field $\boldsymbol{v}^{\mathrm{h}}$ defined on a standard finite element discretized surface, problem in Eq. (6.10) simply reverses, that is,

$$\mathbf{C}_{\mathrm{nn}} \hat{\boldsymbol{v}}^{\mathrm{h}} = \mathbf{C}_{\mathrm{nr}} \hat{\boldsymbol{v}} , \tag{6.15}$$

where $\mathbf{C}_{\mathrm{nn}}$ is defined similar to $\mathbf{C}_{\mathrm{rr}}$ in Eq. (6.11a) with entries,

$$C_{\mathrm{nn}(i,j)} = \left\langle \boldsymbol{\phi}_i^{\mathrm{h}}, \boldsymbol{\phi}_j^{\mathrm{h}} \right\rangle_{0,\Omega_{\mathrm{d}}} , \tag{6.16}$$

and where $\mathbf{C}_{\mathrm{nr}} = \left(\mathbf{C}_{\mathrm{rn}}\right)^{\mathrm{T}}$, see in Eq. (6.11b). The fact that the variational problem of the isogeometric mortar-based mapping method is well-posed

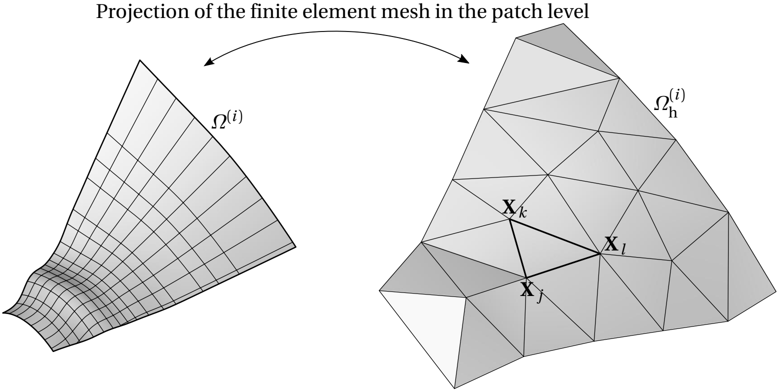

Figure 6.2: Realization: NURBS patch $\Omega^{(i)}$ and the part of the finite element mesh $\Omega_{\mathrm{h}}^{(i)} \subset \Omega_{\mathrm{h}}$ which has a projection on $\Omega^{(i)}$.

is reflected onto the fact that matrices $\mathbf{C}_{\mathrm{rr}}$ and $\mathbf{C}_{\mathrm{nn}}$, are square, symmetric and positive definite, see Eqs. (6.10) and (6.15), respectively.

6.1.2 Realization

In this section the technicalities and the implementational aspects of the isogeometric mortar-based mapping method are discussed. As already mentioned in Sec. 6.1.1, the isogeometric mortar-based mapping method is used for the transformation of fields between a multipatch NURBS and a low order discretized surface. Since the technical details for dealing with surface multipatches in terms of IGA and the corresponding handling of the interface conditions is discussed in Chap. 3, herein only one NURBS surface patch and the corresponding part $\Omega_{\mathrm{h}}^{(i)} \subset \Omega_{\mathrm{h}}$ of the finite element mesh Ω_{h} which has a projection on $\Omega^{(i)}$ is considered, see Fig. 6.2. The focus is then drawn on the evaluation of the integrals on $\Omega^{(i)}$, see Eqs. (6.12a), (6.12b) and (6.16), respectively. Within this thesis, the exact geometry $\Omega^{(i)}$ for each patch is chosen as the integration surface. Accordingly, the finite element mesh is projected on the NURBS surface, by projecting each node $\mathbf{X}_i$, $i = 1,\dots,n_{\mathrm{n}} \in \mathbb{N}$ onto $\Omega^{(i)}$ through the nonlinear map $\boldsymbol{\theta}_j^{(i)} = \left(\mathbf{S}^{(i)}\right)^{-1}\left(\mathbf{X}_j\right)$ for all nodes in the finite element mesh using a Newton-Raphson scheme. Consider the finite element $\mathbf{X}_j$-$\mathbf{X}_k$-$\mathbf{X}_l$ in right

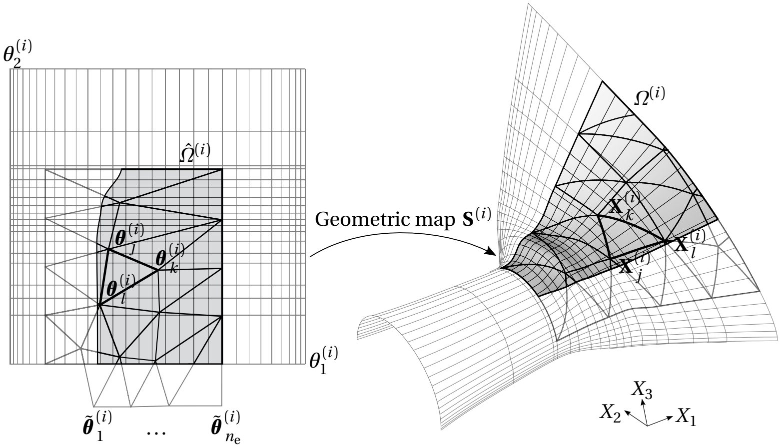

Figure 6.3: Realization: Projection of $\Omega_\mathrm{h}^{(i)}$ onto $\Omega^{(i)}$.

part of Fig. 6.2. Each of its nodes are projected onto $\Omega^{(i)}$ to obtain the corresponding parametric coordinates in the parametric space $\hat{\Omega}^{(i)}$ of the patch. Subsequently, a linear interpolation between the projected nodes in the parametric space $\hat{\Omega}^{(i)}$ is made in order to obtain the image of the finite element in the parametric space of the patch, namely, $\boldsymbol{\theta}_j^{(i)}$-$\boldsymbol{\theta}_k^{(i)}$-$\boldsymbol{\theta}_l^{(i)}$, see left part of Fig. 6.3. The latter linear approximation of the finite element edges in the parametric space of the patch is a consistent approximation since the projection error tends to zero as the element size gets smaller. Then, the image of the finite element in the geometric space can be obtained using the geometric transformation in Eq. (3.6), see right part of Fig. 6.3.

Typically, there exist finite elements which are partially projected inside and partially outside the boundaries of the patch's parametric space. To obtain the parts of these elements which lie within the computational domain of the patch, the corresponding finite element edges are clipped with the patch boundary using an iterative bisection method. Accordingly, given a finite element edge $\mathbf{X}_n$-$\mathbf{X}_m$ whose vertex $\mathbf{X}_n$ has a projection in patch $\Omega^{(i)}$ and whose other vertex $\mathbf{X}_m$ has no projection on $\Omega^{(i)}$, a sequence of points $\mathbf{X}_\mathrm{i} = (1-\lambda_\mathrm{i})\mathbf{X}_n + \lambda_\mathrm{i}\mathbf{X}_m$ and $\mathbf{X}_\mathrm{o} = (1-\lambda_\mathrm{o})\mathbf{X}_n + \lambda_\mathrm{o}\mathbf{X}_m$, with $\lambda_\mathrm{i}, \lambda_\mathrm{o} \in [0,1]$, is generated along edge $\mathbf{X}_n$-$\mathbf{X}_m$. Then, points $\mathbf{X}_\mathrm{i}$ have a projection $\mathbf{X}_\mathrm{i}^{(i)}$ on

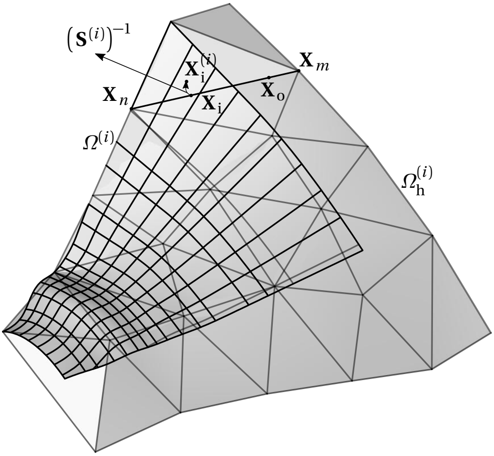

Figure 6.4: Realization: Projection of a finite element edge onto patch's boundary.

patch $\Omega^{(i)}$ through the nonlinear map in Eq. (3.32), while points $\mathbf{X}_{\mathrm{o}}$ do not have such a projection, see Fig. 6.4. Within each iteration the mid-point $\mathbf{X}_{\mathrm{m}} = \left(\mathbf{X}_{\mathrm{i}} + \mathbf{X}_{\mathrm{o}}\right)/2$ is assigned to either $\mathbf{X}_{\mathrm{i}}$ or to $\mathbf{X}_{\mathrm{o}}$ depending on whether or not it has a projection in patch $\Omega^{(i)}$. The aforementioned iterations carry on until a user specified tolerance where in the converged state, point $\mathbf{X}_{\mathrm{m}}$ is assumed to be the closest point of edge $\mathbf{X}_n$-$\mathbf{X}_m$ on patch boundary of $\Omega^{(i)}$. In this way, the part of the finite element edge with a projection within patch's computational domain is obtained.

The set of trimming curves $\gamma_k^{(i)}$, $k = 1, \ldots, n_{\mathrm{t}}^{(i)} \in \mathbb{N}$ which trim patch $\Omega^{(i)}$ is subsequently linearized. For the linearization, $\hat{p}_k^{(i)} + 1$ points equidistantly placed in the parametric space $\hat{\gamma}_j^{(i)}$ of each trimming curve together with the corresponding *Greville Abscissae*[1] of the curve are chosen, where $\hat{p}_k^{(i)}$ stands for the polynomial order of NURBS curve $\gamma_k^{(i)}$, see Sec. 3.1.1. Next, the projected elements in the NURBS parametric space are clipped with

---

[1] The Greville Abscissae are parametric locations where the basis functions attain their highest values.

the aforementioned linearized trimming curves, in order to exclude parts of the elements which are projected outside the patch's computational domain. In this way, the computational domain for the evaluation of the integrals in Eq. (6.6) is obtained, see the shaded area in Fig. 6.3. Then, the projected finite elements in the parametric space of patch $\Omega^{(i)}$ are clipped with the knot lines of the patch's parametric space $\hat{\Omega}^{(i)}$, thus obtaining subregions where the integrands in Eqs. (6.12) are C^{∞}-continuous and where the Gauss integration can be performed. The aforementioned resulting regions may attain an arbitrary polygonal shape and thus they are subsequently triangulated using a very simple triangulation rule since this is merely needed for the distribution of the Gauss points. Finally, the Gauss points are generated on each resulting sub-triangle where the integrals in Eqs. (6.12) are numerically evaluated.

6.2 Computational fluid dynamics

In this study, the *incompressible Navier-Stokes* equations are numerically solved by means of the *Finite Volume Method* (FVM), see in Ferziger et al. [34], within the open-source software OpenFOAM®, see also in Jasak et al. [36]. For the sake of completeness, the Navier-Stokes equations are herein repeated. Given is a volume $\tilde{V} \subset \mathbb{R}^3$ moving with a given velocity field $\mathbf{u}^{\mathrm{d}}$ within which the flow field is defined in an *Arbitrary Lagrangian-Eulerian* (ALE) description of the motion. The unknown fields of the problem are the fluid velocity and pressure fields denoted by $\mathbf{u}$ and p, respectively. Moreover, the fluid density $\tilde{\rho}$ is considered herein constant. In this way, the Navier-Stokes iBVP reads,

$$\tilde{\rho} D\mathbf{u} - \boldsymbol{\nabla} \cdot \boldsymbol{\sigma} = \mathbf{0}\,, \quad \text{in } \tilde{V}\,, \tag{6.17a}$$

$$\boldsymbol{\nabla} \cdot \mathbf{u} = 0\,, \quad \text{in } \tilde{V}\,, \tag{6.17b}$$

$$\mathbf{u} = \tilde{\boldsymbol{v}}\,, \quad \text{on } \tilde{\Omega}_{\mathrm{d}}\,, \tag{6.17c}$$

$$\tilde{\mathbf{t}} = \tilde{\boldsymbol{\tau}}\,, \quad \text{on } \tilde{\Omega}_{\mathrm{n}}\,, \tag{6.17d}$$

where $\tilde{\boldsymbol{v}}$ and $\tilde{\boldsymbol{\tau}}$ stand for the inlet velocity along the inlet boundary $\tilde{\Omega}_{\mathrm{d}} \subset \partial \tilde{V}$ and the prescribed tractions along the outlet boundary $\tilde{\Omega}_{\mathrm{n}} \subset \partial \tilde{V}$. Herein no body forces are assumed for the aforementioned fluid iBVP. The linear momentum and the mass conservation when assuming constant density within $\tilde{V}$ are represented by Eqs. (6.17a) and (6.17b), respectively. Moreover, the material derivative $D\mathbf{u}$, the components of the internal fluid

Cauchy stress tensor $\boldsymbol{\sigma} = \sigma_{ij}\, \mathbf{e}_i \otimes \mathbf{e}_j$ (*Newtonian* fluid) and the boundary traction vector $\tilde{\mathbf{t}}$ along $\partial \tilde{V}$ in Eqs. (6.17), respectively, are defined as,

$$D\mathbf{u} = \frac{\partial \mathbf{u}}{\partial t} + \left(\mathbf{u} - \mathbf{u}^{\mathrm{d}}\right) \cdot \boldsymbol{\nabla}\mathbf{u}\,, \tag{6.18a}$$

$$\sigma_{ij} = -p\delta_{ij} + \mu \frac{1}{2}\left(\frac{\partial u_i}{\partial X_j} + \frac{\partial u_j}{\partial X_i}\right), \tag{6.18b}$$

$$\tilde{\mathbf{t}} = \tilde{\mathbf{e}}_{\mathrm{n}} \cdot \boldsymbol{\sigma}\,. \tag{6.18c}$$

$D\bullet$, μ and $\tilde{\mathbf{e}}_{\mathrm{n}}$ being the material derivative, the dynamic fluid viscosity and the surface normal to $\tilde{\Omega}_{\mathrm{n}}$, respectively, see in Gresho et al. [15] for more information. Additionally, the expressions $\boldsymbol{\nabla} \cdot \mathbf{u}$, $\left(\mathbf{u} - \mathbf{u}^{\mathrm{d}}\right) \cdot \boldsymbol{\nabla}\mathbf{u}$, respectively, in an open-form read,

$$\boldsymbol{\nabla} \cdot \mathbf{u} = \frac{\partial u_i}{\partial X_i}\,, \tag{6.19a}$$

$$\left(\mathbf{u} - \mathbf{u}^{\mathrm{d}}\right) \cdot \boldsymbol{\nabla}\mathbf{u} = \left(u_i^{\mathrm{d}} - u_i\right) \frac{\partial u_j}{\partial X_i}\, \mathbf{e}_j\,, \tag{6.19b}$$

where u_i, u_i^{d} and $\mathbf{e}_i$ with $i = 1, \ldots, 3$, stand for the Cartesian components of the fluid velocity field, the relative domain velocity field and the Cartesian base vectors, respectively. The Einstein's summation convention over the repeated indices is also assumed. In principle, the linear momentum in Eq. (6.17a) can be scaled by $1/\tilde{\rho}$ so that the fluid problem is only characterized by one constant, the so-called *kinematic* viscosity defined as $\tilde{\nu} = \mu/\tilde{\rho}$. For the definition of the fluid properties of the numerical examples in Sec. 6.4 only the kinematic viscosity is given as it fully characterizes the fluid problem.

As aforementioned, the FVM method within open-source software OpenFOAM® is chosen for the discretization of problem in Eqs. (6.17) in the frame of *Computational Fluid Dynamics* (CFD). Among the various solution procedures and adaptations offered by OpenFOAM®, herein a laminar solver for the cavity FSI benchmark (Sec. 6.4.1), a *Large Eddy Simulation* (LES) for the hangar FSI simulation (Sec. 6.4.2) and an *Unsteady Reynolds Averaged Navier-Stokes* (uRANS) for the NREL phase VI wind turbine FSI simulation (Sec. 6.4.3) are employed, see in Breuer et al. [30], Ferziger et al. [34], and Sagaut [83] for more information. The latter diverse solution approaches are chosen in order to show the applicability of the proposed FSI methodology for different fidelities of the CFD problem.

6.3 Partitioned fluid-structure interaction

In this section the partitioned FSI approach is briefly introduced, see also in Glück et al. [37]. Herein assumed is that the structural and the fluid domains share a common interface $\mathscr{S} = \partial \tilde{V} \cap \mathit{\Omega}$, where $\mathit{\Omega}$ is the domain of definition for the structural iBVP, see Secs. 2.3.2 and 2.3.3 for the Kirchhoff-Love and the membrane iBVP, respectively. In this way, the structural iBVP defined by Eqs. (2.42) and (2.49) for the Kirchhoff-Love and the membrane analysis, respectively, and the fluid iBVP in Eqs. (6.17) are subject to the following Dirichlet and Neumann interface conditions across $\mathscr{S}$,

$$\dot{\mathbf{d}} - \mathbf{u} = \mathbf{0}\,, \quad \text{on}\ \mathscr{S} \times \mathbb{T}\,, \tag{6.20a}$$

$$\tilde{\mathbf{b}} + \tilde{\mathbf{t}} = \mathbf{0}\,, \quad \text{on}\ \mathscr{S} \times \mathbb{T}\,, \tag{6.20b}$$

respectively, to account for a continuous solution across $\mathscr{S}$. Accordingly, the *Computational Structural Dynamics* (CSD) problem governed by either the Kirchhoff-Love or the membrane theory, see Secs. 2.3.2 and 2.3.3, respectively, is discretized using IGA on multipatch surfaces or standard FEM. Additionally, $\dot{\mathbf{d}}$ and $\mathbf{u}$ stand for the structural and fluid velocity fields, respectively, which have to be equal across the common interface as per Eq. (6.20a). Moreover, Eq. (6.20a) enforces also the continuity of the interface displacements across the common interface, namely,

$$\mathbf{d} - \boldsymbol{\mathcal{U}} = \mathbf{0}\,, \quad \text{on}\ \mathscr{S} \times \mathbb{T}\,, \tag{6.21}$$

when integrating Eq. (6.20a) on time, $\boldsymbol{\mathcal{U}}$ being the fluid displacement field across the FSI interface. Concerning the traction equilibrium across $\mathscr{S}$, see Eq. (6.20b), the surface traction vector $\tilde{\mathbf{b}}$ of the structural FSI interface contributes to the body force vector $\mathbf{b}$ on the right-hand side of weak forms in Eqs. (2.45) and (2.51) for the Kirchhoff-Love shell and the membrane problems, respectively, and the fluid traction vector $\tilde{\mathbf{t}}$ is given in Eq. (6.18c), see in Quarteroni et al. [84] for more information. Evidently, the structural surface traction field $\tilde{\mathbf{b}}$ is defined by means of the 2nd Piola-Kirchhoff stress tensor whereas the fluid traction field $\tilde{\mathbf{t}}$ is defined by means of the Cauchy stress tensor due to the different descriptions of motion assumed for the structural and the fluid iBVPs, respectively. In this case the Piola transformation can be used to define the Neumann interface constraint in Eq. (6.20b) consistently, see in Zienkiewicz et al. [85].

Since the FVM within OpenFOAM® is chosen for the solution of the CFD problem, the fluid FSI interface is represented by a low order faceted surface, see Sec. 6.2. Additionally, the herein presented FSI simulations involving IGA discretizations for the structure or the ECL, employ the isogeometric mortar-based mapping method introduced in Sec. 6.1 and are compared against FSI simulations of the same problems involving standard FEM structural discretizations using the standard mortar-based mapping method (Wang [86]). Let $\mathscr{S}$ and $\mathscr{S}_{\mathrm{h}}$ denote in the sequel the exact CAD representation and a low order discretization of the FSI interface. The restriction of the FSI interface at each patch is denoted by $\mathscr{S}^{(i)} = \mathscr{S} \cap \Omega^{(i)}$. Moreover, $\mathscr{S}_{\mathrm{h}}$ may represent the FSI interface of the fluid domain since the FVM is employed as discretization method for the CFD problem or the FSI interface of the structural domain whenever FEM is used for the CSD problem. A distinction should be then made clear from the context.

The solution of the CSD and CFD problems subject to interface conditions in Eqs. (6.20) and Eq. (6.21) is achieved using a fixed-point iterative approach known as *Gauss-Seidel* (GS) iterative method, see also in Glück et al. [37] and Sicklinger et al. [82]. Accordingly, the CFD problem is solved as a Dirichlet problem by complying with the resulting interface displacement and velocity field from the solution of the CSD problem, whereas the CSD problem is in turn solved as a Neumann problem subject to the interface traction field emanating from the solution of the CFD problem. In this way, the displacement field of the structural FSI interface $\mathbf{d}_{|\mathscr{S}}$ is transformed onto the fluid FSI interface displacement field $\boldsymbol{\mathcal{U}}$ and accordingly the fluid traction field at the FSI interface $\tilde{\mathbf{t}}_{|\mathscr{S}_{\mathrm{h}}}$ is transformed onto the traction field on the structural FSI interface $-\tilde{\boldsymbol{b}}$. This interaction takes place at each time step $t_{\hat{n}}$, assuming a matching time discretization for both the CSD and the CFD problems, until a specified termination criterion based on the relative change of the structural displacement across the FSI interface in the 2-norm at each FSI iteration $\hat{k}$ is met, given a user defined tolerance

$\tilde{\epsilon}$, namely,

$$\frac{\| \hat{\mathbf{d}}_{\hat{n},\hat{k}\,|_{\mathscr{S}}} - \hat{\mathbf{d}}_{\hat{n},\hat{k}-1\,|_{\mathscr{S}}} \|_2}{\| \hat{\mathbf{d}}_{\hat{n},\hat{k}\,|_{\mathscr{S}}} - \hat{\mathbf{d}}_{\hat{n}-1\,|_{\mathscr{S}}} \|_2} < \tilde{\epsilon}\,, \tag{6.22}$$

$\hat{\mathbf{d}}_{\hat{n},\hat{k}\,|_{\mathscr{S}}}$ being the vector of structural displacement DOFs on the FSI interface at time step $t_{\hat{n}}$ and at k-th FSI iteration. Moreover, $\hat{\mathbf{d}}_{\hat{n}-1\,|_{\mathscr{S}}}$ stands for the vector of structural displacement DOFs on the FSI interface at the converged coupled FSI state at time step $t_{\hat{n}-1}$. In Eq. (6.22) index $\hat{i}$ introduced in Sec. 2.4.2 on $\hat{\mathbf{d}}$ representing the Newton-Raphson iteration is omitted since $\hat{\mathbf{d}}_{\hat{n},\hat{k}}$ is assumed to be the set of displacement DOFs at the converged state of the CSD problem for the geometrically nonlinear analysis at time step $t_{\hat{n}}$ and at $\hat{k}$-th FSI iteration. The aforementioned interface fixed point iterations are stabilized and accelerated using the *Aitken relaxation method*, see in Küttler et al. [87]. The implementation of the aforementioned methodology as well as both the standard and the isogeometric mortar-based mapping methods are hosted in the open-source software EMPIRE (Wang [86]).

Accordingly, the displacement and the traction fields can be transformed using Eq. (6.10) or Eq. (6.15) depending on the transformation direction which is known as *consistent transformation*, see also in Küttler et al. [87]. In case Eq. (6.10) is used for the transformation of displacements, all additional Penalty terms defined in Eqs. (6.11c) are considered, since the displacement and the rotation continuity across the multipatches along with the Dirichlet boundary conditions need in this case to be weakly enforced. On the other hand, only the additional Penalty matrix $\mathbf{C}_{\hat{\alpha},0,0}$ is employed in case Eq. (6.10) is used for the transformation of the tractions, excluding continuity of the rotation field and weak application of the Dirichlet boundary conditions. This is so because the interest in this case lies only in the continuity of the transformed traction field across the multipatches. Let $\tilde{\mathbf{F}}_{\mathrm{b}}$ and $\tilde{\mathbf{F}}_{\mathrm{t}}$ be the consistent force vectors corresponding to the traction field $\tilde{\mathbf{b}}$ on the CPs of the multipatch surface (or finite element nodes when FEM is used for the discretization of the CSD problem) and to the traction field $\tilde{\mathbf{t}}$ on the nodes of the polygonal mesh representing the fluid FSI interface. Similar to Eq. (3.10), in case the force vector $\tilde{\mathbf{F}}_{\mathrm{b}}$ is computed on a multipatch NURBS surface, it can be split among each patch $\Omega^{(i)}$, namely,

$$\tilde{\mathbf{F}}_{\mathrm{b}} = \left[\tilde{\mathbf{F}}_{\mathrm{b}}^{(1)} \quad \cdots \quad \tilde{\mathbf{F}}_{\mathrm{b}}^{(n_{\mathrm{s}})} \right]^{\mathrm{T}} . \tag{6.23}$$

The entries of the force vectors $\tilde{\mathbf{F}}_{\mathrm{b}}^{(i)}$ and $\tilde{\mathbf{F}}_{\mathrm{t}}$ are then given by,

$$\tilde{F}_{\mathrm{b}(j)}^{(i)} = \left\langle \bar{\boldsymbol{\phi}}_j^{(i)}, \tilde{\mathbf{b}} \right\rangle_{0,\mathscr{S}^{(i)}} , \tag{6.24a}$$

$$\tilde{F}_{\mathrm{t}(i)} = \left\langle \boldsymbol{\phi}_i^{\mathrm{h}}, \tilde{\mathbf{t}} \right\rangle_{0,\mathscr{S}_{\mathrm{h}}} , \tag{6.24b}$$

respectively, $\boldsymbol{\phi}_i^{\mathrm{h}}$ and $\bar{\boldsymbol{\phi}}_j^{(i)}$ being the vector-valued standard FEM and the NURBS basis functions, see in Eqs. (6.8a) and (6.8b), respectively. In case the CSD problem is discretized using standard FEM, the consistent force vector $\tilde{\mathbf{F}}_{\mathrm{b}}$ on the structural FSI interface is computed similar to the fluid consistent force vector in Eq. (6.24b). In this way, the fluid traction field $\tilde{\mathbf{t}}$ can be transformed into the traction field on the structural domain $\tilde{\mathbf{b}}$ using Eq. (6.15), which can then be transformed into the consistent force vector $\tilde{\mathbf{F}}_{\mathrm{b}}$ similar to Eq. (6.24b).

An alternative to fulfilling Eq. (6.20b) is the satisfaction of the discrete virtual work on the FSI interface, which in matrix form reads,

$$\delta \hat{\boldsymbol{\mathcal{U}}}^{\mathrm{T}} \tilde{\mathbf{F}}_{\mathrm{t}} - \delta \hat{\mathbf{d}}_{|\mathscr{S}}^{\mathrm{T}} \tilde{\mathbf{F}}_{\mathrm{b}} = 0 , \tag{6.25}$$

where $\delta \hat{\boldsymbol{\mathcal{U}}}$ and $\delta \hat{\mathbf{d}}_{|\mathscr{S}}$ stand for the virtual fluid displacement DOFs on $\mathscr{S}_{\mathrm{h}}$ and the virtual structural displacement DOFs on $\mathscr{S}$. The transformation of the virtual displacement field as per Eq. (6.15) then reads,

$$\delta \hat{\boldsymbol{\mathcal{U}}} = \mathbf{C}_{\mathrm{nn}}^{-1} \mathbf{C}_{\mathrm{nr}} \delta \hat{\mathbf{d}}_{|\mathscr{S}} . \tag{6.26}$$

Substituting Eq. (6.26) into Eq. (6.25) results in,

$$\tilde{\mathbf{F}}_{\mathrm{b}} = \left(\mathbf{C}_{\mathrm{nn}}^{-1} \mathbf{C}_{\mathrm{nr}} \right)^{\mathrm{T}} \tilde{\mathbf{F}}_{\mathrm{t}} . \tag{6.27}$$

The relation above in Eq. (6.27) is known as *conservative mapping*, see also in Wang [86] and Küttler et al. [87], and can be used only for the transformation of forces ensuring the satisfaction of the discrete interface virtual work in Eq. (6.25) instead of the satisfaction of the traction equilibrium condition in Eq. (6.20b). Similar to the consistent mapping, if the conservative transformation of forces takes place from the CAD surface to the low order discretized surface in the frame of the ECL method, relation in Eq. (6.27) simply inverses, namely,

$$\tilde{\mathbf{F}}_{\mathrm{b}}^{\mathrm{h}} = \left(\mathbf{C}_{\mathrm{rr}}^{-1}\,\mathbf{C}_{\mathrm{rn}}\right)^{\mathrm{T}}\,\tilde{\mathbf{F}}_{\mathrm{b}}\,, \tag{6.28}$$

where in this thesis the additional Penalty terms are excluded for the conservative transformation of the force vectors and where $\tilde{\mathbf{F}}_{\mathrm{b}}^{\mathrm{h}}$ stands for the consistent force vector on the standard FEM discretized CSD problem whose entries are computed similar to Eq. (6.24b). Thus, a direct transformation of the consistent force vectors is offered by the conservative mapping as per Eqs. (6.27) and (6.28) bypassing the computation of the traction fields. A thorough comparison of both the consistent and the conservative transformation of tractions and forces, respectively, is provided in Wang [86] and in practice either can be used.

6.4 Numerical examples

In the following sections three numerical examples are provided for the demonstration and the validation of the proposed isogeometric mortar-based mapping method. The first one is the well-established cavity FSI benchmark (Sec. 6.4.1), see in Kassiotis et al. [88], which due to the ease of its geometry allows for a detailed evaluation of the field transformation properties and attributes of the isogeometric mortar-based mapping method. The second numerical example consists of the FSI simulation of the hangar (Sec. 4.2.3) in numerical wind tunnel for three different inner pressure magnitudes extending isogeometric membrane analysis on multipatches to FSI. Lastly, the FSI simulation of the NREL phase VI wind turbine with flexible blades in numerical wind tunnel is investigated (Sec. 6.4.3), see also in Sicklinger et al. [82], thus extending isogeometric analysis of Kirchhoff-Love shells on multipatches in large scale engineering multiphysics problems. For the sake of clarity, let in the sequel $\hat{\mathbf{d}}_{\mathrm{h}\,|_{\mathscr{S}}}$ and $\tilde{\mathbf{b}}_{\mathrm{h}}$ be the displacement and traction fields at the structural FSI interface when standard FEM is used for the discretization of the CSD problem.

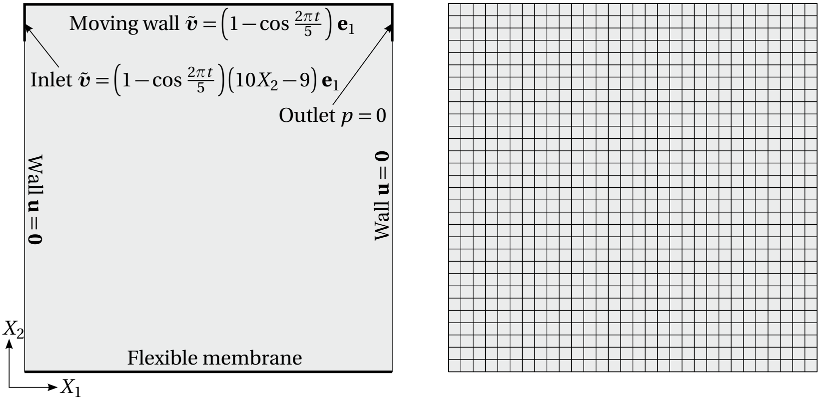

(a) Problem placement.

(b) CFD computational domain.

Figure 6.5: Lid-driven cavity: Problem placement and CFD computational domain.

6.4.1 Lid-driven cavity

In this section the lid-driven cavity FSI benchmark is employed (Fig. 6.5), see also in Kassiotis et al. [88], for the demonstration and evaluation of the isogeometric mortar-based mapping method and the application of isogeometric membrane analysis on multipatches in multiphysics problems, due to the simplicity of its geometry while relatively large deformations are allowed. For this case, the kinematic viscosity is chosen as $\tilde{\nu} = 10^{-2}$ m^2/s, the left and right walls are fixed where the fluid velocity is zero, the top wall is moving with a time varying velocity $\tilde{\boldsymbol{v}} = \big(1 - \cos(2\pi t/5)\big)\mathbf{e}_1$ [m/s] and a flexible membrane is attached at the bottom, see left part of Fig. 6.5(a). The whole surface of the flexible membrane represents the FSI interface, thus $\mathscr{S}$ and Ω are in this identical. Additionally, a small portion of the left and right fixed walls towards the upper moving wall are chosen as inlet and the outlet, respectively. Accordingly, the part representing the inlet allows for a transition from the zero to the prescribed velocity at the moving top wall whereas the pressure is prescribed to zero along the part representing the outlet. This allows for easier convergence in the fluid domain since the incompressibility condition in Eq. (6.17b) can be easier

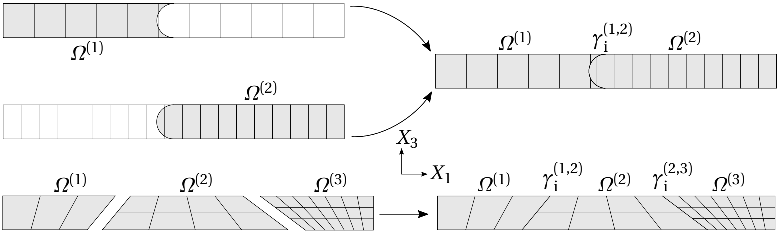

Figure 6.6: Lid-driven cavity: Trimmed vs untrimmed representation of the flexible membrane's geometry.

satisfied. Regarding the flexible membrane at the bottom, its Young's modulus, Poisson ratio, density and thickness are chosen as $E = 250$ Pa, $\nu = 0$, $\rho = 500$ Kg/m^3 and $\bar{h} = 2$ mm, respectively. For this numerical example, the applied prestress is zero. This can cause problems to some linear equation solvers as the CSD problem is singular in the first solution step due to the negligible structural stiffness in X_2-direction. The aforementioned problem can be circumvented by adding a small amount of prestress at the first Newton-Raphson iteration of the CSD problem and then release it. The time span and the time step size for the coupled problem is chosen as $\mathbb{T} = [0, 20]$ s and $\Delta t = 10^{-2}$ s, respectively, whereas the implicit Euler time integration scheme within OpenFOAM® is herein employed for the time discretization of the fluid problem. The Reynolds number[2] in this case does not exceed 200, thus resulting in a laminar flow.

Accordingly, the CFD domain is a unit square with thickness of 10 cm. The CFD problem is solved as two-dimensional in X_1-X_2 plane, meaning that the velocity and pressure are constant in the width X_3-direction. Accordingly, the CFD domain is discretized using a 30×30 grid for all employed simulations, see Fig. 6.5(b). On the other hand, the membrane structure is discretized using a reference finite element mesh with 100 bilinear elements (FEM100), a coarse finite element mesh with six bilinear elements (FEM6), a single patch geometry with twenty quadratic in X_1-direction and

---

[2] The Reynolds number is given by $\text{Re} = uL/\tilde{\nu}$ where u and L is a characteristic velocity and a characteristic length, respectively, and it can be used for classification of fluid flows as laminar or turbulent.

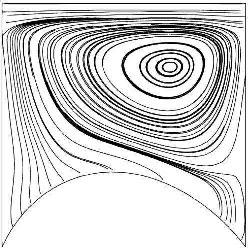

(a) Reference FSI-FEM100.

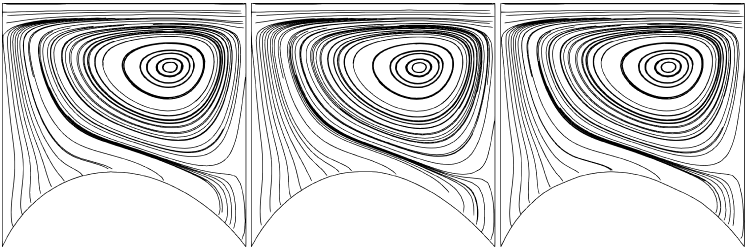

(b) FSI-IGA1. (c) FSI-IGA2. (d) FSI-IGA3.

Figure 6.7: Lid-driven cavity: Streamlines of the CFD solution over the deformed domain at time $t = 19$ s.

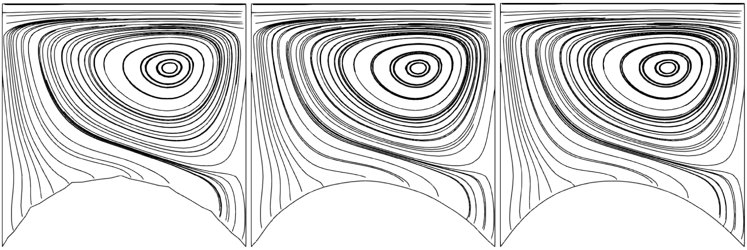

(a) FSI-FEM6. (b) FSI-FEM6-IGA1. (c) FSI-FEM6-IGA2.

Figure 6.8: Lid-driven cavity: Streamlines of the CFD solution over the deformed domain without and with ECL at time $t = 19$ s.

linear in the X_3-direction elements (IGA1), a trimmed two-patch geometry where the interface is an arc of a circle (IGA2) see top part of Fig. 6.6 and

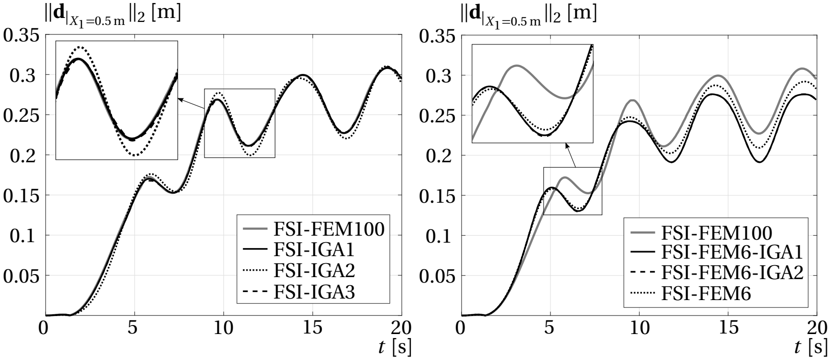

(a) Time-displacement curves.

(b) Time-displacement curves using ECL.

Figure 6.9: Lid-driven cavity: Time-displacement curves for the structural displacement at $X_1 = 0.5$ m.

an untrimmed three-patch geometry with straight interfaces (IGA3), see bottom part of Fig. 6.6. The CSD problem is also two-dimensional and accordingly the displacement field d_3^0 in the X_3-direction is set to zero. However, the latter does not necessarily mean that a constant deformation along the X_3-axis is obtained and thus a small variation of the structural deformation along the X_3-axis occurs for some of the employed structural discretizations.

A set of FSI simulations is accordingly performed involving FEM100 mesh for the structure as reference (FSI-FEM100), IGA1 structural discretization (FSI-IGA1), IGA2 structural discretization (FSI-IGA2), IGA3 structural discretization (FSI-IGA3), FEM6 mesh for the structure (FSI-FEM6), FEM6 mesh for the structure with IGA1 parametrization for the ECL (FSI-FEM6-IGA1) and FEM6 mesh for the structure with IGA2 parametrization for the ECL (FSI-FEM6-IGA2). The streamlines of the FSI simulations at time $t = 19$ s using the IGA structural discretizations against the reference solution using FEM100 is shown in the set of Figs. 6.7 demonstrating an excellent qualitative accordance of the results. Accordingly, the streamlines of the FSI simulations at time $t = 19$ s considering the FEM6 structural mesh and the ECL with a single and a two-patch representation, namely, the FSI-FEM6-IGA1 and FSI-FEM6-IGA2 simulations, respectively, against

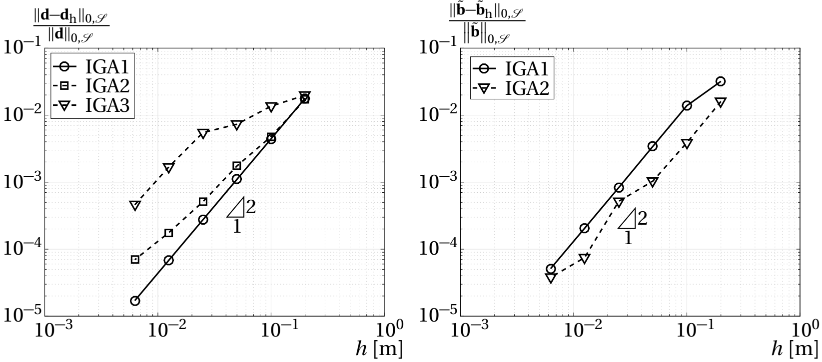

(a) Relative error in the $\mathcal{L}^2(\mathscr{S})$-norm for the displacement transformation.

(b) Relative error in the $\mathcal{L}^2(\mathscr{S})$-norm for the traction transformation.

Figure 6.10: Lid-driven cavity: Relative error in the mapping from IGA to FEM using a reference field defined on IGA1, IGA2 and IGA3 surface representations at $t = 19$ s of the corresponding FSI simulation.

the pure FSI-FEM6 simulation is shown in the set of Figs. 6.8 where the smoothing of the displacement field when using the ECL is exhibited. For the quantitative comparison of the results, the time-displacement curves of the structural displacement at the middle of the membrane, namely at $X_1 = 0.5$ m, are shown, see Fig. 6.9. Accordingly, the time-displacement curves for the FSI simulations and the FSI simulations with the ECL are depicted in Figs. 6.9(a) and 6.9(b), respectively. As it can be observed, the FSI simulations using IGA on single patch and on multipatch surfaces for the structural discretization deliver highly accurate results when compared to the reference FSI simulation involving a highly refined finite element structural discretization. On the other hand, the application of the ECL improves the quality of the interface displacement field, see Figs. 6.8(b) and 6.8(c) for the single and multipatch representation of the ECL, respectively, whereas it produces highly accurate results given that the CSD problem is only discretized using six elements, see Fig. 6.9(b).

Next, the isogeometric mortar-based mapping method is evaluated with regard to its convergence behaviour. In the following convergence graphs the observed convergence rates are mentioned, for which rigorous proofs

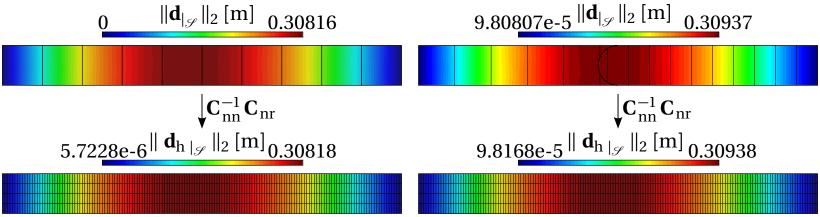

(a) Displacement transformation from IGA1 to FEM.

(b) Displacement transformation from IGA2 to FEM.

Figure 6.11: Lid-driven cavity: Mapping of the displacement field defined on IGA1 and IGA2 surface representations at $t = 19$ s from FSI-IGA1 and FSI-IGA2 simulations, respectively, to FEM for a given discretization level.

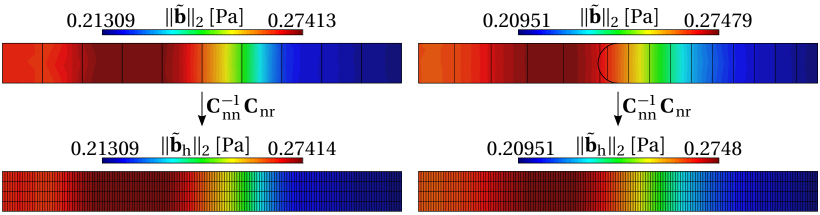

(a) Traction transformation from IGA1 to FEM.

(b) Traction transformation from IGA2 to FEM.

Figure 6.12: Lid-driven cavity: Mapping of the traction field defined on IGA1 and IGA2 surface representations at $t = 19$ s from FSI-IGA1-ECL and FSI-IGA2-ECL simulations, respectively, to FEM for a given discretization level.

are however pending. Accordingly, the quantities of interest are the displacement and the traction fields along with their corresponding transformations. The first set of graphs in Fig. 6.10 shows the convergence of the consistent mapping in the displacement and traction fields onto $\mathscr{S}_{\mathrm{h}}$, when these are originally defined on the CAD surface. More specifically, the convergence graph in Fig. 6.10(a) shows the convergence based on the relative error in the $\mathcal{L}^2(\mathscr{S})$-norm for the displacement field defined on the CAD surface for the FSI-IGA1, the FSI-IGA2 and FSI-IGA3 simulations at time $t = 19$ s against its transformed field on $\mathscr{S}_{\mathrm{h}}$, for various mesh densities with 5, 10, 20, 40, 80 and 160 elements, respectively, where h stands for

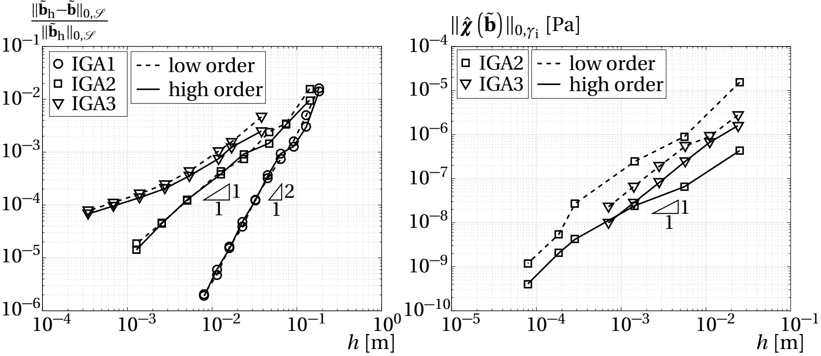

(a) Relative error in the $\mathcal{L}^2(\mathscr{S})$-norm for the mapping of the traction field defined on the FE surface.

(b) Absolute error in the $\mathcal{L}^2(\gamma_i)$-norm of the jump of the tractions.

Figure 6.13: Lid-driven cavity: Error in the transformation of tractions from FEM to IGA using a reference traction field defined on the FE surface at $t = 10$ s of the FSI simulation.

the minimum finite element edge in $\mathscr{S}_h$. Similarly, Fig. 6.10(b) shows the convergence based on the relative error in the $\mathcal{L}^2(\mathscr{S})$-norm of the traction field defined on the CAD surface for the FSI-FEM6-IGA1 and FSI-FEM6-IGA2 simulations at time $t = 19$ s against its transformed field on $\mathscr{S}_h$. Both graphs demonstrate excellent convergence rates for all geometries employed, notwithstanding the optimal convergence behaviour observed for the transformation of the fields defined on the single patch geometry when compared to the multipatch geometries, as expected. The displacement and traction fields defined on the IGA1 and IGA2 surface representations from FSI-IGA1, FSI-IGA2 and FSI-IGA1-ECL, FSI-IGA2-ECL simulations at time $t = 19$ s along with their corresponding transformations on the low order discretized surface are then shown in Figs. 6.11 and 6.12, respectively.

Subsequently, Fig. 6.13 shows the convergence graphs corresponding to the isogeometric mortar-based mapping of the fields defined on the fluid FSI interface onto the different CAD surface representations. For the refinement study, IGA1 is refined successively using 3, 6, 12, 24, 48, 96, 192, 384, 768 and 1536 elements with quadratic (low order) and cubic (high order) basis functions in X_1-direction, whereas one linear element is chosen in the X_3-direction. Then, IGA2 is refined using (5,1)-(2,1), (9,2)-(5,1),

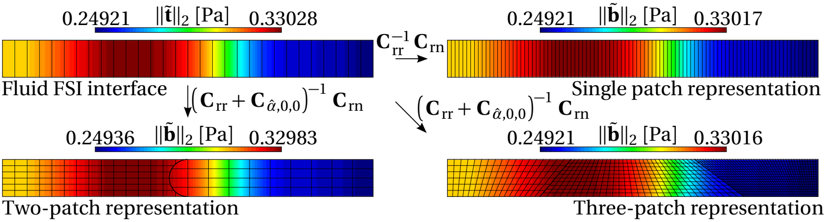

Figure 6.14: Lid-driven cavity: Mapping of the traction field defined on fluid FSI interface at $t = 19$ s from FSI-FEM100 simulation to the various CAD surface representations of $\mathscr{S}$ for given refinement levels.

(15,3)-(9,2), (30,6)-(18,4), (57,11)-(34,7), (123,31)-(81,21), (246,62)-(162,42), (492,124) and (324,84) elements in X_1, X_3-directions for patch $\mathscr{S}^{(1)}$ and patch $\mathscr{S}^{(2)}$, respectively, where the corresponding polynomial order of the basis is chosen as bilinear-biquadratic (low order) and biquadratic-bicubic (high order). Lastly, IGA3 is discretized using (3,1)-(5,1)-(8,2), (6,2)-(10,5)-(15,7), (9,4)-(15,7)-(21,10), (18,9)-(31,15)-(46,23), (36,18)-(60,30)-(89,44), (70,35)-(115,57)-(177,88), (140,70)-(230,115)-(354,177) and (280,140)-(460-230)-(708,354) elements in X_1-, X_3-directions for patch $\mathscr{S}^{(1)}$, patch $\mathscr{S}^{(2)}$ and patch $\mathscr{S}^{(3)}$, respectively, where the polynomial order of the basis is chosen as biquadratic-bilinear-bilinear (low order) and bicubic-biquadratic-bilinear (high order).

In this case, the square root of the smallest area among the isogeometric elements in the multipatch model is chosen as characteristic measure for the discretization density h for the relative errors in the domain $\mathscr{S}$, see Fig. 6.13(a). Regarding the interface error, the smallest element edge length along the interface γ_{i} is chosen as characteristic measure h of the mesh density, see Fig. 6.13(b). The relative error in the $\mathcal{L}^2(\mathscr{S})$-norm for the traction field taken from the FSI-FEM100 simulation at time $t = 19$ s when transformed onto the different CAD surface representations with the aforementioned refinement is shown in Fig. 6.13(a), for both the low and the high order bases. Accordingly, the jump in the traction field along the interface γ_{i} for the multipatch CAD representations of the surface in the $\mathcal{L}^2(\gamma_{\mathrm{i}})$-norm is shown in Fig. 6.13(b). It can be observed that the single patch solution demonstrates quadratic convergence for both polynomial

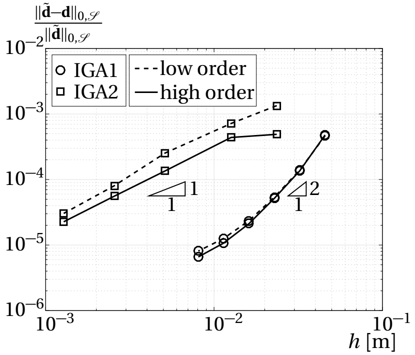

(a) Relative error in the $\mathcal{L}^2(\mathscr{S})$-norm for the mapping of the displacement field defined on the fluid FSI interface.

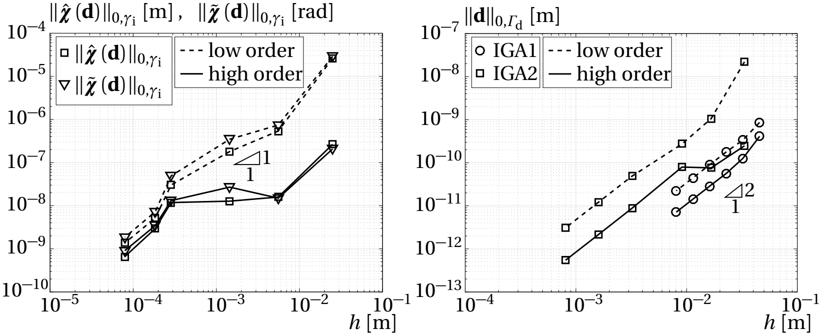

(b) Absolute error in the $\mathcal{L}^2(\gamma_i)$-norm of the jump of the displacements and rotations.

(c) Absolute error in the $\mathcal{L}^2(\Gamma_d)$-norm of the Dirichlet condition.

Figure 6.15: Lid-driven cavity: Error in the transformation of tractions from FEM to IGA using a reference displacement field defined on the FE surface at $t = 10$ s of the FSI simulation.

order settings, whereas the convergence order drops to linear concerning the multipatch models with Penalty. Moreover, the two-patch model demonstrates better convergence rates than the three-patch one does, a fact which can be attributed to the skewness of the isogeometric elements in the three-patch model in contrast to the two-patch model where only one element in X_3-direction is used. The traction field defined on the fluid FSI interface from FSI-FEM100 simulations at time $t = 19$ s and its

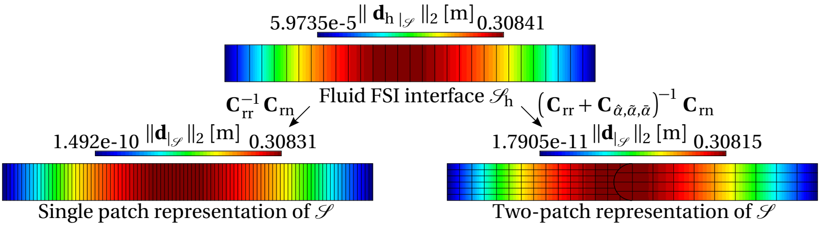

Figure 6.16: Lid-driven cavity: Transformation of the displacement field defined on the low order surface discretization at $t = 19$ s from FSI-FEM100 simulation to the various CAD surface representations of $\mathscr{S}$ for given refinement levels.

transformation onto the various CAD representations of the surface are then shown in Fig. 6.14 for a qualitative assessment of the isogeometric mortar-based mapping from a low order surface discretization to CAD surface representations.

Lastly, convergence graphs for the isogeometric mortar-based mapping of the displacement field defined on the fluid FSI interface mesh from simulation FSI-FEM100 at time $t = 19$ s onto IGA1 and IGA2 surface representations are drawn, corresponding to the ECL concept (Fig. 6.15). The refinement studies of IGA1 and IGA2 surface models are the same as previously, where herein the complete Penalty matrix $\mathbf{C}_{\hat{\alpha},\tilde{\alpha},\bar{\alpha}}$ is taken into account. The relative error on the displacement field in the $\mathcal{L}^2(\mathscr{S})$-norm is shown in Fig. 6.15(a) where as before quadratic rates of convergence are observed for the single patch model and linear convergence rates are observed for the multipatch model. The solution accuracy however is not significantly improved for the high order bases when compared to the low order bases. The interface error on the jump of the displacement field and its rotation around the tangent to the patch boundary vector for the different refinement levels in the $\mathcal{L}^2(\gamma_{\mathrm{i}})$-norm is shown in Fig. 6.15(b) regarding the trimmed two-patch model IGA2. One can observe here an improvement of the fulfilment of the interface conditions for the high order bases and an almost linear convergence rate. Then, Fig. 6.15(c) shows the error in the fulfilment of the Dirichlet condition in the $\mathcal{L}^2(\Gamma_{\mathrm{d}})$-norm for both CAD models where quadratic convergence rates are observed. Additionally, an improvement of the solution for the high order bases is

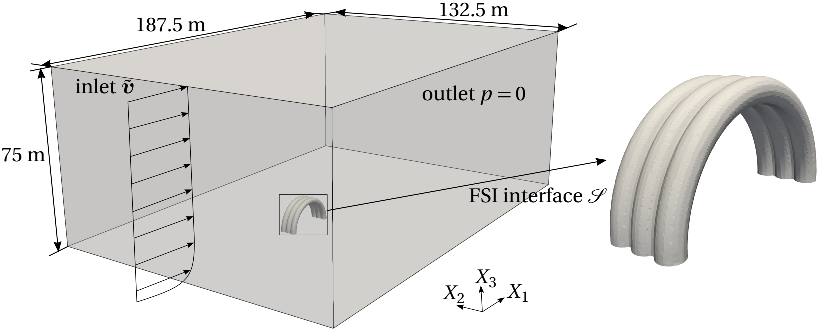

Figure 6.17: Hangar in numerical wind tunnel: Problem placement.

also observed in this case. In the latter case, the minimum element edge size along $\varGamma_\mathrm{d}$ is chosen as a measure of the discretization density h. Lastly, the 2-norm of the displacement field defined on the fluid FSI interface and the corresponding 2-norms of its transformation on the IGA1 and IGA2 surface representations is shown in Fig. 6.16. Once more, an excellent transformation can be seen which in addition respects the interface and boundary conditions when using the isogeometric mortar-based mapping method in combination with Penalty.

6.4.2 Inflatable hangar in numerical wind tunnel

In this section the FSI simulation of the inflatable hangar introduced in Sec. 4.2.3 in numerical wind tunnel is investigated, see Fig. 6.17. The material properties of the hangar are described in the corresponding Sec. 4.2.3, with the only difference that herein three different magnitudes for the inner pressure are chosen, namely, $||\mathbf{b}||_2 = 1$ KPa (p1000), $||\mathbf{b}||_2 = 2$ KPa (p2000) and $||\mathbf{b}||_2 = 4$ KPa (p4000) and the prestress is adapted using Eqs. (4.14) so that the hangar remains in equilibrium with respect to its shape. The wind is modelled through the incompressible Navier-Stokes in Eq. (6.17) with kinematic viscosity of the air equal to $\tilde{\nu} = 1.5451 \times 10^{-5}\ \mathrm{m}^2/s$. Regarding the CFD domain a mesh with ~hundred thousand polyhedral elements is employed, which is successively refined towards the hangar region whereas the locally refined region around the hangar is made using the snappy-

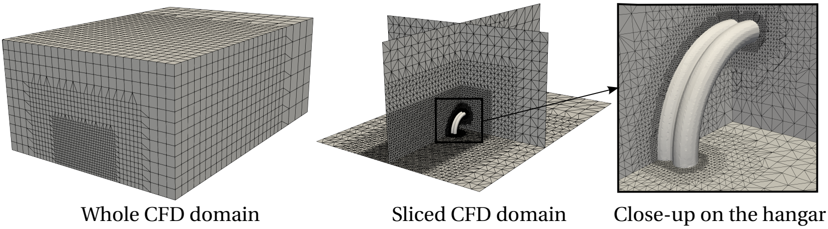
Whole CFD domain

Sliced CFD domain

Close-up on the hangar

Figure 6.18: Hangar in numerical wind tunnel: CFD computational domain.

HexMesh mesh generator of OpenFOAM®, see Fig. 6.18. Accordingly, an LES solution approach is employed using an *one equation eddy-viscosity Subgrid-Scale Model* for the turbulence modelling, see in Yoshizawa et al. [89] and Huang et al. [90] for more details. The inlet velocity $\tilde{\boldsymbol{v}}$ is chosen using an 1/7-power law from the bottom up to the height of the hangar and then is kept constant with an amplitude of 35 m/s corresponding to a hurricane condition. The latter extremely strong wind conditions are chosen to obtain significant deformations on the inflatable hangar and to investigate its behaviour when the inner pressure is successively increased. No-slip conditions are assumed at the two sides and the bottom walls whereas slip conditions[3] are assumed at the top wall of the wind tunnel. Lastly, the pressure is set to zero at the outlet. The time domain is chosen as $\mathbb{T} = [0, 5]$ s with time step size $\Delta t = 2 \times 10^{-3}$ s and the *Backward Differentiation formula 2* (BDF2) is herein employed, see in Hairer et al. [91] for more details. Before the beginning of the FSI simulation, the CFD problem is solved irrespective of the structure for twenty seconds with time step size equal to 5×10^{-3} s in order to start the FSI simulation with a divergence free velocity field, in other words a converged fluid pressure field.

Concerning the partitioned FSI approach, the consistent mapping method is chosen for the transformation of the displacement fields whereas the conservative mapping method is chosen for the transformation of the consistent force vectors as described in Sec. 6.3. Accordingly, nine simulations are performed: FSI simulations for the standard FEM structural

---

[3] A slip condition imposes the normal to the wall velocity component to zero.

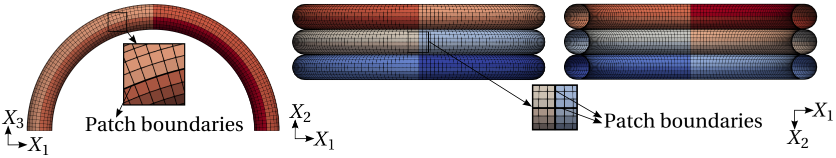

Figure 6.19: Hangar in numerical wind tunnel: Mapped finite element mesh of the hangar onto the NURBS multipatch surface (the different colors indicate the different NURBS patches).

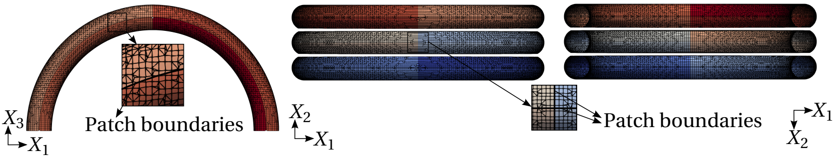

Figure 6.20: Hangar in numerical wind tunnel: Mapped fluid FSI interface mesh onto the NURBS multipatch surface (the different colors indicate the different NURBS patches).

discretization which are used as reference (see also in Sec. 4.2.3) for all three inner pressure magnitudes (FSI-FEM-p1000, FSI-FEM-p2000 and FSI-FEM-p4000), FSI simulations for the standard FEM structural discretization with an ECL whose geometry corresponds to the multipatch isogeometric discretization in Sec. 4.2.3 for all three inner pressure magnitudes (FSI-FEM-ECL-p1000, FSI-FEM-ECL-p2000 and FSI-FEM-ECL-p4000) and FSI simulations with the multipatch isogeometric structural discretization as presented in Sec. 4.2.3 (FSI-IGA-p1000, FSI-IGA-p2000 and FSI-FEM-p4000) once more for all three inner pressure magnitudes. In the following, the FSI simulations for which wrinkling occurs are separated from those ones where wrinkling does not occur. In principle, wrinkling in the standard membrane theory is not permitted as it represents deformation patterns associated with zero energy, see Sec. 2.3.3. However, these results are herein used for the demonstration of the advantages when using the ECL method in FSI simulations where the mesh distortion might be critical for the robustness of the CFD solver. According to the methodological procedure concerning the isogeometric mortar-based mapping method described in Sec. 6.1.2, the low order discretized surface is projected on

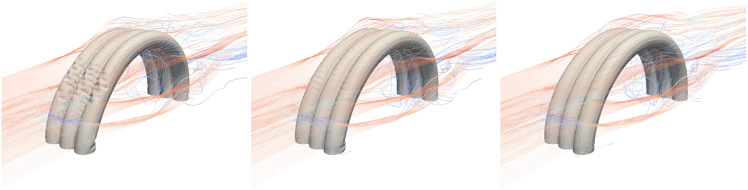

(a) FSI-FEM-p1000. (b) FSI-FEM-p2000. (c) FSI-FEM-p4000.

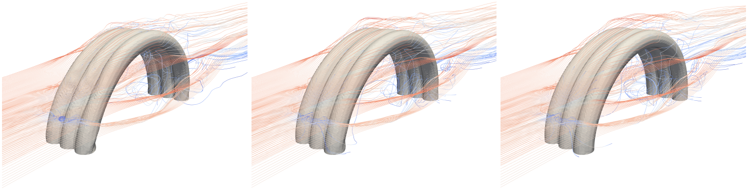

(d) FSI-FEM-ECL-p1000. (e) FSI-FEM-ECL-p2000. (f) FSI-FEM-ECL-p4000.

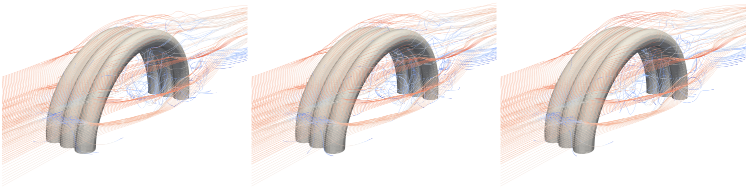

(g) FSI-IGA-p1000. (h) FSI-IGA-p2000. (i) FSI-IGA-p4000.

Figure 6.21: Hangar in numerical wind tunnel: Streamlines at $t = 0.42$ s for all performed simulations.

the NURBS multipatch geometry. The projected structural finite element mesh onto the multipatch NURBS geometry in the frame of simulations FSI-IGA-p1000, FSI-IGA-p2000 and FSI-IGA-p4000 and the projected fluid FSI interface mesh onto the multipatch NURBS geometry concerning the simulations FSI-FEM-ECL-p1000, FSI-FEM-ECL-p2000 and FSI-EFM-ECL-p4000 are depicted in Figs. 6.19 and 6.20, respectively, highlighting the boundary projection algorithm for elements with projection on more than one patch (see Fig. 6.4 from the theory Sec. 6.1.2). Moreover, the fluid FSI interface mesh does not follow the exact torus shape and the tori com-

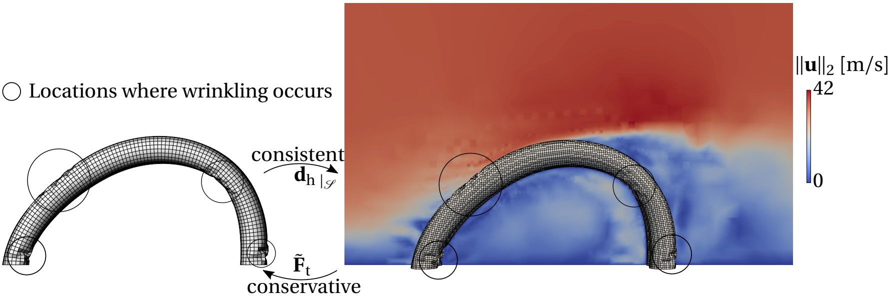

(a) FSI simulation with FEM discretization for the structural iBVP Wang [86].

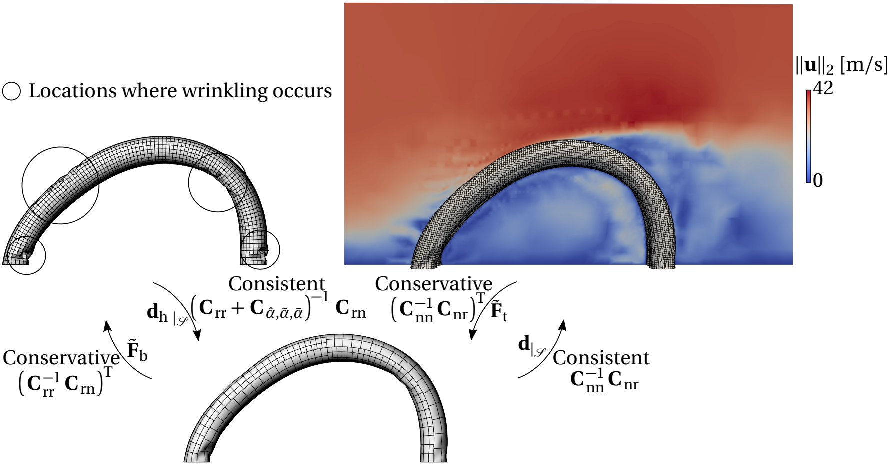

(b) FSI simulation with FEM discretization for the structural iBVP and ECL.

Figure 6.22: Hangar in numerical wind tunnel: Structural (FEM) and fluid interface deformation along with the fluid velocity magnitude $\|\mathbf{u}\|_2$ in $\tilde{V}$ at time $t = 0.61$ s for the FSI-FEM-p1000 and FSI-FEM-ECL-p1000 simulations.

prising the hangar geometry from the fluid FSI interface mesh side are not connected with each other through a shared curved interface as for the finite element and the multipatch isogeometric structural models but with straight planes allowing for a better fluid mesh between the tori. The latter choice is critical for the fluid mesh at these locations which otherwise

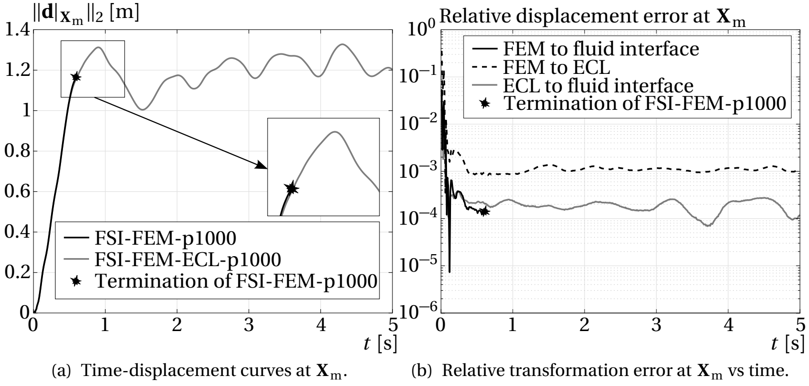

(a) Time-displacement curves at $\mathbf{X}_\mathrm{m}$. (b) Relative transformation error at $\mathbf{X}_\mathrm{m}$ vs time.

Figure 6.23: Hangar in numerical wind tunnel:
Time-displacement curves corresponding to FSI-FEM-p1000 and
FSI-FEM-ECL-p1000 simulations.

would be highly distorted. Therefore, a gap between the tori can be observed in Fig. 6.20 as the elements comprising the planes between the tori have no unique projection on the multipatch NURBS surface. This however causes no problem to the displacement transformation as it can be seen in the sequel, but it does not allow for the consistent transformation of tractions. Therefore, the conservative mapping approach is herein chosen for the transformation of the consistent force vectors, see also in Sec. 6.3. For the forthcoming investigations based on the time-displacement curves, the material point $\mathbf{X}_\mathrm{m} = 2.5\,\mathbf{e}_2 + 12.5\,\mathbf{e}_3$ in the middle of the hangar is used.

The streamlines of the CFD solution at time $t = 0.42$ s of all FSI simulations are shown in set of Figs. 6.21, where the wrinkling of the FSI-FEM-p1000 and FSI-FEM-p2000 can be observed in Figs. 6.21(a) and 6.21(b), respectively. In simulations FSI-FEM-ECL-p1000 and FSI-FEM-ECL-p2000 it can be observed how the wrinkles are not transferred onto the fluid FSI interface by means of ECL, see Figs. 6.21(d) and 6.21(e), respectively. For the corresponding FSI-IGA-p1000 and FSI-IGA-p2000 no wrinkling is observed, a fact which can be attributed to the relatively large high order elements within the corresponding highly smooth IGA discretization on multipatches. Lastly, simulations FSI-FEM-p4000, FSI-FEM-ECL-p4000

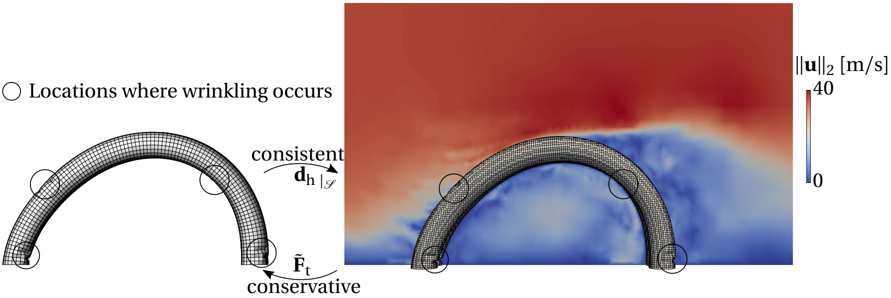

(a) FSI simulation with FEM discretization for the CSD Wang [86].

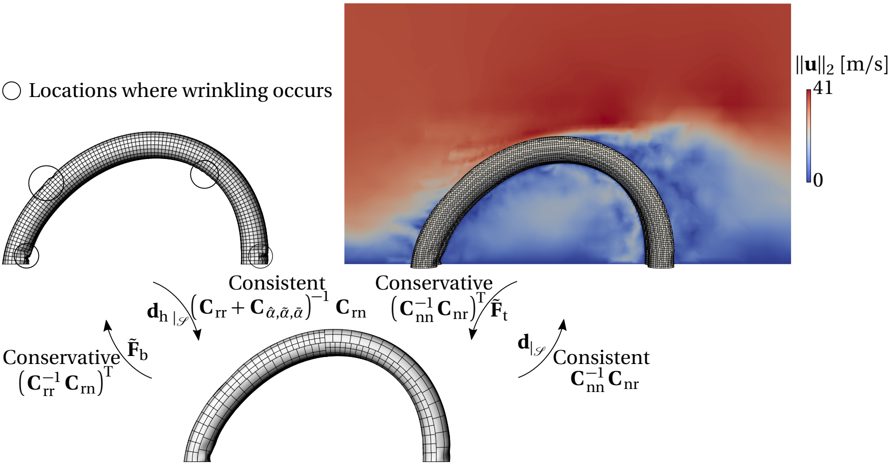

(b) FSI simulation with FEM discretization for the structural iBVP and ECL.

Figure 6.24: Hangar in numerical wind tunnel: Structural (FEM) and fluid interface deformation along with the fluid velocity magnitude $\|\mathbf{u}\|_2$ in $\tilde{V}$ at time $t = 2.1$ s for the FSI-FEM-p2000 and FSI-FEM-ECL-p2000 simulations.

and FSI-IGA-p4000 produce similar results, something which is expected as no wrinkling for this set of simulations is observed.

Firstly, the results of simulations FSI-FEM-p1000 and FSI-FEM-ECL-p1000 are evaluated and compared. For both simulations, the discretized using

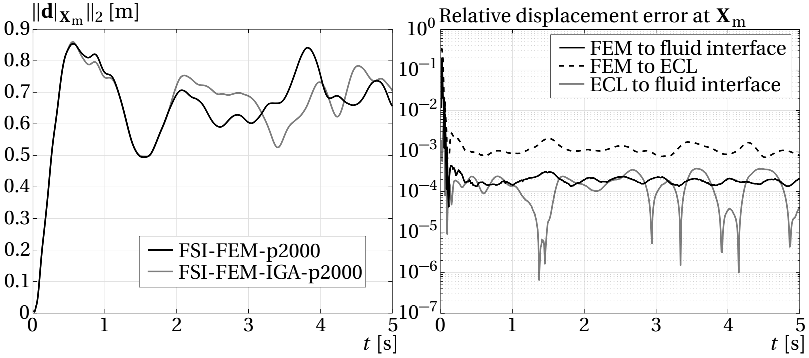

(a) Time-displacement curves at $\mathbf{X}_\mathrm{m}$. (b) Relative transformation error at $\mathbf{X}_\mathrm{m}$ vs time.

Figure 6.25: Hangar in numerical wind tunnel:
Time-displacement curves corresponding to FSI-FEM-p1000 and
FSI-FEM-ECL-p2000 simulations.

the standard FEM CSD solution is associated with wrinkling behaviour, see set of Figs. 6.22. In Fig. 6.22(a) it can be observed that the wrinkles are transferred into the fluid FSI interface whereas Fig. 6.22(b) shows how the transformed displacement field onto the fluid FSI interface is smoothed through the ECL. The latter is significant for the CFD solution as the mesh quality within the CFD domain is not only critical in terms of the solution accuracy but also from the viewpoint of the robustness of the CFD simulation. The latter means that termination of the CFD simulation due to solution singularity may occur due to severe distortion of the fluid mesh. Concerning the FSI simulation, the fluid interface displacement field is obtained by the transformation of the structural displacement field, possibly through the ECL, which is then transformed onto the displacement field of the cells in the interior of the CFD domain. The latter is achieved herein by means of a Laplacian problem using the quadratic inverse distance method towards the hangar, provided by OpenFOAM®. The corresponding time-displacement curves are shown in Fig. 6.23. A termination due to solution singularity of the CFD simulation is observed for the FSI-FEM-p1000 case at time $t = 0.618$ s, which does not occur for the FSI-FEM-ECL-p1000 simulation where the smoothing when using the ECL allows for an uncritical, with respect to CFD simulation, fluid FSI interface displacement field thus

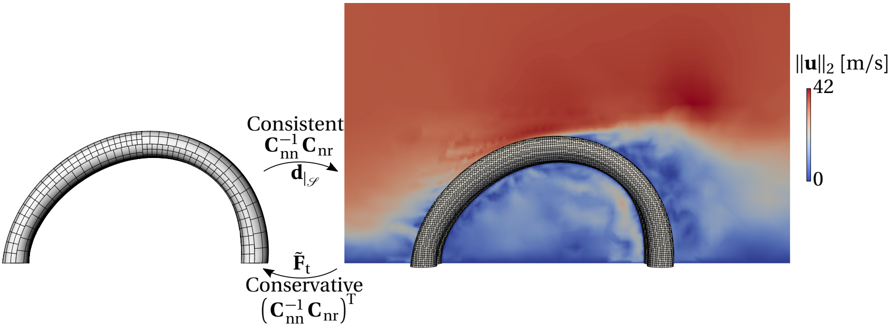

(a) Inner pressure $p = 1000$.

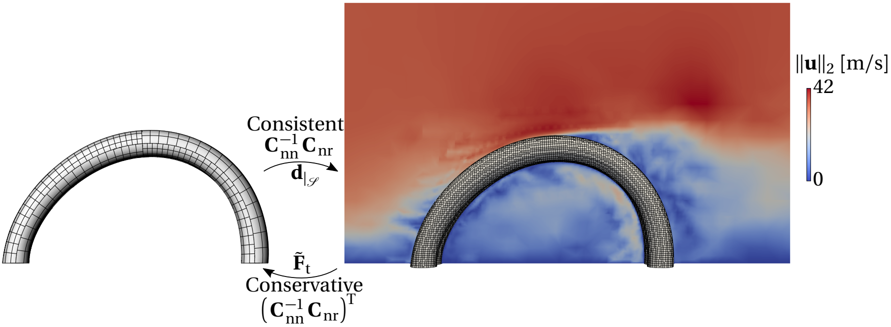

(b) Inner pressure $p = 2000$.

Figure 6.26: Hangar in numerical wind tunnel: Structural (IGA on multipatches with Nitsche) and fluid interface deformation along with the fluid velocity magnitude $\|\mathbf{u}\|_2$ in $\tilde{V}$ at time $t = 1.96$ s for the FSI-IGA-p1000 and FSI-IGA-p2000 simulations.

allowing for the simulation to carry on until the end time, that is, $t = 5$ s, see Fig. 6.23(a). Fig. 6.22 shows the structural deformation, the corresponding ECL deformation and the fluid FSI interface mesh deformation at time $t = 0.61$ s, that is, a little before the FSI-FEM-p1000 simulation terminates due to solution singularity. Moreover, the relative error in the displacement magnitude at $\mathbf{X}_{\mathrm{m}}$ against the time for each involved transformation of the displacement field is shown in Fig. 6.23(b), demonstrating a highly accurate performance of both mortar-based mapping methods.

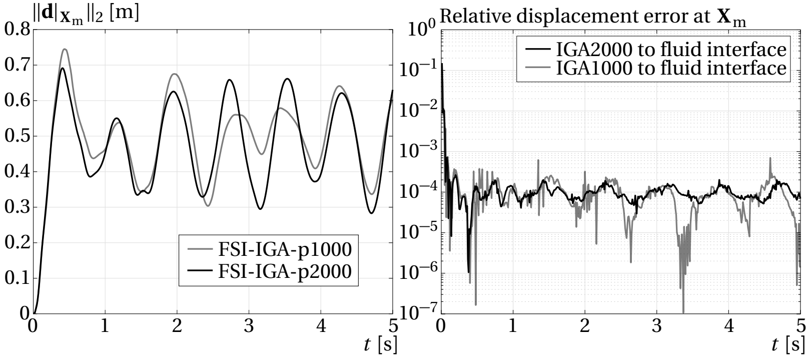

(a) Time-displacement curves at $\mathbf{X}_\mathrm{m}$. (b) Relative transformation error at $\mathbf{X}_\mathrm{m}$ vs time.

Figure 6.27: Hangar in numerical wind tunnel:
Time-displacement curves corresponding to FSI-IGA-p1000 and
FSI-IGA-p2000 simulations.

Next, the simulations FSI-FEM-p2000 and FSI-FEM-ECL-p2000 are investigated. Wrinkling behaviour is observed at isolated locations in the CSD solution herein as well, but not as significant as in the previous simulation set. However, no termination due to solution singularity of the CFD simulation is observed while the structural deformations, the corresponding ECL deformation and the fluid FSI interface mesh deformations are shown in Fig. 6.24. As before, the localized wrinkling behaviour is not transferred into the fluid FSI interface when employing the ECL, thus allowing for a smooth deformation pattern. The corresponding time-displacement curves of the structural displacements at $\mathbf{X}_\mathrm{m}$ and the relative error of the displacement transformation at $\mathbf{X}_\mathrm{m}$ (Fig. 6.25) are shown in Figs. 6.25(a) and 6.25(b), respectively. It can be observed that simulations FSI-FEM-p2000 and FSI-FEM-ECL-p2000 produce almost identical time-displacement curves up to $t = 2$ s and then a deviation is noted which can be attributed to the deformation smoothing that the ECL offers. As before, the error of the displacement transformation for all employed mortar-based mapping approaches is highly satisfactory.

Then, the FSI-IGA-p1000 and FSI-IGA-p2000 are evaluated and compared. As aforementioned, no wrinkling for these simulations is observed in con-

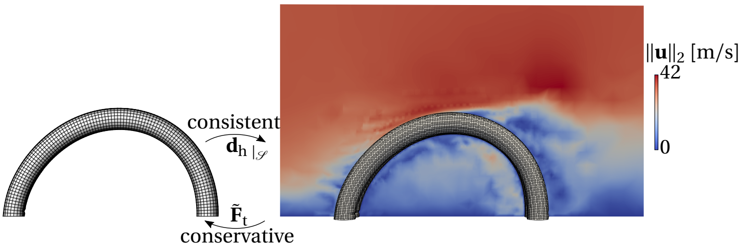

(a) FSI simulation with FEM discretization for the CSD Wang [86].

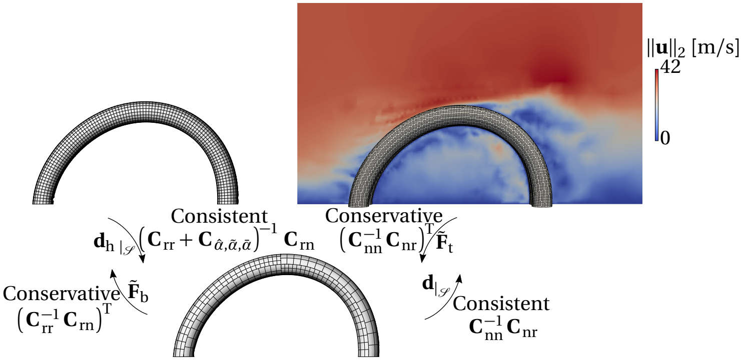

(b) FSI simulation with FEM discretization for the CSD and ECL.

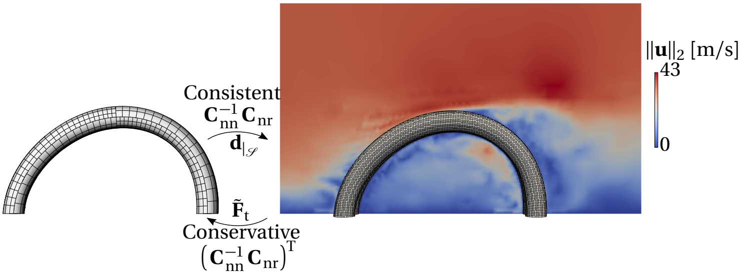

(c) FSI simulation with multipatch isogeometric discretization with Nitsche for the CSD.

Figure 6.28: Hangar in numerical wind tunnel: Structural (FEM and IGA on multipatches with Nitsche) and fluid interface deformation along with the fluid velocity magnitude $\|\mathbf{u}\|_2$ in $\tilde{V}$ at time $t = 1.9$ s with inner pressure $p = 4000$ Pa.

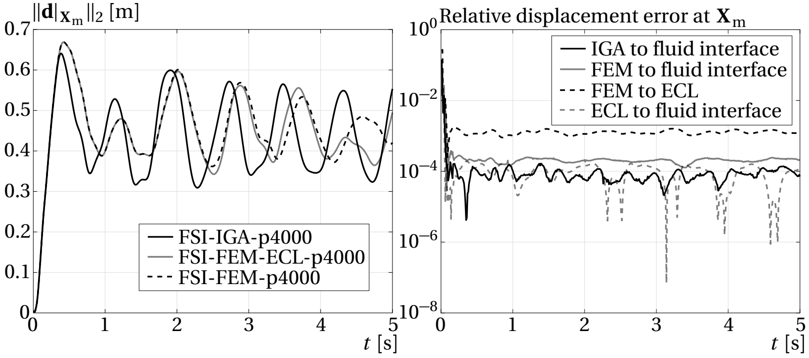

(a) Time-displacement curves at $\mathbf{X}_\mathrm{m}$. (b) Relative transformation error at $\mathbf{X}_\mathrm{m}$ vs time.

Figure 6.29: Hangar in numerical wind tunnel:
Time-displacement curves corresponding to FSI-FEM-p4000,
FSI-FEM-ECL-p4000 and FSI-IGA-p4000 simulations.

trast to the corresponding ones when using a standard finite element discretization for the CSD problem, see Figs. 6.26 for the structural and the transformed onto the fluid FSI interface deformation patterns at time $t = 1.96$ s. The corresponding time-displacement curves and the relative error in the displacement mapping at $\mathbf{X}_\mathrm{m}$ (Fig. 6.27) are shown in Figs. 6.27(a) and 6.27(b), respectively. It can be observed that the maximum oscillation amplitude decreases as the inner pressure, and accordingly the prestress, are increased, whereas the dynamic behaviour of the FSI-IGA-p2000 simulation is more stable than that for the FSI-IGA-p1000 simulation due to the added structural stability from the increased internal pressure and prestress.

Subsequently, the results from the FSI-FEM-p4000, FSI-FEM-ECL-p4000 and FSI-IGA-p4000 simulations are evaluated and compared. In this case the resulting deformation of the inflatable hangar is significantly smaller and more stable in terms of wrinkles than in the previous cases, thus exhibiting the way that the inner pressure and prestress field can be adjusted relative to each other, in order to obtain a structure with the desired stiffness without needing to modify the material parameters in the frame of FSI with pneumatic membrane structures. The structural, ECL and fluid FSI interface deformations at time $t = 1.9$ s are shown in Fig. 6.28 demonstrating good agreement of the solutions from all involved FSI simulations. For the quantitative comparison of the results (Fig. 6.29), the time-displacement curves of the structural displacement at $\mathbf{X}_{\mathrm{m}}$ is shown in Fig. 6.29(a). The amplitude and the frequency of the resulting time-displacement curves demonstrate very good agreement for the displacement at $\mathbf{X}_{\mathrm{m}}$ where a phase shift can also be observed. This can be attributed to the sensitivity of the CFD solution against the fluid FSI interface mesh quality and to the diverse CSD discretization methods. Accordingly, the relative error of the displacement transformation at $\mathbf{X}_{\mathrm{m}}$ for all involved transformations using the isogeometric and standard mortar-based mapping methods are shown in Fig 6.29(b), demonstrating that the error of the displacement transformation at $\mathbf{X}_{\mathrm{m}}$ can be considered negligible.

Lastly, the results from the isogeometric mortar-based mapping method for the transformation of the displacement field defined on the multipatch NURBS surface onto the fluid FSI interface mesh and from the structural finite element mesh to the multipatch NURBS surface are demonstrated. Accordingly, the FSI solution in terms of the displacement field from FSI-IGA-p1000 simulation at time $t = 0.9$ s defined on the multipatch NURBS geometry is transformed on the fluid FSI interface mesh, see Fig. 6.30, demonstrating an excellent accuracy even for highly non-matching surface representations.

The corresponding relative error of the displacement in the $\mathcal{L}^2(\mathscr{S})$-norm is found in this case ~0.92%. In the same way, the displacement field defined on the finite element discretized structural domain from the FSI-FEM-ECL-p1000 simulation also at time $t = 0.9$ s is transformed onto the multipatch NURBS surface, see Fig. 6.31. The relative displacement error in the $\mathcal{L}^2(\mathscr{S})$-norm is found in this case to be ~1.84%. Moreover, concerning the displacement and rotation interface jump in the $\mathcal{L}^2(\gamma_{\mathrm{i}})$-norm, these are $\|\hat{\boldsymbol{\chi}}\|_{0,\gamma_{\mathrm{i}}} = 0.02778$ m and $\|\tilde{\boldsymbol{\chi}}\|_{0,\gamma_{\mathrm{i}}} = 0.02089$ rad, respectively, whereas the $\mathcal{L}^2(\Gamma_{\mathrm{d}})$-norm of the displacement field along the Dirichlet boundary Γ_{d} is computed as $\|\mathbf{d}\|_{\Gamma_{\mathrm{d}}} = 0.0008185$ m.

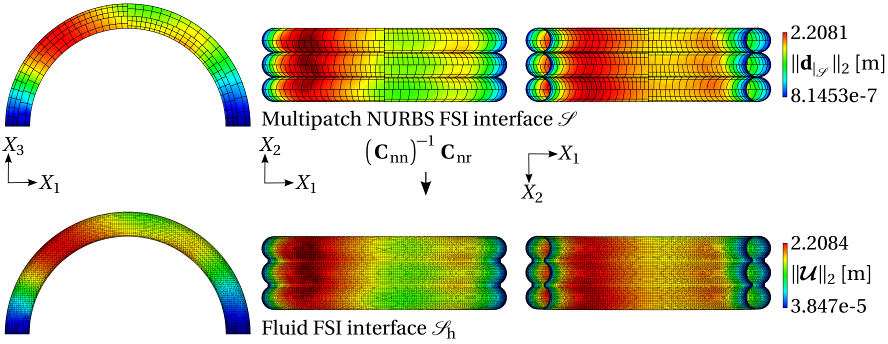

Figure 6.30: Hangar in numerical wind tunnel: Mapping of the displacement field defined on the multipatch NURBS surface at time $t = 0.9$ s from FSI-IGA-p1000 simulation onto the fluid FSI interface mesh.

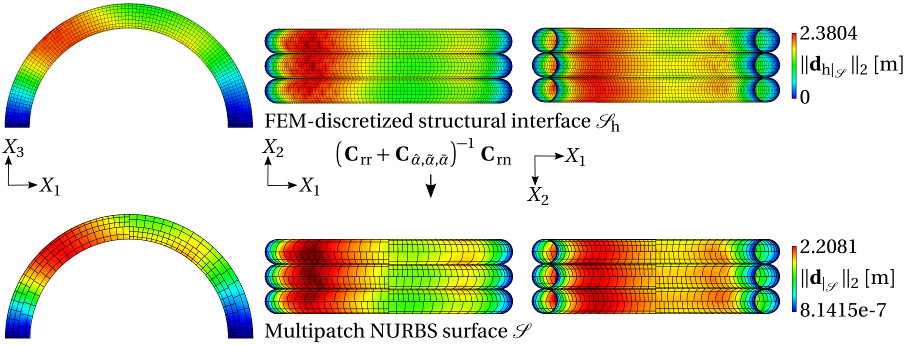

Figure 6.31: Hangar in numerical wind tunnel: Mapping of the displacement field defined on the FEM structural discretization of the hangar at time $t = 0.9$ s from FSI-FEM-ECL-p1000 simulation onto the multipatch NURBS surface.

6.4.3 NREL phase VI wind turbine in numerical wind tunnel

In this section the FSI simulation of the NREL phase VI wind turbine with flexible blades (see Sec. 5.2.4) in numerical wind tunnel is investigated, see also in Simms et al. [7], Sicklinger et al. [82], Sørensen et al. [92], and Wüchner et al. [93]. The selected material parameters for the flexible blades are presented in Sec. 5.2.4 and the kinematic viscosity for the air is as before $\tilde{\nu} = 1.5451 \times 10^{-5}$ m$^2/s$. The inlet velocity is chosen constant as $\tilde{\boldsymbol{v}} = -7\,\mathbf{e}_2$ m/s and the pressure is set equal to zero at the outlet, see Fig. 6.32. Accordingly, the side walls, the top and the bottom walls of the wind tunnel are set to slip boundary conditions. Moreover, the domain consists of two parts[4]: One non-rotating outer part and a rotating inner cylindrical part containing the rotor hub and the wind turbine blades which is rotating around X_2-axis with constant angular velocity $\omega = 7.5398$ rad/s. The fluid FSI interface is assigned to be the part containing the flexible blades. Note that $\mathscr{S}$ contains only the flexible blades across which the aerodynamic forces are acting, that is, the inner spars of the flexible blades are not part of $\mathscr{S}$, see Fig. 5.14. The time interval for the coupled problem is chosen as $\mathbb{T} = [0,5]$ s with a time step size of $\Delta t = 10^{-3}$ s and herein also the BDF2 time integration method is used for the fluid problem. As in the previous numerical example, herein also the CFD problems is solved independently of the structure for 5 seconds with the same time step size as for the FSI simulation in order to have a divergence free fluid velocity field at the start of the FSI simulation. Concerning the CSD problem, the multipatch NURBS Kirchhoff-Love shell model with Penalty is employed, see Sec. 5.2.4. Since the flexible blades are subject to constant angular velocity, a rotational frame is assumed for the structural problem. To achieve this, the corresponding CSD problem is solved with time varying gravitational $\mathbf{b}_{\mathrm{g}}$ and constant centrifugal $\mathbf{b}_{\mathrm{c}}$ body forces given by,

$$\mathbf{b}_{\mathrm{g}}(t) = \rho g \bar{h}\, \boldsymbol{\Omega}_2(t) \cdot \mathbf{e}_3\,, \tag{6.29a}$$

$$\mathbf{b}_{\mathrm{c}}(t) = \rho |X_1| \bar{h}\, \omega^2\, \mathbf{e}_1\,, \tag{6.29b}$$

respectively, where X_1 is the distance from the center of rotation. The rotation tensor $\boldsymbol{\Omega}_2(t) = \Omega_2^{ij}(t)\mathbf{e}_i \otimes \mathbf{e}_j$ around X_2-axis is defined as,

$$\Omega_2^{ij}(t) = -\sin(\omega t)\, \epsilon_2^{ij} + \cos(\omega t)\, \delta_2^{ij}\,, \tag{6.30}$$

where $\epsilon_2^{ij} = \epsilon^{\alpha\beta}$ and $\delta_2^{ij} = \delta^{\alpha\beta}$ for $\alpha, \beta = 1,3$ stand for the components of the permutation and delta Kronecker tensor on the X_1-X_3 plane, respectively, meaning that $\epsilon_2^{i2} = \epsilon_2^{2i} = \delta_2^{i2} = \delta_2^{2i} = 0$ for all $i = 1, \ldots, 3$. Concerning

---

[4] In the original study in Sicklinger et al. [82] also an independent rotation of the flexible blades around X_1-axis was considered to achieve an emergency brake manoeuvre.

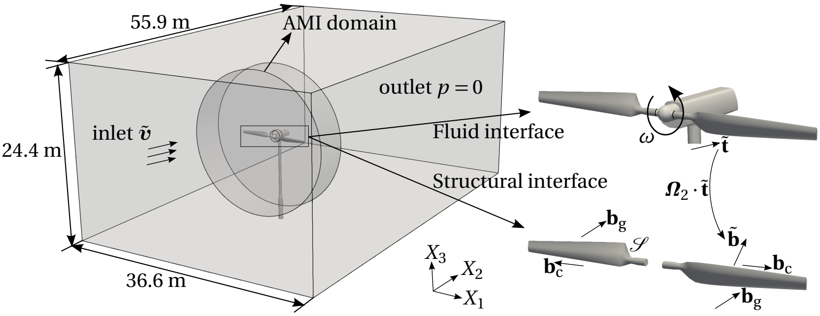

Figure 6.32: NREL phase VI wind turbine in numerical wind tunnel: Problem placement.

the aerodynamic body forces $\tilde{\mathbf{b}}$ acting along the flexible blades on $\mathscr{S}$, these are computed similar to the gravitational body forces $\mathbf{b}_\mathrm{g}$ in Eq. (6.29a), namely,

$$\tilde{\mathbf{b}}(t)=\boldsymbol{\Omega}_2(t)\cdot\tilde{\mathbf{t}}\,, \tag{6.31}$$

given that the fluid tractions $\tilde{\mathbf{t}}$ are referred to the initial configuration of the flexible blades at each time instance t. The latter approach allows for solving the CSD problem without considering inhomogeneous Dirichlet boundary conditions which accelerates the solution process. A limitation is however that only flexible blades rotating with constant angular velocity can be confronted with this approach, where in another case additional rotational inertial effects need to be addressed. Concerning the CFD setup, this is taken from the study in Sicklinger et al. [82] and corresponding views of the CFD mesh with a close-up on the right blade are depicted in Fig. 6.33 where a mesh refinement in the neighbourhood of the wind turbine can be observed and the CFD mesh comprises ~ten million cells. Concerning the CFD solution approach, the *Arbitrary Moving Interface* (AMI) method provided in OpenFOAM® is employed, in order to couple the solution between the steady and rotating parts of the fluid domain $\tilde{V}$, see also in Fig. 6.32. For the CSD, the standard finite element mesh of a shell with Reissner-Mindlin kinematics and the multipatch isogeometric model with Penalty and Kirchhoff-Love kinematics introduced in Sec. 5.2.4 are herein employed and evaluated.

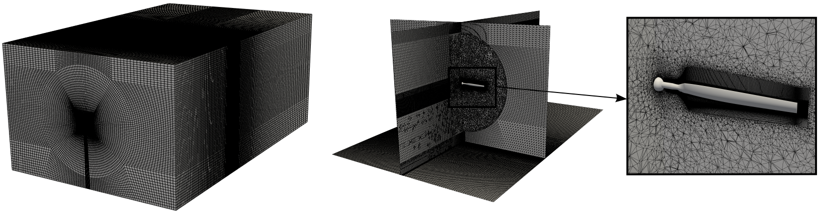

Whole CFD domain Sliced CFD domain Close-up on the right blade

Figure 6.33: NREL phase VI wind turbine in numerical wind tunnel: CFD computational domain.

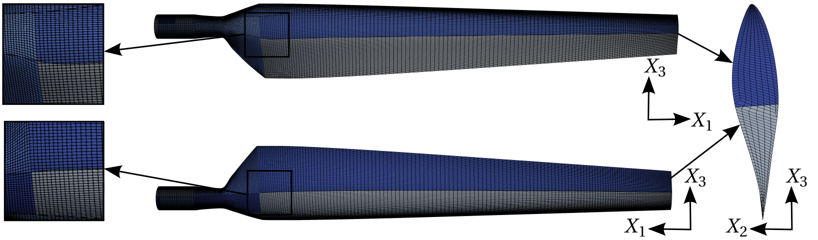

Close-up Right blade Tip

Figure 6.34: NREL phase VI wind turbine in numerical wind tunnel: Mapped fluid interface mesh onto the NURBS multipatch surface (the different colors indicate the different NURBS patches).

For the FSI simulation using the standard finite element mesh of the flexible blades, the standard mortar-based mapping method elaborated in Wang [86] is used whereas for the FSI simulation using the multipatch isogeometric discretization of the flexible blades, the isogeometric mortar-based mapping method introduced in Sec. 6.1 is used. Accordingly, the mapped elements from the fluid FSI interface onto $\mathscr{S}$ of the multipatch NURBS surface are shown in Fig. 6.34 highlighting once more the excellent performance of the proposed methodology especially across the patch boundaries (see Fig. 6.4).

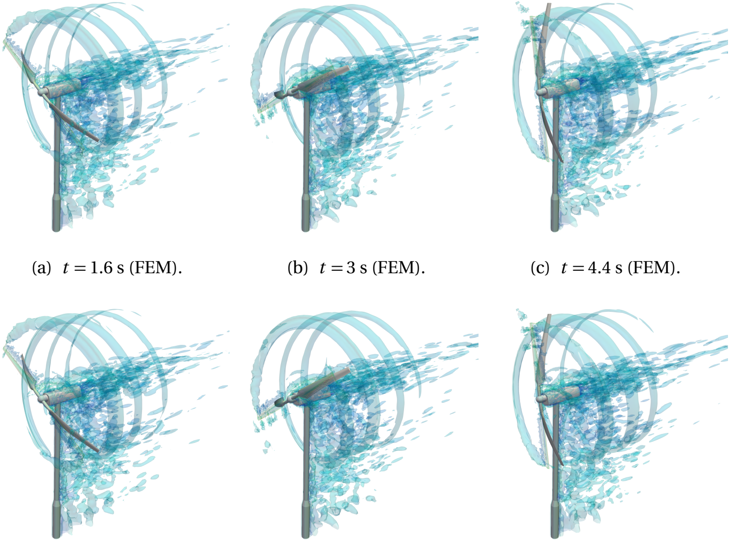

(a) $t = 1.6$ s (FEM).

(b) $t = 3$ s (FEM).

(c) $t = 4.4$ s (FEM).

(d) $t = 1.6$ s (IGA on multi-patches with Penalty).

(e) $t = 3$ s (IGA on multi-patches with Penalty).

(f) $t = 4.4$ s (IGA on multi-patches with Penalty).

Figure 6.35: NREL phase VI wind turbine in numerical wind tunnel: Q-criterion and blade deformation scaled by 170 at exemplary time instances for both the finite element and the multipatch isogeometric (Penalty) discretizations.

The Q-criterion [5] coloured with the corresponding fluid velocity magnitude at exemplary time instances for both FSI simulations with the standard finite element and multipatch isogeometric discretizations is shown in the set of Figs. 6.35 where the deformation of the flexible blades is herein scaled by 170. The results demonstrate excellent qualitative accordance regardless of the highly diverse structural discretizations and mapping techniques, thus extending the isogeometric mortar-based mapping method to real world engineering applications.

---

[5] The Q-criterion is used for vortex identification based on the second invariant of the fluid velocity gradient.

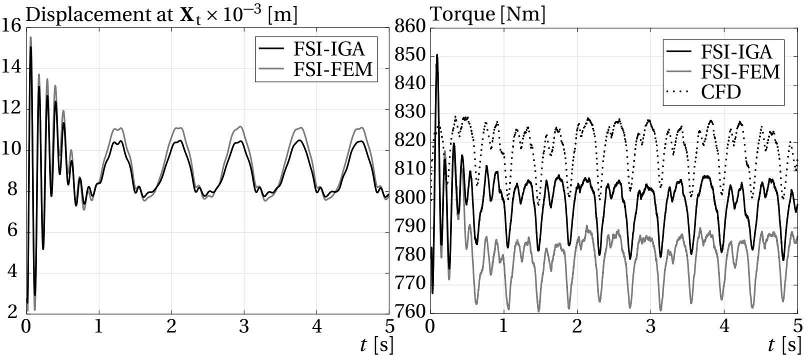

(a) Displacement at the tip versus time.

(b) Total torque versus time.

Figure 6.36: NREL phase VI wind turbine in numerical wind tunnel: Displacement at the tip $\mathbf{X}_t$ and total torque versus time.

Next, a quantitative comparison of the results in Fig. 6.36 is provided. Accordingly, the time-displacement curves at the tip of the right blade $\mathbf{X}_t = 5.029\,\mathbf{e}_1 - 0.013007\,\mathbf{e}_2 + 0.24821\,\mathbf{e}_3$ [m] and the rotor shaft torque are depicted in Figs. 6.36(a) and 6.36(b), respectively. The magnitude of the displacement field at the tip of the right blade from the CSD solution shows excellent accordance between the standard finite element mesh and the multipatch isogeometric discretization of the flexible wind turbine blades in terms of the pattern and frequency of the oscillations. However, the FEM solution exhibits slightly larger displacements which can be attributed to the underlying Reissner-Mindlin kinematics of the employed model for the standard FEM discretization in contrast to the Kirchhoff-Love shell kinematics associated with the multipatch isogeometric discretization of the flexible wind turbine blades. The error of the transformed displacement fields onto the fluid FSI interface at the tip is found negligible for this case. Concerning the rotor shaft torque, it can be observed that the pure CFD simulation produces the largest values and the FSI simulation with the FEM discretization of the flexible blades the lowest ones.

Subsequently, two points $\mathbf{X}_u = -4.7603\,\mathbf{e}_1 - 0.03568\,\mathbf{e}_2 + 0.00997\,\mathbf{e}_3$ [m] and $\mathbf{X}_d = -0.74041\,\mathbf{e}_1 + 0.07505\,\mathbf{e}_2 - 0.06956\,\mathbf{e}_3$ [m] are chosen in the upstream and the downstream sides of the left wind turbine blade, respectively, for

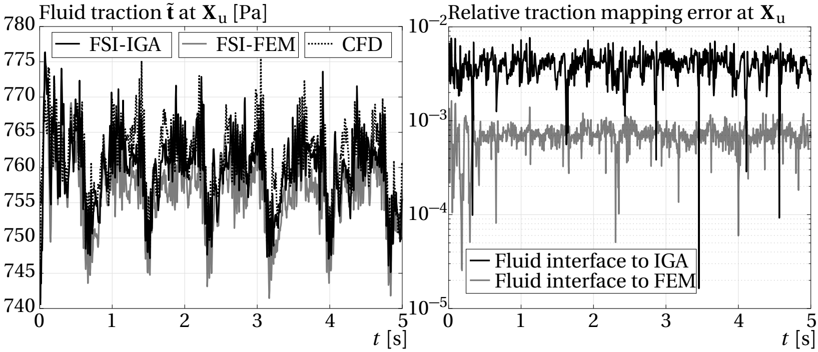

(a) Traction magnitude at $\mathbf{X}_\mathrm{u}$.

(b) Relative error of the traction transformation at $\mathbf{X}_\mathrm{u}$.

Figure 6.37: NREL phase VI wind turbine in numerical wind tunnel: Traction magnitude and the corresponding relative error of the transformation at $\mathbf{X}_\mathrm{u}$ in the upstream side versus time.

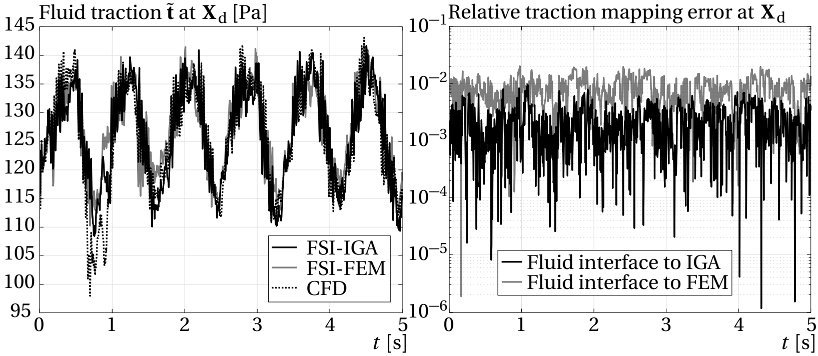

(a) Traction magnitude at $\mathbf{X}_\mathrm{d}$.

(b) Relative error of the traction transformation at $\mathbf{X}_\mathrm{d}$.

Figure 6.38: NREL phase VI wind turbine in numerical wind tunnel: Traction magnitude and the corresponding relative error at $\mathbf{X}_\mathrm{d}$ in the downstream side versus time.

the evaluation of the corresponding traction fields, see Figs. 6.37 and 6.38, respectively. Accordingly, the fluid traction field $\tilde{\mathbf{t}}$ versus the time is shown

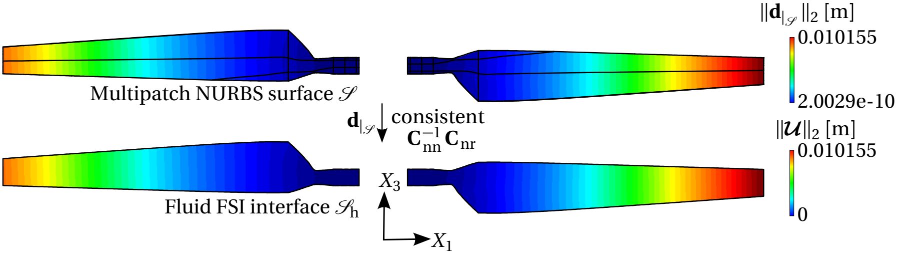

Figure 6.39: NREL phase VI wind turbine in numerical wind tunnel: Transformation of the displacement field defined on the multipatch NURBS surface at time $t = 3$ s onto fluid FSI surface.

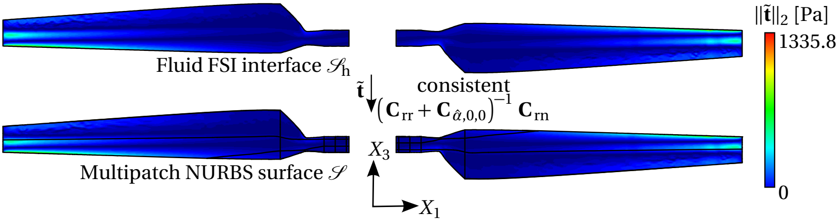

(a) Traction mapping (upstream side).

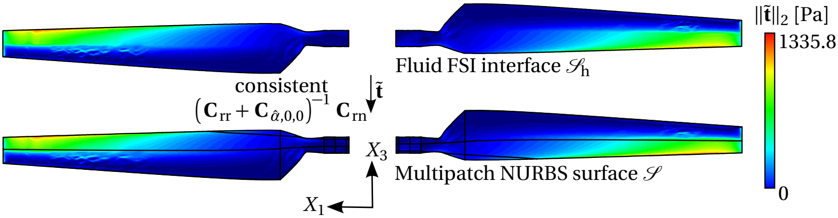

(b) Traction mapping (downstream side).

Figure 6.40: NREL phase VI wind turbine in numerical wind tunnel: Transformation of the traction field defined on the fluid FSI surface at time $t = 3$ s onto the multipatch NURBS surface.

in Figs. 6.37(a) and 6.38(a) for both FSI and the pure CFD simulations, respectively. It can be observed that taking into consideration the FSI coupling has an effect on the fluid traction field, see Fig. 6.38(a), even for relatively small displacement fields as in this numerical example. Additionally, the relative error of the traction transformation at $\mathbf{X}_\mathrm{u}$ and $\mathbf{X}_\mathrm{d}$ versus time is shown in Figs. 6.37(b) and 6.38(b), respectively, where it can be observed that both the standard and the isogeometric mortar-based mapping methods produce excellent transformations for the traction fields on the flexible wind turbine blades.

Next, the transformation of fields using the isogeometric mortar-based mapping method developed in 6.1 is quantified. Firstly, the displacement field taken from the FSI simulation with the multipatch isogeometric discretization for the flexible blades at time $t = 3$ s and transformed onto the fluid FSI interface using Eq. (6.10), see Fig. 6.39, demonstrating excellent performance of the proposed method. For this case, the relative transformation error of the displacement field in the $\mathcal{L}^2(\mathscr{S})$-norm is found 0.038% which is highly satisfactory given the complexity and the size of the geometry. Lastly, the traction field from the same FSI simulation defined on the fluid FSI interface is taken at time $t = 3$ s and transformed onto the NURBS multipatch geometry $\mathscr{S}$ using Eq. (6.15), see Fig. 6.40. For the sake of clarity, both the upstream and the downstream sides are herein depicted, see Figs. 6.40(a) and 6.40(b), respectively. The results show once more excellent accordance even for a highly oscillatory field, such as the traction field in this case, and the corresponding relative transformation error in the traction field is in this case found 4.31% based in the $\mathcal{L}^2(\mathscr{S})$-norm whereas the interface jump of the traction field between the multipatches is equal to $\|\hat{\boldsymbol{\chi}}\|_{0,\gamma_\mathrm{i}} = 0.215\ \mathrm{N/m}^2$.

6.5 Concluding remarks

This chapter demonstrates the FSI application of thin-walled structures of membrane and Kirchhoff-Love shell type discretized using isogeometric analysis on multipatches. Accordingly, a novel isogeometric mortar-based mapping method is developed for the transformation of fields between trimmed multipatch and low order discretized surfaces. The herein proposed isogeometric mortar-based mapping method can be used directly in FSI when IGA on multipatches for the CSD problem is employed and for smoothing the fields defined on the FSI interface for FSI applications where the CSD problem is discretized using standard FEM. The numerical examples comprise the lid-driven cavity FSI benchmark as standard in literature and two examples of practical relevance, that is, the inflatable hangar and the NREL phase VI wind turbine with flexible blades in corresponding numerical wind tunnels. The results suggest that isogeometric analysis on multipatches can be successfully used for multiphysics applications of the fluid-structure interaction type with many advantages stemming from the exact representation of the FSI interface via NURBS multipatches and the smooth high order fields that isogeometric analysis offers as opposed to standard FEM.

Chapter 7

Conclusions and Outlook

In this thesis the *Isogeometric Analysis* (IGA) of thin-walled structures on multiple, possibly trimmed, patches using *Non-Uniform Rational B-Splines* (NURBS) and its extension to coupled *Fluid-Structure Interaction* (FSI) is shown. Accordingly, two-dimensional linear elasticity, three-dimensional membrane and Kirchhoff-Love shell analyses are considered where also nonlinear strain measures are taken into account, see Chaps. 3, 4 and 5, respectively. Regarding the multipatch coupling and the application of weak Dirichlet boundary conditions, different constraint enforcement methods are elaborated and tested (Penalty, Lagrange Multipliers and Nitsche-type methods) in the context of IGA of thin-walled structures on multipatches.

Concerning the application of IGA for thin-walled structures in FSI a novel isogeometric mortar-based mapping method is elaborated and evaluated for geometries stemming directly from *Computer-Aided Design* (CAD), see Chap. 6. As synthesis of this work, the FSI of the inflatable hangar (introduced in 4.2.3) and the NREL phase VI wind turbine with flexible blades (introduced in 5.2.4) within corresponding numerical wind tunnels is shown in Secs. 6.4.2 and 6.4.3, respectively, as a demonstration of the aforementioned methodology to real world engineering applications in

the context of multiphysics.
Firstly, the basics are laid regarding geometric modelling, variational problems, existence and uniqueness of solutions to special types of variational problems in addition to structural analysis of Kirchhoff-Love shells and membranes. Accordingly, an introduction to the corresponding discrete equation systems of the finite element discretization is provided.
Then, an introduction to IGA is given and subsequently the application of various constraint enforcement methods consisting of Penalty, Lagrange Multipliers and Nitsche-type formulations in the context of linear elasticity is provided. This is due to the ease of two-dimensional linear elasticity compared to three-dimensional membrane and Kirchhoff-Love shell analysis, allowing for detailed evaluation of the aforementioned methods. The underlying formulations and the corresponding discrete equation systems are provided and compared using two benchmark examples, one in linear static and one in modal analysis.
Concerning IGA of three-dimensional thin-walled structures on multipatches, the aforementioned methods are selectively chosen for their application to membranes and Kirchhoff-Love shells. Accordingly, the Penalty method is extended to both membranes and Kirchhoff-Love shell analyses. The advantages of the Penalty method for these kinds of problems lie in its implementational simplicity and computational efficiency, whereas its main disadvantages are that it is variationally inconsistent and that one or more Penalty parameters have to be chosen. Nevertheless, a rule for the choice of the Penalty parameters is provided in this work. The application of the Lagrange Multipliers method is herein extended to account for the isogeometric Kirchhoff-Love shell analysis on multipatches. Accordingly, two independent Lagrange Multipliers fields are used for the enforcement of the displacement and rotation continuity between the multipatches. It is concluded that piecewise constant discontinuous discretizations for the Lagrange Multipliers fields provide accurate and stable results. Moreover, it is observed that a finer discretization for the Lagrange Multipliers field associated with the displacement continuity constraint rather than for the discretization of the Lagrange Multipliers field associated with the rotation continuity constraint leads to more stable results for the underlying discrete saddle point formulation. The Nitsche-type method is then extended to account for the isogeometric membrane analysis on multipatches within form-finding and geometrically nonlinear transient analysis. The main benefits of the Nitsche-type method lie in the consistency of its variational

formulation and in that no user interference is necessary. Accordingly, stabilization of the corresponding variational form is needed to render the method coercive. This is achieved using Penalty-like stabilization terms where the stabilization parameters can be estimated solving a series of interface and boundary eigenvalue problems. The effort involved in the latter procedure is considered minimal as the eigenvalue problems are of relatively small size. Since the Nitsche-type methods involve the interface fluxes which are nonlinear for geometrically nonlinear problems, the corresponding interface and boundary contributions need to be recomputed at each nonlinear iteration which compromises the computational efficiency. However, the latter has the advantage that the interface and boundary coupling terms are adapted during the transient analysis as opposed to Penalty and Lagrange Multipliers methods.
The novel approach of the isogeometric mortar-based mapping method is also shown as an extension of the standard mortar-based mapping method to account also for geometries stemming directly from CAD. The methodological and implementational aspects are accordingly discussed. The underlying formulation is extended with Penalty terms for the continuity enforcement of the transformed fields and the application of weak Dirichlet boundary conditions when fields are transformed onto a surface consisting of trimmed NURBS multipatches, whenever desirable. Subsequently, the concept of the *Exact Coupling Layer* (ECL) is introduced and a series of FSI simulations are used for validating the proposed methodology.

Regarding the continuity enforcement and the application of weak Dirichlet boundary conditions in IGA on multipatches, the Lagrange Multipliers method needs to be deeper investigated. In this thesis, only the original saddle point formulation of the Lagrange Multipliers method is used. This led in many cases to ill-conditioned systems, a fact which can be attributed to the failure of meeting the *Ladyzhenskaya-Babuška-Brezzi* (LBB) condition. This is because it is not a trivial problem to show that the LBB condition is met for any isogeometric and Lagrange Multipliers discretization. Alternative Lagrange Multipliers formulations, such as the mortar method, the perturbed Lagrange Multipliers method etc., need to be developed and systematically evaluated for the isogeometric membrane and the Kirchhoff-Love shell analysis on multipatches.
In this work, the Penalty method is also used for the continuity of the trans-

formed fields and the application of weak Dirichlet boundary conditions in the context of the isogeometric mortar-based mapping method. Since the mortar-based mapping method for surfaces is a linear problem, it would be beneficial to study alternative formulations, based on Lagrange Multipliers or Nitsche-type methods, for the enforcement of the aforementioned constraints. The proposed isogeometric mortar-based mapping method needs to be tested and evaluated for additional multiphysics and surface coupled problems such as, thermal-fluid-structure interaction, aeroacoustics, contact mechanics etc. Additionally, the isogeometric mortar-based mapping method needs to be extended to account for transformation of fields between two multipatch NURBS surfaces for its application to multiphysics problems where the coupled fields along the common interface are both discretized using IGA on multipatches stemming from different CAD parametrizations. The aforementioned extension could be applied to FSI using IGA for the structural discretization and the NURBS-enhanced finite element method for the fluid discretization.

Concerning the FSI simulation of the hangar in numerical wind tunnel, additional investigations need to be done. Firstly, an FSI simulation using a highly resolved finite element mesh needs to be performed for all three inner pressure magnitudes to minimize the influence of the non-smooth finite element solution in the flow fields and obtain a better quality reference solution. Then, a successive refinement of the multipatch isogeometric discretization needs to be done for the FSI simulation with all three inner pressure magnitudes to obtain a sufficiently fine structural resolution with respect to the resulting structural deformations of the herein employed FSI problems. Moreover, the influence of the volume change in the hangar on the inner pressure and nonlinear constitutive laws ought to be taken into account in order to obtain results of physical relevance since the resulting deformations are significantly large in this case.

Conclusively, regarding the FSI simulation of the NREL phase VI wind turbine with flexible blades in numerical wind tunnel, additional physical behaviours may be studied. The proposed framework can be extended to account also for varying rotational velocity of the blades which is directly exerted from the wind and to account also for the emergency brake manoeuvre studied in Sicklinger et al. [82]. Additionally, a composite material can be chosen to obtain a structural model closer to the experimental one in Simms et al. [7] within the isogeometric discretization of the Kirchhoff-Love shell problem on multipatches.

Appendix A

Discretization Aspects

Herein, a brief introduction to the discretization of the fields introduced in Chap. 2 is provided inspired by Kiendl [81]. To ease the notations, the surface normal vector in the current configuration of the surface Ω_t is written as,

$$\mathbf{a}_3 = \frac{1}{\bar{a}_3} \tilde{\mathbf{a}}_3 \,, \tag{A.1a}$$

$$\tilde{\mathbf{a}}_3 = \mathbf{a}_1 \times \mathbf{a}_2 \,, \tag{A.1b}$$

$$\bar{a}_3 = \|\tilde{\mathbf{a}}_3\|_2 \,. \tag{A.1c}$$

Given is the finite dimensional admissible space $\mathcal{V}_\mathrm{h}$ with basis $\boldsymbol{\phi}_i$, $i = 1, \ldots, \dim \mathcal{V}_\mathrm{h}$, see Sec. 2.4.1. The first derivative of each membrane strain component $\varepsilon_{\alpha\beta}$ with respect to DOF $\hat{d}_i$ in Eq. (2.58a) is given by,

$$\frac{\partial \varepsilon_{\alpha\beta}}{\partial \hat{d}_i} = \frac{1}{2} \left(\frac{\partial \boldsymbol{\phi}_i}{\partial \theta_\alpha} \cdot \mathbf{a}_\beta + \mathbf{a}_\alpha \cdot \frac{\partial \boldsymbol{\phi}_i}{\partial \theta_\beta} \right) . \tag{A.2}$$

Accordingly, the first derivative of each bending strain component $\kappa_{\alpha\beta}$ with respect to DOF $\hat{d}_i$ in Eq. (2.58a) reads,

$$\frac{\partial \kappa_{\alpha\beta}}{\partial \hat{d}_i} = -\frac{\partial \beta_{\alpha\beta}}{\partial \hat{d}_i}\,, \tag{A.3}$$

where the first derivative of each curvature component $\beta_{\alpha\beta}$ with respect to DOF $\hat{d}_i$ in the current configuration is given by,

$$\frac{\partial \beta_{\alpha\beta}}{\partial \hat{d}_i} = \frac{\partial^2 \boldsymbol{\phi}_i}{\partial \theta_\alpha \partial \theta_\beta} \cdot \mathbf{a}_3 + \frac{\partial \mathbf{a}_\alpha}{\partial \theta_\beta} \cdot \frac{\partial \mathbf{a}_3}{\partial \hat{d}_i}\,, \tag{A.4}$$

and where the first derivative of the surface normal vector in the current configuration with respect to DOF $\hat{d}_i$ is,

$$\frac{\partial \mathbf{a}_3}{\partial \hat{d}_i} = \frac{1}{\bar{a}_3} \frac{\partial \tilde{\mathbf{a}}_3}{\partial \hat{d}_i} - \frac{1}{\bar{a}_3^2} \frac{\partial \bar{a}_3}{\partial \hat{d}_i} \tilde{\mathbf{a}}_3\,, \tag{A.5}$$

with,

$$\frac{\partial \bar{a}_3}{\partial \hat{d}_i} = \frac{1}{\bar{a}_3} \tilde{\mathbf{a}}_3 \cdot \frac{\partial \tilde{\mathbf{a}}_3}{\partial \hat{d}_i}\,, \tag{A.6a}$$

$$\frac{\partial \tilde{\mathbf{a}}_3}{\partial \hat{d}_i} = \frac{\partial \boldsymbol{\phi}_i}{\partial \theta_1} \times \mathbf{a}_2 + \mathbf{a}_1 \times \frac{\partial \boldsymbol{\phi}_i}{\partial \theta_2}\,. \tag{A.6b}$$

The constitutive laws in Eqs. (2.37) are written in matrix form as,

$$\mathbf{n}_\mathrm{v} = \mathbf{D}_\mathrm{m} \boldsymbol{\varepsilon}_\mathrm{v}\,, \tag{A.7a}$$

$$\mathbf{m}_\mathrm{v} = \mathbf{D}_\mathrm{b} \boldsymbol{\kappa}_\mathrm{v}\,, \tag{A.7b}$$

$\bullet_\mathrm{v} = [\bullet^0_{11} \quad \bullet^0_{22} \quad \bullet^0_{12}]^\mathrm{T}$ being the Voigt notation of the aforementioned tensors expressed on a local orthonormal basis where the constitutive law is applicable. Accordingly, the material matrices for the membrane and the bending parts of the stiffness write,

$$\mathbf{D}_\mathrm{m} = \frac{E\,\bar{h}}{1-\nu^2} \begin{bmatrix} 1 & \nu & 0 \\ \nu & 1 & 0 \\ 0 & 0 & 1-\nu \end{bmatrix}\,, \tag{A.8a}$$

$$\mathbf{D}_\mathrm{b} = \bar{h}^2\,\mathbf{D}_\mathrm{m}\,. \tag{A.8b}$$

E, ν and $\bar{h}$ being the Young's modulus, the Poisson ratio and the thickness, respectively. The second derivative of each membrane strain component $\varepsilon_{\alpha\beta}$ with respect to DOFs $\hat{d}_i$ and $\hat{d}_j$ in Eq. (2.59a) then reads,

$$\frac{\partial^2 \varepsilon_{\alpha\beta}}{\partial \hat{d}_i \partial \hat{d}_j} = \frac{1}{2}\left(\frac{\partial \boldsymbol{\phi}_i}{\partial \theta_\alpha}\cdot\frac{\partial \boldsymbol{\phi}_j}{\partial \theta_\beta} + \frac{\partial \boldsymbol{\phi}_j}{\partial \theta_\alpha}\cdot\frac{\partial \boldsymbol{\phi}_i}{\partial \theta_\beta}\right). \tag{A.9}$$

Accordingly, the second derivative of each bending strain component $\kappa_{\alpha\beta}$ with respect to DOFs $\hat{d}_i$ and $\hat{d}_j$ in Eq. (2.59a) is given by,

$$\frac{\partial^2 \kappa_{\alpha\beta}}{\partial \hat{d}_i \partial \hat{d}_j} = -\frac{\partial^2 \beta_{\alpha\beta}}{\partial \hat{d}_i \partial \hat{d}_j}, \tag{A.10}$$

where the second derivative of each curvature component $\beta_{\alpha\beta}$ with respect to DOFs $\hat{d}_i$ and $\hat{d}_j$ is computed as,

$$\frac{\partial \beta_{\alpha\beta}}{\partial \hat{d}_i \hat{d}_j} = \frac{\partial^2 \boldsymbol{\phi}_i}{\partial \theta_\alpha \partial \theta_\beta}\cdot\frac{\partial \mathbf{a}_3}{\partial \hat{d}_j} + \frac{\partial^2 \boldsymbol{\phi}_j}{\partial \theta_\alpha \partial \theta_\beta}\cdot\frac{\partial \mathbf{a}_3}{\partial \hat{d}_i} + \frac{\partial \mathbf{a}_\alpha}{\partial \theta_\beta}\cdot\frac{\partial^2 \mathbf{a}_3}{\partial \hat{d}_i \hat{d}_j}. \tag{A.11}$$

The second derivative of the surface normal $\mathbf{a}_3$ in the current configuration with respect to DOFs $\hat{d}_i$ and $\hat{d}_j$ is given by,

$$\begin{aligned}\frac{\partial^2 \mathbf{a}_3}{\partial \hat{d}_i \partial \hat{d}_j} = {} & \frac{1}{\bar{a}_3}\frac{\partial^2 \tilde{\mathbf{a}}_3}{\partial \hat{d}_i \partial \hat{d}_j} - \frac{1}{\bar{a}_3^2}\frac{\partial \bar{a}_3}{\partial \hat{d}_j}\frac{\partial \tilde{\mathbf{a}}_3}{\partial \hat{d}_i} - \frac{1}{\bar{a}_3^2}\frac{\partial \bar{a}_3}{\partial \hat{d}_i}\frac{\partial \tilde{\mathbf{a}}_3}{\partial \hat{d}_j} + \\ & \frac{1}{\bar{a}_3^2}\left(-\frac{\partial^2 \bar{a}_3}{\partial \hat{d}_i \partial \hat{d}_j} + \frac{2}{\bar{a}_3}\frac{\partial \bar{a}_3}{\partial \hat{d}_i}\frac{\partial \bar{a}_3}{\partial \hat{d}_j}\right)\tilde{\mathbf{a}}_3,\end{aligned} \tag{A.12}$$

where the second derivatives of $\tilde{\mathbf{a}}_3$ and $\bar{a}_3$ with respect to DOFs $\hat{d}_i$ and $\hat{d}_j$ is,

$$\frac{\partial^2 \tilde{\mathbf{a}}_3}{\partial \hat{d}_i \partial \hat{d}_j} = \frac{\partial \boldsymbol{\phi}_i}{\partial \theta_1}\times\frac{\partial \boldsymbol{\phi}_j}{\partial \theta_2} + \frac{\partial \boldsymbol{\phi}_j}{\partial \theta_1}\times\frac{\partial \boldsymbol{\phi}_i}{\partial \theta_2}, \tag{A.13a}$$

$$\begin{aligned}\frac{\partial^2 \bar{a}_3}{\partial \hat{d}_i \partial \hat{d}_j} = {} & \frac{1}{\bar{a}_3}\left(\frac{\partial^2 \tilde{\mathbf{a}}_3}{\partial \hat{d}_i \partial \hat{d}_j}\cdot\tilde{\mathbf{a}}_3 + \frac{\partial \tilde{\mathbf{a}}_3}{\partial \hat{d}_i}\cdot\frac{\partial \tilde{\mathbf{a}}_3}{\partial \hat{d}_j}\right) - \\ & \frac{1}{\bar{a}_3^3}\left(\frac{\partial \tilde{\mathbf{a}}_3}{\partial \hat{d}_i}\cdot\tilde{\mathbf{a}}_3\right)\left(\frac{\partial \tilde{\mathbf{a}}_3}{\partial \hat{d}_j}\cdot\tilde{\mathbf{a}}_3\right),\end{aligned} \tag{A.13b}$$

respectively. From the above definitions it is clear that basis functions $\boldsymbol{\phi}_i$ need to be at least one time continuously differentiable for the structural analysis of Kirchhoff-Love shells but not for the structural analysis of membranes where only C^0-continuous basis functions are needed. The first derivative with respect to DOF $\hat{d}_i$ and the second derivative with respect to DOFs $\hat{d}_i$ and $\hat{d}_j$ of the cable's strain tensor $\hat{\boldsymbol{\varepsilon}}$, see Eqs. (2.58b) and (2.59b), respectively, is defined similar to Eqs. (A.2) and (A.9), respectively. The rotation vector $\boldsymbol{\omega}$ defined in Eq. (2.40) is a linear differential operator on the displacement field $\mathbf{d}$. Accordingly, the first derivative of its contravariant component ω^ζ with respect to DOF $\hat{d}_i$ appearing in Eq. (2.60a) writes,

$$\frac{\partial \omega^\zeta}{\partial \hat{d}_i} = -\left(\frac{\partial \boldsymbol{\phi}_i}{\partial \theta_\alpha} \cdot \mathbf{A}_3 + \boldsymbol{\phi}_i \cdot \mathbf{A}^\gamma \mathcal{B}_{\gamma\alpha} \right) \epsilon^{\alpha\zeta} \,. \tag{A.14}$$

Then, the B-operator matrix for the rotation vector ω_t in Eq. (2.41b) around the tangent to the boundary vector $\hat{\mathbf{e}}_\mathrm{t}$ whose norm is used as scaling for the Penalty parameter in Eq. (6.13b) is given by,

$$\mathbf{B}_\mathrm{t} = \begin{bmatrix} \frac{\partial \omega^\zeta}{\partial \hat{d}_1} \hat{e}_\mathrm{t}^\zeta & \cdots & \frac{\partial \omega^\zeta}{\partial \hat{d}_{\dim \mathcal{V}_\mathrm{h}}} \hat{e}_\mathrm{t}^\zeta \end{bmatrix} . \tag{A.15}$$

Lastly, the derivatives of the traction vector $\mathbf{t}$ with respect to DOFs is considered, as this plays an important role in the Nitsche-type formulations. The following derivations are based on membrane analysis which naturally includes two-dimensional linear elasticity. Accordingly, the first derivative of the traction vector in Eq. (2.50a) with respect to DOF $\hat{d}_i$ in Eqs. (4.8) and (4.10) reads,

$$\frac{\partial \mathbf{t}}{\partial \hat{d}_i} = \frac{\partial n^{\alpha\beta}}{\partial \hat{d}_i} \hat{e}_\alpha \mathbf{a}_\beta + \left(n^{\alpha\beta} + n_0^{\alpha\beta} \right) \hat{e}_\alpha \frac{\partial \boldsymbol{\phi}_i}{\partial \theta_\beta} \,, \tag{A.16}$$

where $\partial n^{\alpha\beta} / \partial \hat{d}_i = \mathcal{C}^{\alpha\beta\gamma\delta} \partial \varepsilon_{\gamma\delta} / \partial \hat{d}_i$ and where the derivative $\partial \varepsilon_{\gamma\delta} / \partial \hat{d}_i$ is defined in Eq. (A.2). Lastly, the second derivative of the traction vector with respect to DOFs $\hat{d}_i$ and $\hat{d}_j$ appearing in Eqs. (3.27a) and (3.30a) writes,

$$\frac{\partial^2 \mathbf{t}}{\partial \hat{d}_i \partial \hat{d}_j} = \frac{\partial n^{\alpha\beta}}{\partial \hat{d}_i} \hat{e}_\alpha \frac{\partial \boldsymbol{\phi}_j}{\partial \theta_\beta} + \frac{\partial n^{\alpha\beta}}{\partial \hat{d}_j} \hat{e}_\alpha \frac{\partial \boldsymbol{\phi}_i}{\partial \theta_\beta} + \frac{\partial^2 n^{\alpha\beta}}{\partial \hat{d}_i \partial \hat{d}_j} \hat{e}_\alpha \mathbf{a}_\beta \,, \tag{A.17}$$

where as before $\partial^2 n^{\alpha\beta} / (\partial \hat{d}_i \partial \hat{d}_j) = \mathcal{C}^{\alpha\beta\gamma\delta} \partial^2 \varepsilon^{\gamma\delta} / (\partial \hat{d}_i \partial \hat{d}_j)$ and the second derivative of the membrane strain components with respect to the DOFs is given in Eq. (A.9).

Appendix B

Co-Simulation

In a *Co-Simulation* environment, multiple programs can be combined and exchange data in arbitrary ways for solving multiphysics problems, see also in Sicklinger et al. [82]. Herein, the co-simulation environment in open-source software EMPIRE (Wang [86]) is used and extended for the prediction of *Fluid-Structure Interaction* (FSI) phenomena detailed in this thesis. The communication of the different programs is done through an *Application Programming Interface* (API) embedded into the participating programs using a *Message Passing Interface* (MPI). Given a set of $n_{\mathrm{p}} \in \mathbb{N}$ programs each of which has a set of fields $\boldsymbol{v}_i^{[j]}$ where $i = 1, \ldots, n_{\mathrm{f}}^{[j]} \in \mathbb{N}$ and $j = 1, \ldots, n_{\mathrm{p}}$, the task is to appropriately exchange these fields between the programs with predefined connections at each *Gauss-Seidel* (GS) iteration as mentioned in Sec. 6.3 for the FSI co-simulation, see Fig. B.1. The aforementioned field exchanges might be also subject to a set of filters Φ_i, $i = 1, \ldots, \bar{n}_{\mathrm{f}} \in \mathbb{N}$. The filters in this thesis comprise the standard *Mortar-based Mapping method* (MM), the *Field Integration* (FI), see in Wang [86], and the *Isogeometric Mortar-based Mapping method* (IMM) elaborated in this work. The mortar-based mapping methods are used for the transformation of fields between two non-matching interfaces. The FI filter is herein used for the transformation of traction fields into force vectors as

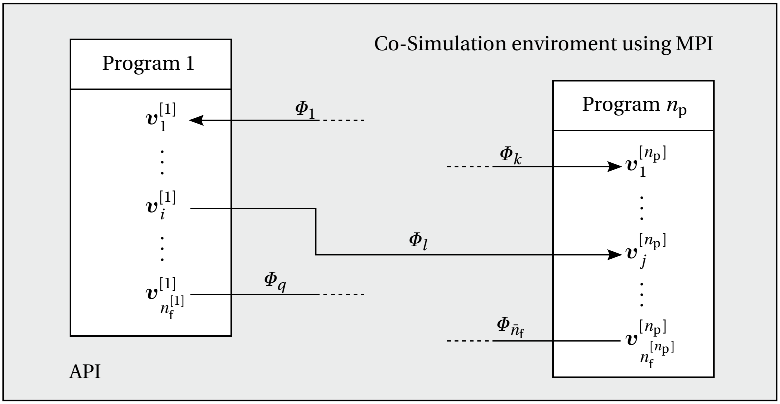

Figure B.1: Co-Simulation: Schematic of the co-simulation environment.

per Eqs. (6.24). Due to the fact that the tractions are discretized with the same basis functions as the displacement fields in the frame of the partitioned FSI approach using the mortar-based mapping method, Eq. (6.24) can be inverted and the corresponding filter is called *inverse Field Integration* (iFI), so that the force vectors can be transformed into traction fields by multiplying the discrete vector of traction *Degrees of Freedom* (DOFs) with $\mathbf{C}_\mathrm{rr}^{-1}$ or $\mathbf{C}_\mathrm{nn}^{-1}$ (Eqs. (6.11a) and (6.16)) depending on whether they are defined on a multipatch NURBS or a low order discretized surface, respectively.

Regarding the lid-driven cavity FSI benchmark, see Sec. 6.4.1, two types of simulations are used. Fig. B.2 summarizes the employed solution approaches within the corresponding co-simulation environments. The one type consists in FSI simulations where the CSD and CFD problems are directly coupled while the CSD problem is discretized using both standard FEM and IGA on both single patch and multipatch surfaces within `Carat++` or Matlab®, see Fig. B.2(a). The other type consists in FSI simulations where the CSD problem is discretized with standard FEM within `Carat++` or Matlab® and the coupling to CFD takes place through an ECL within `Carat++` or Matlab®, see Figure B.2(b). For this example, the

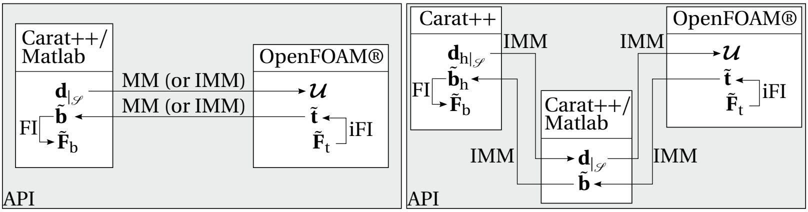

(a) FSI simulation. (b) FSI simulation with ECL.

Figure B.2: Co-Simulation for the lid-driven cavity: Co-simulation environments with participating programs and connections at each GS iteration.

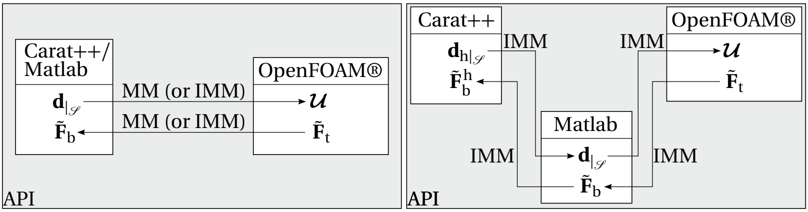

(a) FSI simulation. (b) FSI simulation with ECL.

Figure B.3: Co-Simulation for the inflatable hangar in numerical wind tunnel: Co-simulation environments with participating programs and connections at each GS iteration.

consistent approach is used for both the transformation of displacements and tractions, see also in Sec. 6.3.

Concerning the inflatable hangar in numerical wind tunnel (Sec. 6.4.2) the same two types of simulations as in the lid-driven cavity FSI benchmark are used (Fig. B.3). Herein, the difference is that the consistent force vectors are transformed using the conservative approach (Figs. B.3(a) and B.3(b)) for the traditional FSI simulations and the FSI simulations with the ECL, respectively. For this example a Matlab® code is employed for the CSD and the ECL problems using a multipatch isogeometric discretization, whereas `Carat++` is used for the standard FEM discretization of the hangar.

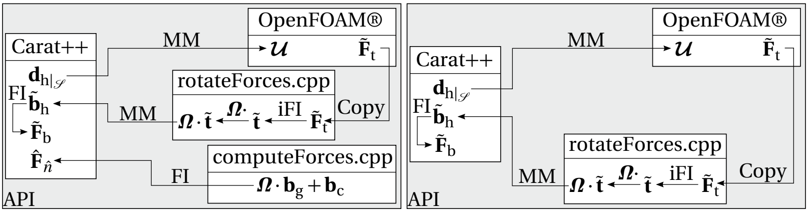

(a) FSI simulation with FEM discretization for the CSD problem.

(b) FSI simulation with multipatch isogeometric discretization for the CSD problem.

Figure B.4: Co-Simulation for the NREL phase VI wind turbine in numerical wind tunnel: Co-simulation environments with participating programs and connections at each GS iteration.

Lastly, regarding the NREL phase VI wind turbine in numerical wind tunnel, see Sec. 6.4.3, two FSI simulations are performed: One using standard FEM and one using a multipatch isogeometric discretization for the CSD problem within `Carat++`. Herein, the CSD problem is solved as non-rotating by adding time-varying gravitational forces and constant centrifugal forces, since the blades are rotating with constant angular velocity. In order to demonstrate the modularity of the aforementioned co-simulation environments, the cases are modelled differently, see Fig. B.4. For the FSI simulation with FEM discretization of the CSD problem, see Fig. B.4(a), two additional C++ programs, `rotateForces.cpp` and `computeForces.cpp` are employed. Program `rotateForces.cpp` is used for the transformation of the fluid forces $\tilde{\mathbf{t}}$ to account for the rotation of the blades. The second program `computeForces.cpp` computes the rotating gravitational body forces $\mathbf{b}_\mathrm{g}$ and the constant centrifugal body forces $\mathbf{b}_\mathrm{c}$ due to the rotational inertia on the fluid FSI interface $\mathscr{S}$ and subsequently transforms them onto the structural FSI interface using the standard mortar-based mapping method. Regarding the second FSI simulation using the multipatch isogeometric discretization for the CSD problem, see Fig. B.4(b) the C++ program `rotateForces.cpp` is employed. Accordingly, the rotating gravitational body and constant centrifugal forces are computed within the CSD program and the aerodynamic tractions are rotated using `rotateForces.cpp` program. Then, for the transformation of the resulting traction field onto the NURBS multipatch geometry the isogeometric mortar-based mapping method is used.

Bibliography

[1] Y. Başar and W. B. Krätzig. *Mechanik der Flächentragwerke. Theorie, Berechnungsmethoden, Anwendungsbeispiele*. Braunschweig: Vieweg, 1985. ISBN: 978-3-322-93983-8. DOI: `10.1007/978-3-322-93983-8`.

[2] T. J. R. Hughes, J. A. Cottrell, and Y. Bazilevs. “Isogeometric analysis: CAD, finite elements, NURBS, exact geometry and mesh refinement.” In: *Computer Methods in Applied Mechanics and Engineering* 194.39-41 (2005), pp. 4135–4195. DOI: `10.1016/j.cma.2004.10.008`.

[3] J. A. Cottrell, T. J. R. Hughes, and Y. Bazilevs. *Isogeometric analysis: Toward integration of CAD and FEA*. Chichester et al.: Wiley, 2009. ISBN: 978-0-470-74873-2.

[4] A. Buffa, G. Sangalli, and C. Schwab. “Exponential Convergence of the hp Version of Isogeometric Analysis in 1D.” In: *Spectral and high order methods for partial differential equations ICOSAHOM 2012*. Ed. by M. Azaïez, J. S. Hesthaven, and H. El Fekih. Vol. 95. Lecture notes in computational science and engineering, 1439-7358. Cham: Springer, 2014, pp. 191–203. ISBN: 978-3-319-01600-9. DOI: `10.1007/978-3-319-01601-6_15`.

[5] M. Papadrakakis. *Solving large-scale problems in mechanics: The development and application of computational solution methods / edited by Manolis Papadrakakis.* 1993. ISBN: 0471938092.

[6] M. Breitenberger, A. Apostolatos, B. Philipp, R. Wüchner, and K.-U. Bletzinger. "Analysis in computer aided design: Nonlinear isogeometric B-Rep analysis of shell structures." In: *Computer Methods in Applied Mechanics and Engineering* 284 (2015), pp. 401–457. DOI: `10.1016/j.cma.2014.09.033`.

[7] D. Simms, S. Schreck, M. Hand, and L. J. Fingersh. "NREL unsteady aerodynamics experiment in the NASA-Ames wind tunnel: a comparison of predictions to measurements." In: *National Renewable Energy Laboratory Colorado, USA* (2001).

[8] J. D. Sanders, J. E. Dolbow, and T. A. Laursen. "On methods for stabilizing constraints over enriched interfaces in elasticity." In: *International Journal for Numerical Methods in Engineering* 78.9 (2009), pp. 1009–1036. DOI: `10.1002/nme.2514`.

[9] I. Babuška. "The Finite Element Method with Penalty." In: *Mathematics of Computation* 27.122 (1973), pp. 221–228. DOI: `10.2307/2005611`.

[10] A. Apostolatos, R. Schmidt, R. Wüchner, and K.-U. Bletzinger. "A Nitsche-type formulation and comparison of the most common domain decomposition methods in isogeometric analysis." In: *International Journal for Numerical Methods in Engineering* 97.7 (2014), pp. 473–504. DOI: `10.1002/nme.4568`.

[11] I. Babuška. "The finite element method with Lagrangian multipliers." In: *Numerische Mathematik* 20.3 (1973), pp. 179–192. DOI: `10.1007/BF01436561`.

[12] B. Simeon. "On Lagrange multipliers in flexible multibody dynamics." In: *Computer Methods in Applied Mechanics and Engineering* 195.50-51 (2006), pp. 6993–7005. DOI: `10.1016/j.cma.2005.04.015`.

[13] F. Brezzi and K.-J. Bathe. "A discourse on the stability conditions for mixed finite element formulations." In: *Computer Methods in Applied Mechanics and Engineering* 82.1-3 (1990), pp. 27–57. DOI: `10.1016/0045-7825(90)90157-H`.

[14] E. Brivadis, A. Buffa, B. Wohlmuth, and L. Wunderlich. “Isogeometric mortar methods.” In: *Computer Methods in Applied Mechanics and Engineering* 284 (2015), pp. 292–319. DOI: `10.1016/j.cma.2014.09.012`.

[15] P. M. Gresho, R. L. Sani, and M. S. Engelman. *Incompressible flow and the finite element method.* Chichester: Wiley, 2000, 1998. ISBN: 0471492507.

[16] T. Teschemacher, A. M. Bauer, T. Oberbichler, M. Breitenberger, R. Rossi, R. Wüchner, and K.-U. Bletzinger. “Realization of CAD-integrated shell simulation based on isogeometric B-Rep analysis.” In: *Advanced Modeling and Simulation in Engineering Sciences* 5.1 (2018), p. 276. DOI: `10.1186/s40323-018-0109-4`.

[17] A. Fritz, S. Heber, and B. I. Wohlmuth. “A comparison of mortar and Nitsche techniques for linear elasticity.” In: *CALCOLO* 41.3 (2004), pp. 115–137. DOI: `10.1007/s10092-004-0087-4`.

[18] T. Klöppel, A. Popp, U. Küttler, and W. A. Wall. “Fluid--structure interaction for non-conforming interfaces based on a dual mortar formulation.” In: *Computer Methods in Applied Mechanics and Engineering* 200.45-46 (2011), pp. 3111–3126. DOI: `10.1016/j.cma.2011.06.006`.

[19] J. Nitsche. “Über ein Variationsprinzip zur Lösung von Dirichlet-Problemen bei Verwendung von Teilräumen, die keinen Randbedingungen unterworfen sind.” In: *Abhandlungen aus dem Mathematischen Seminar der Universität Hamburg* 36.1 (1971), pp. 9–15. DOI: `10.1007/BF02995904`.

[20] A. Hansbo and P. Hansbo. “An unfitted finite element method, based on Nitsche’s method, for elliptic interface problems.” In: *Computer Methods in Applied Mechanics and Engineering* 191.47-48 (2002), pp. 5537–5552. DOI: `10.1016/S0045-7825(02)00524-8`.

[21] P. Hansbo and J. Hermansson. “Nitsche’s method for coupling non-matching meshes in fluid-structure vibration problems.” In: *Computational Mechanics* 32.1-2 (2003), pp. 134–139. DOI: `10.1007/s00466-003-0467-7`.

[22] J. D. Sanders, T. A. Laursen, and M. A. Puso. “A Nitsche embedded mesh method.” In: *Computational Mechanics* 49.2 (2012), pp. 243–257. DOI: `10.1007/s00466-011-0641-2`.

[23] V. P. Nguyen, P. Kerfriden, M. Brino, S. P. A. Bordas, and E. Bonisoli. “Nitsche’s method for two and three dimensional NURBS patch coupling.” In: *Computational Mechanics* 53.6 (2014), pp. 1163–1182. DOI: `10.1007/s00466-013-0955-3`.

[24] X. Du, G. Zhao, and W. Wang. “Nitsche method for isogeometric analysis of Reissner--Mindlin plate with non-conforming multi-patches.” In: *Computer Aided Geometric Design* 35-36 (2015), pp. 121–136. DOI: `10.1016/j.cagd.2015.03.005`.

[25] Y. Guo, M. Ruess, and D. Schillinger. “A parameter-free variational coupling approach for trimmed isogeometric thin shells.” In: *Computational Mechanics* 59.4 (2017), pp. 693–715. DOI: `10.1007/s00466-016-1368-x`.

[26] M. Ruess, D. Schillinger, Y. Bazilevs, V. Varduhn, and E. Rank. “Weakly enforced essential boundary conditions for NURBS-embedded and trimmed NURBS geometries on the basis of the finite cell method.” In: *International Journal for Numerical Methods in Engineering* 95.10 (2013), pp. 811–846. DOI: `10.1002/nme.4522`.

[27] J. Parvizian, A. Düster, and E. Rank. “Finite cell method.” In: *Computational Mechanics* 41.1 (2007), pp. 121–133. DOI: `10.1007/s00466-007-0173-y`.

[28] M. Griebel and M. A. Schweitzer. “A Particle-Partition of Unity Method Part V: Boundary Conditions.” In: *Geometric analysis and nonlinear partial differential equations*. Ed. by S. Hildebrandt and H. Karcher. Berlin and London: Springer, 2003, pp. 519–542. ISBN: 978-3-540-44051-2. DOI: `10.1007/978-3-642-55627-2_27`.

[29] A. Apostolatos, K.-U. Bletzinger, and R. Wüchner. “Nitsche’s method for form-finding of multipatch isogeometric membrane analysis.” In: *PAMM* 18.1 (2018), e201800106. DOI: `10.1002/pamm.201800106`.

[30] M. Breuer, G. De Nayer, M. Münsch, T. Gallinger, and R. Wüchner. “Fluid--structure interaction using a partitioned semi-implicit predictor--corrector coupling scheme for the application of large-eddy simulation.” In: *Journal of Fluids and Structures* 29 (2012), pp. 107–130. DOI: `10.1016/j.jfluidstructs.2011.09.003`.

[31] G. De Nayer, J. N. Wood, M. Breuer, A. Apostolatos, and R. Wüchner. “Coupled Simulations Involving Light-weight Structures within Turbulent Flows: A Complementary Experimental and Numerical Application.” In: *PAMM* 18.1 (2018), e201800030. DOI: `10.1002/pamm.201800030`.

[32] G. De Nayer, A. Apostolatos, J. N. Wood, K. U. Bletzinger, R. Wüchner, and M. Breuer. “Numerical studies on the fuid-structure interaction of an air-inflated flexible hemisphere in turbulent flows.” In: *Journal of Fluids and Structures* 82 (2018), pp. 577–609. DOI: `10.1016/j.jfluidstructs.2018.08.005`.

[33] Y. Bazilevs, M.-C Hsu, and M. A. Scott. “Isogeometric fluid--structure interaction analysis with emphasis on non-matching discretizations, and with application to wind turbines.” In: *Computer Methods in Applied Mechanics and Engineering* 249-252 (2012), pp. 28–41. DOI: `10.1016/j.cma.2012.03.028`.

[34] J. H. Ferziger and M. Perić. *Computational Methods for Fluid Dynamics.* third, rev. edition. Berlin, Heidelberg and s.l.: Springer Berlin Heidelberg, 2002. ISBN: 9783540420743. DOI: `10.1007/978-3-642-56026-2`.

[35] R. Wüchner. “Mechanik und Numerik der Formfindung und Fluid-Struktur-Interaktion von Membrantragwerken.” Dissertation. Munich, Germany: Technical University of Munich, 2006.

[36] H. Jasak, A. Jemcov, and Z. Tukovic. “OpenFOAM: A C++ library for complex physics simulations.” In: *International Workshop on Coupled Methods in Numerical Dynamics* 1000 (2007).

[37] M. Glück, M. Breuer, F. Durst, A. Halfmann, and E. Rank. “Computation of wind-induced vibrations of flexible shells and membranous structures.” In: *Journal of Fluids and Structures* 17.5 (2003), pp. 739–765. DOI: `10.1016/S0889-9746(03)00006-9`.

[38] R. Unger, M. C. Haupt, and P. Horst. “Application of Lagrange multipliers for coupled problems in fluid and structural interactions.” In: *Computers & Structures* 85.11-14 (2007), pp. 796–809. DOI: `10.1016/j.compstruc.2007.01.006`.

[39] A. Apostolatos, K.-U. Bletzinger, and R. Wüchner. “Weak imposition of constraints for structural membranes in transient geometrically nonlinear isogeometric analysis on multipatch surfaces.” In: *Computer Methods in Applied Mechanics and Engineering* (2019). DOI: `10.1016/j.cma.2019.01.023`.

[40] A. Apostolatos, M. Breitenberger, R. Wüchner, and K.-U. Bletzinger. “Domain Decomposition Methods and Kirchhoff-Love Shell Multipatch Coupling in Isogeometric Analysis.” In: *Isogeometric analysis and applications 2014*. Ed. by B. Jüttler and B. Simeon. Vol. 107. Lecture Notes in Computational Science and Engineering. Cham, Heidelberg, and New York: Springer, 2015, pp. 73–101. ISBN: 978-3-319-23314-7. DOI: `10.1007/978-3-319-23315-4_4`.

[41] B. O’Neill. *Elementary Differential Geometry*. Academic Press, 2006.

[42] J. D. Logan. *Applied mathematics*. 3rd ed. Hoboken, N.J.: Wiley-Interscience, 2006. ISBN: 0471746622.

[43] R. Courant and D. Hilbert. *Methods of Mathematical Physics: Partial Differential Equations*. Weinheim, Germany: Wiley-VCH Verlag GmbH, 1989. ISBN: 9783527617234. DOI: `10.1002/9783527617234`.

[44] N. Kikuchi and J. T. Oden. *Contact Problems in Elasticity: A Study of Variational Inequalities and Finite Element Methods*. Studies in Applied and Numerical Mathematics. Society for Industrial and Applied Mathematics, 1988. ISBN: 978-0-89871-468-5. DOI: `10.1137/1.9781611970845`.

[45] P. G. Ciarlet. *The Finite Element Method for Elliptic Problems*. Society for Industrial and Applied Mathematics, 2002. ISBN: 978-0-89871-514-9. DOI: `10.1137/1.9780898719208`.

[46] D. Boffi, F. Brezzi, and M. Fortin. *Mixed Finite Element Methods and Applications*. Vol. 44. Berlin, Heidelberg: Springer Berlin Heidelberg, 2013. ISBN: 978-3-642-36518-8. DOI: `10.1007/978-3-642-36519-5`.

[47] J. M. Kiendl, K.-U. Bletzinger, J. Linhard, and R. Wüchner. “Isogeometric shell analysis with Kirchhoff--Love elements.” In: *Computer Methods in Applied Mechanics and Engineering* 198.49-52 (2009), pp. 3902–3914. DOI: `10.1016/j.cma.2009.08.013`.

[48] M. H. Gross, P. Kaufmann, S. Martin, and M. Botsch. *Implementation of discontinuous Galerkin Kirchhoff-Love shells.* 2009. DOI: `10.3929/ETHZ-A-006733717`.

[49] L. Noels and R. Radovitzky. “A new discontinuous Galerkin method for Kirchhoff--Love shells.” In: *Computer Methods in Applied Mechanics and Engineering* 197.33-40 (2008), pp. 2901–2929. DOI: `10.1016/j.cma.2008.01.018`.

[50] B. Philipp and K.-U. Bletzinger. “Hybrid Structures - Enlarging the Design Space of Architectural Membranes.” In: *Journal of the International Association for Shell and Spatial Structures* 54.4 (2013), pp. 281–291.

[51] B. Philipp, F. Dieringer, R. Wüchner, and K.-U. Bletzinger. “Form-finding and structural analysis for the design of hybrid structures.” In: *Journal of the International Association for Shell and Spatial Structures* 56.1 (2015), pp. 17–24.

[52] B. Philipp, M. Breitenberger, I. D’Auria, R. Wüchner, and K.-U. Bletzinger. “Integrated design and analysis of structural membranes using the Isogeometric B-Rep Analysis.” In: *Computer Methods in Applied Mechanics and Engineering* 303 (2016), pp. 312–340. DOI: `10.1016/j.cma.2016.02.003`.

[53] B. Philipp, R. Wüchner, and K.-U. Bletzinger. “Advances in the Form-finding of Structural Membranes.” In: *Procedia Engineering* 155 (2016), pp. 332–341. DOI: `10.1016/j.proeng.2016.08.036`.

[54] A. M. Bauer, M. Breitenberger, B. Philipp, R. Wüchner, and K.-U. Bletzinger. “Embedded structural entities in NURBS-based isogeometric analysis.” In: *Computer Methods in Applied Mechanics and Engineering* 325 (2017), pp. 198–218. DOI: `10.1016/j.cma.2017.07.010`.

[55] A. S. Day. “An introduction to dynamic relaxation.” In: *The Engineer* 219.5688 (1965), pp. 218–221.

[56] M. R. Barnes. “Form-finding and analysis of prestressed nets and membranes.” In: *Computers & Structures* 30.3 (1988), pp. 685–695. DOI: `10.1016/0045-7949(88)90304-5`.

[57] D. S. Wakefield. “Engineering analysis of tension structures: theory and practice.” In: *Engineering Structures* 21.8 (1999), pp. 680–690. DOI: `10.1016/S0141-0296(98)00023-6`.

[58] K. Linkwitz and H.-J. Schek. “Einige Bemerkungen zur Berechnung von vorgespannten Seilnetzkonstruktionen.” In: *Ingenieur-archiv* 40.3 (1971), pp. 145–158. DOI: `10.1007/BF00532146`.

[59] K. Linkwitz. “Formfinding by the ”Direct Approach” and Pertinent Strategies for the Conceptual Design of Prestressed and Hanging Structures.” In: *International Journal of Space Structures* 14.2 (1999), pp. 73–87. DOI: `10.1260/0266351991494713`.

[60] K.-U. Bletzinger and E. Ramm. “A General Finite Element Approach to the form Finding of Tensile Structures by the Updated Reference Strategy.” In: *International Journal of Space Structures* 14.2 (1999), pp. 131–145. DOI: `10.1260/0266351991494759`.

[61] R. Wüchner and K.-U. Bletzinger. “Stress-adapted numerical form finding of pre-stressed surfaces by the updated reference strategy.” In: *International Journal for Numerical Methods in Engineering* 64.2 (2005), pp. 143–166. DOI: `10.1002/nme.1344`.

[62] F. Dieringer, R. Wüchner, and K.-U. Bletzinger. “Practical advances in numerical form finding and cutting pattern generation for membrane structures.” In: *Journal of the International Association for Shell and Spatial Structures* 53.3 (2012), pp. 147–156.

[63] N. M. Newmark. “A method of computation for structural dynamics.” In: *Journal of the Engineering Mechanics Division* 85.3 (1959), pp. 67–94.

[64] R. W. Clough and J. Penzien. *Dynamics of structures.* New York: McGraw-Hill, 1975. ISBN: 0070113920.

[65] K. Thomsen, J. T. Petersen, E. Nim, S. Øye, and B. Petersen. “A Method for Determination of Damping for Edgewise Blade Vibrations.” In: *Wind Energy* 3.4 (2000), pp. 233–246. DOI: `10.1002/we.42`.

[66] I. Chowdhury and S. P. Dasgupta. “Computation of Rayleigh damping coefficients for large systems.” In: *The Electronic Journal of Geotechnical Engineering* 8.0 (2003), pp. 1–11.

[67] L. Piegl and W. Tiller. *The NURBS Book*. Berlin, Heidelberg: Springer Berlin Heidelberg, 1997. ISBN: 978-3-540-61545-3. DOI: `10.1007/978-3-642-59223-2`.

[68] J. M. Kiendl, Y. Bazilevs, M.-C Hsu, R. Wüchner, and K.-U. Bletzinger. "The bending strip method for isogeometric analysis of Kirchhoff--Love shell structures comprised of multiple patches." In: *Computer Methods in Applied Mechanics and Engineering* 199.37-40 (2010), pp. 2403–2416. DOI: `10.1016/j.cma.2010.03.029`.

[69] A. Toselli and O. B. Widlund. *Domain Decomposition Methods --- Algorithms and Theory*. Vol. 34. Berlin, Heidelberg: Springer Berlin Heidelberg, 2005. ISBN: 978-3-540-20696-5. DOI: `10.1007/b137868`.

[70] T. J. R. Hughes and L. P. Franca. "A new finite element formulation for fluid dynamics: VII. The Stokes problem with various well-posed boundary conditions: Symmetric formulations that converge for all velocity/pressure spaces." In: *Computer Methods in Applied Mechanics and Engineering* 65 (1987), pp. 85–96.

[71] T. J. R. Hughes, A. Reali, and G. Sangalli. "Efficient quadrature for NURBS-based isogeometric analysis." In: *Computer Methods in Applied Mechanics and Engineering* 199.5-8 (2010), pp. 301–313. DOI: `10.1016/j.cma.2008.12.004`.

[72] J. R. Barber. *Elasticity*. 3rd rev. ed. Vol. v. 172. Solid mechanics and its applications, 0925-0042. Dordrecht: Springer, 2010. ISBN: 9789048138098.

[73] M. Fischer. "Finite Element Based Simulation, Design and Control of Piezoelectric and Lightweight Smart Structures." Dissertation. Munich, Germany: Technical University of Munich, 2013.

[74] F. Otto. *Zugbeanspruchte konstruktionen*. Vol. 1. Ullstein, 1962.

[75] F. Dieringer. "Numerical Methods for the Design and Analysis of Tensile Structures." Dissertation. Munich, Germany: Technical University of Munich, 2014.

[76] B. Philipp. “Methodological Treatment of Non-linear Structural Behavior in the Design, Analysis and Verification of Lightweight Structures.” Dissertation. Munich, Germany: Technical University of Munich, 2017.

[77] R. Wüchner, H. AlSofi, M. Andre, R. Fisch, S. Sicklinger, T. Wang, K. U. Bletzinger, R. Rossi, and R. Scotta. *Computational wind-structure interaction for analysis and design of flexible, light-weight and complex-shaped structures.* Hamburg, 2014.

[78] D. M. Fryer and J. F. Harvey. *High Pressure Vessels.* Boston, MA and s.l.: Springer US, 1998. ISBN: 9781461377443. DOI: `10.1007/978-1-4615-5989-4`.

[79] A. C. Scordelis and K. S. Lo. “Computer Analysis of Cylindrical Shells.” In: *Journal Proceedings* 61.5 (1964), pp. 539–562. DOI: `10.14359/7796`.

[80] K. Y. Sze, X. H. Liu, and S. H. Lo. “Popular benchmark problems for geometric nonlinear analysis of shells.” In: *Finite Elements in Analysis and Design* 40.11 (2004), pp. 1551–1569. DOI: `10.1016/j.finel.2003.11.001`.

[81] J. M. Kiendl. “Isogeometric analysis and shape optimal design of shell structures.” Dissertation. Munich, Germany: Technical University of Munich, 2011.

[82] S. Sicklinger, V. Belsky, B. Engelmann, H. Elmqvist, H. Olsson, R. Wüchner, and K.-U. Bletzinger. “Interface Jacobian-based Co-Simulation.” In: *International Journal for Numerical Methods in Engineering* 98.6 (2014), pp. 418–444. DOI: `10.1002/nme.4637`.

[83] P. Sagaut. “Large Eddy Simulation for Incompressible Flows. An Introduction.” In: *Measurement Science and Technology* 12.10 (2001), pp. 1745–1746. DOI: `10.1088/0957-0233/12/10/707`.

[84] A. Quarteroni, A. Veneziani, and C. Vergara. “Geometric multiscale modeling of the cardiovascular system, between theory and practice.” In: *Computer Methods in Applied Mechanics and Engineering* 302 (2016), pp. 193–252. DOI: `10.1016/j.cma.2016.01.007`.

[85] O. C. Zienkiewicz, R. L. Taylor, and J. Z. Zhu. *The finite element method: Its basis and fundamentals.* 6th ed. Amsterdam and London: Elsevier Butterworth-Heinemann, 2005. ISBN: 0750663200.

[86] T. Wang. "Development of Co-Simulation Environment and Mapping Algorithms." Dissertation. Munich, Germany: Technical University of Munich, 2016.

[87] U. Küttler and W. A. Wall. "Fixed-point fluid--structure interaction solvers with dynamic relaxation." In: *Computational Mechanics* 43.1 (2008), pp. 61–72. DOI: `10.1007/s00466-008-0255-5`.

[88] C. Kassiotis, A. Ibrahimbegovic, R. Niekamp, and H. G. Matthies. "Nonlinear fluid--structure interaction problem. Part I: implicit partitioned algorithm, nonlinear stability proof and validation examples." In: *Computational Mechanics* 47.3 (2011), pp. 305–323. DOI: `10.1007/s00466-010-0545-6`.

[89] A. Yoshizawa and K. Horiuti. "A Statistically-Derived Subgrid-Scale Kinetic Energy Model for the Large-Eddy Simulation of Turbulent Flows." In: *Journal of the Physical Society of Japan* 54.8 (1985), pp. 2834–2839. DOI: `10.1143/JPSJ.54.2834`.

[90] S. Huang and Q. S. Li. "A new dynamic one-equation subgrid-scale model for large eddy simulations." In: *International Journal for Numerical Methods in Engineering* 81.7 (2010), pp. 835–865. DOI: `10.1002/nme.2715`.

[91] E. Hairer, G. Wanner, and S. P. Nørsett. *Solving ordinary differential equations I: Nonstiff problems.* 2nd rev. ed. Vol. 8. Springer series in computational mathematics, 0179-3632. Heidelberg and London: Springer, 2009. ISBN: 9783540566700. DOI: `10.1007/978-3-540-78862-1`.

[92] N. N. Sørensen, J. A. Michelsen, and S. Schreck. "Navier-Stokes predictions of the NREL phase VI rotor in the NASA Ames 80 ft × 120 ft wind tunnel." In: *Wind Energy* 5.2-3 (2002), pp. 151–169. DOI: `10.1002/we.64`.

[93] R. Wüchner, A. Apostolatos, G. De Nayer, M. Breuer, and K.-U. Bletzinger. "Coupled simulations involving light-weight structures within turbulent flows: FSI strategy and non-matching interface treatment for isogeometric b-rep analysis." In: *PAMM* 18.1 (2018), e201800107. DOI: `10.1002/pamm.201800107`.

Bisherige Titel der Schriftenreihe

Band	**Titel**
1	Frank Koschnick, *Geometrische Lockingeffekte bei Finiten Elementen und ein allgemeines Konzept zu ihrer Vermeidung,* 2004.
2	Natalia Camprubi, *Design and Analysis in Shape Optimization of Shells,* 2004.
3	Bernhard Thomee, *Physikalisch nichtlineare Berechnung von Stahlfaserbetonkonstruktionen,* 2005.
4	Fernaß Daoud, *Formoptimierung von Freiformschalen - Mathematische Algorithmen und Filtertechniken,* 2005.
5	Manfred Bischoff, *Models and Finite Elements for Thin-Walled Structures,* 2005.
6	Alexander Hörmann, *Ermittlung optimierter Stabwerkmodelle auf Basis des Kraftflusses als Anwendung plattformunabhängiger Prozesskopplung,* 2006.
7	Roland Wüchner, *Mechanik und Numerik der Formfindung und Fluid-Struktur-Interaktion von Membrantragwerken,* 2006.
8	Florian Jurecka, *Robust Design Optimization Based on Metamodeling Techniques,* 2007.
9	Johannes Linhard, *Numerisch-mechanische Betrachtung des Entwurfsprozesses von Membrantragwerken,* 2009.
10	Alexander Kupzok, *Modeling the Interaction of Wind and Membrane Structures by Numerical Simulation,* 2009.
11	Bin Yang, *Modified Particle Swarm Optimizers and their Application to Robust Design and Structural Optimization,* 2009.

Band	**Titel**
12	Michael Fleischer, *Absicherung der virtuellen Prozesskette für Folgeoperationen in der Umformtechnik*, 2009.
13	Amphon Jrusjrungkiat, *Nonlinear Analysis of Pneumatic Membranes - From Subgrid to Interface*, 2009.
14	Alexander Michalski, *Simulation leichter Flächentragwerke in einer numerisch generierten atmosphärischen Grenzschicht*, 2010.
15	Matthias Firl, *Optimal Shape Design of Shell Structures*, 2010.
16	Thomas Gallinger, *Effiziente Algorithmen zur partitionierten Lösung stark gekoppelter Probleme der Fluid-Struktur-Wechselwirkung*, 2011.
17	Josef Kiendl, *Isogeometric Analysis and Shape Optimal Design of Shell Structures*, 2011.
18	Joseph Jordan, *Effiziente Simulation großer Mauerwerksstrukturen mit diskreten Rissmodellen*, 2011.
19	Albrecht von Boetticher, *Flexible Hangmurenbarrieren: Eine numerische Modellierung des Tragwerks, der Hangmure und der Fluid-Struktur-Interaktion*, 2012.
20	Robert Schmidt, *Trimming, Mapping, and Optimization in Isogeometric Analysis of Shell Structures*, 2013.
21	Michael Fischer, *Finite Element Based Simulation, Design and Control of Piezoelectric and Lightweight Smart Structures*, 2013.
22	Falko Hartmut Dieringer, *Numerical Methods for the Design and Analysis of Tensile Structures*, 2014.
23	Rupert Fisch, *Code Verification of Partitioned FSI Environments for Lightweight Structures*, 2014.
24	Stefan Sicklinger, *Stabilized Co-Simulation of Coupled Problems Including Fields and Signals*, 2014.

Band	**Titel**
25	Madjid Hojjat, *Node-based parametrization for shape optimal design*, 2015.
26	Ute Israel, *Optimierung in der Fluid-Struktur-Interaktion - Sensitivitätsanalyse für die Formoptimierung auf Grundlage des partitionierten Verfahrens*, 2015.
27	Electra Stavropoulou, *Sensitivity analysis and regularization for shape optimization of coupled problems*, 2015.
28	Daniel Markus, *Numerical and Experimental Modeling for Shape Optimization of Offshore Structures*, 2015.
29	Pablo Suárez, *Design Process for the Shape Optimization of Pressurized Bulkheads as Components of Aircraft Structures*, 2015.
30	Armin Widhammer, *Variation of Reference Strategy - Generation of Optimized Cutting Patterns for Textile Fabrics*, 2015.
31	Helmut Masching, *Parameter Free Optimization of Shape Adaptive Shell Structures*, 2016.
32	Hao Zhang, *A General Approach for Solving Inverse Problems in Geophysical Systems by Applying Finite Element Method and Metamodel Techniques*, 2016.
33	Tianyang Wang, *Development of Co-Simulation Environment and Mapping Algorithms*, 2016.
34	Michael Breitenberger, *CAD-integrated Design and Analysis of Shell Structures*, 2016.
35	Önay Can, *Functional Adaptation with Hyperkinematics using Natural Element Method: Application for Articular Cartilage*, 2016.
36	Benedikt Philipp, *Methodological Treatment of Non-linear Structural Behavior in the Design, Analysis and Verification of Lightweight Structures*, 2017.
37	Michael Andre, *Aeroelastic Modeling and Simulation for the Assessment of Wind Effects on a Parabolic Trough Solar Collector*, 2018.